Andreia Lucia do Nascimento Pinto

Master in Molecular Biology in Health

New methods for the study of Primary Ciliary Dyskinesia

Dissertação para obtenção do Grau de Doutor em Biologia

Orientador: **Susana Santos Lopes**
Investigadora Principal, Faculdade de Ciências Médicas | Nova Medical School da Universidade Nova de Lisboa

Co-orientador: **Thomas Burgoyne**
Investigador Senior, Royal Brompton Hospital, Londres

Co-orientador: **Jaime Mota**
Departamento de Ciências da Vida, Faculdade de Ciências e Tecnologia da Universidade Nova de Lisboa

Júri:

Presidente: **Doutor Pedro Miguel Ribeiro Viana Batista,**
Professor Catedrático, Faculdade de Ciências e Tecnologia da Universidade Nova de Lisboa

Arguentes: **Doutor Kyriacos Kyriacou**
Professor in Biochemistry, Dean of Cyprus School of Molecular Medicine, Chipre

Doutora Jane Sarah Anne Lucas
Professor in Paediatric Respiratory Medicine, University of Southampton, Reino Unido

Vogais: **Doutor Pedro Miguel Ribeiro Viana Batista,**
Professor Catedrático, Faculdade de Ciências e Tecnologia da Universidade Nova de Lisboa

Doutor Duarte Custal Ferreira Barral
Professor Associado, Faculdade de Ciências Médicas | Nova Medical School da Universidade Nova de Lisboa

Doutora Susana Santos Lopes
Professor Associado, Faculdade de Ciências Médicas | Nova Medical School da Universidade Nova de Lisboa

FACULDADE DE CIÊNCIAS E TECNOLOGIA
UNIVERSIDADE NOVA DE LISBOA

July, 2021

Andreia Lucia do Nascimento Pinto

Master in Molecular Biology in Health

New methods for the study of Primary Ciliary Dyskinesia

Dissertação para obtenção do Grau de Doutor em Biologia

Orientador: **Susana Santos Lopes**
Investigadora Principal, Faculdade de Ciências Médicas | Nova Medical School da Universidade Nova de Lisboa

Co-orientador: **Thomas Burgoyne**
Investigador Senior, Royal Brompton Hospital, Londres

Co-orientador: **Jaime Mota**
Departamento de Ciências da Vida, Faculdade de Ciências e Tecnologia da Universidade Nova de Lisboa

Júri:

Presidente: **Doutor Pedro Miguel Ribeiro Viana Batista,**
Professor Catedrático, Faculdade de Ciências e Tecnologia da Universidade Nova de Lisboa

Arguentes: **Doutor Kyriacos Kyriacou**
Professor in Biochemistry, Dean of Cyprus School of Molecular Medicine, Chipre
Doutora Jane Sarah Anne Lucas
Professor in Paediatric Respiratory Medicine, University of Southampton, Reino Unido

Vogais: **Doutor Pedro Miguel Ribeiro Viana Batista,**
Professor Catedrático, Faculdade de Ciências e Tecnologia da Universidade Nova de Lisboa
Doutor Duarte Custal Ferreira Barral
Professor Associado, Faculdade de Ciências Médicas | Nova Medical School da Universidade Nova de Lisboa
Doutora Susana Santos Lopes
Professor Associado, Faculdade de Ciências Médicas | Nova Medical School da Universidade Nova de Lisboa

July, 2021

New methods for the study of Primary Ciliary Dyskinesia

ACKNOWLEDGMENTS

First and foremost I am extremely grateful to my supervisors, Dr. Susana Lopes and Dr. Thomas Burgoyne for their invaluable advice, continuous support, and patience during my PhD study. Their immense knowledge and plentiful experience have encouraged me in all the time of my academic research and daily life. Also want to thank NOVA University Lisbon, CEDOC, iMM-JLA and the Royal Brompton Hospital.

Two people essential on this journey were my oldest daughter Francisca, which gave me daily motivational speech, constantly checked on my progress and always said she believed in me, especially when she had no idea what was this or for what. And to Isabel, my youngster, for always giving her best not to disturb me, even when it was so, so tempting. They were the supporting team that made me crawl back to the surface every time I was in a bad place. And this work is for them. Not the words, but the meaning of it, the endurance and the perseverance behind it.

To my husband, Pedro, for never complaining, even during those times when I had to be left alone, when I was frustrated, grumpy and absolutely 'insuportavel'. He was always a strong pilar of serenity and balance.

'Mestre' Moura Nunes and 'Chefe' Pedro Branco were the white rabbits that led me inside the rabbit hole and allowed me to feel like Alice and discover the wonderland of Electron Microscopy, which I have been exploring for the past 11 years, To them, I want to leave the most sincere thank you.

To all the friends (impossible to go through the names without forgetting someone), some more engaged than others, some far in Portugal, but still so close, and others, my safe places in London. To my friends, a significant sincere acknowledgement, we still made it, through a pandemic, through the biggest ordeal of our generation.

A special thank you to Lisbon PCD Team, especially to Carolina Constant and Susana Lopes. Susana as someone always present ever since I discovered science. To Leonor Saude, who introduced me to cilia and zebrafish, and to Tania Carvalho, who fully supported me when I decided to enrol in this work still at iMM-JLA. To the London and Southampton PCD diagnosis teams for always making me feel included and always so helpful.

None of the works in this dissertation could have been possible without Tom, Ranjit, Amelia and Claire. To them, I owe the closing of this chapter. A special thank you to Tom for accepting this challenge. It was like having suddenly a big unlimited oxygen bottle.

Finalmente um obrigada carregado de amor e afeto aos meus pais e ao meu avô. Por terem estado sempre seguros, por nunca me terem feito preocupar nem divergir numa altura tão importante da minha vida. Quando estivermos juntos, vamos chorar abraçados,comer e beber e falar todos aos mesmo tempo, e no fim vamos ficar ligeiramente irritados, mas não faz mal. Obrigada por serem felizes e fazerem o que vos faz feliz, estando longe, essa é a minha maior recompensa.

SUMÁRIO

Os cilios e flagelos são projeções celulares encontradas nas células eucariotas, são altamente conservados entre espécies e envolvidos na locomoção e movimentação de fluídos. A Discinésia Ciliar Primária (DCP) é uma doenca genética autossómica recessiva dos cílios móveis, que tem como consequência várias manifestações clínicas. Estima-se que a DCP afete ~1 em cada 10.000 pessoas, mas é mais prevalente em grupos com marcada consanguinidade. A DCP está associada até à data a mais de 40 genes causadores de doença. O diagnóstico da DCP envolve a combinação de vários testes, entre eles a microscopia electrónica (ME), teste determinante na classificação de anomalias ciliares. Neste trabalho foquei-me nos cílios móveis e em como se classificam as derivações à estrutura considerada normal. Este estudo levou ao desenvolvimento de feramentas e diretrizes que tornam o diagnóstico de DCP por EM mais estandardizado, informativo e fidedigno. A DCP necessita de ser modelada em organismos vertebrados como o ratinho, a rã e o peixe-zebra (PZ) para melhor conhecimento dos seus mecanismos moleculares. O PZ é um bom modelo de DCP porque apresenta diversos órgãos ciliados durante os estados larvares (cílios moveis e imoveis) e tem, até agora, homólogos de todos os genes causadores da doença humana. Desta forma a utilização de peixes mutantes tem sido um bom contributo para compreender esta doença humana. Neste trabalho investiguei por ME dois tipos de cílios móveis do PZ concluindo que estes apresentam semelhanças estruturais conservadas com os cílios móveis das vias aéreas do ser humano saudável e com DCP.

Palavras chave: A Discinesia Ciliar Primária (DCP), peixe-zebra (PZ), cílios móveis, microscopia electrónica (ME), diagnóstico

ABSTRACT

Cilia and flagella are cellular protrusions found in eucaryotic cells, highly conserved between species and found in almost every cell type. Motile cilia are known for their motility properties and are involved in propelling and moving fluids. Primary ciliary dyskinesia (PCD) is an inherited autosomal-recessive disorder of motile cilia that results in several clinical manifestations. The estimated prevalence of PCD is ~1 per 10,000 births, but it is more prevalent in populations where consanguinity is common, it is currently associated with mutations in more than 40 genes. To diagnose PCD it involves a combination of tests, in particular, electron microscopy (EM) that is essential for determining the type of ciliary ultrastructural defect. In this work I have focused on motile cilia ultrastructure and how the differences in cilia can be identified and classified, through the development of tools and guidelines to make the quantification and analysis of cilia more reliable and informative. The differential diagnosis of PCD is complex but crucial, and the development of new potential targeted treatments is essential. For better investigating the molecular mechanisms underlying PCD, it has been modelled in several organisms like mice, frogs and Zebrafish (ZF). ZF is a teleost vertebrate used in many areas of research, and a well-known animal model. ZF embryos develop quickly and allow unique advantages for research studies owing to their transparency during larval stages. ZF has many ciliated organs and presents primary cilia as well as motile cilia together with homologs for all the disease causing genes. The use of mutant zebrafish has been contributing to the better understanding of PCD molecular aetiology. Here, I investigated whether zebrafish cilia are ultrastructurally suitable for the study of PCD and concluded that the motile cilia of zebrafish resemble the cilia in the human airway in healthy conditions and in PCD.

Keywords: Primary Ciliary Dyskinesia (PCD), zebrafish, motile cilia, electron Microscopy (EM), diagnosis

TABLE OF CONTENTS

LIST OF FIGURES

LIST OF TABLES

LIST OF ABREVIATIONS

-/-	Homozygous
+/-	Heterozygous
2D	Two-dimensional
3D	Three-dimensional
3D-SIM	Three-dimensional structured illumination microscopy
AAA	ATPases associated with diverse cellular activities
aa	Amino acid
ALI	Air-Liquid Interface
ALMS1	Alström syndrome protein 1
AR	Autosomal Recessive
ARMC4	Armadillo repeat containing protein 4
ATP	Adenosine triphosphate
BB	Basal bodies
BBS	Bardet-Biedl syndrome
BFS	Bovine foetal serum
BMI	Body mass index
BMP	Bone morphogenic protein
BS	Blocking solution
C11orf70	Chromosome 11 open reading frame 70
C21orf59	Chromosome 21 open reading frame 59
CBF	Cilia beat frequency
CBP	Cilia beat pattern
Cep20	Centrosomal protein 20
CEP290	Centrosomal protein 290
CF	Cystic Fibrosis
CCDC39	Coiled-Coil Domain Containing protein 39
CCDC40	Coiled-Coil Domain Containing protein 40
CCDC65	Coiled-Coil Domain Containing protein 65
CCDC78	Coiled-Coil Domain Containing protein 78
CCDC103	Coiled-Coil Domain Containing protein 103
CCDC114	Coiled-Coil Domain Containing protein 114
CCDC151	Coiled-Coil Domain Containing protein 151
CCDC164	Coiled-Coil Domain Containing protein 164
CCNO	Cyclin O
CDC20B	Cell division cycle 20B
CFAP57	Cilia and flagella associated protein 57
CFAP221	Cilia and flagella associated protein 221
CFTR	Cystic fibrosis transmembrane conductance regulator
CP	Central Pair
CRISPR	Clustered regularly inter-spaced short palindromic repeats
crRNA	CRISPR RNA
Cryo-ET	Cryo-Electron Tomography
DAPI	4′,6-diamidino-2-phenylindole
Dand5	DAN Domain BMP Antagonist Family Member 5
DC	Docking complex
DCP	Discinésia Ciliar Primária
DEUP1	Deuterossome assembly protein
DHC	Dynein heavy chain
DIC	Dynein intermediate chain
DLC	Dynein light chain
DNA	Desoxyribonucleic acid
DNAAF1	Dynein axonemal assembly factor 1
DNAAF2	Dynein axonemal assembly factor 2
DNAAF3	Dynein axonemal assembly factor 3
DNAAF5	Dynein axonemal assembly factor 5
DNAH1	Dynein axonemal heavy chain 1
DNAH5	Dynein axonemal heavy chain 5
DNAH6	Dynein axonemal heavy chain 6
DNAH9	Dynein axonemal heavy chain 9
DNAH11	Dynein axonemal heavy chain 11
DNAI1	Dynein axonemal intermediate chain 1
DNAI2	Dynein axonemal intermediate chain 2
DNAJB13	DnaJ shock protein family member B13
DNAL1	Dynein axonemal light chain 1
Dpf	Days post fertilization
DRC1	Dynein regulatory complex 1
DRC2	Dynein regulatory complex 2
dsDNA	Double strand DNA
DYX1C1	Dyslexia susceptibility 1 candidate 1
EM	Electron Microscopy
EPR	Electronic patient record
ET	Electron Tomography
FGF	Fibroblast growth factor
FOXJ1	Forkhead Box protein 1
Fps	Frames per second
GAS2L2	Growth arrest specific 2 like 2
GAS8	Growth arrest specific 8
GEMC1	Geminin coiled-coil-domain containing protein 1
HDR	Homologous Directed
HH	Hedgehog
HSVM	High-Speed Video Microscopy
HYDIN	Axonemal central pair apparatus protein
Hz	Hertz
Icos	Calcium oscillation
IDA	Inner Dynein Arm
IF	Immunofluorescence
IFT	Intraflagellar transport
kD	Kilodaltons
KS	Kartagener' syndrome
KV	Kupffer's Vesicle
LC	Lead Citrate
Lefty1	Left-right determination factor 1
Lefty2	Left-right determination factor 2
LLE	Locally linear embedding
LPM	Lateral Plate Mesoderm
LM	Light Microscopy
L-R	Left-Right
LRRC6	Leucine reach repeat containing 6
LRRC56	Leucine reach repeat containing 56
MATLAB	Matrix laboratory
MC	Mucociliary clearance

MCC	Multiciliated cells
MCIDAS	Coiled-coil domain-containing protein multicilin
MDT	Microtubular Doublet
ME	Microscopia Eletrónica
MIP	MT inner protein
µm	Micrometres
MO	Morpholino
mRNA	messenger ribonucleic acid
MT	Microtubule
MV	Microvilli
MYB	Myeloblastosis transcription factor
N-DRC	Nexin-Dynein Regulatory Complex
NEK10	Never in mitosis A-related kinase 10
NGS	Next generation sequencing
nm	Nanometres
NME5	Non-metastatic cell 5
nNO	Nasal Nitric Oxide
NO	Nitric Oxide
Nodal	Nodal growth differentiation factor
NRDS	Newborn Respiratory Distress Syndrome
OB	Olfactory bulb
ODA	Outer Dynein Arm
ODAD2	Outer dynein docking complex subunit 2
ODAD4	Outer dynein docking complex subunit 4
OE	Olfactory epithelium
OFD1	Oral-facial-digital syndrome 1 protein
OID	Outer-inner dynein
OMP	Olfactory marker protein
OOD	Outer-outer dynein
OP	Olfactory pit or placode
OR	Odour receptor
OSN	Olfactory sensory neurons
Otx2	Orthodenticle homeobox 2
PAM	Protospacer adjacent motif
Pax6	Paired box 6
PBS	Phosphate buffer saline
PCA	Principle component analysis
PCD	Primary ciliary Dyskinesia
PCP	Planar cell polarity
PF	Protofilaments
PFA	Paraformaldehyde
PHD	Potential HYDIN defect
PICADAR	Primary Ciliary Dyskinesia rule
PIH1D3	PIH1 domain-containing protein 3
Pitx2	Paired like homeodomain 2
PKD	Polycystic Kidney Disease
PKD2	Polycystin 2
PZ	Peixe-zebra
qPCR	Quantitative polymerase chain reaction
RFX	Regulatory factor X
RFX1	Regulatory factor X1
RFX2	Regulatory factor X2
RFX3	Regulatory factor X2
RNA	Ribonucleic Acid
RPGR	Retinitis pigmentosa GTPase regulator
RS	Radial spoke
RSPH1	Radial spoke head component 1
RSPH3	Radial spoke head component 3
RSPH4A	Radial spoke head component 4 homolog A
RSPH9	Radial spoke head component 9
SBFSEM	Serial block face scanning electron microscopy
SEM	Scanning Electron Microscopy
SIM	Structural illumination microscopy
Six3	SIX homeobox 3
sgRNA	Guided RNA
SNP	Single nucleotide polymorphism
SPAG1	Sperm associated antigen 1
SPEF2	Sperm flagellar 2
Ss	Somites
STK36	Serine/Threonine kinase 36
TEM	Transmission Electron Microscopy
trcrRNA	Trans-activating crRNA
TTC12	Tetratricopeptide repeat domain 12
TTC25	Tetratricopeptide repeat domain 25
TXNDC3	Thioredoxin domain containing protein 3
TZ	Transition zone
UA	Uranyl Acetate
UAZ	UA-zero
VUS	Variant of uncertain significant
WNT	Wingless-related integration site
ZF	Zebrafish
ZMYND10	Zinc finger MYND-type containing 10

CHAPTER 1

Introduction

Cilia and Flagella

Cilia and flagella are finger-like organelles that protrude from the apical part of eukaryotic cells [1] [2] [3–7] and are present in nearly every cell type [8]. For most ciliated cells, this happens in a stationary phase of the cell cycle [9]. The only exception is in insect gametes or unicellular ciliates or flagellates [9]. During cell division, the centrosome is recruited to form the mitotic spindle, and so, in most cells, the cycle of ciliogenesis is coordinated with the cell cycle [9]. There are two main types of cilia: motile cilia, in this group, there are two main subtypes of cilia regarding their structure, cilia that have a 9+2 structure, meaning they have nine microtubule doublets (MTD) and a central pair complex (CP) that is formed by the combination of two microtubules, these cilia or flagella beat in a specialised fashion, by a series of bends, originating at the base and propagating towards the tip. Beating can be planar or three-dimensional (3D), and it can be described according to its amplitude and wavelength (pattern) and frequency [10]. The other subgroup of motile cilia are those that have a 9+0 structure, nine MTDs but no CP, characterised by a rotation planar movement [11,12,13] (panel on the left in Figure 1).

On the other hand, there are non-motile primary cilia in almost every cell, where several ultrastructural configurations can be found (mainly 9+0 and 9+2 lacking dynein motor for movement) depending on the organism, the tissue and the function, and these cilia are usually involved in sensory functions [13] (panel on the right in Figure 1). The ultrastructure of the cilium has been widely studied by researchers like Kozminski, who reported the importance of intraflagellar transport (IFT) in *Clamydomonas reinhardtii* flagella [14]. Bui and Ishikawa, showed in their work the benefits of cryo-Electron Tomography (Cryo-ET) to study molecular structures of cilia and flagella, since it provides a sub-atomic resolution of around 30 Å. Daniela Nicastro lab has been studying cilia and flagella in detail, through the use of Cryo-ET. In Nicastro's lab, they analysed in detail the ciliary axonemal components of *Chlamydomonas reinhardtii* and sea urchin, they also described new important molecular components of motile cilia with extra detail, structures like the CP and the dynein machinery [15,16,17]. Gaia Pigino lab, has been focusing on the studies of eukaryotic cilia of mammals using the same high resolution techniques and Volume Electron Microscopy (EM) workflows [18]. Through the same advance techniques Stepanek and Gaia described in detail the process of Intraflagellar transport (IFT) using a time resolved correlative fluorescence and 3D-electron microscopy (3D-EM) approach. They showed the asymmetric dynamics of IFT, which carries ciliary components along the microtubules during the assembly and disassembly of the cilium [19]. Jordan et al. also showed the importance of cargo transport along the microtubules in cilia and flagella. In recent work, they stressed the important role of anterograde and retrograde Intraflagellar transport (IFT) by *kinesin 2* and *dynein 1b,* respectively, and the crucial role this coordinated movement plays in cilia assembly and in transporting specific components back to the cell body [20].

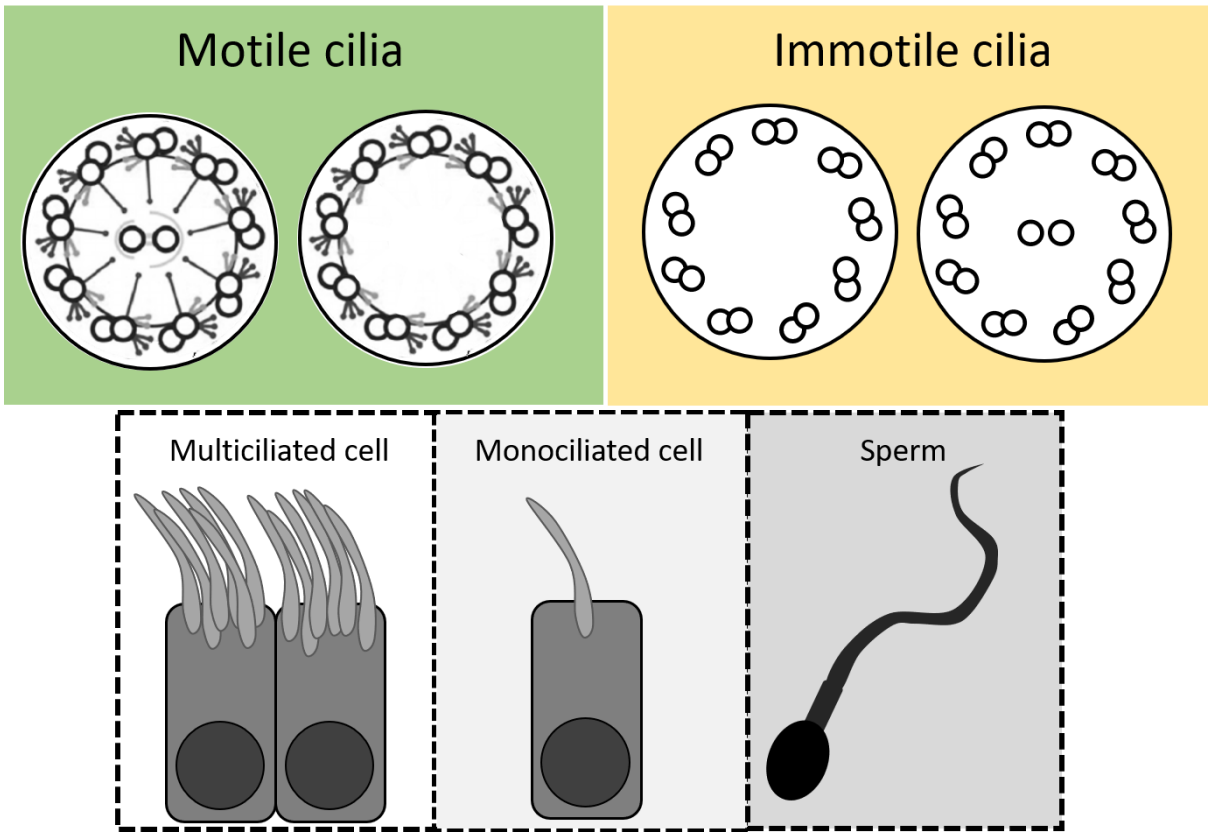

Figure 1. Most common types of cilia found in vertebrates (mammals, fish, and frogs). Top left: Motile cilia showing 9+2, that can be found in airway or lungs, epidermis of some organisms, reproductive system, brain ventricles and spinal cord, laterality organ and kidney and vestibular organ of zebrafish [13]; and motile 9+0 conformation present in spinal cord [13], and in the laterality organ in zebrafish [21]; top right: non-motile primary cilia with 9+0 ultrastructure found in most signalling cilia and retina, and in the auditory/vestibular organ only described in mammals [22]; and non-motile 9+2 organisation, that were already identified in auditory vestibular organ of mammals and in the rat olfactory neurons multiciliated cells [23] and adult zebrafish olfactory neuron multicilia [24]; bottom panel: three main types of ciliated cells, left to right: multiciliated cells, depending on the organ, can nucleate dozens to hundreds of cilia protruding on the apical end of the cell [25] multiciliated cells are most commonly found in the airway, in the reproductive system and in the brain [13], but also found in the epidermis and kidney of some organisms (*Xenopus laevis* [26], and zebrafish [27]); monociliated cells are associated with the laterality organ, and the signalling cilia [13], but were already described in brain and spinal cord of *X. laevis* and zebrafish respectively [2827], in kidney and in the auditory vestibular organ in both mammals and aquatic organisms [13]; the sperm tail is part of the reproductive system of vertebrates (and some invertebrates such as *Drosophila melanogaster* [29]), the flagellum moves in a whip-like motion and measures around 50-60 µm [13] .

Cilia are commonly classified as motile or non-motile, however, this is just the tip of the iceberg, as each group accommodates numerous subtypes that need to be addressed and recognised in different organs and organisms [13]. Eukaryotic cilia evolution traces back in billions of years with the existence of a known common ancestor [30]. But the evolutionary path of cilia is not linear, an example is the homology found between the algae *Chlamydomonas reinhardtii* and the human cilia (genes of the central apparatus). Adding to that, IFT [30] proteins are also known to be present in distant branches of phylogeny (insect, parasites and algae [31]). Mitchell (2007) showed in his work [32], where he describes the evolution of cilia in eukaryotic cells, evidence of a last common eukaryotic ancestor presenting a 9+2 flagellum anchored to a basal body or similar structure in the cell body and requiring IFT for axonemal assembly [30]. Evolutionarily, the different cilia types may arise from loss of ciliary components no longer needed for the organism or cell type, as is the case of loss of rows of dyneins, loss of central

pair, radial spokes and some microtubule doublets. Given the case of completely non-motile sensory cilia, all the components that are essential for movement or propelling may be absent, leaving only the ciliary membrane and the microtubule doubles that will support IFT and receptor localisation [30,32].

It is becoming clear that the different morphology leads to specialised function. As examples of complex ciliary evolution, function and structure, some parasitic flagellated do not require full flagellar motility for propelling or locomotion as a consequence of simplified flagellar structures (3+0), with the absence of central pair (CP) or radial spokes (RS), as what happens to the known simplest motile eukaryotic parasitic protozoan *Diplauxis hatti* [33]. The same features are observed in the embryonic left-right organiser (LRO) 9+2 motile cilia in vertebrates, where a unidirectional fluid current is generated to guarantee the correct establishment of left-right asymmetry [34]. A Similar feature is also seen in Eel spermatozoa. In this case, the 9+0 axoneme provides the organism a propelling rapid progression, result of a left-handed helicoidal wave propagated distally towards the tip of the flagellum [35]. Some insect sperm axonemes (for instance, those from marine invertebrates that adapted to land environment after having achieved internal fertilisation), that lack RS and CP, show instead multiple doublets (hundreds), which might be a possible adaptation to a long dysfunctional axoneme [36]. This example shows how in evolution, the cilium was conserved to accommodate the RS, CP regulatory complex. However, if any of these components are not needed, successful axonemes have evolved, showing alternative structural patterns [36].

The evolution of cilia and its relation to function and variation in ultrastructure will remain a fundamental question. It is accepted that the ancestral cilia are hybrids with both motility and sensory functions as seen in *Chlamydomonas* and *Tetrahymena*, and some organs and organisms show this feature today [37,38].

Nonetheless, in this work, the most relevant types of cilia will be described. The way they are assembled and maintained and the link between their most conserved components and ciliary disease.

Cilia biogenesis

Despite the focus of this work on motile cilia, non-motile primary cilia play an important role in vertebrates' development and require introduction and summary for later understanding of ciliogenesis [6]. Primary cilia, also called sensory cilia, are considered dynamic structures that assemble and disassemble coordinated with the cell cycle. Cilia form when the cell becomes quiescent and begins to disassemble when the cells re-enter the cell cycle [39]. Primary cilia are generally short and lack some of the ciliary components. Sensory or primary cilia have special characteristics that allow them to successfully sense the environment around the cell, either fluid or light, odours or signalling [40]. The more extensive group of primary cilia are the solitary sensing cilia, with a 9+0 ultrastructure (containing 9 peripherical doublets and no CP) that are found on most quiescent or post-mitotic cells throughout the vertebrate body (some differentiated cell lineages lack primary cilia such as lymphocytes, hepatocytes, mature adipocytes and skeletal muscle) [40]. Examples of non-motile cilia with 9+0

configuration are the monocilia that protrude from the mammalian kidney tubules epithelial cells, these cilia have a mechanosensory role [41]. Similar monocilia are found in the embryonic LRO of vertebrates. These are believed to sense leftward fluid flow that is generated by the motile cilia in the same cavity (more attention will be given to the motile cilia of the LRO, further in this chapter) [42]. Non-motile cilia are also known to be found in the retina nose and ears [43]. In this group of cilia, the kinocilia stand out as a particular type of cilia found in the inner ear. This cilium differs from the other sensory cilia not only because it presents a 9+2 immotile profile (the kinocilium shows an organisation of 9 microtubular doublets and a CP, with absent dynein arms), but also because it has a precise role as a generator of accurate planar polarised arrangement of stereocilia, which are bundles of actin-based microvilli involved in earing and balance [44,13]. Primary cilia are crucial from the early stages of development and known to be involved in embryonic patterning, where they are known to regulate the activity of important morphogens, specially by those of the *HH* (hedgehog) family. Non-motile primary cilia have a huge impact in the development and homeostasis of many tissues [6].

The IFT, an evolutionarily conserved mechanism first described in *Chlamydomonas,* is an essential mechanism for the assembly and maintenance of cilia [40]. Evidence came in the early nineties, with the discovery of a mouse homologue of the *Chlamydomonas IFT88* gene that was found mutated in a model of Polycystic kidney disease (PKD). In this case, the cells lining the urinary epithelium failed to assemble primary cilia completely. This was the first evidence of the importance of primary cilia [6]. However, IFT is not the only mechanism hypothesised to be involved in ciliogenesis, experiments suggest that the Planar cell polarity pathway (*PCP*) signalling pathway might be involved in the regulation of the formation of cilia and ciliary position [6]. *PCP* signalling pathway is a powerful development regulator of directional cell behaviours, and it is considered a non-canonical *WNT* (wingless-related integration site) pathway due to the involvement of *WNT* ligands. An example of the connection between primary cilia and the *PCP*, is again the kinocilium, in normal conditions the kinocilium is always oriented on the lateral side of the developing cell. The position of the kinocilium regulates the polarity of the chevron of stereocilia on the hair cell. The core components of the non-canonical *WNT* pathway are required for the polarity of the hair cells [6,40].

Intraflagellar transport (IFT) is a shared mechanism between primary non-motile cilia and motile cilia. IFT is crucial for the assembly and maintenance of the axoneme and mediation of the bidirectional transport of both structural and signalling molecules along the microtubular axoneme [45]. In this process two significant complexes are involved, IFT-A (6 subunits) and IFT-B (10 subunits), that mediate retrograde and anterograde trafficking, respectively, along the ciliary axoneme. These IFT complexes form linear arrays or “trains” that are transported to the tip of the axoneme, in an anterograde IFT powered by *kinesin-2* motors [46]. The retrograde IFT back to the base of the axoneme is driven by cytoplasmic *dynein-2* [47]. Focusing on the IFT-B complex, some of its subunits are essential for ciliogenesis while others are dispensable for ciliogenesis but important for trafficking [45]. As an example of the importance of IFT, in the IFT-B complex, when specific subunits, like IFT20, IFT38 or IFT88 are knocked out, this results in a lack of cilia, probably linked to deficient incorporation of tubulin [45,48]. In

opposition, knock out of IFT B complex subunits IFT25, IFT27, IFT56, located in the periphery of the axonemal shaft, seems only to impair the trafficking of certain ciliary proteins [49–51]. This stresses the importance of the IFT in the assembly of cilia their morphology and function [45,52,48]. Another player in the IFT mechanism is the BBSome. The BBSome consists of a third coat like complex and refers to eight Bardet-Biedl Syndrome (BBS) proteins [53,54]. BBS was the first-ever syndromic ciliopathy to be described and is characterised by phenotypic heterogenicity. Some of its clinical manifestations are retinal degeneration, polydactyly, cystic kidneys, obesity, anosmia and male infertility [55]. Twenty-two genes account for more than 80% of all known patient mutations, suggesting an enriched molecular pathway that converges with the BBSome function [56]. Unlike the IFT-A and IFT-B, which can be separated into dissociated complexes, BBSome appears to remain octameric in all known conditions, so the deletion of most of the subunits completely collapses the complex [53]. BBSome seems to be tightly regulating Hh pathway in many organisms, working as an essential contributor for the cilia stability [53] and is required for the ciliary export of activated signalling receptors [57]. Even though mutations in BBS genes generally impair ciliary function, it does not interfere with ciliogenesis [54].

Developmental biology and extensive human genetics studies had been revealing much of the function of cilia. Abnormalities, or lack of primary cilia, have been vastly associated with well-known human cystic kidney diseases [58] and with other rare recessive human syndromic disorders (like BBS) known as ciliopathies. Syndromic ciliopathies are caused by mutations in proteins co-localising with cilia and basal bodies and cause clinical manifestations such as cystic kidneys, mental retardation, blindness and various developmental malformations [6]. Primary cilia are also known to be involved in metabolic disorders like obesity or diabetes [59].

So far, it is estimated that there are 180 known ciliopathy-associated proteins and more than 250 ciliary proteins that might be good candidates as ciliopathy proteins since they can be in the pathway to important cascades involved in ciliopathies [37]. In addition, advances in genetics based on many patients' data allow the search and discovery of new genes and new mutations that might be involved in the onset of a ciliopathy and help identify new ciliopathies [60].

The motile cilia, on which this work will focus, are usually long, finger-like structures with well-described ultrastructure and functions [3,15,18]. Motile cilia have a classical, but not exclusive 9+2 ultrastructure and the 9 microtubular doublets are outlined by chains of dynein motor proteins that use energy from the ATP hydrolysis to generate the rhythmic movement of the axonemes [3]. Among the motile cilia, are the monocilia (existing as a single cilium per cell) such as the cilia of the proximal and distal regions of the pronephric kidney in the zebrafish embryo and the flagellum of the sperm tail. The sperm tail is determinant for the movement of the sperm. These cilia are characterised by wavelike or corkscrew kinetics to generate fluid movement or cellular locomotion [27]. Another type of motile monocilia is those found in the LRO of vertebrate organisms, namely, the ventral node in mammals [61], the *gastrocoel* roof plate (GRP) in frogs [62] and the Kupffer's Vesicle (KV) in teleost fish [42]. Both ultrastructural presentations (9+2 and 9+0) have been described in teleost fish [63]. Cilia from the LRO structures show either a planar rotational movement or a wavy pattern and establish a counter

clockwise-directed fluid flow within the embryonic structure [64]. Finally, the multiple motile cilia protruding from multiciliated cells, which are known to harbour from 2 to hundreds of motile cilia [13]. These cilia are designed to move high viscosity fluid. As an example, multi motile cilia can be found projecting from epithelial cells of the respiratory tract, reproductive system and those from ependymal cells in the central nervous system of mammals. 9+2 arranged cilia beat metachronically with a planar stroke to clear viscous fluid [65,66]. Albeit the function of motile cilia is mainly mechanical, they can also display sensory functions [67].

The leading recognised players in cilia biogenesis signalling pathways are the transcription regulatory complex formed by the *RFX* (Regulatory Factor X) and the *FOXJ1* (Forkhead box protein J1), *Hh*, *FGF* (Fibroblast Growth Factor*), WNT* and *NOTCH* [13]. *RFX* comprises a family of transcription factors that were shown essential for directing the expression of core components of all types of cilia (*Rfx1-4*) [68]. Mutation in *Rfx2* show different phenotypes depending on the cell type and organism, and the abnormalities can range from mild to more severe (short and, or dysfunctional cilia) [69,68]. *RFX1* and *RFX2* had been described by Purvis et al. (2010) to regulate the transcription of *ALMS1 (*Alström Syndrome Protein 1*),* a gene that encodes a basal body-associated protein found to be mutated in the ciliopathy Alström Syndrome Mice with *Rfx3* deficiency showed left-right asymmetry defects [70]. *FOXJ1* is an extremely important factor for the biogenesis of motile cilia [13]. Knockdown experiments in different organisms revealed complete loss of all motile cilia of the airway, choroid plexus, and left-right asymmetry defects [71,72]. Several studies convey that, based on loss of function phenotypes in multiple model organisms, the *RFX* factor seems to be required to assemble both motile and immotile cilia, while *FOXJ1* is more likely to be involved in the assembly of motile cilia [28,68,77–79,69–76 80–83,84]. However, both *RFX* and *FOXJ1* interact with each other and regulate signalling pathways towards ciliogenesis [69,74,80,85]. It was previously described that in zebrafish, mouse and chick, the expression of *Foxj1* in the ciliated floor of the spinal cord is induced by midline Hh [69,86]. Additionally, *Foxj1* and *Rfx2* are induced by *FGF* in zebrafish Kupffer's vesicle [87]. Furthermore, in many zebrafish tissues, *WNT* signalling seems to be acting downstream of the *FGF,* directly controlling *Foxj1* [88]. Other than *Hh*, *FGF* and *WNT* signalling, *NOTCH* signalling has been linked to ciliogenesis and motile cilia differentiation, and it has been implicated in the proper *Foxj1* expression and ciliogenesis in the LRO of the zebrafish [89]. *NOTCH* signalling has a crucial role in specifying precursors of the motile multiciliated cells in the zebrafish, mouse and *Xenopus*, repressing the multiciliated cell fate [73,76,90,91].

In summary, the *RFX/FOXJ1* transcriptional cassette is essential for cilia biogenesis. The cassette is modulated by different transcriptional factors and signalling pathways to generate different cilia [13]. *NOTCH* and *WNT* signalling induce the formation of rotational motile monocilia in the LRO of zebrafish [89] and the GRP of the *Xenopus* [92]. In addition, *PCP* genes independently regulate cilia polarity in the mouse node [93]. Cruz and colleagues (2010) described how *Hh* induces the generation of rotational motile cilia in the floor plate of zebrafish and mouse [86]. It was also previously reported that *NOTCH* signalling acts as an inhibitor of the airway multicilia in mouse, the epidermal cilia in *Xenopus* and the cilia from the zebrafish pronephric duct [76,90,91]. The cascade is alternatively activated by

MCIDAS (coiled-coil domain-containing protein multicilin) and *MYB* (myeloblastosis transcription factor), which activates the *RFX* and *FOXJ1* factors [73,76,90,91]. According to Stubbs (2012), *MCIDAS* and *MYB* regulate genes required for basal body synthesis and docking, this happens independently from the *RFX/FOXJ1* cassette [73].

Ciliogenesis of multiciliated cells

Multiciliated cells (MCC) are epithelial cells with unique features. A single MCC projects n+ cilia from its cell surface [25]. These cilia, with a classical 9+2 motile profile, are indispensable for respiratory, renal, brain and reproductive processes in vertebrates [25]. In humans, these cells can be found in the airway to clear the mucus and pathogens through a mechanism called mucociliary clearance (MC) [25]. These cells are around 20-µm high cylindrical or pyramidal cells that carry about 200-300 motile cilia across the apical surface, measuring around 6 µm [94]. Multiciliated cells can also be found in the choroid plexus and the ependyma of the brain to move the cerebrospinal fluid and in the efferent ducts and oviducts for gamete transport [25]. Depending on the organ, a few dozens to hundreds of cilia beat in a coordinated, directional fashion to generate fluid motion [25,95].

In order to make hundreds of motile cilia protruding from a single cell, it is first essential to generate hundreds of basal bodies (BB) from which effective ciliary axonemes will protrude [96,97]. Biogenesis of BB in MCCs consists of a *de novo* process; BB are generated from procentrioles formed from deuterossomes, which consist of globular electrodense structures that work as organising centres [96,97]. It was already published that *FOXJ1* is not required for the generation of multiple basal bodies but rather involved in their docking to the cellular apical region, close to the membrane, observed by TEM as a random distribution of the BB when *Foxj1* is absent [71]. Furthermore, other previous TEM studies showed that loss of *Foxj1* targets 9+2 motile cilia, not interfering with 9+0 non-motile cilia [71].

MCIDAS is a currently well-known protein required to form MCC in the frog epidermis and the airway of mice [73]. In both cases, *MYB* acts downstream of *MCIDAS* to generate multiciliated cells. *MCIDAS* and *MYB* seem to be functionally redundant, however, isolated impairment of *MYB* does not entirely disrupt ciliogenesis in the airway [91] but seems to strongly interfere in the formation of multiciliated cells in the zebrafish kidney [98]. Previous loss of function and overexpression experiments provided evidence of *MCIDAS* and *MYB* acting in a single pathway where MCIDAS acts downstream of *NOTCH* but upstream of *MYB* to i) activate genes essential for the BB formation and ii) to switch on *FOXJ1* and activate the cascade that will lead to BB docking, ciliary outgrow and motility [73,91,98]. More recently, another mediator of ciliogenesis was identified, the *GEMC1* (geminin coiled-coil-domain containing protein 1), which is believed to act upstream of *MCIDAS*, and be a critical regulator of multiciliated cell differentiation program that is activated upon *NOTCH* inhibition [99–102] (part of the pathway mentioned above). Lack of *GEMC1* in the mouse shows absence of MCC in every tissue where they usually are found, leading to hydrocephalus and infertility. The animals' short life span might explain the difficulty in accessing the phenotypical effects in the airway [99,101]. On the other hand, ALI cultures from *Mcidas* deficient mice showed no increased expression in genes involved in centriole amplification namely *CCNO* (cyclin O), *CDC20B* (cell division cycle 20B), *CCDC78* (coiled-coil domain

containing 78)*, DEUP1* (deuterossome assembly protein 1), indicating that *GEMC1* alone is not enough to activate those genes under its normal physiological regulation [103]. Recently, Lu et al. (2019) proposed a hypothesis that explains this process: *GEMC1* activates *MCIDAS* (and other key transcription factors) to promote MCC fate, and *MCIDAS* subsequentially activates the expression of genes required for ciliogenesis [103].

There are still many unknown links regarding the ciliogenesis of MCCs, as reviewed very recently by Lewis and Stracker [104]. For instance, how the inhibition by *NOTCH* seems to activate the *GEMC1* through an unknown mechanism; how *CCNO* mutants show elevated levels of *MCIDAS* expression, suggesting perhaps there is a negative feedback role of *CCNO*, a mechanism that remains to be determined. It is also not certain which proteins and processes precisely regulate the deuterossome formation. In addition, the molecular crosstalk between the transcription factors known to be playing a role in cilia biogenesis (such as *FOXJ1, MYB* and *RFX*) and the dynamic processes (BB and cilia formation) and the interaction with the *PCP*, remains unclear [104].

Ciliogenesis is a complex multifactorial process, and most of it is still unclear, especially the way the factors and processes interact and evolve. Important factors are certainly involved in the ciliogenesis of both motile and non-motile cilia, such as IFT, and that the *Hh* signalling is actively involved in the biogenesis of non-motile [13]. In the motile cilia biogenesis *FGF, FOXj1/RFX, GEMC*1, *CCNO* and *MCIDAS* are essential to produce functional motile cilia both in mono and multiciliated cells [21,88,100,101].

Motile Cilia components

The cilium projects from the cells as a structure called the ciliary axoneme [105]. The cilium attaches to the cell at the BB, has a transition zone (TZ) and finishes in the ciliary tip [106]. BB are formed by microtubules (MT) arranged in a ninefold symmetry [107]. The BB is formed by the mother centriole that approaches the cell membrane in a docking process. The BB will generate a cilium with a special membrane that starts as a lipidic vesicle on top of the mother centriole [108]. In multiciliated cells, the centrioles (two in S-phase for cell division) replicate to increase the number of cilia projecting from the cell membrane, and this occurs by autonomous replication, as in mitochondria and peroxisomes [106,105].

Ciliary base

The centrioles are microtubule (MT) based organelles framed with triplet arranged in nine-fold symmetry. Centrioles are required to form the cilium and the centrosome [109]. Centrosomes are crucial for microtubule organisation and spindle formation in cell division and serve as a template of BB for posterior cilia or flagella formation [109], which happens upon centrosome recruitment during the G0/G1 phase of the cell cycle [110].

The cilium can be segmented into two main regions, the 'ciliary base' and the 'ciliary shaft' [111]. The base is composed of the BB, TZ and ancillary structures that anchor the BB to the cytoskeleton and cell membrane [112]. The base nucleates into the protruding shaft provides stability and mediates essential elements for trafficking along the axoneme [107,113,114].

Like the centriole, the BB has a nine-fold triplet conformation (organised in A-, B- and C-tubules [115]), with an average diameter of 250 nm and an overall length of around 600 nm [116]. The MT triplets span longitudinally for about 400 nm (proximal to distal), where the C-tubule terminates (marked in the longitudinal scheme of the BB in Figure 2). The A and B tubules continue as doublets for about 150 nm until the TZ or plate, the area designated between the ciliary and BB MT [115,117,118]. A molecular mechanism was described by Rasi (2009) involving the severing of the MT in the TZ and *katanin*, a candidate player for the deciliation in the TZ in *Chlamydomonas reinhardtii* [119]. The proximal end of each triplet microtubule is connected to a structure called the cartwheel (visible in the schematic cross-section in Figure 2). Any missing part of the cartwheel structure will disassemble the nine-fold symmetry, stressing the importance of the cartwheel for the stability of the BB [120]. The cartwheel was also connected to the TZ by Ishikawa as a star shape structure connected to the inside of the MTD in an area close to the interface with the MT triplet [3].

Visible, protruding from the A-tubule, are electrodense structures known as A-tubule feet. These feet are located along the wall of the triplets projecting towards the lumen of the BB barrel [115,118]. The A-tubule feet present characteristic 8 or 16 nm periodicity (visible in the schematic longitudinal view in Figure 2, as triangles facing the lumen of the barrel, marked with arrows) [116]. The region containing the A-tubule feet starts at about 100 nm from the triplet proximal end (towards the cell body, bottom region in Figure 2 longitudinal view), spans for about 250 nm and terminates at about 45 nm before the triplets turn into doublets. This section altogether forms the central core of the BB [116].

Regarding the structure of the MT, the A-tubule is a complete MT arranged by 13 protofilaments (PF). The organisation of the PF starts from the lumen of the BB and numbers clockwise (A1-A13) [121]. PF A10 is the location where the B-tubule joins with the A-tubule. PF A10 to A13 seemed to be shared by both A- and B-tubule and are described as partition PF. The B-tubule contains 10 PF, again numbered clockwise and starting from the outside surface of the MT triplet. The C-tubule has also 10 PF and PF1 starts from the PF B4 and is numbered clockwise. PF B5 to PF B8 are believed to partition with the PF of the C-tubule. This detailed description of the BB triplet was done by Li and colleagues (2012) using cryo-ET, and posterior pseudo-atomic model of the tubulins within the triplet, as a mask to subtract its density from the 3D density map. Through these elaborate methods, they were able to access a resolution of 33 Å [116]. This allowed the visualisation and confirmation of non-tubulin components associated with the triplet (previously shown by Keller (2005) the existence of nearly 50 non-tubulin components [122]). Several filamentous and protein structures were segmented, protruding from the MT triplet [116]. For this section, I will only focus on the observation of a cone-shaped density attached to the luminal side of the PF A5, with 8 nm periodicity, which is believed to work as a stabiliser for the A-tubule and/or as part of the structures that connect to the neighbour triplet. This density is like what was observed by Nicastro in the axonemal doublet [15,123,124].

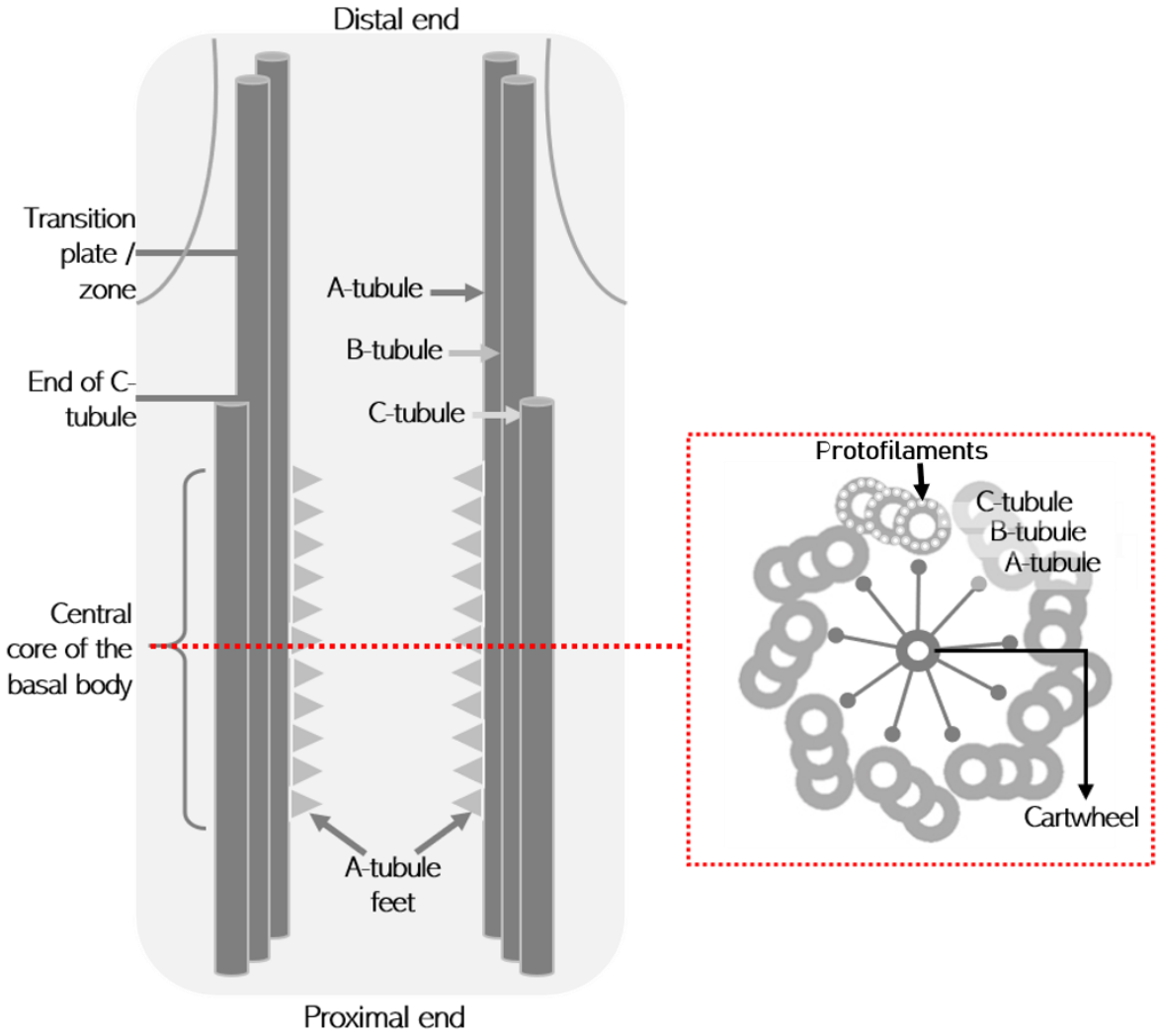

Figure 2. Schematic representation (not scaled) of a BB presented longitudinally and a cross-section through the central core of the BB. The longitudinal scheme is across the centre of the BB barrel. The proximal end is at the bottom, and the distal end presents at the top. 'The A-tubule feet' are marked with the arrows and schematised as triangles. The cross-section scheme shows the nine-fold triplet MT organisation containing the PF, configuration of A- B- and C-tubules and the internal cartwheel [116].

The 'Ciliary shaft' - microtubules, motor dyneins and nexin-dynein regulatory complex

The 'ciliary shaft' is composed of the ciliary axoneme that protrudes from the cell measuring around 7 µm in length and ~0.3 µm in diameter [94]. Starting from the distal end of the TZ elongates to the extracellular region. The axoneme is involved by the ciliary membrane and has enclosed a set of polymerised tubulin molecules (α and β-tubulin) organised in PF [3,7,15]. The PF are arranged in MT and configured inside the ciliary axoneme as a nine-fold set of MT doublets [2]. These MTs are composed of two PF loops; A-tubule, containing 13 tubulin PF [15], parallel to the axis of the tubule without twisting [125]. The B-tubule is slightly larger than the A-tubules and is considered an incomplete tubule, containing only 11 PF [15]. Some authors refer to the B-tubule as containing 15 PF, numbering the partition zone between A and B tubules [3,116]. Cryo-ET studies describe PF B11 as being thinner, leading to some

confusion in the classification of the structure (the exact number of PF) [15]. Decorating the MTD are dynein motor protein subtypes, divided into outer and inner arms (ODA and IDA). These arms are periodically repeated on each outer doublet MT (A-tubule [3]). Dyneins are actively involved in the motion of the axoneme, however, cytoplasmic dyneins are responsible for the transport of nucleotides, proteins and organelles along the axoneme (plus to minus end [3])

Axonemal dyneins are organised in two rows along each MTD [15]. All dyneins have one or more Dynein Heavy Chains (DHC) of >500 kD each; one or more Dynein Intermediate Chains (DIC) ranging from 45 kD to 14 kD; and 1 to 10 Dynein Light Chains (DLC) that can range from around 8 kD up to 28 kD [126]. The dynein motor domains weighting around 350 kD, are located in the C-terminal region of the DHC and have a direct relationship with the family of ATPases associated with diverse cellular activities (AAA) [127]. The AAA family is composed of 6 AAA domains consisting of ~3000 amino acids, making the dynein motor a gigantic ATP (adenosine triphosphate) driven motor [128].

High-resolution ultrastructural studies (around 4 nm image resolution limit) conducted by Nicastro et al. in *Chlamydomonas* and sea urchin gave great insight into axonemal components configuration [15]. Their studies confirmed the 24 nm axial periodicity of the ODA (~400kD [129]) as well as IDA complex and RS arrangement within the axoneme's 96 nm longitudinal repeat [16,127,130] (Figure 3). It is believed that the ODA link each other along the length of the axoneme through a group of protein subunits called the outer-arm Docking Complex (DC) [131]. The DC creates a small, pointed structure on the A-tubule at the base of the ODA. The typical presentation of the ODA occurs due to the elongated DC polypeptides, which are thought to join the ODA at every 24 nm interval [15]. Another critical component of the dynein motor is the Outer-Outer Dynein (OOD) linker [15]. These structures are believed to be bridging from the ODA motor domain closer to the A-tubule in the peripheral motor domain of the next ODA. The linkers seem to be ideally positioned to control dynein activity along the outer doublets during the waveform propagation [15]. Another linker identified by cryo-ET was the Outer-Inner Dynein (OID) linker. The presence of these linkers bridging the ODA and IDA (at the I1/f), suggests the existence of a mechanism that coordinates IDA and ODA activities. For instance, signalling received from the CP and RS is transmitted first to the I1/f IDA to generate movement. The signal can then be canalised through the OID linkers to the ODA to control and shape beat frequency [15].

IDA, contrary to ODA, are very complex structures, and they are known to be essential to generate effective movement [132]. *Chlamydomonas* MTD show at least eight different DHC's together with several DIC's and DLC's into seven distinct complexes; one two-headed dynein referred to as I1/f and six single-headed isoforms (a-e and g [133]) (Figure 3). the IDA complexes are seen to repeat every 96 nm along the axoneme [127,129,134,135]. The way IDA attaches to the A-tubule is by a long tail, and several structures of the complex are in close contact with elements of the RS and/or the dynein regulatory complex (DRC), potentially explaining the failure of certain IDA's to assemble in DRC mutants [135]. Ishikawa made an in-depth analysis of MTD dyneins using advanced cryo-EM techniques and mentioned the asymmetry of the IDA in respiratory cilia and related that feature with the asymmetric profile of the cilia motion [3,136].

Nexin was early identified as a fundamental component for the stability and function of the axoneme [137], measuring around 40 nm [15], is described as a flexible protein connecting neighbouring MTD's [127,138,139]. Nexin is also thought to confer elastic resistance that converts doublet sliding into axonemal bending [137,138] (the theory behind this hypothesis might be connected to the fact that the size of the Nexin (~40 nm) is bigger than the gap between the MTD (~30 nm), forcing the protein to fold, making it flexible and adaptable to bending and motion). Nexin seems to be part of the DRC (which contacts both IDA and ODA and the RS-2). The data acquired by Nicastro supports the model that the DRC and Nexin interact with and mediate regulatory signals between the dynein arms and the radial spokes [15,134,135,138]. More recently, Song et al. (2015) described the Nexin-DRC (N-DRC) to be composed of at least 11 proteins, namely DRC1-DRC11 (including the Primary Ciliary Dyskinesia (PCD) causing genes *CCDC164* and *CCDC65*). Mutations observed in one or more subunits in the Nexin-Dynein regulatory complex (N-DRC), are known to be involved in impairment of cilia movement [140].

Image averages of the MTD revealed the presence of densities in the lumen of the MT. These were classified as microtubular inner proteins (MIP). These proteins differ in complexity, location and size, and are consistent along the MT's [15]. The smallest is the MIP1, which lays next to the PF A5 and repeats every 8 nm longitudinally (a similar density is found in the 9-fold triplet barrel shape organisation of the BB [15,116]). MIP2 is positioned between PF A9 and A10 and repeats every 16 nm, and finally, MIP3 is the largest and can be found between PF B9 and B10, with 16 nm periodicity [15]. The theory proposed by Nicastro et al. (2011) is that MIP may alter the stability of the MT PF. According to the authors, it is notable that MIP1 is localised close to the DRC, and the MIP3 is located near the Nexin. Suggesting these MIP provide structural reinforcement in sites more mechanically challenged [15].

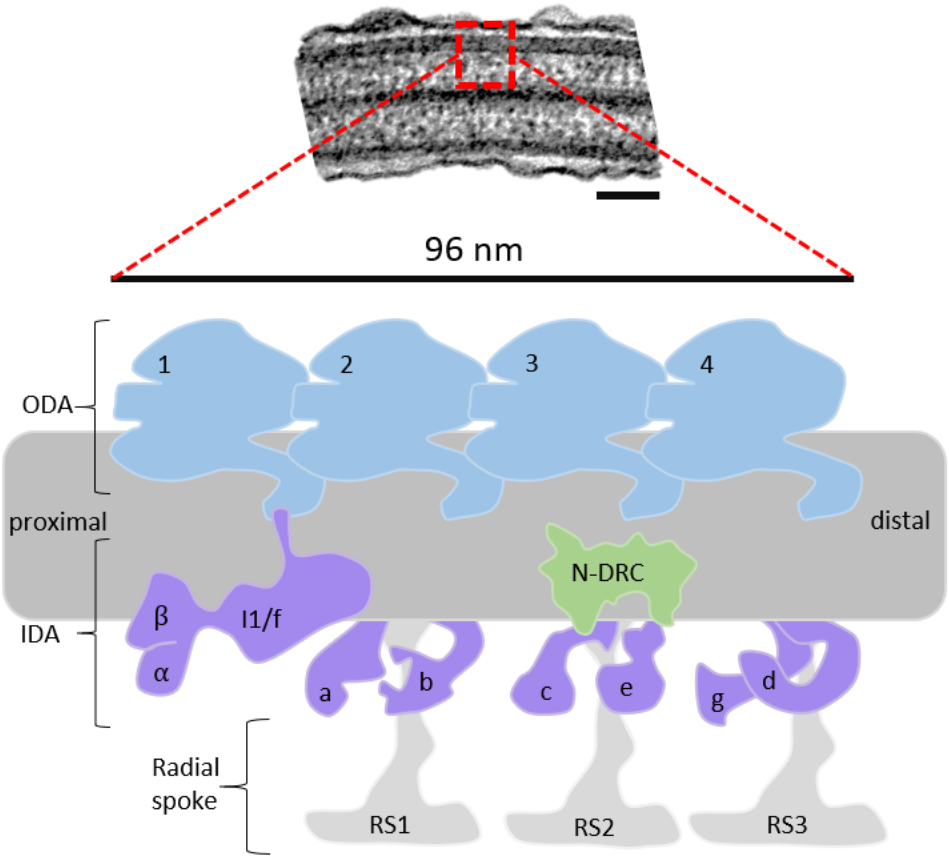

Figure 3. Organisation of ODA and IDA, N-DRC and RS along the axonemal A-tubule. The electron micrograph shows a longitudinal view of the ciliary axoneme, prepared for TEM, scale bar: 100nm. The non-scaled scheme represents a 96 nm length fragment of the axoneme showing the organisation of the macro-complexes. ODA are in blue and occur every 24 nm; IDA appear in purple with a 96 nm axial periodicity; N-DRC can be seen in green, and the three RS contained in the 96 nm repeat in grey [15,133]

Radial spoke, and Central Pair

The ciliary movement is not only regulated by the dynein proteins but also involves other structures in the axoneme, the RS and the CP [141]. T-shaped RS extend toward the CP from the A-tubule and are known to be involved in mechanical and signal regulation of the dynein activity in eukaryotic cells together with the CP [142]. Using cryo-ET was possible to identify the three RS proteins (RS1, RS2, RS3) distributed on the 96 nm repeat. RS2 is 32 nm apart from the RS1, and RS3 and RS2 are 24 nm apart [143]. Mutations in the proteins of the RS head genes (RSPH4 or RSPH9, for instance) were reported to be linked to respiratory abnormalities and fertility problems [144].

Work done in *Chlamydomonas* and *Tetrahymena* flagella demonstrated that the CP starts distal of the TZ and extends to the tip of the axoneme, terminating in a cap structure [145–148]. While in some organisms, the CP has a fixed orientation in the axoneme kept during motion [35,149], in *Chlamydomonas,* the CP is twisted and is thought to rotate during bending [150,151]. Early results regarding the structure of the CP remain until today as structural guidelines. The CP is a complex composed of two different

microtubules and their associated projections [152–154]. Between the two tubules there is a bridge that repeats every 16 nm and is believed to be involved in the CP stability [154,141]. Each MT of the CP has its own biochemical footprint, and they are typically distinguished as C1 and C2. Using unicellular organisms, it was possible to characterise the CP projections [153]. The MT with the longer projections is C1, containing C1a and C1b projections that repeat every 16 nm along the length of the CP. C2 shows two main projections, C2a and C2b, smaller in size and repeating every 16 nm. Two other projections were described using rapid freeze/deep-etch EM, the C2c repeating every 6 nm and C1c and C1d with 32 nm repeat spaced along the CP.[153,154]

Advanced cryo-ET techniques using *Chlamydomonas* and *Strongylocentrus* flagella revealed new structural evidence in CP ultrastructure [152]. Adding to the already described set of CP projections (C1 - 1a to 1d and C2 - 2a to 2c), 4 extra projections were identified: 1e and 1f from the C1 MT, and the 2d and 2d projecting from the C2 MT [152]. High-resolution 3D studies brought light to the structure previously classified as sheath density (S) (grey structures connecting projection 1b to 1d, and 1a to 1c in the schematic Figure 4). Through cryo-ET was possible to understand that the S densities are CP projections, that due to their lack of contrast in 2D TEM are hard to assess and therefore not considered projections of the CP complex [152]. The bridge between the MT, previously considered to be composed of three separated densities [155], is a more complex structure with organism-specific features [152]. All the findings around the CP support the theory that the CP is a complex, highly connected structure [152]. The continuous dense network surrounding the CP MT will eventually facilitate the communication of the regulatory signals across the CP and to the RS. Although most of these detailed works were done in invertebrate organisms, the highly conserved structure of the axoneme suggests most of the structures will retain similarities, if not homology to mammals [152]. Unfortunately, there is a lack of studies using high-resolution techniques in the CP of more complex organisms, due probably to the methodology, since the CP is a fragile structure that easily disassembles [156].

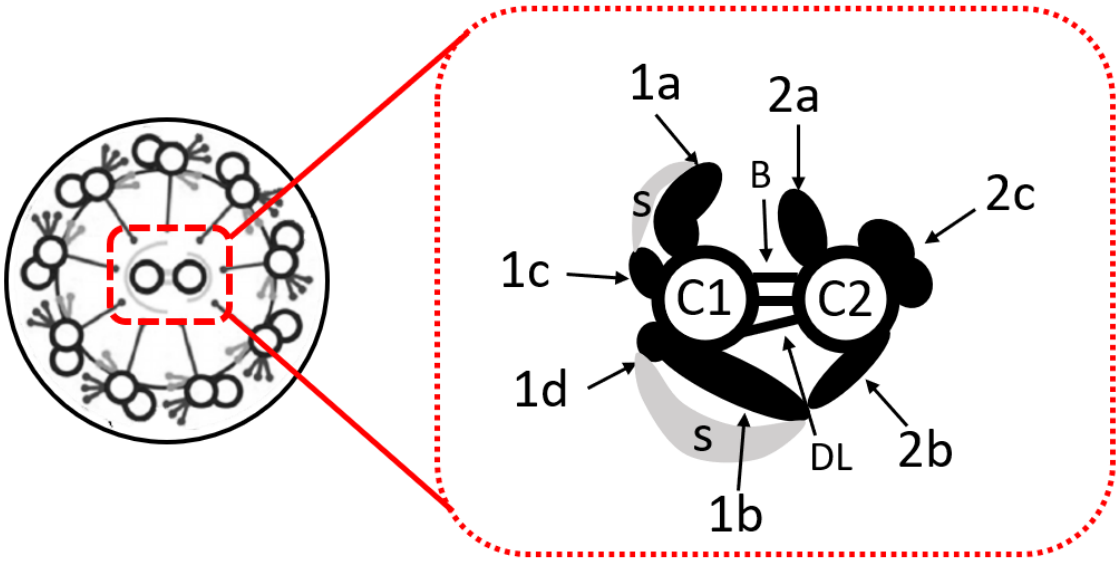

Figure 4. Simplified schematic model of a motile cilium cross-section (left) and a detail of the CP (right). Microtubule C1 shows densities 1a, b, c and d, and microtubule C2 shows densities 2a, b and c. Spanning the gap between the microtubules, there is a bridge (B) and a diagonal link (DL). Making an arc between subunit 1a and 1c, and between the tip of 1b and subunit 1d thinner arcs are observed, named sheath material (s) by Warner in 1976 [155,157]

Motile cilia disease

In human disease, mutations in motile cilia genes generate a range of phenotypes [158]. Motile cilia diseases are multisystemic, where many organs are affected, giving rise to several clinical manifestations like heterotaxy, *situs inversus*, fertility problems, hydrocephaly and airway implications [60]. The role of malformed cilia on these diseases is still seen as complex and multifactorial. Nevertheless, with the upturn of genetic analysis and whole exome sequencing, it has been possible to study and discover new target genes playing important roles in the phenotypical presentation of the ciliary syndromes [159].

The hallmark disease of motile cilia is Primary Ciliary Dyskinesia (PCD), characterised either by defects in the ultrastructure of cilia or by oligocilia or reduced generation of motile cilia [160]. Motile cilia in the airways have a prominent role in host-pathogen defence through ciliary movement (other locations where motile cilia show important function is in the brain and the reproductive female system [158]). Airway MC promoted by the ciliary movement, together with the mucus-producing epithelial goblet cells, moves the mucus-containing trapped pathogens and pollutants either up or down the throat to be ingested or expelled [161,162]. Failure in this mechanism leads to neonatal respiratory distress, and throughout life, there is a progressive accumulation of mucus and pathogens that will cause obstruction and might lead to infection in the sinuses, ears and lungs [160]. The persistent infections may ultimately lead to severe lung damage [94,160].

Due to the highly conserved ultrastructure of motile cilia, it is possible to perform many *in vitro* and *in vivo* experiments using cilia and flagella, to understand the cause of ciliopathies [28,163]. Many of the discoveries in cilia biology were made many years ago, using invertebrates like *Chlamydomonas reinhardtii* and *Caenorhabditis elegans (C. elegans*), however, they lack the organs that are affected in ciliopathies, and this made researchers use vertebrate models, such as mouse, frog/amphibian, and fish. These models became popular to study ciliopathies, especially for studying diseases linked to abnormal organogenesis or organ position, which are also observed in human patients diagnosed with PCD [159,28].

Animal models used in the study of cilia and flagella

Motile cilia have an essential role in fluid generation and propulsion. Flagella are involved in protists' movement and locomotion; the same feature is recognised in the gametes of several species [159,164]. First studies on flagellar motility were made in aquatic invertebrates with small similarity with humans, this was possibly due to the conserved nature of cilia [165].

Throughout the history of cilia, many animal models were assessed for cilia structure, mainly because cilia are conserved organelles between species [2] and between organs [8]. Examples are the adult drosophila antenna, which are specialised cilia containing three distinct morphological sensilla, with singlet 9+0 configuration [166]; and the outer segments of the photoreceptors in the retina, which are well known specialised sensory cilia [167]. Some animal models were already pinpointed as the pioneers of cilia studies, unicellular organisms like the algae *Chlamydomonas reinhardtii* and the nematode *C. elegans*, as well as *Paramecium tetraurelia*, which is outlined with cilia to promote motility [2]. Growing in complexity, parasites like protist *Trypanosoma brucei* and *Leishmania donovani* are still fashionable in cilia research due to their long flagellum, which also assists in movement [2]. Already in the vertebrate family, larger and more complex organisms are widely used, like *Mus musculus* (mouse), *Danio rerio* (zebrafish) and *Xenopus* (amphibian). These animals have complex organ morphogenesis and it is possible to trace the effects of cilia disfunction [8,106,164,168–171].

Zebrafish | Danio rerio

Zebrafish was identified and described as a popular model for developmental biology for the first time by a researcher in Oregon called George Streisinger [172,173]. Since then, it became widely used in research due to its unique embryonic and molecular characteristics, being easy to handle and maintain. Zebrafish are more affordable to keep in a dedicated facility compared to mice [174]. Zebrafish are known to have rapid development from larvae to fully sexual mature adult fish in three months, and a single female can lay hundreds of externally fertilised eggs per week [175]. After three days of development, all major organs are formed in larvae [175]. Mice are considered mature when they reach three months of age, but mice gestation is *in utero* and can last between 19-21 days. Mice generate on average 6-8 pups per litter [176,174,177]. The accessibility and study of zebrafish embryos are also remarkable due to

their external fertilisation and transparent nature from egg to larval stages [178]. It is also easy to administrate drugs either to their environment (tank water) or by injection the egg at one-cell stage [179].

Zebrafish is a vertebrate, and so, an excellent model to study how mutations affect specific organs in the body [173]. In evolutionary terms, the human and zebrafish common ancestor is around 400 million years old [180]. In 2001, the Sanger Institute initiated a study to sequence the zebrafish genome. The study revealed that 71.4% of the human genes are found in zebrafish. Furthermore 84% of the genes known to be associated with disease in humans have also a counterpart in the zebrafish [181].

Nowadays, it is known that some mutations in the early stages of zebrafish lead to a range of perturbations in some of the most basic developmental processes, from complex organ morphogenesis to the organisation of brain and vascular architecture, recognised to be similar to human disease [172,173,174].

Throughout the years, several genetic resources were created for zebrafish, and its genome has been completely sequenced [182]. Online platforms compare the genome of the zebrafish with other animal models and with the human genome. However, there is still work being done using sequencing techniques to improve zebrafish genome studies for research improvement and reliability. The *Danio rerio* sequencing project is an online platform that facilitates the study and comprehension of the disease-causing mutations [182].

Zebrafish is already recognised as a valuable model organism in gene function studies that can be performed in embryos using transient instead of stable misexpression for reverse genetic analysis [183]. These interventions are technically easier than those performed in mice for some of the reasons already mentioned above. Microinjection of messenger Ribonucleic acid (mRNA) or antisense morpholino oligonucleotides (MO) at one-cell stage are currently widely used in transient gene overexpression or specific gene knockdown, respectively [184,183]. In zebrafish, due to their easy adaptation and conditioning, it is possible to apply specific conditions of compartmentalisation and caging techniques, allowing tissue targeted experiments, temporal-specific expression and even circadian cycle alterations [185]. All these techniques make the zebrafish a valuable animal for disease modelling. It is relatively quick to examine genetic interactions in zebrafish (severity or penetrance of a mutation) and evaluate therapeutic effects when removing or adding specific drugs or gene products in the context of a given mutation [182].

The cilia of the zebrafish

Zebrafish is a valuable animal model to study cilia and ciliogenesis since motile and sensory cilia are found in many of its embryonic and larval structures [8,63]. Motile cilia are found in the Kupffer's vesicle or LRO at 8-14 somite stage and in the Olfactory Pit or Placodes (OP) at 2-3 days of development [178]. Around 1-3 days of development, motile cilia are also observed in the spinal canal and the pronephros [76,186]. It was previously shown that cilia motility in these organs is important for fluid movement,

morphogenesis, proper organ function and positioning. The generation of flow in the OP, is combined with the ability of these cilia to sense odours in the environment [178159].

Following the nature of this work, I will focus only on two ciliated tissues of the zebrafish embryo, the LRO and the OP.

Kupffer's vesicle the Left-Right Organiser of the zebrafish

During the early stages of development, several pathways are used in the determination of axis formation in zebrafish, namely, antero-posterior, dorso-ventral and Left-Right (L-R), the latter breaking down the initial bilateral symmetry of the embryo [187]. The L-R asymmetry of the internal organs of the zebrafish is established through gene expression regulation occurring in an organ shaped as a vesicle called the Kupffer's vesicle (KV) consisting of a LRO [42]. The LRO is a transient embryonic structure that appears at the end of the notochord. It is already known that for the establishment of the L-R asymmetry, a directional counter clockwise fluid flow inside the vesicle is required [188,189]. This happens by the action of rotating monocilia lining the lumen of the LRO, presented as 5 µm hair-like structures protruding from the surface of cells (one cilium per cell) [190].

The classical asymmetry of the internal organs is called *situs solitus* and it is the normal presentation of the organs, a feature conserved across many vertebrate species [191]. In humans, the heart sits on the left side together with the spleen, stomach, and pancreas, while the liver and the gallbladder are on the right. The lungs are asymmetric organs specially configured in lobes to accommodate the heart [191]. These asymmetries are preceded by asymmetric gene expression that starts in the LRO during the early stages of development [191]. The exact mechanism leading to the asymmetric placement of the internal organs is not yet fully understood, but the directional flow occurring in the LRO is known to be central in this establishment [188]. Several authors previously described that leftward flow leads to asymmetric gene expression in the mice LRO surrounding cells [192–194].

Nodal (nodal growth differentiation factor) and *Dand5 (*DAN domain BMP antagonist family member 5) were already described as critical factors in L-R, both initially symmetrically expressed in the LRO [195]. The asymmetric expression of *Nodal*, which will activate the *Nodal-Lefty-Pitx2* pathway, is dependent on the motile cilia rotation and generation of flow in a leftward way [196]. Absence of cilia or mutants showing movement impairment display similar phenotypes – alterations in gene expression and organ asymmetry displacement [34]. After being lateralised in the LRO, *Nodal* regulates its own expression and *Lefty1* (left-right determination factor 1), *Lefty2* (left-right determination factor 2) and *Pitx2* (paired like homeodomain 2). Lefties occur only on the left side, and *Lefty1* acts as a midline barrier preventing the left side established factors to cross to the right side [197]. *Pitx2,* on the other hand, works as an informer of the cells on the left, that they are to adopt a leftward conformation [198]. It is acknowledged that the correct generation of flow in the LRO is the key point for the correct expression

and fate of the L-R genes [196]. To better understand how dynamics and gene expression communicates, two theories were generated.

The morphogen gradient model initially proposed that motile cilia create a unidirectional flow that secretes morphogens to the left. Consequentially, leading to a more significant concentration of morphogens on the left side of the LRO. However, in the loss of function experiments, mutants lacking motile cilia seem to show a different phenotype from those only with motionless cilia (bilateral expression of *Nodal-Lefty-Pitx2* versus completely random to absence of *Nodal-Lefty-Pitx2* respectively [199]). This suggests that other factors are involved in how the flow is sensed, such as *PKD2* (Polycystin *2*), which is not required for the generation of cilia but seems to be important in sensing it [193].

On the other hand, the two cilia model attempts to justify the phenotype differences in the previous model. It is recognised that the mice LRO has two types of cilia, i) motile cilia that generate movement through a planar rotation like movement and ii) non-motile cilia that might show sensing properties [42,63,200]. The model suggests that the flow can bend the cilia, stimulating the mechanosensors to induce an asymmetric signalling pathway leading, consequentially, to an asymmetric release of signalling molecules [201]. This mechanism may provide clarification since even in motionless cilia, the signal can still be randomly activating mechanosensors, while lack of cilia inhibits both generation and sense of flow [202]. The explanation behind this model connects the Polycystin complex and *PKD2* to the L-R signalling, which was first connected to the Polycystic Kidney Disease and is known to be present in the primary cilia of kidney cells [203].

The motile monocilia of the LRO generate directional fluid that will lead to the asymmetric calcium (Ca2+) oscillations (*icos*) in the zebrafish LRO [204]. These *icos* were described as being mainly on the left side of the LRO and were shown to depend on *PKD2* as caption channel [192–194]. Consequently, the presence of *icos* on the left side was correlated to a left-biased expression of genes in the lateral plate mesoderm (LPM) (*Nodal, Lefty and Pitx2*). *PKD2* has been pointed as an essential player in the mechanosensor-channel complex, interchanging signalling information between the LRO flow and the adjacent tissues. Impairment of *Pkd2* alone (despite being part of a complex) was shown to lead to randomisation of *situs* both in mice and zebrafish [205,206]. Recently Lopes lab showed that, contrary to what was published previously, *Pkd2* loss of function studies also affects cilia length and flow dynamics (reduced flow speed [207]) and LRO architecture and fluid volume [208]. The diminished LRO flow speed is believed to be triggering early L-R abnormalities. Jacinto et al. (2021) [207] showed that short cilia length impacts LRO flow speed, and therefore one cannot discern a *Pkd2* sensory role from its role in flow dynamics [207]. This study indicates that the mechanosensory hypothesis cannot be studied solely based on *Pkd2* because to assess flow sensing, flow generation should be stabilized [207].

The Olfactory Pit or Placode

All peripheral sensory neurons in vertebrates are originated from the ectoderm [209]. Placodes are regions of condensed ectoderm that accumulate in the head of the organism to generate non-neural and neural structures [210]. The neurogenic placodes include the olfactory, trigeminal, profundal, lateral line, epibranchial and otic placodes [210]. Developmental of placode derived olfactory sensors start upon subdivision of the embryonic ectoderm into epidermal ectoderm and neural ectoderm, and neural plate border region. Olfactory placode cells emerge in the late gastrula and express *Six3* (SIX homeobox 3), *Pax6* (paired box 6) and *Otx2* (orthodenticle homeobox 3) [209,211]. After induction of the olfactory placodes in the early embryo, these structures cavitate (term used in zebrafish), transforming from a thick sheet of ectoderm into a pit and then an epithelial cavity. This epithelial floor is initially outlined by a single thick layer of cells and then later transforms into a multi-layered structure and undergoes neurogenesis [212].

In vertebrates, the olfactory placodal cells are specified at a gastrula stage where cells that can be either lens or olfactory. Later in development, olfactory placodal cells become spatially separated from the lens [211]. During olfactory placodal cells maturation, *Fgf8* is expressed anteriorly and is linked to the emergence of sensory epithelial cells [212]. Furthermore, *FGF* signalling is dependent on the Bone Morphogenic Protein (BMP), and this signalling is known to be involved in the generation of a nonneurogenic olfactory domain, while *FGF* signalling is required to maintain the neurogenic region [212].

Diverse cell types mediate the functions of the multimodal sensory olfactory epithelium (OE). The two main classes of sensory receptors in zebrafish are the ciliated and the microvillous [213]. Olfactory sensory neurons (OSN) give rise to smell and are bipolar neurons that link the OE to the olfactory bulb (OB) [214]. Six classes of OSN were identified so far [213] 1) the ciliated neurons, equipped with odorant receptions (OR), and expressing olfactory marker protein (OMP), extend from the OE up to the OB, configuring as a slender dendrite that extends to the surface of the OP, where the dendritic knob bears a cluster of primary cilia projecting into the olfactory cavity [24,215,216]. 2) Microvillous OSN's are characterised by cell bodies lying in the intermediary layer of the OE. Those are also connected to the OB and contain a tuft of short actin-rich microvilli (MV) [24,215,216]. 3) Crypt neurons are less frequent and are round shape cells sitting apically in the OE and may contain both cilia and MV [24,215,217–220]. 4) Kappe neurons show an actin enriched cap presumed to be composed of MV. Kappe neurons lie in the superficial layers of the adult zebrafish OE [221]. 5) Pear-shaped neurons are also characteristic of adult zebrafish OE and express some common markers with ciliated neurons. 6) lastly, and only recently described, are the olfactory rod cells. Their origin is still not clear, nonetheless, they are believed to have a mechanosensory role in detecting ciliary movement or ciliary driven fluid flow [213]. It is also hypothesised that they have a similar function to microvillous cells that lack axons in mammals [222].

The OE is an exposed epithelium and contains neuronal tissue and non-sensorial material such as basal cells, goblet cells, immune cells and multiciliated cells [24,60,220,223–225,226]. Multiciliated cells were

described by Reiten (2017) as organising a rim around the OP in the fish, containing multiple motile cilia beating at around 24 Hz, generating an asymmetric flow that draws water and odorants into the olfactory cavity and then flushes them out again [227].

Visualisation and imaging in Zebrafish

Regarding methods to visualise cilia in these organs, the LRO is an internalised vesicle and therefore hard to access and visualise. However, the zebrafish is transparent until the larval stage, and this allows to perform imaging techniques, such as live and whole-mount imaging [42,178]. To maximise embryo transparency in late larval stages, the pigmentation can be delayed or blocked using Phenylthiourea [178] or bleach. Zebrafish larvae are small enough to be screened in a confocal microscope, and z-stacks of the whole animal can be easily acquired to visualise the internal organs [178]. Cilia of the OP are the most accessible since they are at the surface and can be imaged easily, either in fixed animals and live imaging [228,178].

Zebrafish embryos or larvae can be easily processed for histological studies, in which orientation is critical. Early-stage embryos are extremely fragile to paraffin embedding so, cryostat sectioning of gelatine embedded embryos is recommended, not only because the samples are fully hydrated, preventing extreme damage from infiltration processes, but because gelatine embedding is better to keep the embryo in a particular orientation. Cryostat sections are easy to label with fluorochromes and visualise using different light microscopes [178].

Zebrafish as a model organism for disease

Based on what is described above, zebrafish is a good model to study PCD. Previous studies used zebrafish for PCD investigation. Castleman et al. (2008) stressed the importance of the protein RSPH9 undergoing knock-down/knock-out experiments using zebrafish orthologue *rsph9. T*his gene was found to be restricted to regions containing motile cilia in zebrafish. In this work, *rsph9* was described as essential to maintaining an effective movement of the axoneme (beating pattern). The same was seen in human PCD patients [229]. Later, Austin-Tse, et al. (2013) also identified PCD causing disease genes in zebrafish (namely *C21orf59* and coiled-coil domain containing protein 65 - *CCDC65*) and used MO to knock them down. The authors screened the effects caused in the zebrafish and compared those with the phenotypes in PCD patients with similar genetic profiles. The abnormalities caused by the knockdown of these genes in the zebrafish were similar to those in humans, namely, mutation in the *C21orf59* caused loss of both dynein arm components, leading to lack of ciliary movement [4].

The use of antisense MO was highly popular in the past 20 years as a general loss of function approach; however, several concerns were raised, and their use started to be discouraged due to some pitfalls in their specificity [4]. However, well-controlled experiments were shown to be possible using MO

on zebrafish. Most of the studies supporting the correct use of MOs were done by Didier Stainier lab [230–232].

Zebrafish is considered a good organism for gene editing and brings many advantages as a model organism [8,175,182,233]. Ever since its discovery, CRISPR-Cas9 was considered a ground-breaking technology and has quickly become a powerful method of choice for genome engineering, not only in zebrafish but also in other model organisms. Knowledge on CRISPR dates back to the 1980's when the CRISPR (clustered regularly inter-spaced short palindromic repeats) mechanism was firstly published by a group at the Osaka University [234]. CRISPR-Cas9 is a mechanism that was based on a defence system developed by bacteria to protect themselves from virus [235,236]. The system works by introducing a double-stranded break in DNA (desoxyribonucleic acid) at a targeted locus. There are at least three known types of CRISPR systems [237], but the most widely used in gene editing is type II. This system works in three distinct phases identified in bacteria: i) an adaptative phase where the bacteria integrates small fragments of the invader; ii) the expression and interference phase when is given the transcription of the spacer element into pre-CRISPR RNA (pre-crRNA) complementary to the invader; iii) and finally the target and recognition phase, done by the crRNA, which will direct to silencing by means of a Cas protein [238,239]. Type II system constitutes a family of enzymes (Cas9) that require a crosstalk complex between the activating trans-activation-CRISPR RNA (tracrRNA) and the targeting crRNA (referred to as guided RNA (sgRNA)) to cleave the target double-strand DNA (dsDNA). The specificity of the break is given by pair-base complementarity between the crRNA and the target protospacer DNA, and a short motif called Protospacer Adjacent Motif (PAM), that is collated to the complementary region in the target DNA [239]. As a summary, the Cas9 family of endonucleases can be programmed with sgRNA molecules to cleave specific DNA sites, and is hence considered as a versatile gene editing tool that uses a RNA-directed system to generate dsDNA breaks in virtually any site of the genome [239].

CRISPR-Cas9 has been used to study the effects of mutated PCD genes in mice with the investigation of Wallmeier et al. (2016), where *Ttc25* mutant mice generated by CRISPR-Cas9 technology presented laterality defects, and when confirmed by TEM, presented ODA absence. The same was found in PCD patients with *TTC25* biallelic mutation [240]. Lewis et al. (2016) generated the first *Gas8* mouse mutant using the same method and reported it as the cause of severe PCD phenotype [241]. Abbasi et al. (2018) observed impairment of male fertility in mice in the presence of an induced *rsph6* mutation [242]. Application of CRISPR-Cas9 technology to zebrafish has also been published in ALS (Amyotrophic Lateral Sclerosis) [243] and cardiovascular syndromes [244 245]. Jaffe et al. (2016) used CRISPR-Cas 9 and stressed the importance of *C21orf59* gene (identified as a PCD gene in humans) for cilia motility, causing dynein arm defects observed by TEM [246]. More recently, Xie and colleagues (2019) compared the effects of using MO and CRISPR on centrosomal protein Cep20 (centrosomal protein 20), an important protein for the cilium-mediated processes during zebrafish embryogenesis. Both procedures generated animals with defected cilia in the LRO and impaired organogenesis [247]. Rasteiro (2017) created a *Ccdc40 -/-* mutant in zebrafish to study the phenotype of this severe human

PCD mutation in zebrafish embryos [248,249,250]. *CCDC40* is a known gene that codifies for a protein involved in the correct assembly of the IDA and N-DRC [250].

Primary Ciliary Dyskinesia

PCD is a genetic disorder characterized by dysfunctional motile cilia and impaired MC, which predisposes patients to recurrent respiratory infections [251]. PCD is a rare disease, with a prevalence of approximately 1:10000 people worldwide [252], it is characterized by recurrent respiratory tract infections. The clinical phenotype of PCD overlap with many more frequently occurring diseases like asthma, common variable immunodeficiencies [253,254], and cystic fibrosis (CF); many children have respiratory tract symptoms as a result of frequent pathogen exposure without any underlying condition being present. Therefore, it can be a challenge for a physician to decide which patients should be referred for further diagnostic testing [253].

It is common to find the designation Kartagener Syndrome (KS) linked to PCD. Historically this is owing to the fact that Kartagener was the first clinician to establish a correlation between the elements of a symptomatic triad in 1933, that includes *situs inversus*, bronchiectasis, and sinusitis. If a patient presents this triad of symptoms, it is likely they will be designated as a probable KS. However, it is now clearer that the KS is a subset of PCD, since all the symptoms described in KS overlap with the clinical description of some cases of PCD [255,256].

The clinical suspicion of PCD should be raised in cases that have a combination of a clinical history of unexplained Newborn Respiratory Distress (NRDS) [257], early onset of nasal congestion, chronic wet sounding cough, recurrent serous otitis, and organ *situs* abnormalities (*situs inversus*) [258]. However, some of these features can be mild or even absent in PCD patients [259]. 50% of PCD patients have normal cardiac and visceral organ laterality. Parents of PCD patients often report nasal discharge starting at the day of birth, commonly persisting throughout life. In addition, most neonates with PCD show NRDS, suggesting that cilia have a role in the effective clearance of foetal lung fluid. Serous otitis occurs frequently and, unlike in healthy children, persists throughout adulthood. Early onset of wet coughing and lower respiratory tract infections occur in nearly all PCD patients. Although limited data on disease progression are available, bronchiectasis is present in about half the paediatric PCD patients and all adult patients [260].

PCD is primarily characterized by defects in motile cilia, the structure of cilia is composed of a circular arrangement of nine microtubule doublets with or without a central pair of microtubules (9+2 or 9+0 structure). 9+2 motile cilia are located on the apical surface of epithelial cells in the upper and lower respiratory tract, paranasal sinuses, middle ear, ventricles of the central nervous system, fallopian tube, and sperm flagella. Motile cilia with 9+0 ultrastructure exist as nodal cilia, being responsible for the establishment of left-right asymmetry during embryogenesis [257]. In summary, defects in motile cilia may lead to chronic respiratory tract infection, infertility/subfertility and laterality defects [160].

The major organs of the respiratory system function primarily to provide oxygen to body tissues for cellular respiration, remove the waste product carbon dioxide, and help to maintain acid-base balance [261]. Portions of the respiratory system are also used for non-vital functions, such as sensing odours, speech production, and for straining, such as during childbirth or coughing. Functionally, the respiratory system can be divided into a conducting zone and a respiratory zone. The conducting zone of the respiratory system includes the organs and structures not directly involved in gas exchange. The gas exchange occurs in the respiratory zone [261].

Focusing on the conducting zone, the major entrance and exit for the respiratory system is through the nose (see nasal cavity/vestibule in Figure 5)

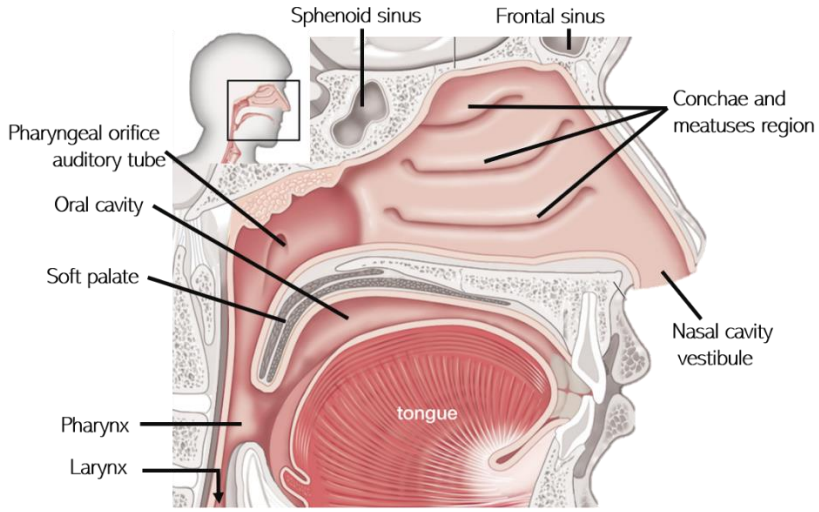

Figure 5. Anatomy of the respiratory conducting zone, adapted from Encyclopaedia Britannica © (2012) [262] [263]

The conchae, meatuses, and paranasal sinuses (maxillary and ethmoid sinus not shown in Figure 5) are lined by respiratory epithelium composed of pseudostratified ciliated columnar epithelium (Figure 6). The epithelium contains goblet cells, one of the specialized columnar epithelial cells that produce mucus to trap debris. Other rarer cells found in the epithelium include ionocytes, neuroendocrine and tuft cells [94]. Cilia of the respiratory epithelium help remove the mucus and debris from the nasal cavity with a constant beating motion, sweeping materials towards the oropharynx; particles deposited on this film are eventually swallowed or expectorated, through MC [161,162]. Capillaries located just beneath the nasal epithelium warm the air by convection. Serous and mucus-producing cells also secrete lysozyme and proteins called defensins, which have antibacterial properties. Immune cells that patrol the connective tissue deep to the respiratory epithelium provide additional protection. [264,261]

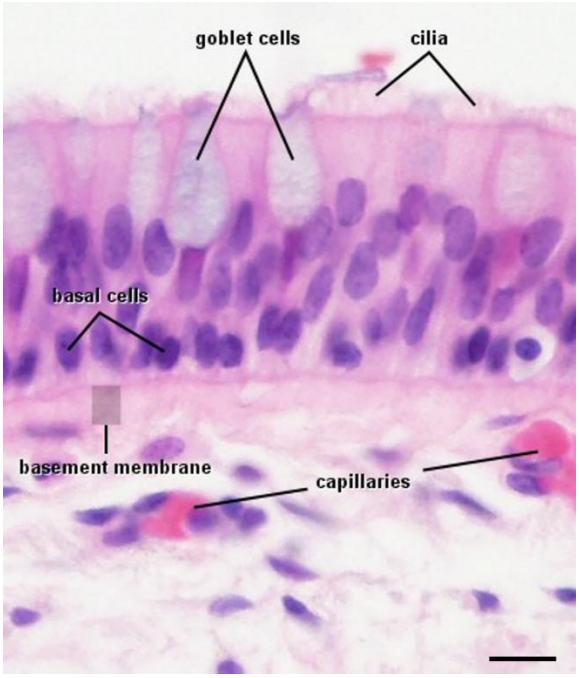

Figure 6. Haematoxylin and Eosin (H&E) of the trachea epithelium scale bar 10 µm

Inhaled particles are deposited largely according to their size. Thus, particles over 10 µm are deposited largely in the turbulent air flow of the nose and upper airways; particles of 3-10 µm lodge in the trachea and bronchi by impaction. Ineffective clearance of the particles from these sites is believed to be crucial to the pathogenesis of respiratory infections [264].

Epithelial multiciliated cells bear approximately 200 motile cilia [25] . The beat pattern of 9+2 motile cilia occurs in a waveform that includes a forward effective stroke followed by a return stroke [265]. The direction of stroke is a function of the directional orientation of the central microtubules. In addition to moving in synchrony, individual cilia in normal healthy cells are very plastic and move fluidly, sometimes deforming briefly upon encountering resistance and/or particles being transported over the mucosal surface. Cilia are embedded in a watery periciliary fluid of low viscosity, which facilitates the rapid beat cycle to move the more viscous overlying layer of mucus. Ciliary beat frequency ranges from approximately 8-20 Hz under normal conditions, however exposure to irritants may increase the ciliary beat frequency [257]. It is also know that hyperactive cilia beat frequency can be related with specific genetic defects like mutations such as in the *DNAH11* gene [266]. Overall, PCD causes an impaired MC due to defective axonemal ultra-structure of the respiratory cilia and/or by oligocilia or reduced generation of motile cilia [267,160,158].

As mentioned previously, not only respiratory cilia are affected, 50% of PCD patients also have defects in visceral organ laterality, reflecting dysfunction of embryological nodal cilia. These cilia are present during embryonic development in a transient monociliated organ called the ventral node and are required for patterning the left-right axis in most vertebrates [268,42] .

Ultrastructure of motile cilia in PCD

The TEM analysis of cilia with the intention to study respiratory syndromes started with Afzelius, when he first described in 1976 that male patients with infertility presented also respiratory distress [258]. Afzelius studied sperm flagella and cilia sampled from the nose of his male patients. He discovered that the axonemal profile was similar in both, in some specific cases, he observed immotile sperm, showing absence of the dynein motors. Afzelius, named this phenotype as immotile cilia disease [258,269]. It was only later that the complexity of this immotile cilia disease became apparent. Cilia were found to not always be completely immotile when examined by light microscopy (LM), residual movement referred to as dyskinetic movement was described that leads to impaired MC in the respiratory tract [270–273]. A new span of defects was unlocked, not only the initial dynein defects leading to immotility, described by Afzelius in 1976 [258], but a range of abnormalities from very mild disarrangements to a complete transformation of the ciliary axoneme configuration. These finding lead to the designation of the disease being changed to ciliary dyskinesia, due to the dyskinetic nature of the cilia in these patients and the range of ultrastructural defects identified by TEM [274].

Advancements in LM techniques, leading to better understanding of PCD, showed healthy (non-PCD) individuals could show signs of dyskinetic movement of cilia, and impaired MC. This has been found to be a result of infections (the common cold for instance), that can lead to some ciliary ultrastructural abnormalities when viewed by TEM [275]. Due to existence of secondary factors causing dyskinesia, the disease was renamed in the seventies to Primary Ciliary Dyskinesia.

TEM allows the ultrastructure of ciliary axonemes to be visualized in detail [3,267]. Ultra-thin sections are prepared for TEM from fixed cells or tissues using standard methods [276]. Sections are examined at magnification to visualize the ultrastructural features (Figure 7) [267], such as the accessory axonemal components including the ODA and IDA, RS, CP and the N-DRC. IDA morphology is heterogeneous in composition and repeats every 96 nm along the axoneme. ODA have a more homogeneous distribution in the axoneme, with 24 nm periodicity [129]. The most common ultrastructural defects are: ODA-defects (25-50%) and combined IDA- and ODA-defects (25-50%), IDA-defects associated with microtubular disorganization occur in 15% of PCD [277]. Isolated IDA-defects as a cause of PCD are controversial because, so far, no biallelic mutation has been clearly identified in IDA proteins, however, *DNAH1* is a potential candidate [278]. IDA are difficult to identify due to their heterogenic structural profile of individual IDA along the 96 nm repeats of the ciliary axoneme [267,267,279]. CP defects occur less frequently (5-15%) and are associated with a mixture of both normal and abnormal cilia. TEM of cell cultures showed CP complex defects in only ~20% of the cilia so adequate numbers of cilia need to be viewed in longitudinal and transversal section [267,267,280].

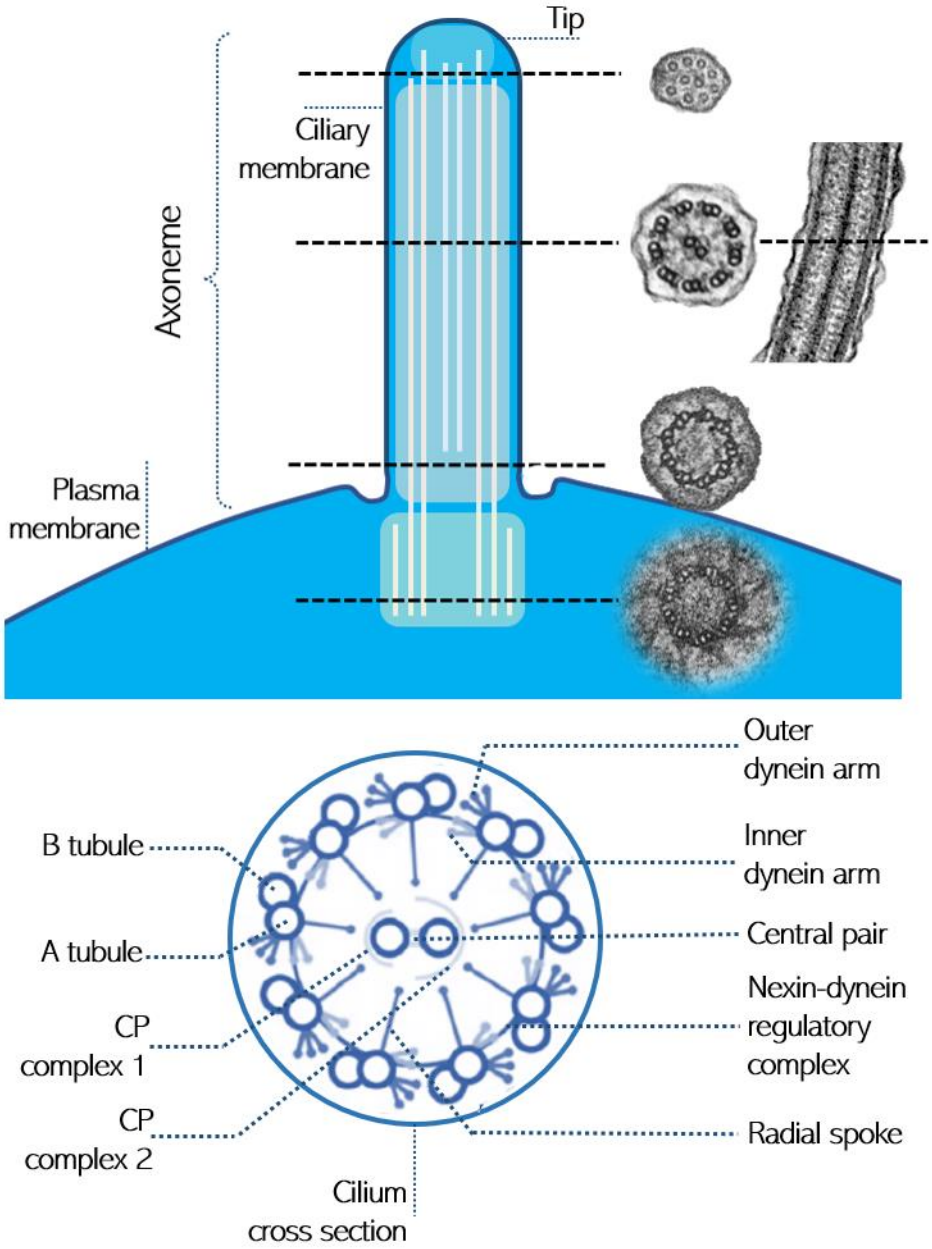

Figure 7. Representation of the motile cilium components. Motile Cilium (plural cilia) is an organelle found in eukaryotic cells. Motile Cilia are hair-like protuberances typically extending some 5–10 µm outwards from the cell body and have a width of around 200 nm. The top figure represents a scheme of a cilium in a longitudinal plane. Some cross sections along the Axoneme show regions of the axoneme acquired by TEM; bottom to top of the axoneme scheme: a cross section of the BB showing a nine-fold triplet organization; a cross section of the axoneme in the TZ, with a ninefold doublet configuration, and no CP; cross-section obtained in the central region of the axoneme shows a 9+2 organization of the MT and a longitudinal section of the axoneme; the last image represents a tip of the cilium, where the nine-fold configuration is replaced by single MTs and CP. Bottom figure is a scheme of a cilium cross-section through the middle part of the axoneme, positioning the major components of the cilium.

It is also known that 20-30% of PCD patients have normal ultrastructure [281] (A-Normal cilia in Figure 8). For example, is difficult to detect by TEM the defects caused by mutations is dynein axonemal

heavy chains (such as *DNAH11)* [266] [281], CP components (*HYDIN* or *SPEF2*) [282], ciliary biogenesis defects (*MCIDAS* or *CCNO*) [283] and some defects of nexin link components (*DRC1* for instance) [284]. Nonetheless, some genes are limited to a specific region of the axoneme (as is *DNAH9*) [285]. Therefore, normal ultrastructure cannot rule out PCD [260]. Consequentially, the PCD diagnostic pathway need to take into account this limitation and consider all other diagnostic evidence before making a diagnosis [251].

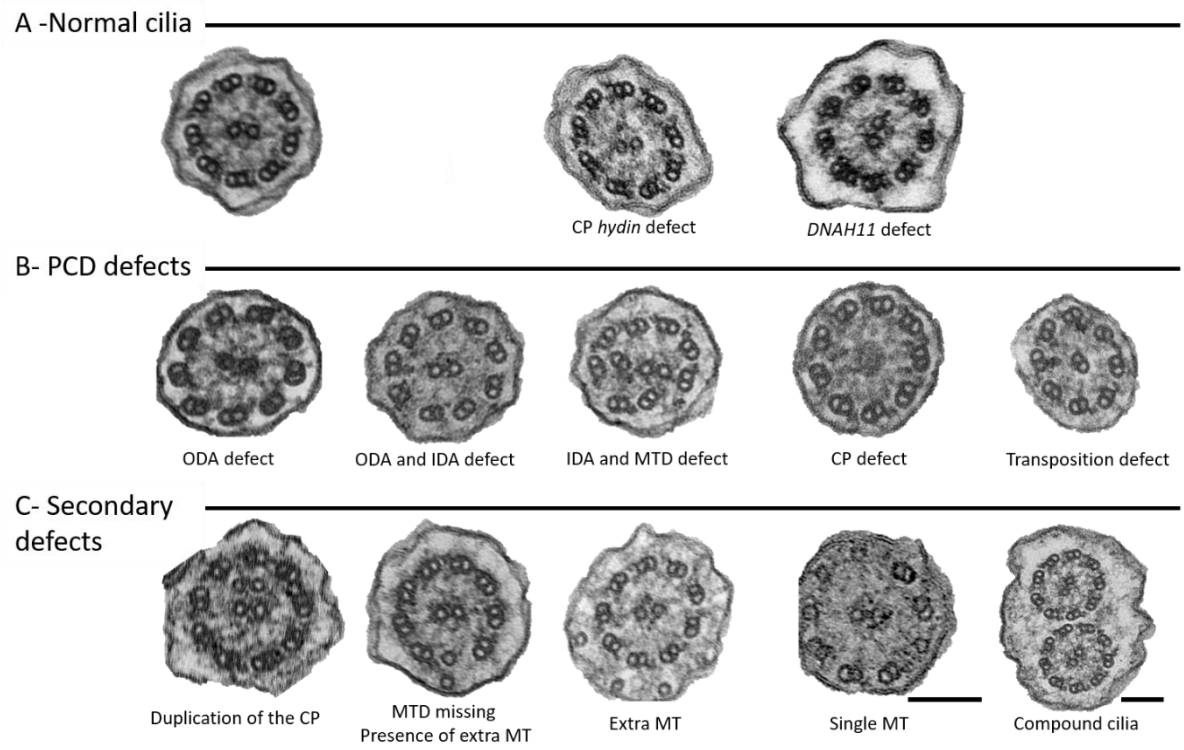

Figure 8. Cross-sections through the cilium axoneme of normal and abnormal cilia. (A) Normal cilium 9+2 ultrastructure and examples of a *HYDIN* and a *DNAH11* mutation, showing apparent normal ultrastructure. (B) Left to right: ODA defect, ODA and IDA, IDA defect combined with MTD disorganization, CP defects and transposition defect (microtubular doublet resembles a central pair, when it translocated to the center). (C) Examples of secondary ciliary defects, left to right: duplicated CP, a cilium cross section showing lacking of MTD and presence of extra MT, one cross section showing extra tubules in the periphery of the cilium, one cilium with single tubules instead of MTD, and an example of a compound cilia (where a group of MT found by the same membrane) scale bars: 100 nm.

More recently, and to fill a gap of lack of standardization in analysing ciliary brushings by electron microscopy, a consensus guideline was developed by PCD electron microscopy experts representing 18 centres in 14 countries [286]. An initial meeting and discussion were followed using the Delphi method to reach a consensus. The agreed guideline was tested and enhanced through exchange of samples and electron micrographs between the 18 diagnostic centres.

The final guideline provides the following: a) Agreed terminology and a definition of class 1 defects which are diagnostic for PCD; b) Identifies class 2 defects which can indicate a diagnosis of PCD in combination with other supporting evidence; c) Describes features which should be included in

a ciliary ultrastructure report to assist multidisciplinary diagnosis of PCD d) Defines adequacy of a diagnostic sample [286].

Genetics of PCD

PCD is an autosomal recessive (AR) disease, however in rare cases other modes of inheritance have been described (X-linked or autosomal dominance). Currently, more than 40 genes have been identified, explaining approximately 70% of cases, where there seems to be a clear association between genetic defects, ciliary ultrastructure and motion defects [260].

AR disorders are only clinically apparent when a patient has a homozygous mutation. The general inheritance pattern might have the following characteristics i) patients parents appear to be clinically normal; ii) a vertical transmission is not expected, the transmission pattern appears to be horizontal; iii) male and female are affected equally iv) when both parents are heterozygous carriers of the mutation, 25% of their offspring will be likely to be affected, 50% with be carriers and 25% will be completely normal (Figure 9) [287].

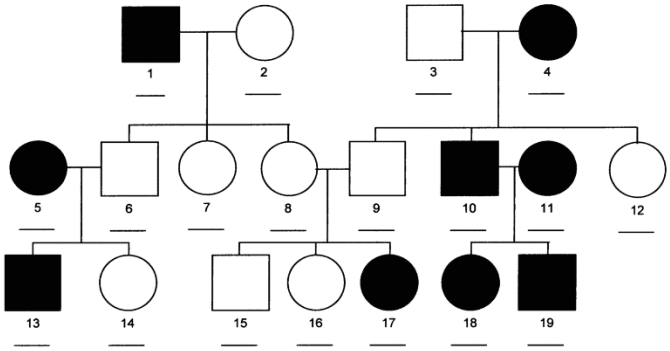

Figure 9. Chart showing two families (squares are males, and circles females) where the gene of an AR disorder is mutated either homozygous (shadowed shapes) or possibly heterozygous (blank). Focusing on individual 6 that is a carrier of the affected gene (inherited from the parents), when he matches with a homozygous individual, their offspring have 50% likelihood of being homozygous. Individual 5 will always pass on an affected copy of the gene. Individuals eight and nine are carriers since their offspring shows a classical AR pattern, in which 25% are homozygous, 50% heterozygous, and 25% have no mutation. Individuals 10 and 11 are homozygous, and will produce affected offspring since they will both provide affected copies of the gene.[287]

Cystic fibrosis (CF) is also an AR disorder but only a gene is involved, the *CFTR* which was discovered in 1989. *CFTR – Cystic fibrosis transmembrane conductance regulator* - encodes the transmembrane conductance chloride channel, and, more than 2000 *CFTR* mutations have been identified and described [288].

Compared to CF, PCD is a genetically heterogeneous disease. The first PCD associated gene, *DNAH5*, was only discovered in the year 2000, and pathogenic mutations cause defects in the ODA [289].

Most of the disease-causing mutations identified to date involve the absence or dysfunction of ciliary axonemal dyneins, but it is well-known, dozens of genes might be implicated in PCD caused by

mutations that are not linked to dynein motor proteins. Below is the most up to date list of genes that are known to be related to PCD based on the work of M. Legendre, et al. (2020) [94]. PCD-causing mutations have been identified on genes that include *DNAH5* (dynein axonemal heavy chain 5), *DNAH11* (dynein axonemal heavy chain 11), *DNAI1* (dynein axonemal intermediate chain 1), *DNAI2* (dynein axonemal intermediate chain 2), *CCDC114* (coiled-coil domain containing protein 114), *ARMC4 (*armadillo repeat containing 4, or outer dynein arm dicking complex unit 2 – *ODAD2), CCDC151* (coiled-coil domain containing protein 151), *TTC25* (tetratricopeptide repeat domain 25 or outer dynein arm docking complex subunit 4 – *ODAD4*), *DNAH9* (dynein axonemal heavy chain 9), *TXNDC3* (thioredoxin domain-containing protein 3), *DNAL1* (dynein axonemal light chain 1) that are known to be linked to absence or truncation of the ODA and are expressed in the ciliary axoneme [240,281,296,297,285,289–295]. *CCDC103* (coiled-coil domain containing protein 103), *ZMYND10* (zinc finger mynd-type containing 10), *C21orf59* (chromosome 21 open reading frame 59 or cilia and flagella associated protein 298), *DNAAF5* (dynein axonemal assembly factor 5), *LRRC6* (leucine rich repeat containing 6), *RPGR* (retinitis pigmentosa gtpase regulator), *SPAG1* (sperm associated antigen 1), *PIH1D3* (PIH1 domain-containing protein 3, also known as dynein assembly factor 6), *DYX1C1* (dyslexia susceptibility 1 candidate 1), *DNAAF1* (dynein axonemal assembly factor 1), *DNAAF2* (dynein axonemal assembly factor 2), *DNAAF3* (dynein axonemal assembly factor 3), *C11orf70* (chromosome 11 open reading frame 70), is the group of published genes connected to mutations in both the ODA and IDA. The expressed protein is typically localised in the cytoplasm where they are involved in the cilia biogenesis, except for *C11orf70* that is also found in the tip of the cilium and was found to be dependant of continuous IFT trafficking [246,298–301,302–309]. Mutation in the inner-arm alone are not frequent but *DNAH1* (dynein axonemal heavy chain 1) has been described to be linked with the IDA in the ciliary axoneme [278] . Cases where there is an absence of the inner dynein arm together with axonemal disorganization have been shown to result from mutations in *CCDC39* (coiled-coil domain containing protein 39), *CCDC40* (coiled-coil domain containing protein 40) and *TTC12* (tetratricopeptide repeat domain) [94]. *CCDC39* and *CCDC40* can be found in the axoneme [310] [311]. However, TTC12, a cytoplasmic protein, has milder microtubular disorganization and absent IDA and ODA observed in patient sperm [312] [94]. It is also known that *DRC1* (dynein regulatory complex 1), *DRC2* (dynein regulatory complex) and *GAS8* (growth arrest specific 8) are involved in the assembly and regulation of the N-DRC [284,313,314], and mutations within the genes can lead to mis-aligned outer doublets in some cilia cross sections. Another large group of genes involved in PCD defects, are those that when mutated show defects in the CP and RS, these include, *RSPH1* (radial spoke head component 1), *RSPH3* (radial spoke head component 3), *RSPH9* (radial spoke head component 9), *RSPH4A* (radial spoke head component 4 homolog A), *HYDIN* (axonemal central pair apparatus protein), *SPEF2* (sperm flagellar 2), *STK36* (serine/threonine kinase 36), *NME5* (non-metastatic cells 5), *DNAJB13* (DnaJ heat shock protein family member B13), and *CFAP221* (cilia and flagella associated protein 221). So far, cytoplasmic *CFAP221* has shown no ultrastructural defects in Transmission Electron Microscopy (TEM) sections, albeit, functional studies, reveal motility defects [315]. Regarding *HYDIN* and *SPEF2*, the CP complex defects might be missed during the TEM analysis. There are genes that are not specifically linked with axonemal abnormalities but rather associated to

multiciliogenesis defects, those are *CCNO*, *MCIDAS* and *FOXJ1* [100,283,316,28]. Patients with symptoms consistent with PCD and marked reduction in the number of motile cilia in the airway cells have been shown to have mutation in one of these two genes, *CCNO* and *MCIDAS*. Both genes code for proteins required in centriole assembly and replication [283,316]. Clinically these patients are unlikely to have *situs inversus* (Constant et al. 2021 accepted for publication) because nodal cilia biogenesis in monociliated cells do not require *CCNO* or *MCIDAS* [283]. Thanks to cilia research using several animal models and *in vitro* experiments, it has been possible to identify genes that are linked to PCD but with normal cilia ultrastructure; namely *OFD1* (oral-facial-digital syndrome 1 protein), *NEK10* (never in mitosis A-related kinase 10) associated with short cilia, *CFAP57* (cilia and flagella associated protein 57) and *LRRC56* (leucine rich repeat containing 56) known to cause motility defects in organisms like *Chlamydomonas* and *Trypanosoma* and *GAS2L2* (growth arrest specific 2 like 2) where cilia orientation seem to be affected [317,318,319–321]. Even with the exhaustive PCD genetics roadmap described here, mutations in PCD genes account for only 70% of all known PCD cases [94,322].

Mutations in the ODA dynein axonemal heavy chain *DNAH5*, are the most common and underlie 28% of the cases in Europe [289]. The second most common mutated gene is the *DNAI1*, accounting for 11% of the cases [289]. Mutations in *DNAH6 (*dynein axonemal heavy chain 6) were described for the first time in 2015 using zebrafish, describing a phenotype of heterotaxy and motility impairment, possibly due to microtubular abnormalities and central pair defects in ~30% of the cilia observed in *Dnah6* knocked down samples, the abundance of ODA was not affected [323]. The authors provide evidence of trans-heterozygous interaction between *DNAH6* and other genes (in patients showing ultrastructural abnormalities in the ODA), an event that can potentially cause a phenotype of PCD (which means that this gene mutated in only one allele, when in combination with other mono-allelic mutation in different PCD gene may case a phenotype) [323]. Generally, mutations are associated with defects in ciliary ultra-morphology, but there are other genes known to harbour PCD mutations, including *DNAH11*, in which patients seem to have normal ciliary ultrastructure by normal TEM and cilia motility defects are the only diagnostic features [324]. These cases highlight the need for complex and multidisciplinary diagnostic methods such as high-speed video microscopy (HSVM), genetics, immunofluorescence (IF), and transmission electron tomography (ET) [325].

Genotype-Phenotype

The correlation between patient gene mutations and clinical manifestations are of great interest in the field of PCD research and diagnostic testing [326]. Groups of patients were analysed using standard statistical analysis to compare the clinical characterization and the results from the laboratory tests and radiology exams of patients with genetically diagnosed PCD, and subsequent correlation between them. This approach led to the main source of knowledge about certain genotype-phenotype relationships. For example, *situs inversus* has been found to be less likely in RSPH mutations and multiciliogenesis impairment, since nodal cilia are not affected [327,328]. Patients with mutation in the *DNAH11* gene show preserved lung function, seen when lung clearing [281], on the other hand , *DNAH5*

patients show the largest spectrum of phenotypes [289]. The reasons behind the range of *DNAH5* phenotypes is unclear but could be due to a large number of different mutations within this large gene, so far, at least 100 different pathogenic mutation have been reported [289].

More recently Shoemark et al. (2021) described a tool called Topological Data Analysis (TDA) clustering [326], to examine genotype-phenotype correlations in almost 400 individuals from three European countries. TDA software by symphony AyasdiAI platform (www.ayasdi.com, v 2.0, Ayasdi Inc., Menlo Park CA) was used to develop the topological models for the genotype-phenotype assessment. Models were generated using automated analysis options. Highly complex data were summarized and compressed into smaller representation of their variability using Locally Linear embedding (LLE non-linear reduction technique). Using this methodology, the authors were able to identify several previously unknown genotype-phenotype relationships. The benefit of TDA cluster analysis for PCD is that many parameters (phenotypic data used was body mass index (BMI), lung function tests, wet cough, rhinitis, glue ear, cardiac *situs*, congenital heart disease, nasal nitric oxide (nNO), cilia beat pattern (CBP) and transmission electron microscopy (TEM)) can be correlated, and therefore, having access to the genetic information, it was possible to explore the underlying patterns in complex datasets by generating clusters of individuals with similar features. A further advantage of TDA clustering is that it allows the observation and analysis of small clusters of interest in large datasets. The most recent genotype-phenotype PCD data suggests that RS and N-DRC/molecular ruler (CCDCs 39/40 and DRC), have worst prognosis regarding lung function, likelihood for ear glue, less rhinitis and no *situs inversus*. Dynein heavy chain proteins, *DNAH5* and *DNAH11*, show preserved lung function and no major NRDS. This confirms an already known phenotype typical of *DNAH11*, whereas *DNAH5* appeared phenotypically diverse regarding lung function, with no clear cluster observed, this also corroborates what was previously described by Hornef et al. [289,326,329].

Understanding the genotype-phenotype association, will ultimately improve the clinical management of patients, identifying those that might need a more aggressive or personalized treatment due to their underlying genetics. Patients with mutation in *CCDC39* and *CCDC40* might benefit from more intense and targeted therapies [330,331]. The link found using the topological analysis between a certain genetic defect, ultrastructural and CBP results, indicated that TEM and HSVM tests play an important role in the classification of novel gene variants and variants of uncertain significance (VUS). These tests can also direct the genetic testing more towards a specific sub-set of genes [326].

Diagnosis of PCD

The first step in diagnosing PCD is the evaluation for clinical features of PCD. To determine the PICADAR (primary ciliary dyskinesia rule), a questionnaire with seven simple questions are answered and used to predict the likelihood of a patient to have PCD. It is used in many PCD specialist centres

as an initial evaluation to determine if diagnostic testing is required. PICADAR was developed and validated using cohorts of known PCD patients and can be used in any patients with chronic respiratory symptoms starting in early childhood. The total score is calculated and the individual probability of a positive PCD diagnosis can be estimated. Patients with a score >10 have >90% probability of testing positive for PCD, and those scoring <5 are more unlikely to test PCD-positive [332].

PICADAR		
Does the patient have a daily wet cough that started in early childhood?	**Yes** – complete PICADAR **No** – **STOP**. PICADAR is not designed for patients without a wet cough	
1. Was the patient born pre-term or full term?	Term	2
2. Did the patient experience chest symptoms in the neonatal period (*e.g.* tachypnoea, cough, pneumonia)?	Yes	2
3. Was the patient admitted to a neonatal unit?	Yes	2
4. Does the patient have a situs abnormality (situs inversus or heterotaxy)?	Yes	4
5. Does the patient have a congenital heart defect?	Yes	2
6. Does the patient have persistent perennial rhinitis?	Yes	1
7. Does the patient experience chronic ear or hearing symptoms (*e.g.* glue ear, serous otitis media, hearing loss, ear perforation)?	Yes	1
	Total score =	

Figure 10. Example of a PICADAR scoring chart. PICADAR is a scoring system that uses seven questions to predict the likelihood of having PCD. It can be used in any patients with chronic respiratory symptoms starting in early childhood. The right-hand column show scores, and any above 5 indicate likelihood of the patient being diagnosed with PCD [332]

Diagnosis of PCD is complex and patient clinical features play a major role in the initial triage. As mentioned above, PICADAR score is a useful tool, however its only trustworthy if the patient shows some or all of the symptoms like *situs* abnormalities, unexplained NRDS, persistent rhinitis from birth, middle ear disease with complications and congenital heart disease [5]. However, it still prioritizes the presence of a wet cough, which is a poor indicator due to its low discriminative value as wet cough is highly prevalent in both PCD positive and negative. The best approach for PCD referral, is to take into consideration many factors of the patients medical history [5].

After referral for PCD, a patient will have assessment of their ciliary function by HSVM and nNO. In the event of an abnormal or equivocal result the samples must be sent for TEM, IF, and cell culture. Genetic testing is recommended either to confirm a positive diagnostic outcome (recommended in case of 'highly likely PCD'), or to clarify in case of a strong clinical history presenting with normal or unclear test results [5].

Diagnostic tests

When patients are referred for diagnostic testing, PCD is one of several different possible diagnoses. Therefore, investigations to exclude other more common conditions have often been managed during clinical consultation by a referral centre. To exclude CF, a sweat test is administered, whereas exclusion of gastro-oesophageal reflux, amongst others, requires immunological investigation. These tests are complex and required specialised training and equipment; therefore, dedicated PCD reference centres are required. The range of PCD phenotypes can be confounded by the presence of secondary defects caused by airway infections, further emphasising the requirement for specialist centres [333].

Listed below are the different diagnostic tests and the guidelines for the diagnosis of PCD developed through a collaboration of multiple centres worldwide.

Screening tests

The most known screening tests are the saccharin test and the nNO measurement test. Saccharin test is an outdated technique to test the MC, it consisted of placing saccharin approximately 1 mm behind the anterior end of the inferior turbinate. In the presence of normal mucociliary action, the saccharin will be swept backwards to the nasopharynx and a sweet taste perceived. Failure to detected sweetness within 10-20 minutes may be the sign of delayed MC [334,333]. Nevertheless, the test has limitations in children, if the child sniffs during the test saccharin may be tasted even in the absence of MC, and the test does not differentiate between primary and secondary dyskinesia [333].

nNO measurement in the nasal airway, shows consistent high reliability with approximately 95% sensitivity and specificity (when measure in a chemiluminescence analyser using velum closure technique), as shown by two Independently conducted systematic reviews [335,336], the accuracy of the test might differ depending on the type of analyser used, age of the patient and sampling method [337]. NO is an important cell-signalling molecule that is implicated in a range of important functions in the organism, such as neurotransmission and neuromediation, relaxation of muscles, vasodilatation and host defence actions [338]. NO is present in the exhaled air of humans, and when is measured in the nose at a rate of 250 ml/min during breath holds, a nNO level of >250 ppb is considered normal, nevertheless there is no consensus on appropriate thresholds determined [340] . nNO is known to be abnormally low in PCD patients when compared to controls, for unknown reasons [341]. The test has limitation in young children, asunder 6-year olds can be uncooperative, or struggle to breath hold. This stresses the need for standardization of protocols and thresholds for tidal breathing, including for cases where a differential diagnosis given between PCD and another respiratory disease (bronchiectasis, CF and even rhinosinusitis) that can lead to low NO values [333].

Ciliary Beating pattern and Frequency

Defects in cilia motility associated with PCD can be screened *ex vivo* by assessment of the activity of ciliated epithelial cells, biopsied from the nose or the bronchus [258]. To estimate CBP and cilia beat frequency (CBF) it is essential that cilia are kept in an enriched medium at optimal conditions (controlled temperature). HSVM is typically performed using a microscope equipped with a heated stage at 37°C, to mimic the human body temperature, but it has been showed that is not mandatory as long as a record of the diagnostic temperature is kept [342]. Cilia beating can be assessed from three planes: sideways profile; beating towards the observer and from the top [343]. To record beating cilia, a digital high-speed camera can be adapted to a LM, to acquire a rate of around 400 frames per second (fps). The camera allows the video sequences to be recorded and played back at a reduced frame rate (slow motion 30-60 fps [340]) or even frame by frame. The precise movement of the cilium may be observed and evaluated during this beat cycle [343]. This procedure grant access to the sample CBP and CBF [340]. The clips must be acquired from several patches of cells (10), to have a reliable test. It is advised that each PCD service sets its own normal CBF ranges based on the population and HSVM setup [344].

CBF and CBP offers the direct readout of the ciliary function. Previously, CBF was the primary measure of ciliary motility dysfunction, but now that it is considered a limitative analysis, giving only the perception of high or low CBFs, the isolated study of CBF is subjective and presents low specificity and sensitivity, leading to a high number of false negatives [340,345]. The limitations of measuring the CBF is resolved by analysing CBP that has higher sensitivity in diagnosing PCD [346,277]. Nevertheless, the evaluation is still mostly done by visual assessment with no consensual metrics. Mostly due to the need of highly skilled staff, there are services that are still not using HSVM as a diagnosis test [347].

Several centres are already using computer analysis for the assessment of cilia function [340]. With the aim of greater standardization, Sampaio et al. (2021) developed software created to evaluate CBF in a semiautomated way, called CiliarMove [342]. This tool allowed the authors to determine the CBF in a cohort of Portuguese PCD patients within a genetic study and determine the normal CBF range for a healthy volunteer target population. The authors assume the sampling may not represent the general population, but the results go in line with what has been described previously [342].

HSVM is yet not sufficiently standardized to exclude PCD, and it is generically agreed that the test needs to be done by experienced staff as part of the diagnosis work-out [340].

Primary Cell Culture

Primary airway cell cultures are developed from airway cells and can be obtained from biopsies, brushings or explanted lungs [348]. Airway cultures date back to the 1980s, where several growth conditions were tested for bronchial cells [349]. Since the introduction of epithelial cell cultures, improved cell culture techniques have boosted the use of cultured airway cells for developing disease relevant models, drug testing and inhalation toxicology [350].

Epithelial cells are usually dissociated from extracellular matrix by protease treatment and unwanted cell type growth (fibroblasts) is inhibited by addition of selective medium. To allow cell expansion, essential growth factors are added, as well as antibiotics that will prevent the microbial overgrowth. In previous procedures, cells would be kept submerged in medium, attached to an extracellular matrix (likely collagen) in a plastic dish. However, primary airway cell cultures that are kept submerged result in loss of cell differentiation (into secretory and ciliated cells) [350]. Primary airway cell cultures became more physiologically relevant with the introduction of growing cells at the air-liquid interface (ALI) [348]. ALI greatly improves differentiation of the epithelial cells, matching an *in vivo* situation [351]. Cells growing in ALI evolve to a pseudostratified epithelium consisting of goblet cells, ciliated cells and basal cells [352]. ALI is a cell culture method where epithelial cells are grown from a nasal biopsy and the apical surface exposed to the air to simulate the human airway. It is frequent to start by seeding the cells onto the permeable membrane of the insert, and initially the cells are fed both from the apical side and the basal side. Once reaching confluence, the cells are fed only via the basal chamber, leaving the apical side exposed. In the particular case of ciliated cells, the exposed apical region is advantageous for reciliation [353]. Ciliary movement and production of mucus can be assessed under a LM for control and analysis.

This method is adequate for ciliated epithelium due to their ability to grow cilia. These ciliated cells can be kept in ALI culture for many months and diagnostically assessed if any uncertainty is raised during the examination of the primary sample.

In some European clinics, specific ALI cultures of patients' nasal epithelia are performed to confirm the first diagnosis [354]. This is preferable for ambiguous cases where infection or inflammation are present, or the sampling may damage the epithelium. It is assumed that in culture there will be no secondary defects caused by infection or inflammation, and therefore only defects link to gene mutations remain [265,340].

Immunofluorescence

Many PCD diagnostic centres now use IF antibody labelling to help determine the presence or absence of key ciliary proteins in patient samples. This antibodies used are raised against axonemal motor proteins or assembly factors.[340,355].

IF has been paramount in the diagnosis and understanding of PCD in many ways, for instance in the distribution of proteins like DNAH11 and DNAH9, which expression is not transversal along the axoneme, but found in specific regions. In the case of DNAH11 its localisation is to the proximal region of the cilium, which when mutated, by HSVM might be seen as reduced bending capacity of the axoneme or static in patches, and classic hyperkinetic CBF (CBF > 11 Hertz (Hz)) [266]. In contrast DNAH9 has been showed by IF to be restricted to the apical region of the cilium [356]. In regard to the CBP in cases with *DNAH9* loss-of-function, stiffness towards the tip is the most commonly observed phenotype and varies depending on the severity of the mutation [285].

IF is a straight forward method to detect PCD proteins, however, as a diagnostic test it has limited sensitivity for PCD due to the lacking of validated commercial antibodies, and low imaging resolution [356]. Super resolution confocal microscopy is considered a future improvement for PCD diagnosis but is not available to most PCD centres. Zhen Liu et al. (2020), described a tool using a super resolution workflow to assist in the diagnosis of PCD [356]. They showed in their work that super resolution imaging is a powerful tool to investigate PCD proteins. For this study they used a panel of 21 antibodies that recognize ciliary proteins liked to PCD, named by the authors as the PCD proteome. With high-resolution 3D-SIM (three-dimensional structured illumination microscopy), it was possible to characterize the distribution of the markers in the PCD proteome. *PIH1D3*, a recently described X-linked PCD gene known to be a putative axonemal dynein assembly factor, showed punctate labelling found in the cell body [304]. They also presented a machine learning tool using IF 3D-SIM, based on a quantitative analysis, designated as rotational polarity analysis [356]. Consists of an automated image analysis to quantify rotation polarity of BB and basal feet pairs in PCD cells. Through the creation of a MATLAB (matrix laboratory) script, the authors could automatically identify BB and basal feet, and calculate orientation of each pair in comparisson to the image axis [356]. The authors consider IF 3D-SIM workflow a promising tool for translational into clinical diagnostic that can be improved by the implementation of high-throughput staining and data collection methods. Rotational polarity can be seen as a quantitative alternative in cases that cannot be diagnosed by other methods [356]

Currently, surveys are also being done to reach a consensus, not only in the analysis of IF but also guidelines for the preparation of samples and which antibodies are more adequate to each situation. This emphasises the important of exchange of knowledge in improving the diagnostic pathway for PCD [357,358]. Nevertheless, according to the most recent task force guideline (2017) [340], it is still unfitted to determine the accuracy of IF testing for diagnosis. However, task force experts agree that IF can be useful in clinical settings. IF is cheaper and easier than other diagnosis tests, and presents as a potential test for resource-limiting centres [340].

Genetic testing

In PCD, to establish a genetic diagnosis, non-ambiguous biallelic mutations and hemizygous mutation in X-linked genes, should be identified [340]. Most of the reported mutations in PCD genes are:

nonsense, or a stop mutation, changes in the DNA that causes the protein to terminate leading to a non-functional protein; frameshift mutation, in which there is an insertion or deletion of a nucleotide in a way that disrupts the gene reading frame; or splice mutations, where an insertion or deletion of a nucleotide occurs in a specific site at which splicing takes place. On the other hand, missense mutations (incorporation of the wrong amino acid into a protein) are a minority [340]. Most PCD gene mutations are private, meaning they are found in a specific family or population, but, there is knowledge of founder mutations (characteristic of groups geographically or culturally isolated, in which one ancestor was the carrier of the altered gene and passed it on) like *DNAH5* [289] and *DNAI1* [359], and mutational hotspots, such as *CCNO* [360]. Mutation ranking in genetics should follow international guidelines: (1) pathogenic, (2) likely pathogenic, (3) uncertain significance, (4) likely benign, or (5) benign [361].

It is expected that all DNA sequencing technologies can be used to test patients with confirmed or high suspicion of PCD, those technologies are: i) sanger sequencing of all coding regions and flanking intronic regions, ideally targeting to the genes responsible for a specific ultrastructural defect (point mutations); ii) targeted Next Generation Sequencing (NGS) of all coding regions and flanking intronic regions. Like sanger, this technology will detect point mutations; iii) whole exome sequencing has usually a lower coverage and depth than targeted NGS (usually not sufficient to detect deletions or duplications of more than one exon); iv) targeted copy number analysis as already been reported as a semi-quantitative qPCR (quantitative polymerase chain reaction) to characterize large insert/deletions [362]; v) whole genome copy number analysis (single nucleotide polymorphism - SNP array) suitable to detect large rearrangements but shows low sensitivity for intragenic deletions; vi) transcript analysis on airway epithelial cells from the patient, technique used in patients that showed a single heterozygous mutation in a relevant gene. This technology can reveal deep intronic mutations that were missed by any of the above-mentioned techniques [340].

Albeit the high number of technologies available to search for a specific PCD mutation, as mentioned before, it is suggested that genetic testing identifies the gene in only approximately 70% of the PCD cases [326,330,362]. It is likely that this number increases as more genes and pathogenic variants are identified [340]. Nevertheless, it is still essential to incorporate the genetic results together with the other PCD testing results.

Transmission Electron Microscopy (TEM)

TEM is one of most important tests to the diagnose PCD by determining ciliary ultrastructural defects. However, standardization between experts and centres has been hard to reach. According to Shapiro et al. (Department of Paediatrics, Montreal Children's Hospital, Quebec, Canada) at least 20–50 clear ciliary cross-sections are required for diagnostic TEM, and abnormalities should be consistently demonstrated on cross sectional images from multiple different cilia to be considered disease causing [347]. In contrast , PCD clinics in Southampton General Hospital and on the Royal Brompton Hospital (RBH) (London), 50-100 ciliary cross-sections are analysed for each sample [286] . In Belgium, in the

department of paediatric pulmonology, University Hospital Leuven, Boon et al. also studied, per sample at least 50 transversal cross-sections [363]. Based on a questionnaire I made in 2018 between 3 independent hospitals using TEM for diagnosis of PCD (Oncology Institute – Lisbon; Fernando da Fonseca Hospital – Amadora/Sintra and S. João Hospital - Oporto), I found that the services were divided between assessing only up to ten ciliary cross-sections, or at least a thousand cilia before submitting a valid report (unpublished data). This proves how complex and subjective the analyses of cilia cross sections are amongst experts. However, the majority of experts work towards standardization in many areas of PCD, while stressing the complexity of the disease [286].

Some cilia abnormalities are easier to assess than others and so, only a consistent number of ciliary cross sections will contribute for a confident quantitative analysis. According to the most recent guidelines (Shoemark et al. 2020 [286]), during an assessment the specialist should evaluate 50 or more oriented cross sections of cilia, for an accurate analysis. The aim in TEM, is to push the use of the nomenclature (class 1 and class 2 defects) suggested in this international consensus and therefore make a more reliable and transferable analysis [286].

Advanced techniques for the confirmation of a PCD defect

Confidence in diagnosing patients with subtle defects is low, and patients often undergo several repeat nasal biopsies in attempts to establish a diagnosis [364] Electron tomography (ET) can be used to identify the structural defects in some of these cases.

In TEM, 3D objects are projected into two-dimensional (2D) images, but in many cases, 2D projections are insufficient to understand the relationship between 3D structure and the function of nanoscale objects [365]. With ET it is possible to retrieve 3D structural information from a tilt series of 2D projections [366]. Retrieving the missing third dimension is required to determine the functionality of many structures [365]. ET provides a wide range of resolutions taking full advantage of the versatile capabilities of the TEM [366]. As an example, ET and genetics used in combination have identified the absence of *HYDIN* as another cause of PCD [282]. ET showed absence of the projection, C2b, associated with the CP apparatus in patients with a *HYDIN* defect [282].

Pathogenic *DNAH11* mutations, are difficult to assess using conventional TEM, being considered as having a normal phenotype [266]. The incidence of this mutation was previously shown to be around 20% in patients with PCD, without a defined ciliary ultrastructural defect [281]. Biallelic mutation of the gene causes an abnormality in ciliary ultrastructure undetectable by conventional TEM, but with characteristic abnormal CBP detected by HSVM that includes reduced bending capacity and increased CBF [266]. *DNAH11* mutations result in abnormality of the ciliary ultrastructure when visualized by ET. The defect is specific to the “forearm” of the ODA and is detected at the proximal portion of the cilium where *DNAH11* is located. Advantageously, ET established a structural abnormality where TEM showed previously normal. (Figure 11) [364].

Other methods have been created, such as the PCD detect software, to enhance TEM images through image averaging and classification to help clarify the absence of ciliary structures, [367].

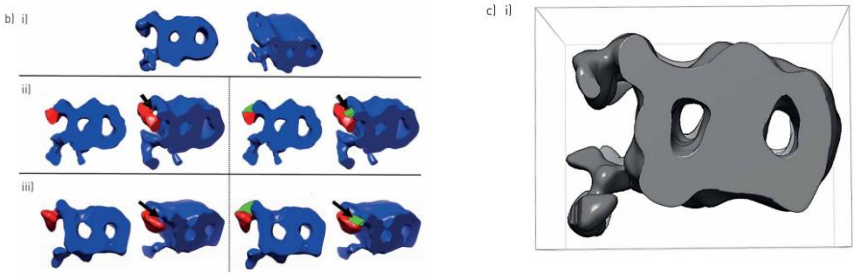

Figure 11. Location of *DNAH11* in the ODA of the microtubular doublet showed by Shoemark et al. using ET [364]. Image shows data from volumes from averaged transverse tomograms from the proximal portion of the axoneme of healthy controls (b) i)), and *DNAH11* mutation patients showing two different mutation types (b) ii) and iii)). Red marks the predicted location of *DNAH5* and the green triangles were added to the images on the right to indicate where *DNAH11* is predicted to be missing. Image on the right (c) i)) represent a tomogram from a healthy control as visualized in Chimera [364].

PCD is a complex multi-systemic disease, and to diagnose it, specialist expertise is required combined with well-established techniques. Therapeutic trials of new drugs and treatments in humans are complex, so it is important to have good reliable animal models for the initial testing to help establish the safety and effectiveness of different therapies.

My objectives are as follows; 1) contribute for the standardization of data analysis, appropriate normative controls, and isolation and analysis techniques to facilitate comparison of results among PCD diagnostic centres, and results regarding this aim can be found in chapters 2 to 4; and also 2) refine and adapt EM techniques for a better classification of motile cilia in both human airway and zebrafish major ciliated organs, which will be described in detail in chapter 5. This will play an important role in establishing zebrafish as a model for ciliopathies, the same way, zebrafish are used as a model in other diseases, such as carcinogenesis, infection, immunological diseases and psychological and behavioural disorders, amongst others [182].

2

CHAPTER 2

Ciliary Feature Counter: A program for the Quantitative Assessment of Cilia to Diagnose Primary Ciliary Dyskinesia

Published Article doi:10.3390/diagnostics10080524

Andreia L. Pinto[1], Ranjit K. Rai[1], Claire Hogg[1,2] and Thomas Burgoyne[1,3,*]

[1] Paediatric Respiratory Medicine, Department of Paediatrics, Royal Brompton & Harefield NHS Trust, London SW3 6NP, UK; a.pinto@rbht.nhs.uk (A.L.P.); r.rai@rbht.nhs.uk (R.K.R.); c.hogg@rbht.nhs.uk (C.H.)
[2] Department of Paediatrics, Imperial College London, London SW3 6LY, UK
[3] UCL Institute of Ophthalmology, University College London, London EC1V 9EL, UK
[*] Correspondence: t.burgoyne@rbht.nhs.uk, Tel: + 44-(0)20-7352-8121

Personal contributions

My contribution to this manuscript was conceptualizing and investigation about the necessity of having a digital counter for PCD, and also in the preparation, reviewing and editing of the manuscript.

Abstract: Primary ciliary dyskinesia (PCD) is a disorder that affects motile cilia in the airway that are required for the removal of mucus, debris, and pathogens. It is important to diagnose PCD in early childhood to preserve lung function. The confirmation of a diagnosis relies on the assessment of ciliary ultrastructure by transmission electron microscopy (TEM). TEM involves the quantitative assessment of the ciliary ultrastructure to identify PCD defects as well as abnormalities resulting from infection. Many specialist diagnostic centres still rely on physical counters to tally results and paper notes to summarise findings before transferring the results to computer databases/records. To speed up the diagnostic data collection and increase the protection of patient information, we have developed digital ciliary feature counters that conform to the PCD reporting international consensus guideline. These counters can be used on a computer or tablet, and automatically generate notes regarding sample observations. We show that the digital counters are easy to use and can generate TEM diagnostic reports that will be useful for many PCD diagnostic centres.

Keywords: cilia; primary ciliary dyskinesia; digital counter.

Introduction

Primary Ciliary Dyskinesia (PCD) is a heterogeneous genetic disorder of the motile cilia. Cilia are hair-like structures which play an essential role in the airway by moving and clearing mucus, debris, and pathogens. PCD results in a failure to clear mucus from the airway, leading to chronic lung disease and rhinosinusitis, as well as impacting on hearing and fertility. It is estimated that the prevalence of PCD is approximately 1 per 10,000 births, but it is more common in populations where there is consanguinity [368]. A diagnosis of PCD at an early age is vital to implement appropriate treatment to preserve lung function and prevent lung damage. Both the European and North American diagnostic guidelines recommend that a diagnosis of PCD should be confirmed by transmission electron microscopy (TEM) in combination with another diagnostic test [340,369].

PCD can present as a number of ultrastructural defects by TEM (Figure 1). These include the complete or partial absence of the outer, inner, or both dynein arms, as well as microtubular disorganisation or a central pair complex defect (Figure 1b). Due to infection, other secondary non-PCD defects are often present and include compound cilia, extra tubules, and the absence of one of the microtubules from the central pair complex (Figure 1c). As the dominant diagnostic assessment for PCD, there are international consensus guidelines for reporting TEM results which involve classifying PCD defects into two classes, as shown in Figure 1d [286].

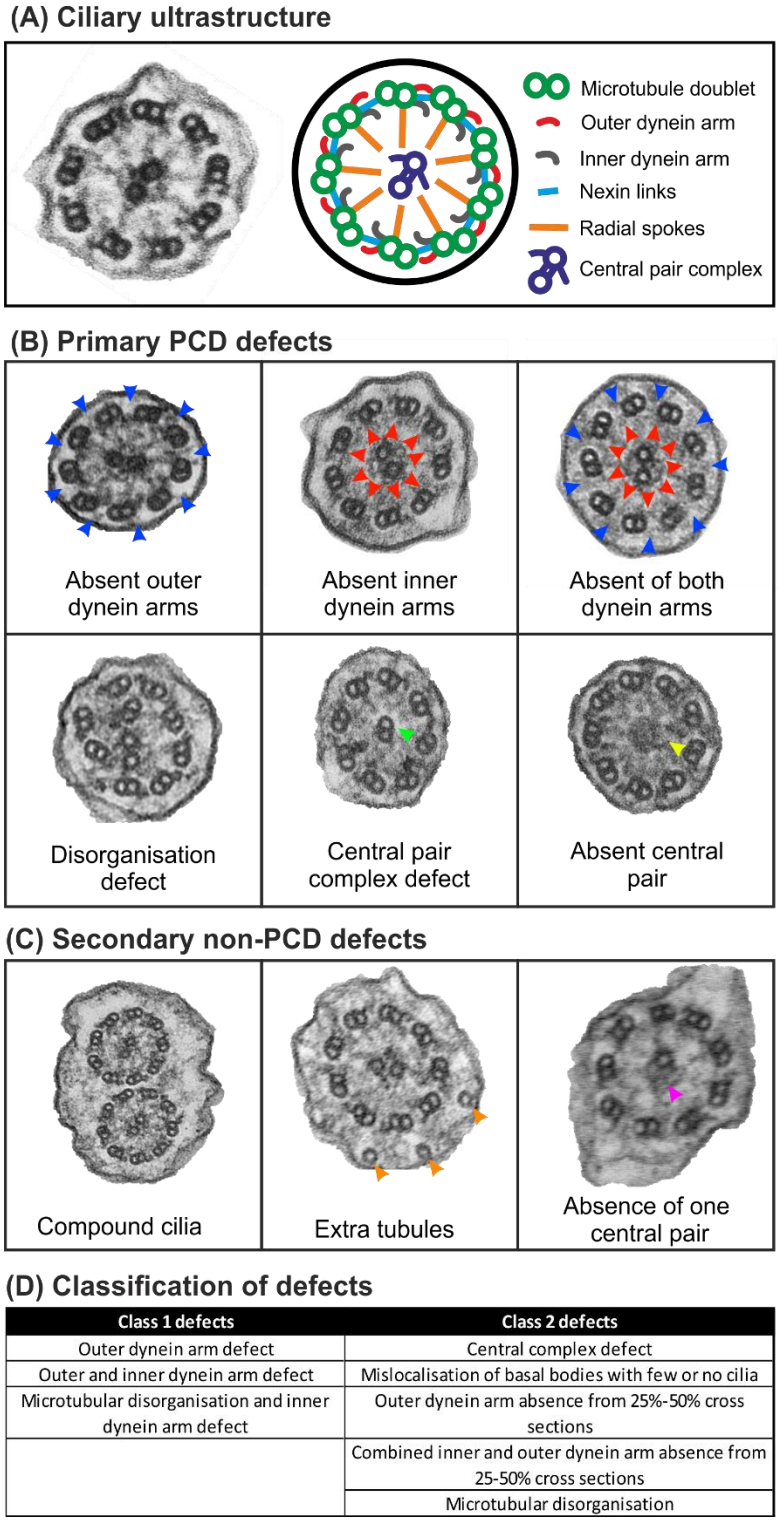

(D) Classification of defects

Class 1 defects	Class 2 defects
Outer dynein arm defect	Central complex defect
Outer and inner dynein arm defect	Mislocalisation of basal bodies with few or no cilia
Microtubular disorganisation and inner dynein arm defect	Outer dynein arm absence from 25%-50% cross sections
	Combined inner and outer dynein arm absence from 25-50% cross sections
	Microtubular disorganisation

Figure 1. Normal healthy ciliary ultrastructure as well as common ciliary defects associated with primary ciliary dyskinesia (PCD) and secondary to infection. (A) Electron microscopy image and diagram of a cross section through a healthy respiratory epithelial cilium, highlighting the main ciliary components. (B) Common PCD defects, including the loss of structures or disarrangement of the cilia. The blue arrows indicate absent outer dynein arms, the red arrows indicate absent inner dynein arms, the green arrow indicates a microtubule doublet that has transposed into the centre of the cilium, and the yellow arrow indicates the absence of the central pair microtubules. (C) Some of the ciliary defects associated with unhealthy respiratory epithelium are caused by bacterial or viral infections. The orange arrow indicates an extra microtubule within the cilium, and the purple arrow indicates the

loss of a single central pair microtubule. (D) The classification of primary PCD defects based on the international consensus guidelines for reporting TEM results [286].

Fifty or more ciliary cross-sections need to be evaluated to reach a diagnosis for PCD, as outlined in the international consensus guidelines [286]. These need to be well-orientated cross-sections, and when assessing them it is vital to be aware of the ultrastructural differences at the base and tip compared to the rest of the cilium (see Figure 2). This involves tallying the assessments of the ultrastructure of each cilium as well as the dynein arms, which is often done using a physical counter (see Figure 3) and paper notes, to score patient cilia and make notes about each diagnostic patient sample. These notes are to be typed up onto a computer, which is time-consuming and poses a patient information confidentially risk. To speed up the collection of results directly to a computer system and to follow NHS (UK) and many international guidelines to phase out paper notes, we have developed a digital PCD ciliary counter. This easy-to-use counter can be used on a computer or tablet and works well with a touch screen, and it generates notes based on the simple selection of options that describe the diagnostic sample.

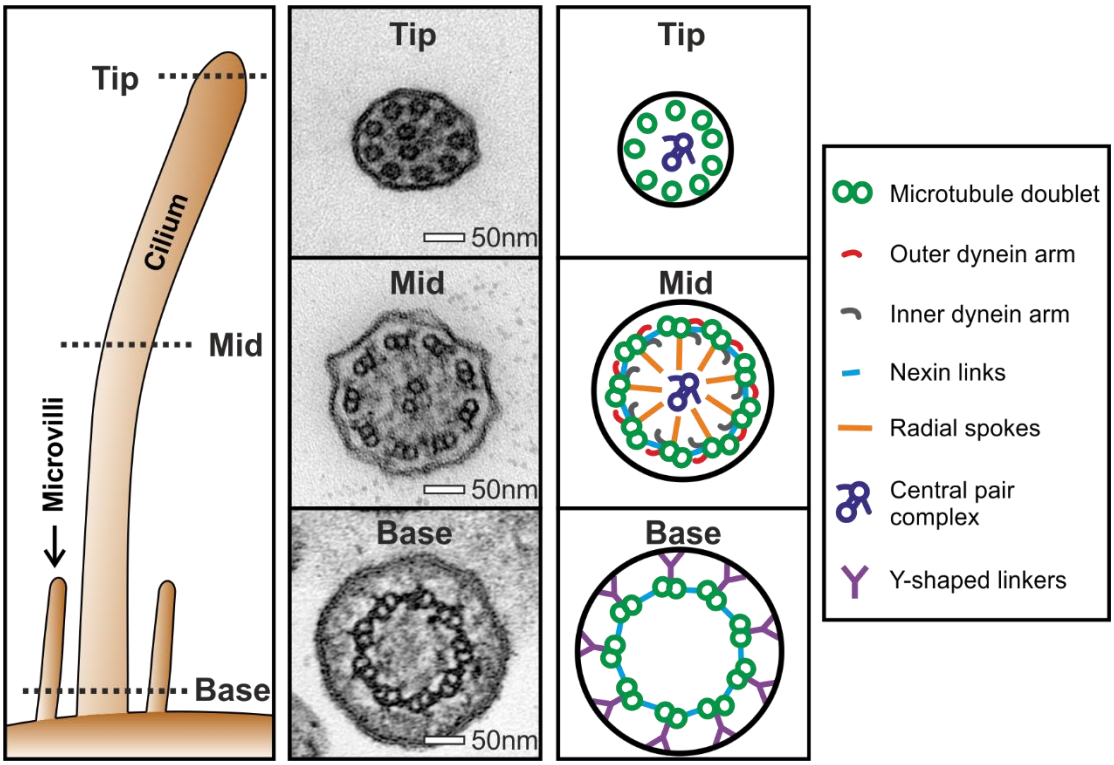

Figure 2. Ultrastructure of the different regions of a respiratory cilium. Respiratory cilia have a "9 + 2" microtubule arrangement (9 microtubule doublets and 2 single microtubules that make up the central pair), as can be seen in the mid region of the cilium. This ultrastructural arrangement runs throughout the cilium apart from at the tip and base where there are different ultrastructures, which include single microtubules and Y-shaped linkers, respectively, and an absence of dynein arms in both regions. When diagnosing PCD by TEM, it is vital to be aware of these differences in ultrastructure. In patients that have a central pair complex defect (see Figure 1b), typically the translocation of a microtubule doublet is observed at the tip, which makes it an important region of the cilium to examine.

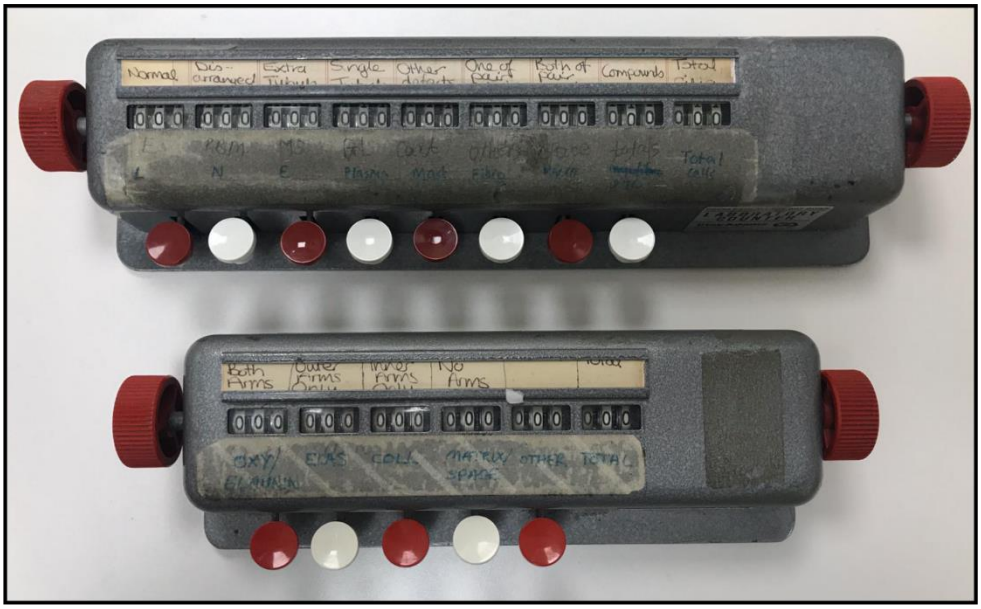

Figure 3. Physical counters used to count cilia features to assist in the diagnosis of PCD.

Materials and Methods

Preparation of Nasal Brushings for Ddiagnostic Electron Microscopy Aassessment

The ciliated respiratory epithelial cells were obtained using 3 mm bronchial cytology brushes inserted into subjects' noses and brushing the nasal turbinate. The biopsies were placed into media 199 (Thermo Fisher Scientific, Waltham, MA, US) before fixing by adding an equal volume of 2.5% gluteraldehyde in 0.05 M sodium cacodylate buffer at pH 7.4 and left overnight or longer (up to 2 weeks) at 4 °C. The biopsies were incubated in 1% osmium tetroxide in 0.05 M sodium cacodylate buffer at pH 7.4 for 1 h and subsequently embedded in a 2% agar aqueous solution. The samples were dehydrated in increasing concentrations of methanol (70%, 90%, and 100%), followed by propylene oxide and mixtures of propylene oxide and araldite (1:1 and 1:3, respectively). Finally, the samples were incubated with araldite overnight to remove any propylene oxide and embedded in araldite at 65 °C for 72 hrs. Then, 90 nm-thick sections were cut from the araldite-embedded nasal brushings onto TEM grids and stained using 2% methanolic uranyl acetate for 7 min and Reynolds lead citrate solution for 5 min.

Diagnostic Electron Microscopy Assessment

Diagnostic sample sections were viewed on a TEM—in our case, a JEOL 1400+ TEM—and images were acquired using an AMT 16X CCD camera. Strips of ciliated epithelial cells were examined, and single cells were ignored (unless there were no sufficient strips of epithelia). For each strip of epithelia, the number of cells were counted and the ciliary ultrastructure was examined and quantified to determine if they were normal or had a defect (disarranged; extra tubule; single tubule; other defects, including the total combined number of 8 + 2 (missing a microtubule doublet), 7 + 2 (missing two microtubule doublets) and 8 + 1 (transposed cilia, where the central pair is absent and a microtubule double is within the centre of the cilium) ciliary arrangements; missing tubule from central pair; missing

central pair; or compound cilia) as well as the assessment of dynein arms (both arms present, inner dynein arm defect, outer dynein arm defect, or the absence of both arms). When the cilia were slightly oblique, the microscope stage was tilted to provide better orientated ciliary cross-sections. While examining the samples, additional notes were taken to determine the following: if the cilia have a normal orientation and longitudinal profile; the number of cilia that have an 8 + 2, 7 + 2 and 8 + 1 ciliary arrangement ; as well as the relative amount of blood, ciliated strips, mucus, single cells, amount of cilia, inflammatory cells, and bacteria. Based on the counts and notes, a normal cilia or ciliary defect option was chosen from one of the following: normal; normal\unhealthy when there are secondary defects associated with infection and the presence of inflammatory cells and bacteria; class 1 defect (see Figure 1); class 2 defect (see Figure 1); or inconclusive due to unclear result or a small count. The counting and reporting follow the methods outlined in the international consensus guideline for reporting TEM results in the diagnosis of Primary Ciliary Dyskinesia [286].

Software Development

Both 32- and 64-bit versions of a basic and advanced counter to quantify ciliary features which assist in the diagnosis of PCD were designed using MATLAB 2020a and 2015b (Mathworks). The programs were built using the MATLAB GUIDE environment, allowing the generation of a graphical user interface and the programming of the underlying code. The two programs have been designed to be used while examining samples on the TEM, and they can be downloaded from the Figshare public repository.

The basic counter is a counter (Figure 4) to tally up ciliary features associated with PCD and secondary infection defects (see Figure 1 for the different types of defects). This has been designed to collect counts to subsequently input into the advanced counter. This approach may be popular with some people due to the large buttons in the basic counter. The counter has been programmed to tally (add one) when pressing the +1 button and to remove a value when pressing the −1 button. Values can also be added by typing numbers directly into the counter interface.

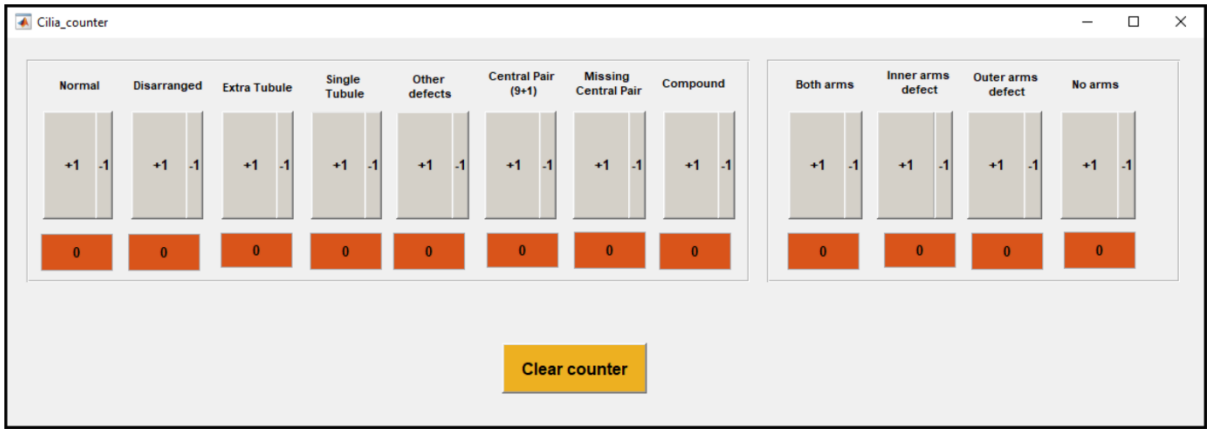

Figure 4. Basic digital counter to count cilia features to assist in the diagnosis of PCD.

The advanced counter includes a counter to quantify cilia at different regions of the diagnostic sample, with options to input sample information and notes (Figure 5). Similar to the basic counter, numbers can be tallied up or down by a value of one by pressing the +1 or −1 buttons, or values can be typed directly into the interface. The advance counter calculates the percentage of normal and defective cilia by dividing by the total number of cilia examined. If the values are modified by pressing +1, −1, or by entering a value, the percentages shown in the program are automatically updated. When viewing the sample on the TEM, there are checkboxes that represent the descriptors that can be used to provide additional notes about the sample. By saving the results, a Microsoft Excel sheet is generated that consists of the quantification of ciliary features and the checkboxes (blue arrowhead in Figure 5a) automatically populate a description of the sample (blue arrowhead in Figure 5b). The type of ciliary defect when selected in the counter (red arrowhead in Figure 5a) provides the main result (red arrowhead in Figure 5b), and comments are transferred to the Excel sheet (purple arrow in Figure 5a,b).

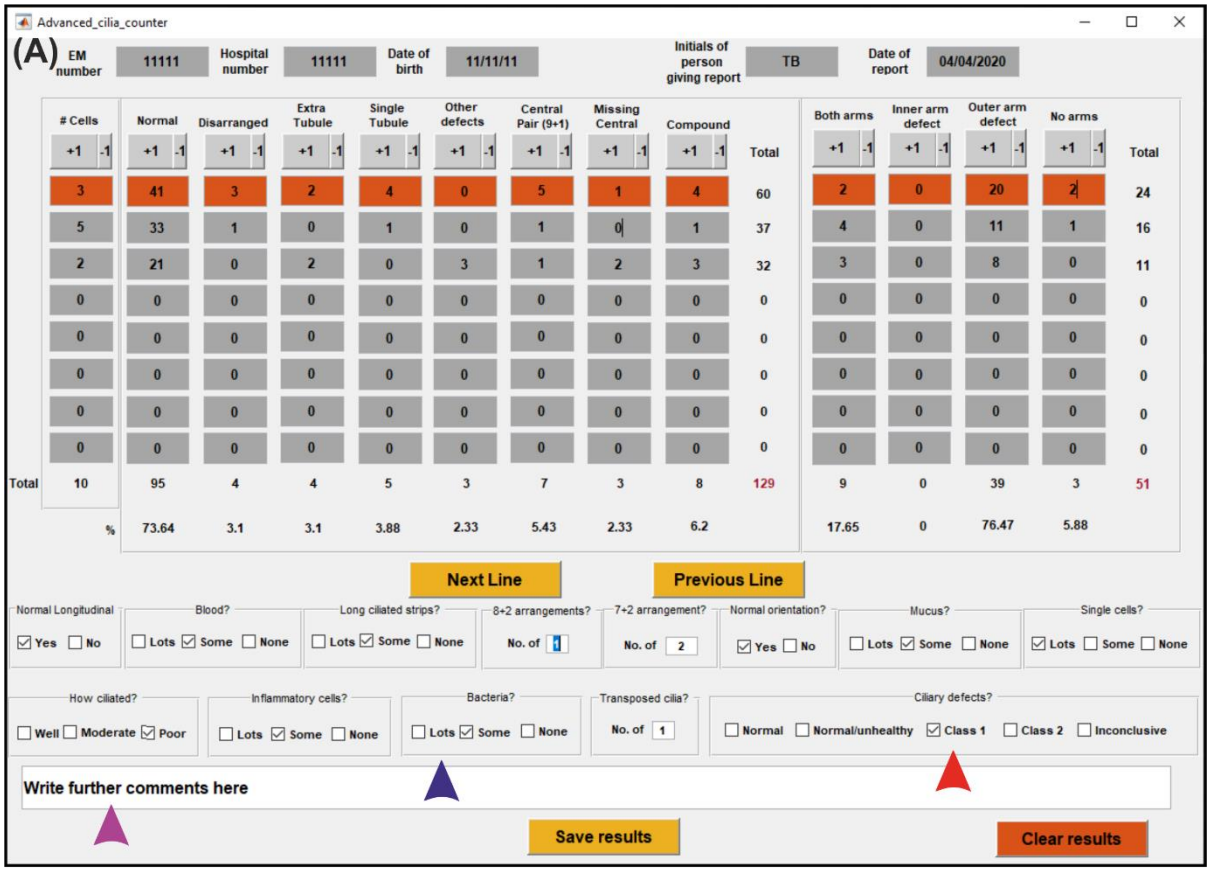

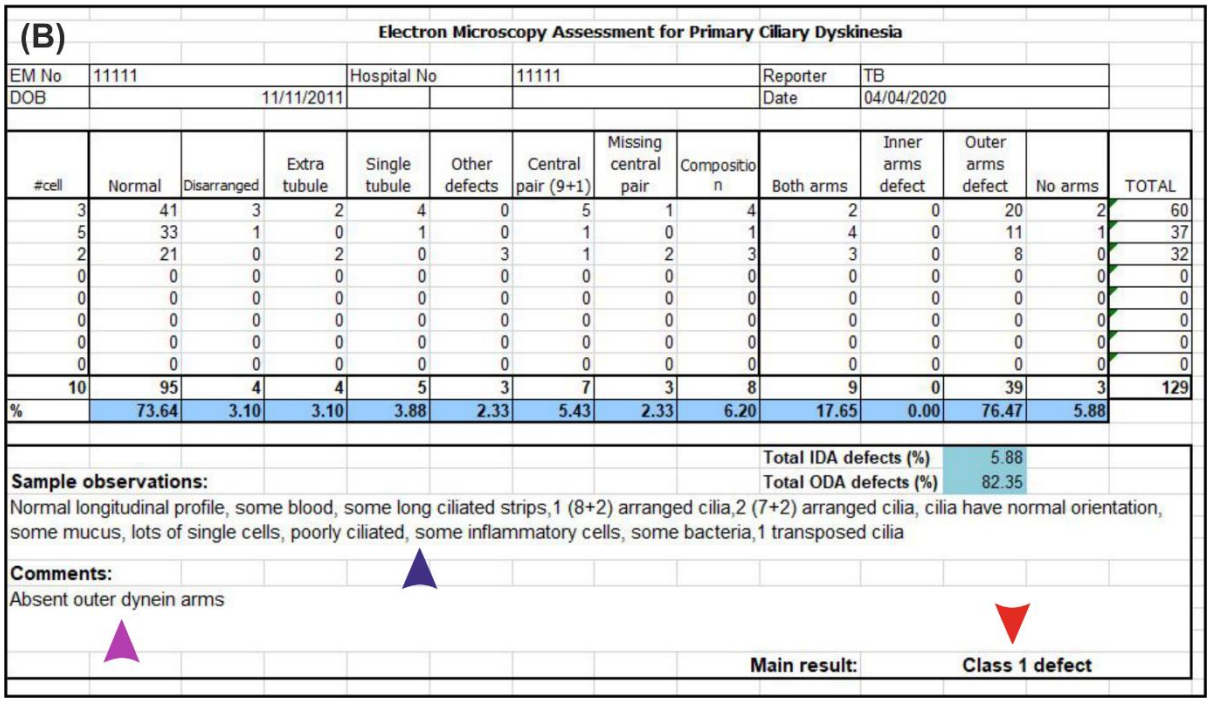

Figure 5. Advance counter that includes samples notes and an example of an Excel sheet that is generated when saving the results. (A) The number of features is tallied up by inputting numbers or by pressing the +1 or −1 buttons. The description of key features is inputted by pressing the checkboxes. (B) Excel sheet generated by the counter, which includes the counts of each type of feature and a description of the sample. The information entered by pressing the checkboxes in the counter populates a description in the Excel sheet (blue arrowhead in A and B).

The ciliary defect class and comments about the sample are automatically transferred from the counter to the Excel sheet (red and purple arrowheads in A and B respectively).

Results and Discussion

The counters provide an easy and efficient method to count ciliary features and make notes to assist in the diagnosis of PCD. We tested the advance counter by simultaneously collecting paper records of the diagnostic cilia feature counts and sample description when assessing 48 patient cases (taken by three individuals). The paper notes were compared to the values and information generated in the Excel sheets by the advance counter, and all the information was found to match without any observed errors. The Excel sheet generated contains all the information required to upload to an electronic patient record (EPR) system and to advise the consultant or clinician overseeing the referred patient. The checkboxes within the advance counter automatically populates the description of the sample observations in the Excel sheet (blue arrowhead in Figure 5a), which promotes the full assessment of each diagnostic sample, removes the risk of spelling mistakes or typos, and leads to a standardised terminology for each sample. This makes the results easier to interpret by the clinicians and is highly beneficial when sharing results across different diagnostic centres for research, auditing, and teaching purposes. By using the advance counter, the same diagnostic methods are the same as the outline in the international diagnostic consensus guidelines [286]. The images are assessed in the same way, but the counter can help to improve the sensitivity and specificity by reducing errors in record taking and maintaining standardised terminologies in the reports. Currently, it is difficult to calculate the sensitivity and specificity of the TEM-based diagnosis of PCD, as previously there lacked agreement in the reporting methods for TEM, and the consensus guidelines to overcome this have only recently been implemented [286]. Therefore, in the future it will be possible to accurately determine the sensitivity and specificity, once a substantial number of cases have been assessed by TEM by multiple diagnostic centres following these guidelines.

It is important to consider the results from other PCD diagnostic tests in combination with the TEM analysis [340,369]. These include genetic testing, measurements of cilia beat frequency, patterns from high speed video microscopy, and the immunofluorescence labelling of ciliary proteins. The results from these tests often correlate well with TEM—for instance, static cilia viewed by high-speed video microscopy are frequently associated with the absence of the outer dynein arm by TEM (see Figure 1b), as found in patients that have pathogenic variants in the *DNAH5* gene [370]. A limitation of TEM diagnostic analysis is that not all PCD defects are detectable by ultrastructural analysis. Approximately 25–30% of genetic mutations [251,259,363], including pathogenic variants in the *DNAH11* gene, cause ciliary defects that cannot be diagnosed by TEM [364]. When a normal diagnosis is given by TEM, the other diagnostic tests need to be considered to rule out PCD. Currently, there are approximately a quarter of PCD patients that have no genetic cause yet established, and in these patients a ciliary function and imaging assessment are required [369]. TEM provides a valuable tool in validating genetic test results, as there is a clear link between ultrastructural defects and many of the affected genes, and this can act as a guide in advancing our knowledge of PCD-causing mutations.

Conclusions

We demonstrate a ciliary feature counting system that can be of great benefit to diagnostic centres testing for PCD using TEM. This system follows international diagnostic consensus guidelines [286], making it relevant to groups globally. Physical counters are costly and hard to come by, thus the digital counter we demonstrate here provides a cost-free solution. As computer technology becomes an ever-growing trend in the diagnosis of disease, the digital counter system removes the need for paper records, and in the future it may be possible to integrate it into a machine learning system for the fully automated diagnosis of PCD.

Author Contributions: Conceptualization, A.L.P. and T.B.; Software, T.B.; Resources, R.K.R.; Investigation, A.L.P. and T.B.; Data curation, T.B.; Supervision, T.B.; Writing—Original Draft Preparation, A.L.P., C.H., and T.B.; Writing—Review and Editing, A.L.P., R.K.R, C.H., and T.B.

Funding: This research received no external funding.

Acknowledgments: We would like to thank the members of the PCD diagnostic team including Paul Griffin, Farheen Daudvohra, and Andrew Rogers for their support and feedback when using the digital counter.

Conflicts of Interest: The authors declare no conflict of interest.

3

CHAPTER 3

UA-Zero as a uranyl acetate replacement when diagnosing primary ciliary dyskinesia by transmission electron microscopy

Accepted for publication in Diagnostics

Andreia L Pinto[1,5,6], Ranjit K Rai[1], Amelia Shoemark[1,2], Claire Hogg[1,3], Thomas Burgoyne[1,4*]

[1] Royal Brompton Hospital, Guy's and St Thomas' NHS Foundation Trust, London SW3 6NP, UK
[2] School of Medicine, University of Dundee, Dundee DD1 9SY, UK
[3] Department of Paediatrics, Imperial College, London, London SW3 6LY, UK
[4] UCL Institute of Ophthalmology, University College London, London EC1V 9EL, UK
[5] Department of Life Sciences, NOVA School of Science and Technology, Caparica, Portugal
[6] CEDOC, NOVA Medical School, Rua Câmara Pestana nº 6, 6-A, Edifício CEDOC II, 1150-082 Lisboa
[*] Correspondence: t.burgoyne@rbht.nhs.uk; Tel.: +44 (0)20 7608 4020

Personal contributions

My contribution to this manuscript was conceptualizing and investigation about suitable non-radioactive alternatives for uranyl acetate in the diagnosis of PCD, and also in the preparation, reviewing and editing of the manuscript.

Abstract: Primary ciliary dyskinesia (PCD) is a disorder affecting motile cilia and an early accurate diagnosis is essential to help prevent lung damage and to preserve lung function. To make a diagnosis an assessment of the ciliary ultrastructure is typically done by transmission electron microscopy (TEM). This allows a quantitative assessment of ciliary components to identify defects associated with PCD. Heavy metal staining is required to provide contrast when imaging cilia in the TEM. One of the most commonly used stains is uranyl acetate (UA) that can be applied to cellular material before embedding (en bloc) or to ultrathin sections of embedded samples (grid staining). UA is radioactive and due to growing safety concerns and restrictions by government bodies, universities and hospitals, it is essential to find a suitable alternative. We show UA-zero (UAZ) when used en bloc provides high contrast and makes an excellent replacement for UA. PCD diagnostic experts, having reviewed ciliary cross sections stained with UAZ en bloc are confident in the staining and PCD defects are readily detectable similar to samples that have been stained with UA.

Keywords: primary ciliary dyskinesia; uranyl acetate; diagnosis; electron micrsocopy

Introduction

Primary Ciliary Dyskinesia (PCD) is a genetic disease affecting motile cilia. Symptoms include chronic lung disease, rhinosinusitis, hearing impairment and subfertility. Diagnosis of PCD is confirmed by identification of a ciliary ultrastructural defect by transmission elec-tron microscopy (TEM) or identification of bi-allelic pathogenic mutations in a known PCD gene [286,340,369]. The normal ultrastructure of respiratory cilia is shown in Figure 1A. Hallmark defects diagnostic of PCD include outer dynein arm defects, Outer and inner dynein arm defects, Inner dynein arm defects with microtubular disorganisation and central complex defects. The dynein arms are small structures of approximately 10 nm in length [371] and in order to visualise these structures accurately at the resolution of diagnostic TEM, good contrast (high signal to noise ratio) is essential. Contrast is usually achieved using a combination of heavy metal stains including osmium tetroxide, lead citrate, and uranyl acetate (UA).

UA is derived from depleted uranium and is radioactive (alpha emitter). It is extensively used as a TEM stain, either en bloc during sample preparation or staining ultrathin sections on electron microscopy grids [372]. Due to increasing concerns around using radioactive material for personal safety and fears of its potential use in terrorism, many institutes have strict regulations on its use (e.g. United Kingdom Government Ionising Radiation Regulations 2017). Justification for procurement and use of UA for diagnostic TEM has become increasingly difficult and there is a global drive to find a safer, non-radioactive replacement. Alternative reagents including platinum-blue [373], oolong tea extract [374] and hafnium chloride [375], have been trialled as alternative stains for TEM but are generally inferior to UA and their use is not widespread. More recently commercially available reagents have become available that include UA-Zero (UAZ, Agar Scientific Ltd, Stansted, Essex, UK) and UAR-EMS (UAR, Electron Microscopy Sciences, Hatfield, PA, USA). These are pre-mixed solutions which contain rare earth elements (lanthanides) for contrast staining. UAZ includes ytterbium(III) chloride hexahydrate and UAR

has both samarium triacetate and gadolinium triacetate [376]. It is im-portant to validate any changes to diagnostic procedures to ensure that providing a safer contrast stain does not compromise the quality of diagnostic ultrastructural studies. Here we compare two UA replacement stains to UA to determine their suitability in the diagnosis of PCD by TEM.

Materials and Methods

Ethical approval

The study was approved by the ethics review board of the Institute of Child Health/Great Ormond Street Hospital, London (UK) (08/H0713/82 15/10/2008). All subjects gave informed signed consent for genetic testing and use of surplus diagnostic samples for the improvement and development of new diagnostic methods.

Preparation of nasal brushing biopsies for transmission electron microscopy

3mm ConMed Cytology Brushes (ConMed, Largo, FL, USA) were used to take biopsies of the respiratory epithelium from the inferior nasal turbinate of four patients (see table 1 for mutations) and a healthy control.

Table 1. Genetic information of PCD subjects that had TEM samples stained in this study.

PCD Gene	Axoneme structure affected	Genotype
DNAH5	ODAs	Unsolved – Heterozygous *DNAH5* NM_001369.2: c.7477G>C (p.Glu2493Arg)
CCDC40	IDAs and microtubular disorganisation	*CCDC40* NM_017950.3: c.2712–1G>T + c.2712–1G>T
HYDIN	CP C2b component	*HYDIN* NM_001270974.1: c.8487del (p.Pro2830Hisfs*23) + c.8489C>A (p.Pro2830Gln)
LRRC6	ODAs and IDAs	*LRRC6* NM_012472.3: c630del (p.Trp210Cysfs*12) + c630del (p.Trp210Cysfs*12)

Translation termination codon is referred to by *

Nasal brushings were fixed with 2.5% glutaraldehyde (VWR International, Lutterworth, Leicestershire, UK) in 0.05M sodium cacodylate buffer (Agar Scientific, Stansted, Essex, UK) at a pH 7.4 and stored at 4oC overnight or for up to 2 weeks. Samples were washed in 0.05M sodium cacodylate buffer and embedded in 1% agar (Oxoid, Basingstoke, Hampshire, UK) before incubating in 1% aqueous osmium tetroxide(TAAB Laboratory Equipment, Aldermaston, Berkshire, UK) for 1 hour followed by washes in distilled water. At this point the healthy control nasal brushing biopsy was split up into four separate samples. The specimens were prepared using one of the following en bloc stains; (i) UA, (ii) UAZ, (iii) UAR, or (iv) no stain. The details of each of these stains is provided in Table 2. All samples were dehydrated in increasing concentrations of ethanol (50%, 70%, 90%, 100%), followed by propylene oxide and a mixture of propylene oxide and resin (1:1) before infiltration and embedding in araldite resin (Agar Scientific, Stansted, Essex, UK). Polymerization was performed at 60°C for 48 hours, and ultrathin sections of 80 nm were obtained using a Reichert Ultracut E ultramicrotome and collected on copper mesh grids (Agar Scientific, Stansted, Essex, UK). For the samples prepared with

no en bloc staining, sections were collected onto grids and stained with either; (i) UA (Agar Scientific, Stansted, Essex, UK), (ii) UAZ (Agar Scientific, Stansted, Essex, UK), (iii) UAR (Electron Microscopy Sciences, Hatfield, PA, USA) or (iv) left unstained. All except the unstained were counter stained with Reynold's lead citrate (Agar Scientific, Stansted, Essex, UK) and the details of the methods used for each of these stains is provided in Table 3. Some of the sections collected from the UAZ en bloc were further grid stained with UAZ. Images were acquired using a JEOL 1400plus (JEOL ltd, Tokyo, Japan) TEM at an accelerating voltage of 120 kV. Digital images were obtained using an Advanced Microscopy Technologies XR16 bottom mid mount digital camera (AMT Imaging Direct, Woburn, MA, USA). The camera software has an autogain system that remaps the pixels values so that they extend across a larger range making it easier to differentiate between lighter and darker pixels. When acquiring images a fast Fourier transform was generate to make sure images were all taken at 0.7 µm from defocus and that there was no drift or beam astigmatism (as shown in Supplementary Materials Figure S1).

Table 2. The different methods of en bloc staining used.

En bloc stain	Method
No stain	No stain added during sample preparation
UA	1% aqueous UA (Agar Scientific Ltd) for 30 minutes
UAR	UAR (Electron Microscopy Sciences) diluted 1:4 in distilled water and applied for 30 minutes
UAZ	undiluted UAZ (Agar Scientific) for 30 minutes

Table 3. Types of grid stain and the methods used.

Grid stain	Method
No stain	No stain
UA	2% aqueous UA for 7 minutes and Reynold's lead citrate for 10minutes
UAR	UAR (Electron Microscopy Sciences) diluted 1:4 in distilled water and applied for 30 minutes and Reynold's lead citrate Reynold's lead citrate
UAZ	undiluted UAZ for 7 minutes and Reynold's lead citrate for 10minutes

Analysis of diagnostic results

Diagnostic results from the assessment of nasal biopsy samples prepared for TEM with either en bloc UAZ (N=58) or UA (N=58) grid stain were examined. The diagnostic assessment included counting; cilia with a normal (9+2), abnormal microtubule arrange-ment (8+2, 8+1 and 7+2), extra microtubules, missing central pair, compound cilia and dynein arm defect. The diagnostic results were analysed using Microsoft Excel.

Image analysis

Cilia were cropped out of the images acquired from samples prepared with the different en bloc and grid stains using Cilia Crop, a program that is part of the PCD Detect toolkit [367]. The cropped images were anonymised using an in-house program designed using MATLAB to allocate random number for files names (DOI - 10.5522/04/14369258)

20 images per staining condition were analysed by 10 electron microscopists experienced in PCD diagnosis and blinded to which stain was used. Images were ranked as ‘good’, ‘useable’ or ‘unusable’ for PCD diagnosis. These terms were converted into the corresponding scores; 100%, 50% and 0% respectively. This allowed the assessment of the confidence the specialists had in the different grid or en bloc stains.

To analyse the contrast range of images of cilia from the different staining methods the standard deviation of the pixel gray value was calculated using ImageJ (NIH). All images are 8-bit greyscale where 0 is black and 255 is white. Statistical significance was determined for the survey results and standard deviation of the pixel gray value using Student’s t-tests.

Results

The results of a survey comparing the different staining methods to determine their suitability in diagnosing PCD is shown in Figure 1. Representative images of the different methods are shown are shown in Figure 1A and Supplementary Materials Figure S2, and it can be clearly seen that all staining methods give better contrast than no stain. Assessment of ciliary cross sections by 10 electron microscopists who routinely analyse cilia cross sections to diagnose PCD revealed similar confidence when comparing UAZ to UA grid stain but lower confidence in UAR (Figure 1 B). UAZ en bloc provided significantly higher confidence than both en bloc UA and UAR of over 80% (Figure 1 C). The standard deviation (SD) of the pixel gray value was calculated from images of the ciliary cross-sections (Figure 1 D & E). All three stains when applied to sections gave similar standard deviations of the pixel gray value (Figure 1 D). UAZ en bloc staining gave significantly higher SD of the pixel value compared to UA, indicating greater image contrast (Figure 1 D). Whereas, UAR gave a significantly low standard deviation of the pixel gray value compared UA.

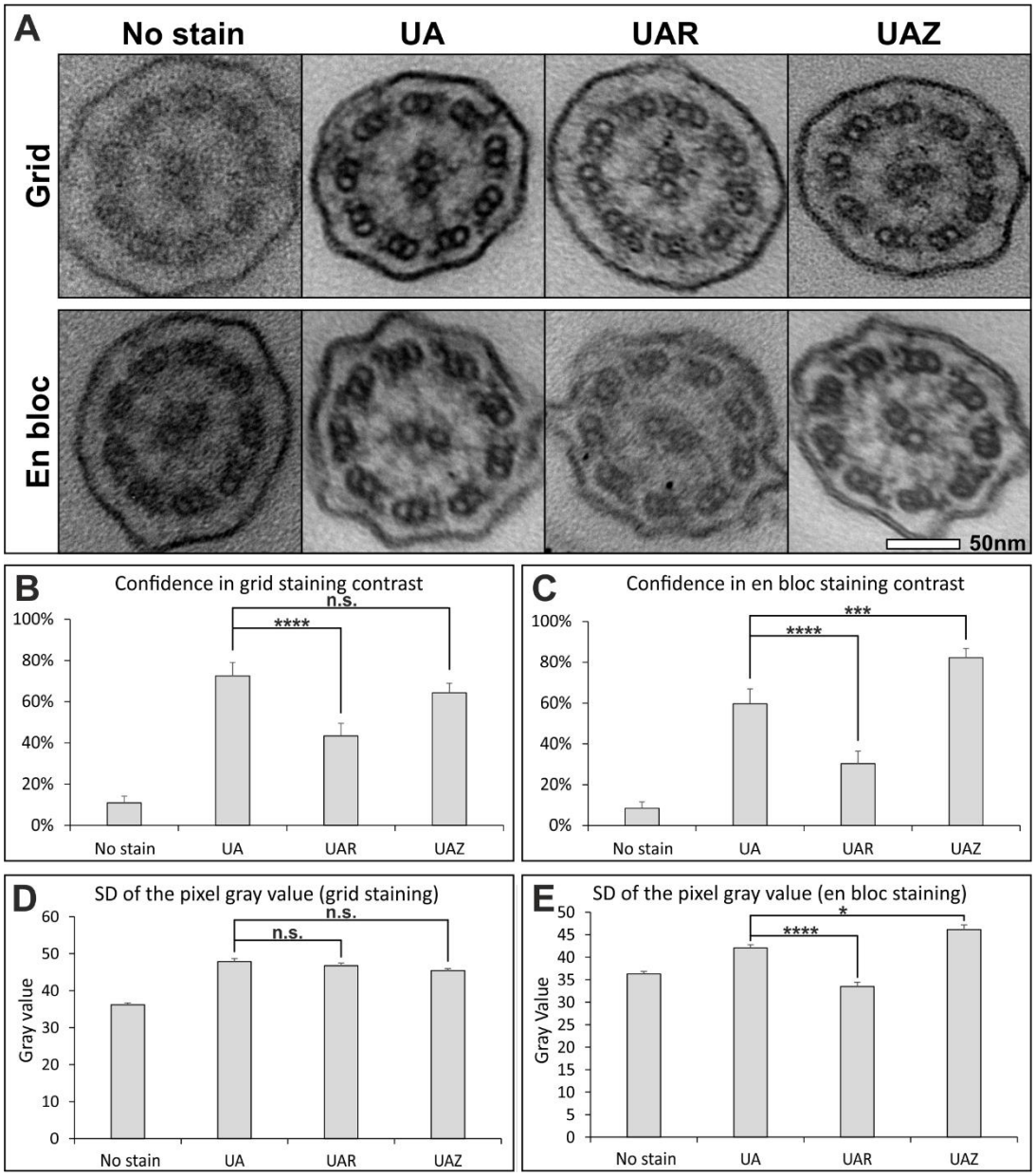

Figure 1. UAZ provides a good alternative to UA when examining ciliary cross sections. (A) Images of ciliary cross sections from samples prepared with grid stained or en bloc using one of following stains; Lead citrate (LC) only, UA, UAR or UAZ. (B – C) Anonymised images were compared by 10 electron microscopy specialists and scored based on the confidence they had in the staining. (B) When staining sections on TEM grids, UA and UAZ gave the greater confidence in staining compared to UAR. No significant difference in the confidence in staining was observed between UA and UAZ. (C) UAZ on bloc provided staining that gave the highest confidence. (D – E) Standard deviation (SD) of the pixel gray value within images of ciliary cross sections was determined to examine the contrast range. (D) No difference in the SD of the pixel gray value was observed between UA, UAR and UAZ. (E) There was a significantly greater SD of pixel gray value when comparing UAZ to UA en bloc staining. A lower standard deviation of the pixel gray value was found for UAR when compared to UA en bloc staining. (B – E) Standard error of mean (SEM) shown and statistical significance was determined using Student's t-test (n.s. $P > 0.05$ * $P < 0.05$ *** $P < 0.01$ **** $P < 0.0001$).

The staining methods were further assessed by examining ciliary cross sections from PCD patients that have known pathogen variants causing absence of ciliary structures as described in Table 1. The missing axoneme components that include ODA, IDA and C2b component of the CP were detectable in patient samples when using UAZ grid staining (Figure 2 A – D and Supplementary

Materials Figure S3). UAZ en bloc staining that provides better confidence in staining quality over using UA (Figure 1 C) provided high contrast allow the detection of absent inner and outer dynein arms (Figure 2 A3 & E1 and Supplementary Materials Figure S3). The addition of UAZ grid staining to samples that had been prepared with UAZ en bloc did not improve the contrast further (Figure 2 A4 & E2 and Supplementary Materials Figure S3).

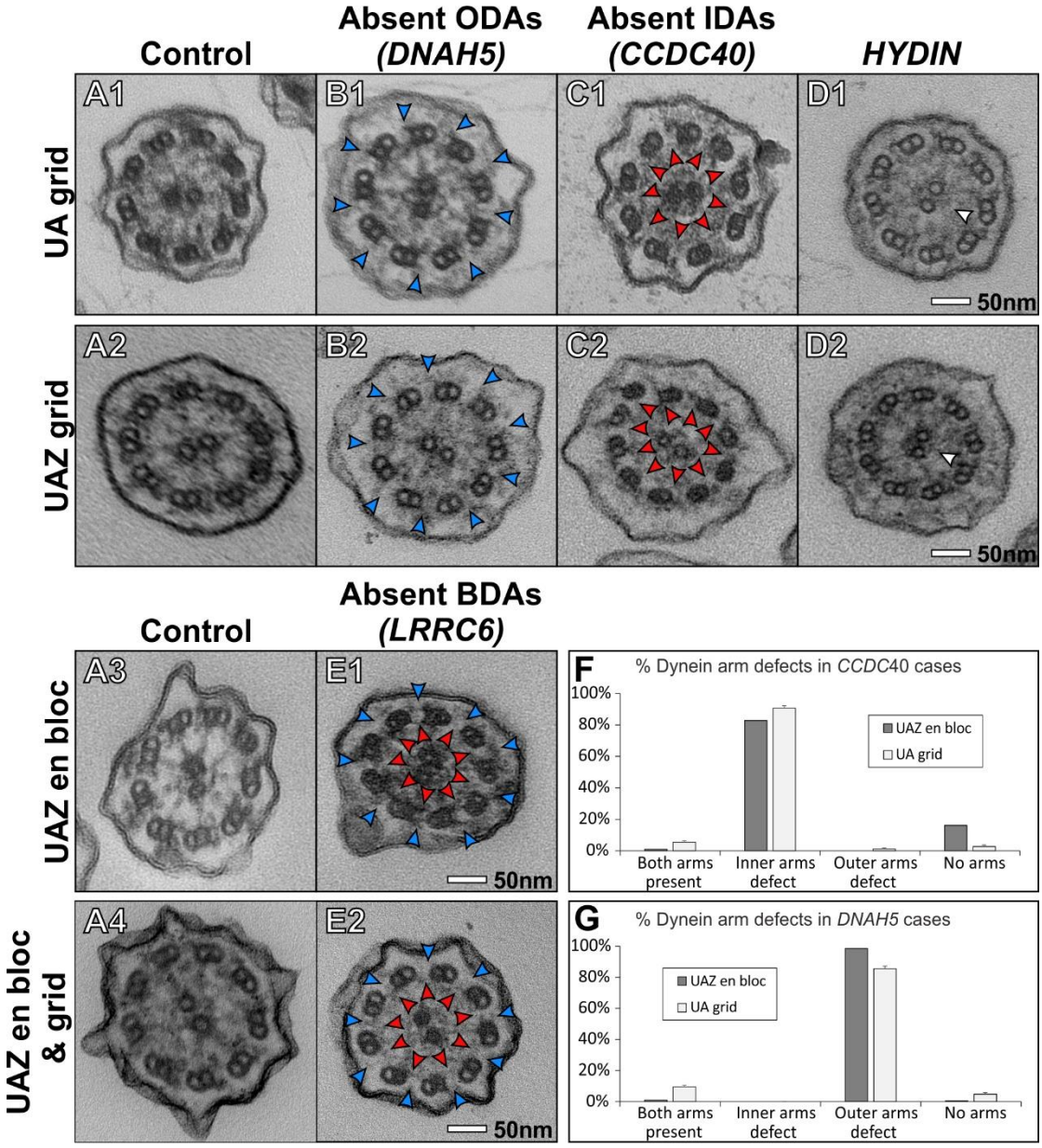

Figure 2. Key structural features for diagnosing PCD are visible when using UAZ to stain grids or en bloc. (A) The control cilia shows a normal cilia ultrastructure that includes the presence of outer and inner dynein arms and a complete central pair complex. (B & C) Outer (blue arrowheads) or inner dynein arms (red arrowheads) can be seen to be absent in patients that have disease causing variants in *DNAH5* or *CCDC40* when staining with UA or UAZ on grid. (D) The loss of the C2b component (white arrowheads) of the central pair can be detect in a *HYDIN* case when staining grids with UAZ and UA. (E) The loss of both dynein arms (blue and red arrowheads) can seen in a LRRC6 case when staining with UAZ en bloc with and without an additional grid stain. The additional stain does not compromise image contrast. (F & G) Diagnostic results from a single UA-Z en bloc prepared samples compared to UA grid stained samples showing similar detection of dynein arm defects. (F) Diagnostic assessment

of patients that have pathogenic variants in *CDCC40* (UAZ en bloc N=1 and UA en grid N=5). (G) Diagnostic results from patients with pathogenic variants in *DNAH5* (UAZ en bloc N=1 and UA en grid N=6).

Following the results of our blinded survey we integrated UAZ staining into our clinical practice. UAZ en bloc has been performed on 58 patient samples and out of these 11 have tested positive for PCD. We audited our clinical practice where up to 100 cilia are counted per case to make a diagnosis. Out of the total cilia cross section examined per case 52.60% ± 1.82% with UA and 53.48% ± 1.54% with UAZ (shown as mean ± standard error of the mean) could be assessed for dynein arm defects. This indicates that the UAZ stain change in protocol did not impact the quality of our clinical practice. Furthermore 2 cases had been previously assessed with UA and were reassessed with UAZ staining. These had gene mutations in *DNAH5* and *CCDC40*. Quantification of these samples showed similar detection of dynein arms defects to previous cases that were UA grid stained (without en bloc staining) as shown in Figure 2 F & G.

In addition to ciliary ultrastructure it is important for PCD diagnosis to assess the health of the cells and quality of the sample, therefore we assessed other cellular structures in the samples. UAZ en bloc provides good contrast staining of other organelles and cellular membrane comparable to UA en bloc (Figure 3). At lower magnification the contents of the cell can be clearly seen with both UAZ and UA en bloc staining (Figure 3 A & D). At higher magnification, organelles such as mitochondria have good contrast and membrane at cellular junctions are very clear and are of similar quality for both stains (Figure 3 C – F).

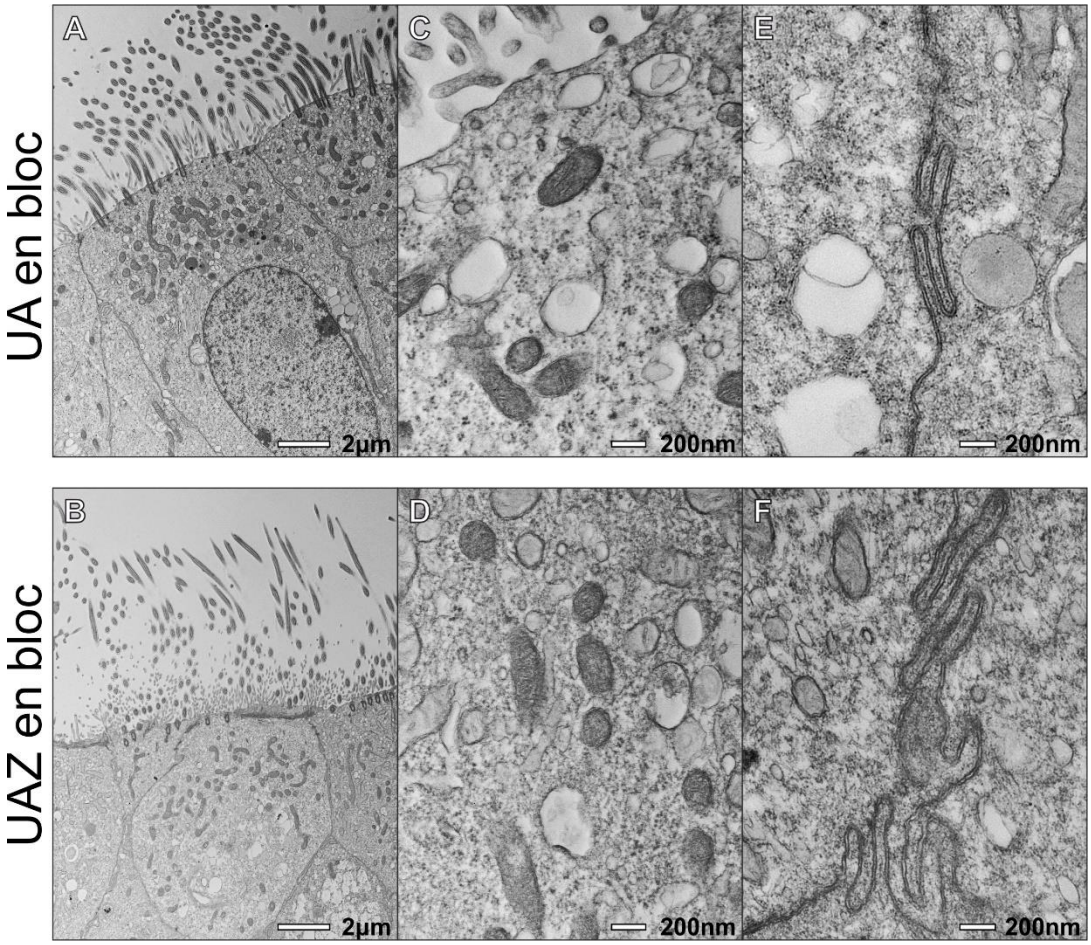

Figure 3. UAZ en bloc provides sample staining comparable to UA en bloc. Images of respiratory epithelium prepared from a nasal brushing with (A – C) UA en bloc and (D – F) UAZ en bloc. (A & D) Low magnification view of ciliated respiratory epithelium show a similar level of contrast between the two stains. (B & E) There is clear staining of intercellular com-partments and organelles including mitochondria. (C – F) Both stains provide good membrane staining as demonstrated by the plasma membrane staining at junctions between cells.

Discussion

We show en bloc staining with UAZ provides a promising replacement for UA for the assessment of ciliary ultrastructure. It gives comparable contrast to UA and allows imaging of the key ciliary components that are linked to PCD.

UAZ en bloc staining applied during sample preparation resulted in TEM images with high signal to noise that when assessed by PCD diagnostic specialists gave more confidence in the staining and ability to detect ciliary features compared to UA. When using UAZ en bloc staining for a PCD patient with a pathogenic variant in *LRRC6*, that encodes a protein required for transport of dynein arms [377], the absence of the IDAs and ODAs was clear. Patients that have been diagnosed with ODA or/and IDA defects associated with pathogenic variant in *DNAH5* or *CCDC40* show the detection of similar ratio of defects to similar cases that were prepared with UA grid staining.

UAZ grid staining conferred similar confidence to UA and was found to be suitable for diagnosing PCD, as absent ciliary structures were detectable in patient samples. This includes cilia from patients with pathogenic variants in the *DNAH5* associated with a loss of ODAs [370], *CCDC40* that leads to loss of IDAs and microtubular disarrangement [311] and *HYDIN* that causes loss of the C2b component of the central pair [282]. Based on our findings we suggest UAZ could be used en bloc as a UA replacement in diagnosing PCD and UAZ grid staining can be used when samples have already been embedded and UA is unavailable.

This is the first time UA replacement stains have been compared for the diagnosis of PCD. This was done blinded and included PCD samples from genotyped patients. The assessment was done by several experts from different centres that specialise in the diagnosis of PCD. We have prepared 58 diagnostic samples with en bloc staining and the assessment of absent ciliary structures and other defects reflects the results found from our previous UA grid staining protocol.

Only a single control nasal brushing sample was assessed in the survey that was split up and prepared using different stains methods. As centres use a range of sampling techniques and different methodology for processing and TEMs, UAZ en bloc need to be validated locally before implementation in other centres.

We predict that the sensitivity and specificity of TEM in the diagnosis of PCD could improve when using UAZ compared to more traditional UA methods due to the greater confidence we found in the staining of cilia. Due to the safety concerns, difficulties of purchasing, handling and storing of UA, it makes UAZ a suitable replacement reagent for assisting in the diagnosis of PCD.

Supplementary Materials: Supplementary Materials: The following are available online at https://www.mdpi.com/article/10.3390/diagnostics11061063/s1, Figure S1: Representative fast Fourier transform (FFT) used to set the defocus when images were acquired for the survey.

Funding: This research received no external funding.

Institutional Review Board Statement: The study was conducted according to the guide-lines of the Declaration of Helsinki, and approved by the Health Research Authority (protocol code HBD2008v1 15/10/2008).

Informed Consent Statement: Informed consent was obtained from all subjects involved in the study

Data Availability Statement: No new datasets were created or analyzed in this study. Data sharing is not applicable to this article. The software used to randomize images names is publicly available and can be found here [doi:10.5522/04/14369258].

Author Contributions: Conceptualization, A.L.P., A.S. and T.B.; Investigation, A.L.P., R.K.R. and T.B.; Software, T.B.; Data curation, T.B.; Supervision, T.B.; Writing—Original Draft Preparation, R.K.R., and T.B.; Writing—Review and Editing, A.L.P., R.K.R., A.S., C.H. and T.B. All authors have read and agreed to the published version of the manuscript.

Acknowledgments: We would like to thank the PCD diagnostics at Royal Brompton Hos-pital (RBH) and Southampton General Hospital (SGH) that include Paul Griffin (RBH), Farheen Daudvohra (RBH), Andrew Rogers (RBH), James Thompson (SGH), Regan Doherty (SGH), Anton Page (SGH) and Patricia Goggin (SGH) for their support completing the survey.

Conflicts of Interest: The authors declare no conflict of interest.

4

CHAPTER 4

PCD Detect: Enhancing ciliary features through image averaging and classification

Published article Am J Physiol Lung Cell Mol Physiol doi:10.1152/ajplung.00264.2020

Amelia Shoemark[1,2], Andreia L. Pinto[1], Mitali P. Patel[4], Farheen Daudvohra[1], Claire Hogg[1,3], Hannah M. Mitchison[4,5], Thomas Burgoyne[1,6 #]

[1] Paediatric Respiratory Medicine, Primary Ciliary Dyskinesia Centre, Royal Brompton & Harefield NHS Trust, London, SW3 6NP, UK
[2] School of Medicine, University of Dundee, Dundee, DD1 9SY, UK
[3] Department of Paediatrics, Imperial College London, London, SW3 6LY, UK
[4] Genetics and Genomic Medicine, University College London, UCL Great Ormond Street Institute of Child Health and NIHR Great Ormond Street Hospital Biomedical Research Centre, London, WC1N 1EH, UK
[5] NIHR Great Ormond Street Hospital Biomedical Research Centre, London, WC1N 1EH, UK
[6] UCL institute of Ophthalmology, London, EC1V 9EL, UK
[#] All correspondence to t.burgoyne@rbht.nhs.uk, Paediatric Respiratory Medicine, Primary Ciliary Dyskinesia Centre, Royal Brompton & Harefield NHS Trust, London, SW3 6NP, UK Tel: 44-(0)20-7352-8121, ORCID: 0000-0002-8428-720X

Personal contributions

My contribution to this manuscript was analysing and interpreting the data generated by the PCD detect software using control samples under unbiased experimental condition. I also tested the system and all the possible outcomes. I also apply it when requested in the diagnostic workflow and assist in troubleshooting.

Abstract

Primary ciliary dyskinesia (PCD) is an inherited disorder of the motile cilia. Early accurate diagnosis is important to help prevent lung damage in childhood and to preserve lung function. Confirmation of a diagnosis traditionally relied on assessment of ciliary ultrastructure by transmission electron microscopy (TEM), however >50 known PCD genes has made the identification of bi-allelic mutations a viable alternative to confirm diagnosis. TEM and genotyping lack sensitivity and research to improve accuracy of both is required. TEM can be challenging when a subtle or partial ciliary defect is present or affected cilia structures are difficult to identify due to poor contrast. Here we demonstrate software to enhance TEM ciliary images and reduce background by averaging ciliary features. This includes an option to classify features into groups based on their appearance, to generation multiple averages when a nonhomogeneous abnormality is present. We validated this software on images taken from subjects with well characterised PCD caused by variants in the outer dynein arm (ODA) heavy chain gene *DNAH5*. Examining more difficult to diagnose cases, we detected (i) regionally restricted absence of the ODAs away from the ciliary base, in a subject carrying mutations in *DNAH9*; (ii) loss of the typically poorly contrasted inner dynein arms; (iii) sporadic absence of part of the central pair complex in subjects carrying mutations in *HYDIN*, including one case with an unverified genetic diagnosis. We show this easy to use software can assist in detailing relationships between genotype and ultrastructural phenotype, improving diagnosis of PCD.

Keywords: primary ciliary dyskinesia, cilia ultrastructure, image averaging, image classification, transmission electron microscopy

Introduction

Motile cilia are hair-like projections on the apical surface of human epithelial cells that have a classical 9+2 microtubule arrangement of their core axoneme structure (Figure 1). Respiratory motile cilia beat in a highly coordinated manner essential for the movement and clearance of mucus, bacteria and debris from the airways. Primary ciliary dyskinesia (PCD) is an inherited disorder of motile cilia that results in failure of mucus clearance, chronic lung disease, rhinosinusitis and hearing impairment, with additional organ laterality defects, subfertility and occasional hydrocephalus. The estimated prevalence is ~1 per 10,000 births, but it is more prevalent in populations where consanguinity is common [368]. An early diagnosis of PCD is vital to implement appropriate treatment with the aim to preserve lung function and prevent lung damage. Diagnosis is often complex, due to disease heterogeneity and incomplete understanding of the molecular and genetic causes of PCD. Diagnosis currently involves combinations of tests, including measurement of nasal nitric oxide (nNO) as well as acquiring cells by nasal brushings for examination of cilia motility functions using high speed video microscopy (HSVM), immunofluorescence microscopy (IF), transmission electron microscopy (TEM) and genotyping [340]. Confirmation of a diagnosis traditionally relied on assessment of ciliary ultrastructure by TEM, however advancements in genetic testing has made the identification of bi-allelic mutations in a known PCD gene a viable alternative to confirm diagnosis. Mutations in more than 50 different genes are known to

cause PCD, defects which account for 65-75% cases. Therefore, more than a quarter of sufferers have no genetic cause yet established despite screening, which can be because they carry no detectable mutations in the known genes, or carry mutations in known genes of unknown significance or have no diagnosis with only single mono-allelic (rather than biallelic) mutations so far identified [369]. In these patients, confirmation with a functional test is required.

TEM diagnosis involves examining a large number (>50) of cilia to verify the frequency of particular ultrastructural defects [378]. The most commonly reported PCD defect affecting patients that can be identified using this approach is the absence of outer dynein arms (ODAs) (Figure 1). Absent ODAs are readily detected due to loss of a well contrasted (high signal to noise) structure in the TEM. The most common cause of this defect is a mutation in the *DNAH5* gene that encodes a large ODA heavy chain that forms a substantial part of the ODA [370]. Unfortunately, there are a range of other ciliary structures affected in PCD that are more challenging to visualise by TEM. These include inner dynein arms (IDAs) that typically have poor contrast and are often masked by the close positioning or overlapping of the radial spokes and nexin links. Also challenging to image are the central pair complex (CP) projections such as the CP C2b component *HYDIN*, which are small and difficult to detect due to the resolution limits of diagnostic electron microscopes [282]. Furthermore, there are specific genetic defects causing PCD that are known to result in partial loss or sporadic loss of a ciliary structure. This includes mutations in the *DNAH9* and *DNAH11* genes which encode heavy chain subunits of the ODA, that are both localised only to a sub-region of the axoneme, the distal or proximal region, respectively. PCD-causing variants in *DNAH9* and *DNAH11* consequently lead to a loss of ODAs restricted to the distal (cilia tip) or proximal (cilia base) regions, as these proteins serve complementary roles in either region [295,325]. Due to the difficulty of detecting the presence or absence of some ciliary structures, many patients end up having multiple nasal brushings, leading to delayed diagnosis. Approximately 30% of patients are considered to have a normal ciliary ultrastructure after TEM analysis [379]. Subtle defects, e.g. *HYDIN* which have been missed, are likely to account for a number of these cases.

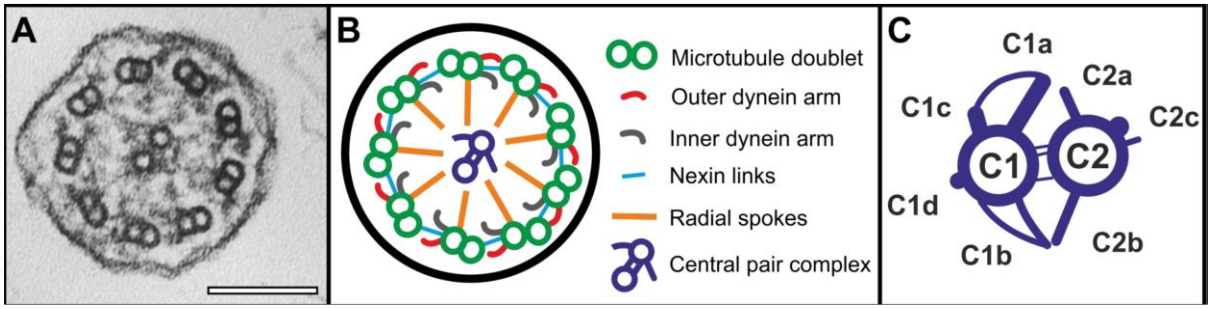

Figure 1. Cilia ultrastructure. A: transmission electron microscopy image of a cross section of healthy 9+2 motile cilium. B: diagram highlighting the different components of a cilium. C: diagram showing the detailed structure of the central pair complex including the projections from the C1 and C2 microtubule. Scale bar (A) 100 nm.

Recently, electron tomography and 3D ciliary averaging have been used to successfully identify subtle cilia defects in samples previously considered to have normal ultrastructure. However this is a time consuming, expensive technique requiring specialist tools and knowledge [98,295,325,364,380]. To

address this clinical need to improve the detection of subtle or partial structural defects in cilia of patients that are likely to have PCD, we have developed PCD detect, a package of programs (toolkit) that allows the selection and averaging of ciliary features (microtubular doublets (MTDs) and CPs) from TEM images. This assists in removing background while enhancing signal, allowing ciliary structures that are critical for motility to be better structurally resolved and evaluated. Of importance for some PCD cases where there is partial or sporadic loss of a ciliary structure, and/or genetic variants identified that are of uncertain clinical significance, the image classification tool has been developed to provide multiple (class) averaged outputs to better study and improve detection of these defects.

Materials and methods

Ethical approval

The study was approved by the ethics review board of the Institute of Child Health/Great Ormond Street Hospital, London (UK) (08/H0713/82). All subjects gave informed signed consent for genetic testing and use of surplus diagnostic samples for development of new diagnostic tools.

Preparation of nasal brushings for electron microscopy analysis

Respiratory epithelial cells were obtained from subjects' nasal turbinate using 3-mm bronchial cytology brushes and placing the biopsy into media 199 (Thermo Fisher Scientific). Each biopsy was fixed and embedded following the protocol outlined in reference[381]. In brief, an equal volume of 2.5% glutaraldehyde in 0.05M sodium cacodylate buffer pH 7.4 was added to the solution containing the biopsies in 199 media and left overnight or longer (up to 2 weeks) at 4°C. The biopsies were incubated in 1% osmium tetroxide in 0.05M sodium cacodylate buffer pH 7.4 for 1 hour before embedding in 2% agar aqueous solution. The samples were then dehydrated and infused with araldite using a Lynx Microscopy Tissue Processor. This involved incubating in increasing concentrations of methanol (70%, 90% and 100%) followed by propylene oxide, mixtures of propylene oxide:araldite (1:1 and 1:3 respectively) and araldite. Finally, the samples were embedded in araldite and incubated at 65°C for 72 hrs. 90 nm sections from archived araldite-embedded nasal brushings were cut onto electron microscopy grids and stained using 2% methanolic uranyl acetate for 7 minutes and Reynolds lead citrate solution for 5 minutes. The sections were viewed on a JEOL 1400+ TEM and when needed the stage was tilted to provide ciliary cross-sections without obliqueness. Images were acquired at 40,000x magnification using an AMT 16X CCD camera.

Image criteria

For optimal analysis of cilia using the PCD detect toolkit, it is important to use clear images (strong signal to background), without stain artefacts, taken at a single magnification, also to include non-oblique cross sections taken at the focus where it is possible to see the most ultrastructural detail. Demonstration images are included along with the toolbox to demonstrate the kind of images that are required. Blinded averaged images generated from control and patient cilia were examined to determine

sensitivity and specificity. It is recommended to pick MTD features from at least 5 cilia cross sections (equivalent to 45 or more MTD features) from different cells for a sensitivity ≥75% and specificity of 100%. More than 10 cilia cross sections from different cells should be used in PCD detect when examining the CP (equivalent to more than 10 CP features), for a sensitivity >63% and specificity >83%.

Software development

The toolkit includes programs to extract cilia from TEM images (Cilia Crop), perform averaging of cilia structures (Cilia Averaging), group and generate class averages (Cilia Classification) and to overlay results for analysis (Cilia Analysis). All programs were written in Matlab (Mathworks).

Cilia Crop: This is a tool to select multiple regions of interest from a larger image. (An example is shown in Figure S1 A).

Cilia Averaging: This tool extracts manually chosen features (some of these are shown in Figure S2) and performs a rotational and translational search (see Figure S1 B). By calculating the cross-correlation, the best alignment of features is determined. The outputs from this tool include two averaged images comprising (i) all features averaged together (ii) only features best matching the reference based on the cross-correlation cut-off value. The latter average outputs are used in this study, as these should contain less background by not including poor quality features (high background, artefacts, tilted or distorted). All averaged images generated include a corresponding colour contour map where dark blue indicates an electron dense feature and yellow indicates the absence of a feature. When using a reference feature (rather than reference-free), it is important to select a well orientated (non-oblique) feature (MTD or CP) that has good contrast and no stain artefacts.

Cilia Classification: The classification tool (Figure S3 A) was developed to allow two methods of grouping features based on their similarity (image classification) as determined by (i) principle component analysis (PCA) and (ii) hierarchical classification. When using PCA, histograms of the first six coefficients are generated and the plots that indicate more than one feature class (multiple peaks) are selected. Using these, k-means clustering then separates the features into two or more classes, which is followed by averaging them together to generate the separate class averages. The hierarchical classification approach was designed to analyse the feature alignment and similarity, using cross-correlation results generated previously through the averaging tool. Using this data, the first class is generated by averaging features aligned to the reference feature (has the most matching other features based on cross-correlation). Subsequent classes are generated by averaging to the reference features that are most dissimilar to the reference features used to generate the first class. The hierarchical classification approach allows a feature to be included in more than one class if there is enough similarity (based on cross-correlation) to more than one of the reference features used to generate the classes. This is to allow any features that cannot be easily classed to contribute towards multiple class averages. It is important to note that class averages can be generated when there is sporadic loss of structure(s), but class averages can also be given by other types of variation between groups of features, such as tilt (obliqueness). In this study, when using PCA (Figure S4), the number of classes

was set to 2 and the PCA and k-means calculated from an averaged version of each feature (each feature acts as reference and all other features are averaged to it). By picking the plots that indicate multiple classes (more than one peak), k-means are calculated to group features before generating class averages.

Cilia Analysis: This tool allows the visualisation and comparison of averaged features (Figure S3B). By opening two features, an overlay on both is provided. The features can be aligned automatically or manually, to allow similarities and differences in the structures to be assessed (Figure S3 B2-4).

Toolkit validation

Image acquisition

The toolkit was initially tested using artificially generated images with added noise (see Figure S5) before using ciliary images taken from patients with PCD. Details of the PCD subjects in this study are provided in Table 1.

Input into PCD Detect

For the validation, the four programs were run sequentially. In cilia crop, cropping size is selected by boxing an entire cross-sectional cilium, with cilia cropped out into a sub-directory by pressing the Select ROI (region of interest) button and selecting the centre of each cilium within an image. The folder containing the cropped images is then opened in the Cilia Averaging tool (Figure S1 B). Each image is checked manually to make sure all cilia are orientated in the same direction by flipping images either horizontally or vertically. A box is drawn around the feature of interest to provide its size before picking the features to be averaged together. For the validation, the feature of interest was either the MTD (*DNAH5, DNAH9*, *CCDC103* or *CCDC40* cases) or the CP (*HYDIN* cases). Reference free averaging was used, as well as a search range of 360° with increments of 1° and a translational search in X and Y of 10 pixels with an increment size of 1 pixel.

After the Cilia Averaging tool performs the rotational and translational search aligning the features, an average feature is generated. The data is opened and further processed within the Cilia Classification tool (Figure S3 A), using both the PCA and hierarchy image classification schemes to group features based on their structure and generate class averages. When using the hierarchy classification, a cross-correlation cut-off of 0.6 (any features that have a cross-correlation when compared to the reference below this value are not included in the class average) and class cut off of 10% (if a reference is found to have less than 10% of the total number of features matching it, no class average is generated) were set. Finally, the analysis tool is used to overlay features between classes as well as between PCD cases and control images. A workflow of PCD Detect is shown in Fig 2.

Results

Averaged MTDs show complete or sporadic absence of the ODAs in subjects with a pathogenic variant in DNAH5

The utility of PCD Detect was first evaluated in the analysis of nasal epithelial cilia structures from PCD patients carrying causal *DNAH5* mutations, already established to have clear-cut defects in conventional TEM analysis, involving loss of the ciliary ODAs. TEM images of transverse orientation cilia were acquired from diagnostic nasal brushing samples taken from control subjects as well as the *DNAH5* PCD subjects (Figure 3 A, B and Table 1). Using the image averaging tool, the MTDs were selected and reference-free alignment and averaging was performed. The averaged MTD generated from a control and three *DNAH5* subjects are shown in Figure 3 C, D. Averages from further controls are given in Fig S6. In all three *DNAH5* cases (*DNAH5* [1-3]), there is a clearly visible absence of the ODA, verifying the ability of PCD Detect to identify PCD. Interestingly in two of these cases, *DNAH5* [1] and *DNAH5* [2], a small visible structure (white filled arrowheads in Figure 3 D) can be seen, indicating that part of the ODA remains, whilst ODA are completely absent in the *DNAH5* [3] case (denoted by the white outline arrowheads in Figure 3 D). Of these cases, *DNAH5* [1] carries two stop-gain mutations (homozygosity confirmed by parental segregation analysis), while in *DNAH5* [2] and the previously reported case *DNAH5* [3] (11) the genetic diagnosis is not complete since only one *DNAH5* variant has so far been identified in each, although it is a highly implicated rare stop-gain allele in *DNAH5* [3]; *DNAH5* [2] carries a single uncharacterised missense mutation (Table 1).

A further subject *DNAH5* [4], with an uncharacterised missense mutation (p.Thr3410Met) plus a previously reported *DNAH5* stop-gain mutation p.Arg1761* (10), was examined using the classification tool to group MTDs and form class averages. Many of the ciliary cross sections look normal by TEM before using the enhancement tools (Figure 4 B). Class averages generated using the hierarchy classification scheme are shown in Figure 4 C, D and plots from the hierarchy classification as well as the PCA classification results are shown in Figure S4. When using this tool, subject *DNAH5* [4] with the combined nonsense and missense mutation (Figure 4 C), had two visibly different MTD classes, with and without the ODA. This reflects a sporadic absence of the ODAs that was not found in the other three *DNAH5* cases, as all classes generated had absent ODA (results for *DNAH5* [1] shown in Figure 4 D, E and other cases not shown).

Multiple MTD classes generated from a subject with pathogenic variants in DNAH9 *due to loss of the ODA at the distal region of the cilia*

To further test the classification tool, we examined ciliary images from a subject that carried a homozygous proven-pathogenic variant in *DNAH9* (p.Asp4123Asn) [295] (Table 1). *DNAH9* protein is a component only of the ODA in the distal cilium, not the proximal region (determining these regions is shown in Figure 5 A) and it is known that *DNAH9* mutations cause a defect where the ODA are only absent in the distal region of the ciliary axoneme [295,382]. Images were acquired in both the proximal (Figure 5 B) and distal regions (Figure 5 C) of the ciliary axoneme. By averaging the MTDs from these images and using hierarchy classification, two distinct classes were generated when compared to control cilia (Figure 5 D, E). When separating the ciliary images into two groups depending on the region, the classification results in single distinct averaged structures for the distal and proximal regions, indicating a clear structural difference (Figure 5 F, G). Images at the proximal region of the cilia resulted

in an averaged structure where the ODA is present, whereas the distal ciliary images resulted in an averaged structure showing absence of the ODA.

Table 1. *Diagnostic, genetic, and image process information for the subjects involved in this study*

Subject	Patients Symptoms and Clinical Diagnostic Criteria	Average nNO nL min^{-1} (Normal Nasal Nitric oxide (nNO) >77 nL min^{-1})	Average Light Microscopy CBF (Hz)	No of Nasal Brushing to Make PCD Diagnosis	Genotype	Number of Ciliary Images Input into PCD Detect to Generate MTD and/or CP Averages	Number of Features Selected in PCD Detect	Features Used by PCD Detect to Generate Final Average
Control [1]		–	–	–	–	MTD: 13 CP: 29	MTD: 112 CP: 29	MTD: 13 CP: 15
Control [2]		–	–	–	–	MTD: 9 CP: 24	MTD: 76 CP: 24	MTD: 22 CP: 15
Control [3]		–	–	–	–	MTD: 11 CP: 25	MTD: 99 CP: 25	MTD: 32 CP: 11
DNAH5 [1]	Situs inversus, neonatal respiratory distress at term, and persistent rhinitis from birth	122	0 (static)	2	DNAH5 NM_001369.2: c.13285C>T (p.Arg4429*) + c.13285C>T (p.Arg4429*)	MTD: 13	MTD: 117	Class 1: 14 Class 2: 13
DNAH5 [2]	Persistent rhinitis and prolonged otorrhea post grommet insertion	19	0 (static)	2	Unsolved – Heterozygous DNAH5 NM_001369.2: c.7477G>C (p.Glu2493Arg)	MTD: 13	MTD: 109	MTD: 18
DNAH5 [3]	Situs inversus, neonatal respiratory distress at term, and early-onset rhinitis	Too young	0 (static)	1	Unsolved – Heterozygous DNAH5 NM_001369.2: c.6261T>G (p.Tyr2087*)	MTD: 11	MTD: 91	MTD: 19
DNAH5 [4]	Rhinitis, recurrent ear infections, and otorrhea	775 (±430 SEM)	6.98 (±0.76 SEM)	2	DNAH5 NM_001369.2: c.10229C>T (p.Thr3410Met) + c.5281C>T (p.Arg1761*)	MTD: 15	MTD: 135	Class 1: 21 Class 2: 19
DNAH9	Congenital heart disease, heterotaxy, rhinitis, and recurrent ear infections	306 (±48 SEM)	9.10 (±0.36 SEM)	4	DNAH9 NM_001372: c.12367G>A (p.Asp4123Asn) + c.12367G>A (p.Asp4123Asn)	All: 16 Base−14 Tip: 7	All: 142 Base: 125 Tip: 63	All Class 1: 35 All Class 2: 25 Base: 49 Tip: 32
CCDC40	–	–	–	2	CCDC40 NM_017950.3: c.2712–1G>T + c.2712–1G>T	MTD: 14	MTD: 119	MTD: 48
CCDC103	Situs inversus, neonatal respiratory distress, rhinitis, and otitis media	250 (±50 SEM)	8.56 (±0.58 SEM)	4	CCDC103 NM_001258395.1: c.461A>C (His154Pro) + c.461A>C (His154Pro)	MTD: 14	MTD: 118	Class 1: 46 Class 2: 34
HYDIN [1]	Normal situs, chronic wet cough, rhinitis, and otorrhea	30	8.94	3	HYDIN NM_001270974.1: c.8487del (p.Pro2830Hisfs*23) + c.8489C>A (p.Pro2830Gln)	CP: 21	CP: 21	Class 1: 6 Class 2: 3
HYDIN [2]	Neonatal respiratory distress, early-onset rhinitis, otitis media, and otorrhea	31	5.98	3	HYDIN NM_001270974.1: c.13709del (p.Pro4570Leufs*2) + c.13709del (p.Pro4570Leufs*2)	CP: 35	CP: 25	Class 1: 19 Class 2: 4
HYDIN [3]	Neonatal respiratory distress, rhinosinusitis, poor hearing, immotile sperm, and retinitis pigmentosa	5	9.86	2	Unsolved – Heterozygous HYDIN NM_001270974.1: c.3786–1G>T	CP: 15	CP: 15	Class 1: 11 Class 2: 6
HYDIN [4]	Wet cough and intermittent rhinitis	442 (±239 SEM)	9.95 (±0.42 SEM)	3	HYDIN NM_001270974.1: c.1491G>C (p.Met497Ile) + c.2702G>T (p.Gly901Val)	CP: 27	CP: 27	Class 1: 8 Class 2: 6

Normal nasal nitric oxide >77 nL min^{-1}. CP, central pair; MTD, microtubular doublet; nNO, nasal nitric oxide; PCD, primary ciliary dyskinesia.

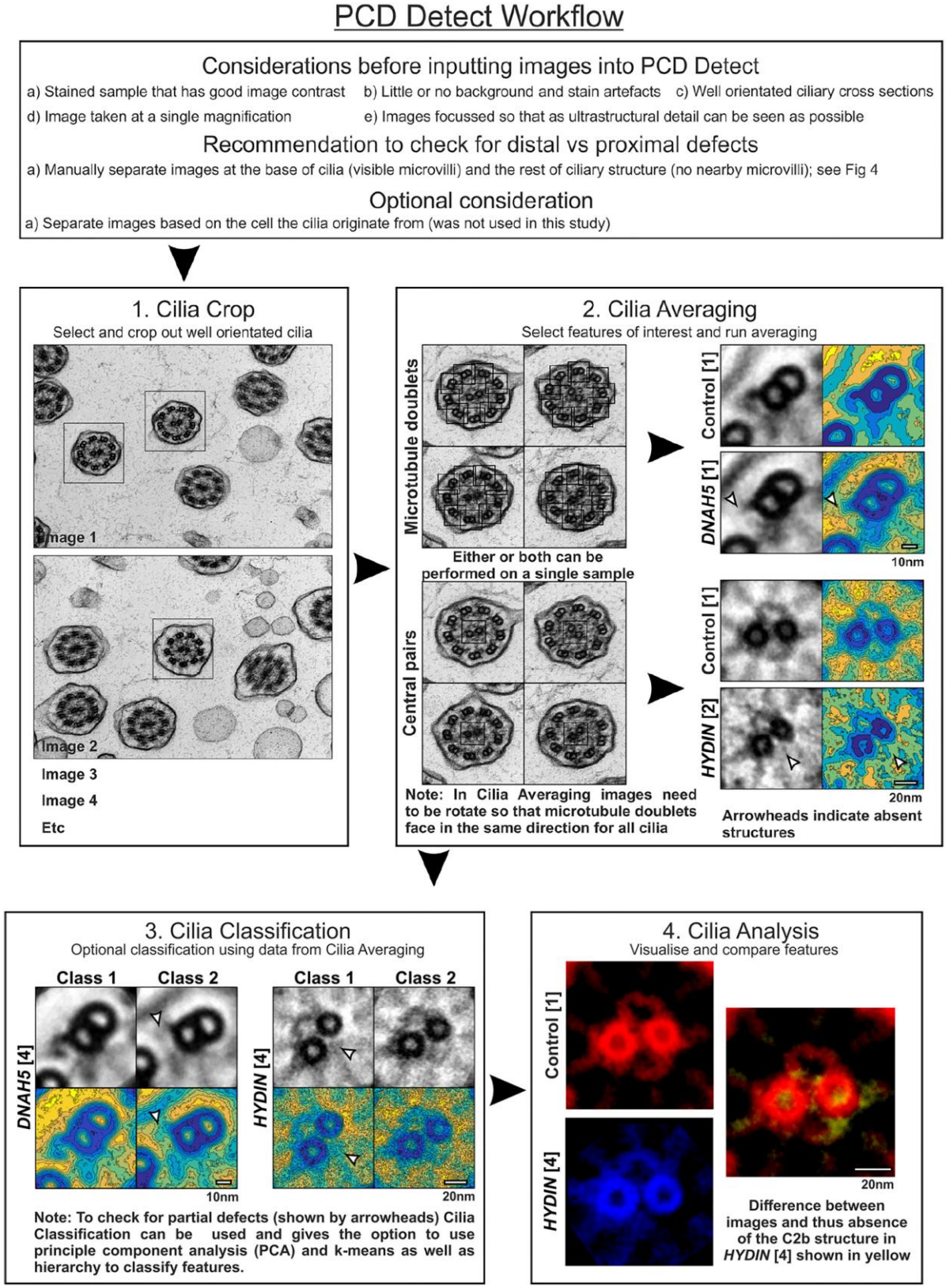

Figure 2. PCD Detect workflow showing the function of the different programs in the tool kit and the order in which to use them. Information is given in regard to the type of ciliary images required for PCD Detect and more information about the *DNAH5* [1], *DNAH5* [4], *HYDIN* [2], and *HYDIN* [4] are provided in Figs. 3, 4, and 7 and Table 1. PCD, primary ciliary dyskinesia.

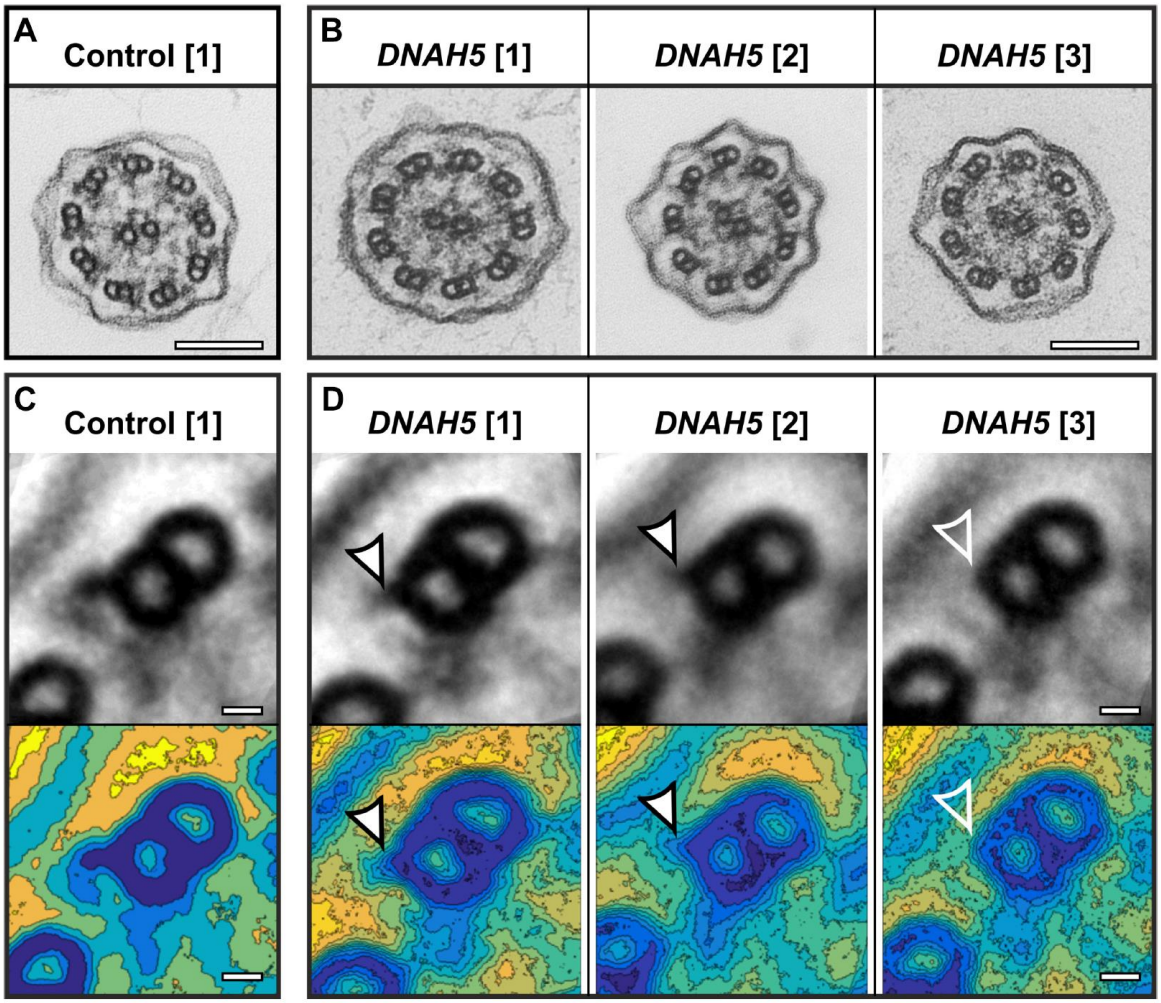

Figure 3. Image averaging shows a clear absence of the ODA in subjects with pathogenic variants in *DNAH5*. A: TEM image of a cilium from a control subject. B: cilia from three unrelated subjects with pathogenic variants in *DNAH5*. (C) average control MTD and (D) shows averaged MTD with absent ODAs from the subjects carrying pathogenic variants in *DNAH5*. The white filled arrowheads indicate MTD that have a projection emanating from the MTD, and the white outlined arrowheads indicate a complete absence of the ODA. Scale bars: 100 nm (A and B) and 10 nm (C and D). ODA, outer dynein arm; TEM, transmission electron microscopy; MTD, microtubular doublet.

The absence of IDAs can be detected in cases with pathogenic variants in CCDC40 *and* CCDC103

As the absence of IDAs can be difficult to detect by TEM, we determined whether averaging MTDs was able to enhance this structure. We examined cilia from subjects with known pathogenic variants in *CCDC40* (subject homozygous for the splice site mutation c.2712-1G>T) [311] or *CCDC103* (subject homozygous for the well-studied missense mutation p.His154Pro) [383] and compared them against a control (Table 1, Figure 6 A-C). Mutations in both these genes confer a loss of IDAs in the cilia of affected patients. When acquiring images, as the *CCDC40* variant also results (as expected [311]) in a proportion of cilia with disarrangement MTDs, only normal 9+2 arranged cilia were selected for IDA imaging. When comparing ciliary cross-section images from both *CCDC40* and *CCDC103* variants against a control, it was clear in conventional TEM that IDA loss, in addition to their being of poor

contrast, can be masked by the nearby or overlapping presence of the electron dense radial spoke and nexin structures as well as remnants of some IDA isoforms (Figure 6 A-C). By averaging the MTDs together using PCD Detect, it became apparent that the IDAs were absent in the *CCDC40* and less dense in the *CCDC103* variant cases when compared to a control (Figure 6 D-F).

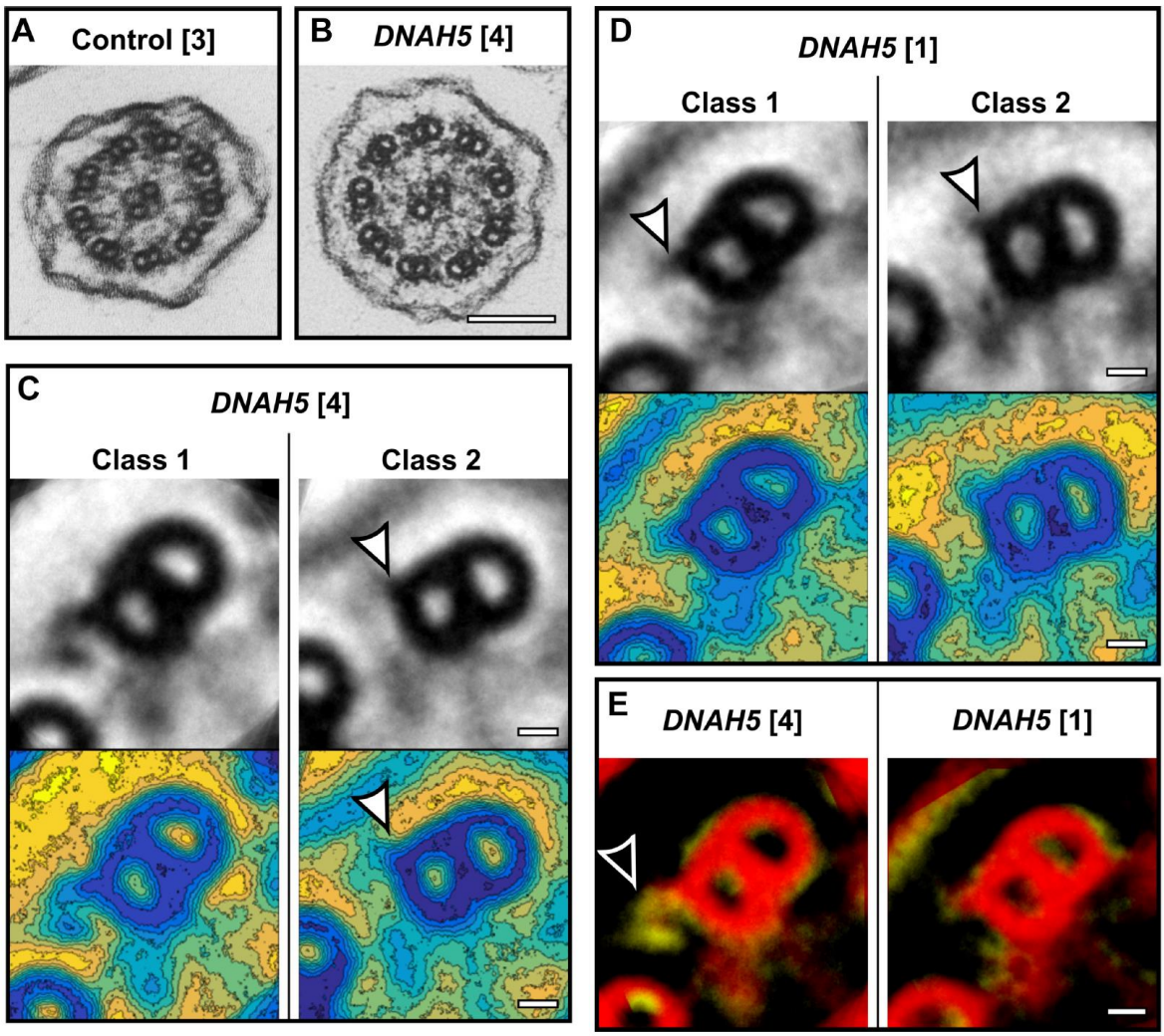

Figure 4. A subject with an atypical pathogenic variant in *DNAH5* has a sporadic absence of the ODA leading to the generation of two averaged classes. A: TEM image of a cilia from a control subject. B: a subject with a pathogenic variant of unknown significance in *DNAH5* (compound heterozygous for a missense mutation p. Thr3410Met, plus a stop-gain mutation p.Arg1761*). C: two averaged classes generated for this subject shows the presence and absence (white filled arrowheads) of the ODA. D: in a subject with pathogenic variants in *DNAH5* (homozygous for the stop-gain mutation p.Arg4429*), the class averages generated both show a loss of the ODA (white filled arrowheads), indicating complete absence of the ODAs. E: the difference, which is the subtraction of the two classes, is shown in yellow (white outlined arrowhead) and is overlaid and replaces part of the class 1MTD image (red). Scale bars: 100 nm (A and B) and 10 nm (C–E). ODA, outer dynein arm; TEM, transmission electron microscopy.

Confirmation of HYDIN *mutations by visualisation of the central pair component C2b*

To examine the absence of the C2b component that arises due to pathogenic variants in *HYDIN*, cilia from three affected subjects (cases *HYDIN* [1-3]) carrying pathogenic variants and a subject with variants of unknown significance in *HYDIN* were compared to control cilia (Figure 7 A, B).

HYDIN [1] and [2] carry compound heterozygous variants of pathogenic consequence while *HYDIN* [3] carries only a single variant but one that was previously published [384]. Subject *HYDIN* [4] is also less well proven for genetic diagnosis, carrying two missense *HYDIN* variants that have not been previously reported or functionally tested for their pathogenicity (Table 1). The CP complex from the ciliary images were averaged together in each case and the hierarchy classification system used to generate class averages (Figure 7 C-E). In the *HYDIN* mutation subjects, two main class averages were generated from the classification tool, indicating a partial defect in the C2b component, where this component is present in some cilia and absent in others (white filled arrowheads in Figure 7 D, E). As the subjects with predicted null-effect causal variants (*HYDIN* [1-3]) generated the same result as the missense mutation-carrying subject (*HYDIN* [4]), we could confirm that all these *HYDIN* [4] variants are highly likely to be pathogenic in effect. To highlight the absence of the C2b component in the *HYDIN* [4] subject, we overlaid the averaged CP complex on top of the control using the 'cilia analysis' tool (white outlined arrowhead in Figure 7 E). While examining *HYDIN* [4], further cases were assessed that either had previous diagnostic tests (semi-circling patches of cilia visualised by HSVM) indicating a potential *HYDIN* defect (PHD) or had variants of unknown significance (VUS) in *HYDIN* (Table S1). These individuals were all found to have a C2b component present in the averaged images generated (Figure S7), suggesting that *HYDIN* variants are unlikely to be their disease cause.

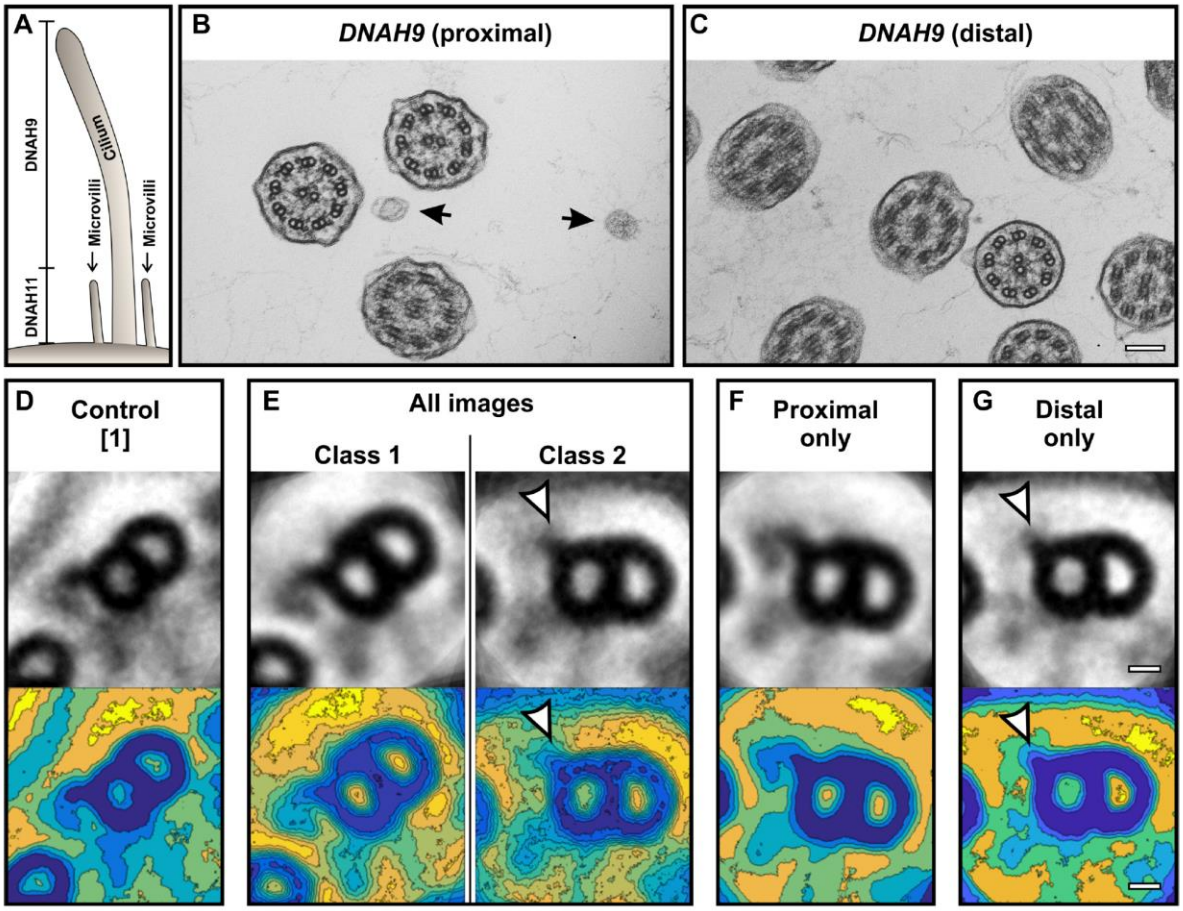

Figure 5. Analysis of MTDs from a subject with pathogenic variants in *DNAH9* gives two class averages when using all cross-sectional images, but only single classes when splitting the images into proximal or distal ciliary regions. A: *DNAH11* instead of *DNAH9* is localised to the base of healthy cilia close to the cell surface where microvilli are observed. Defects in *DNAH9* do not affect the ODA structure within this region, making cilia cross sections surrounded by microvilli ideal internal controls when comparing to ODAs from the tip region. TEM images at the proximal ciliary regions determined by the presence of microvilli (black arrowhead) (B) and the distal ciliary region (C). AverageMTD from a healthy control (D) compared with a subject with pathogenic variants in *DNAH9* (E–G). (E) All cross-sectional ciliary images generate two classes showing the presence and absence of the ODA (white filled arrowhead). Separating the ciliary images into two groups at the proximal and distal region of the cilium generates single classes showing the presence (F) and absence (G) of the ODA (white filled arrowhead). Scale bars: 100 nm (B and C) and 10 nm (D–G). ODA, outer dynein arm; TEM, transmission electron microscopy; MTD, microtubular doublet.

Discussion

To examine important structures in respiratory cilia that can be affected in PCD and other conditions affecting the airway motile cilia [385], we have developed and implemented PCD Detect, a user-friendly package of tools for image averaging and classification. Due to the uniquely conserved structure and abundance of motile cilia in patient respiratory epithelial samples, these are ideal structures for this type of image analysis. By averaging some of the structures that are repeated within cilia cross-sections, background noise can be reduced and the signal and image resolution enhanced. As some PCD defects are well known to be difficult to detect from TEM images due to their small size as well as lack of contrast or resolution, the averaging technique this package employs can provide an

additional approach to assist in the diagnosis of PCD in problematic cases. It has become increasingly recognised that diagnosis of PCD by TEM can be further complicated by the partial or sporadic absence of a ciliary structure [282,295,325,383,386]. The classification tool can assist in these cases by grouping cilia axonemal structures (classes) based on their similarities.

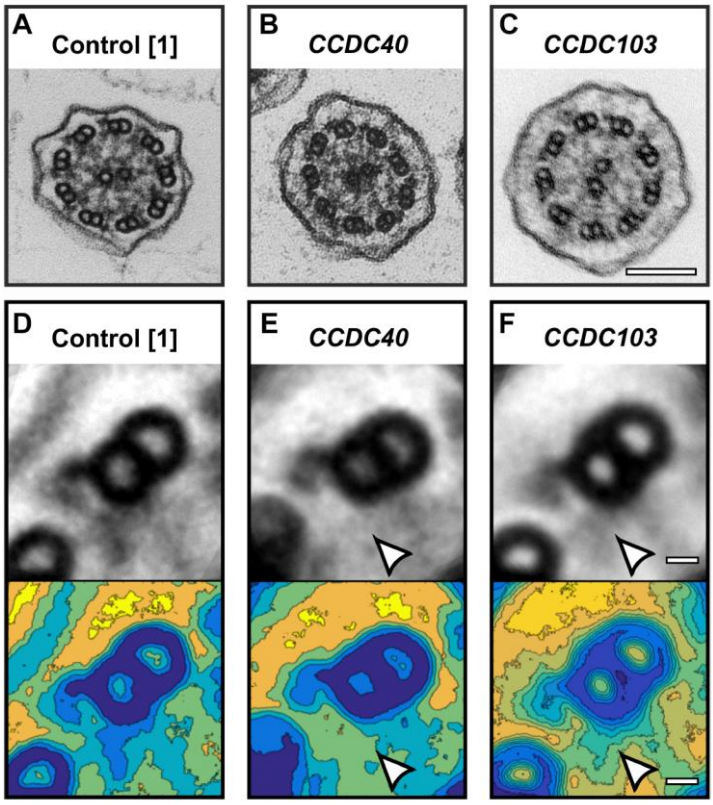

Figure 6. Feature averaging helps in the detection of the absence of the IDA in subjects who have pathogenic variants in *CCDC40* and *CCDC103*. TEM image of a cilium from a healthy control subject (A) and subjects with *CCDC40* (B) and *CCDC103* (C) mutations. D–F: averaged MTD from the different subjects. The pathogenic variants in *CCDC40* (E) and *CCDC103* (F) demonstrate a clear absence of the IDA when compared with the healthy control MTD (D). Scale bars: 100 nm (A–C) and 10 nm (D–F). TEM, transmission electron microscopy; MTD, microtubular doublet; IDA, inner dynein arm.

The first samples we used to test PCD Detect were from subjects with pathogenic variants in *DNAH5*, chosen because these typically present with a clear absence of the ODA. When averaging the first three subjects' MTDs, the ODAs were evidently absent, but in some cases a remnant of the ODA was observed. The ODA is attached to the MTD via a docking complex [294,387]. Depending on the type of variant in *DNAH5*, PCD-causing mutations may result in the loss of a portion or the entire docking complex, which may explain the remaining structure that is present in some cases [240].

When examining the MTDs in a subject (*DNAH5* [4]) carrying a missense variant in *DNAH5* that is uncharacterised for its likely pathogenic effect, using a combination of image averaging and classification, two classes of structure were found, with and without the ODA present. A partial loss of the ODA has been previously shown for a *DNAH5* splice site mutation [388]. Certain gene variants may lead to reduced synthesis of *DNAH5* or of DNAH5 protein that is transported and integrated into the cilium but lacks stability, leading to loss of a portion of the ODAs. Our averaging and classification tool allowed identification of this complex defect. The success of the average classification was further demonstrated in a subject with pathogenic variants in *DNAH9* which are known to lead to a loss of ODA only in the distal region of the cilium, whereas the proximal cilium displayed a normal ultrastructure due to the compensating presence of *DNAH11* [295,325]. When using all images acquired from a *DNAH9* PCD

subject for the averaging and classification scheme, two class averages were generated, with and without the ODA. By splitting the image input for PCD Detect into two groups, either proximal (determined by the presence of epithelial cell apical microvilli) or distal, only single averages of distinct structure were generated when using the classification tool. This shows that PCD Detect can successfully group and average similar structures from a non-homogeneous dataset. The separation of images into the distal and proximal was done manually, but we aim to develop a system that can detect microvilli and segregate images automatically, which can be added to PCD Detect in the future.

The IDAs are typically difficult to detect in conventional ciliary TEM, linked to the fact that within the 96 nm axonemal repeat there are four overlapping homologous double headed ODAs, whereas there are six single-headed and one double-headed IDA of varying morphology [98]. This results in a lower contrast of the IDA than the ODA. Methods to enhance the contrast and reduce background can be highly beneficial in TEM analysis when needing to determine if the IDAs are present or absent. The cilia from subjects carrying pathogenic variants in *CCDC40* and *CCDC103* were both examined, as mutations in both these genes give rise to loss of the IDAs, with the distinction that *CCDC40* mutations are also linked to microtubular disorganisation and *CCDC103* mutations linked to ODA loss [298,311]. The averaged MTDs generated successfully showed a clear absence of the IDA for both mutation types.

To examine CP complex defects in PCD, the cilia of three subjects' that carry pathogenic variants in *HYDIN* were examined as well as cilia from a number of other subjects with less well confirmed genetic results suggestive of *HYDIN* defects or no genetic tests yet performed. Using the averaging and classification scheme, all the three well genetically defined cases were found to have two class averages, as well as one individual (*HYDIN* [4]) carrying biallelic VUS, all of these cases showing the presence and absence of the C2b projection known to be associated with pathogenic variants in *HYDIN*. PCD Detect was also able to confirm the presence of the C2b structure in several other analysed cases that either had suspected *HYDIN* defects based on previous clinical tests, or who carried other *HYDIN* VUS, thus excluding *HYDIN* defects as their disease cause. This is the first time two distinct CP structures have been shown to exist in the positively diagnosed *HYDIN* subjects. The finding of the same two class-averaged structures in the less genetically well-unverified *HYDIN* [4] confirmed the likely causal nature of their *HYDIN* variants, a conclusion that was supported by the subject's history and other diagnostic results.

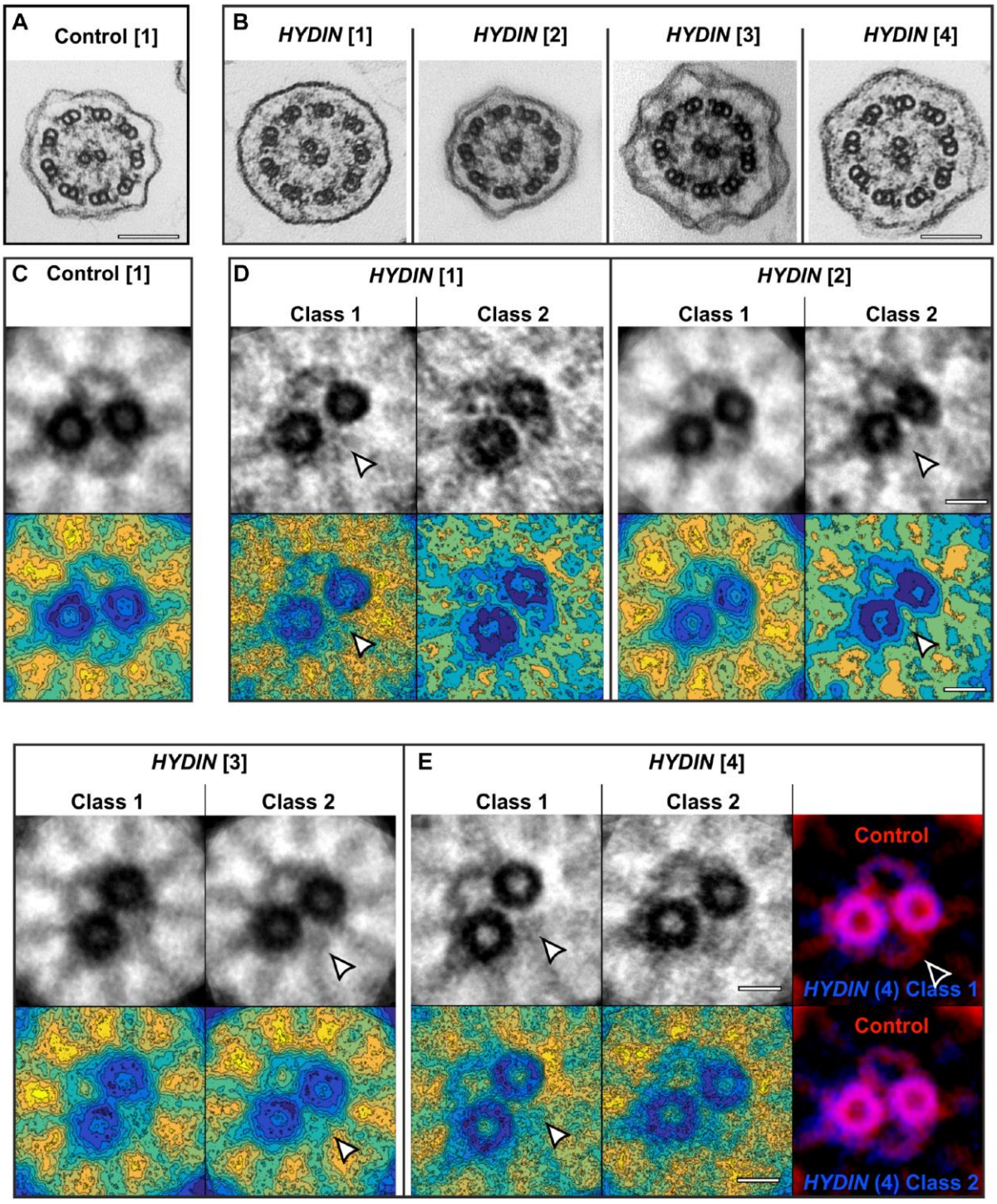

Figure 7. Subjects carrying pathogenic variants in *HYDIN* have two distinct CP complex structures. TEM images of cilia from a control healthy subject (A) and three subjects (*HYDIN* [1–3]) with variants in *HYDIN* and one subject (*HYDIN* [4]) who has variants of unknown significance in *HYDIN* (B). C–E: average CP structures from the subjects examined. D–E: subjects with pathogenic *HYDIN* variants gave two class averages, showing both a complete CP complex and with an absence of the C2b component (white filled arrowheads) when compared with the healthy control subject CP (C). (E) An overlay of genetically undiagnosed *HYDIN* [4] (blue) and the healthy control subject CP (red), highlights the missing C2b component (white outlined arrowhead) *in* *HYDIN* [4] confirming the likely pathogenicity of their *HYDIN* variants. Scale bars: 100 nm (A and B) and 20 nm (C–E). CP, central pair; TEM, transmission electron microscopy.

PCD Detect is a free toolkit that has advantages over other TEM image enhancing techniques such as electron tomography as it requires less specialised knowledge, uses information from a larger number of cilia and does not require prior information about which structure is affected. It does require multiple TEM images of well orientated cilia, knowledge of how to interpret the final averaged images and it has a lower resolution and lack of 3D data that is achievable through electron tomography. This system package has built upon averaging and image enhancement methods previously developed to assist in diagnosing PCD [389–393]. The simple, automated angular and translational searches, cross correlation and class averaging features present advantages over previously designed averaging programs. Previous methods to enhance ciliary structures such as the IDAs have involved using the cilium's axonemal symmetry to average MTD [391]. This involves manually rotating an image of a cilium though steps of 40° and averaging each time. This is therefore limited to an average of only 9 MTD per cilium. In PCD Detect, by allowing the toolkit to extract the features, there is no limit to the number of structures that can be averaged together. The averaging scheme in PCD Detect has a user-friendly interface along with a robust feature comparison and alignment system using cross-correlation, allowing the exclusion of poor-quality features or artefacts. Furthermore, the addition of a classification tool allows analysis of more complex, non-consistent PCD defects associated with non-homogenous structural defects.

The averaging and classification scheme available within PCD Detect is particularly well suited for difficult to diagnose cases that have atypical, poor characterised or difficult to detect ciliary structural defects. Many of these patients have previously had to have multiple nasal brushings to make a diagnosis (Table 1), as their initial TEM diagnostic results were either normal or inconclusive and only after multiple inspections was a defect detected. PCD Detect has the potential to reduce the need for additional nasal brushings, speeding up the diagnostic turnover times as well as reducing the use of diagnostic resources.

In summary, PCD Detect is a toolkit to enhance diagnostic images of PCD patient cilia, through an averaging and classification scheme. It has not been designed for routine use, but instead to assess difficult cases that have had a suggestive HSVM result, TEM result or a variant of unknown significance by genetics when following the conventional diagnostic pathway. PCD Detect should be used alongside other test results as part of a multi-test diagnosis not as a standalone tool. Furthermore, it is important that high quality TEM images are used to provide reliable averaged images. We were able to show successful enhancing of structural detail in samples that have clear-cut as well as more subtle ciliary structural defects and defects affecting only a portion of the axoneme or a minor structure such as the C2b projection of the CP. PCD Detect can in this way form an associated technique that uplifts current conventional PCD genetic diagnosis. This is something that can be helpful where genetic diagnosis is more difficult, due to genetic variants of uncertain significance being identified. It has notable application for the growing number of affected individuals in whom functional tests such as conventional TEM are equivocal and they carry genetic variants that have been identified in known genes but are of less certain causality, for example if they are not previously reported or where single amino acids are

affected [394], or in the specific case of *HYDIN* where variants are hard to call because of the *HYDIN2* copy gene [282]. This study shows PCD Detect has the potential to benefit global PCD diagnostic centres. Furthermore, the principles of the toolkit could also be applied to image data beyond ciliary structure analysis, including homogenous biological structures affected in diseases where diagnostics involves TEM or for investigative structural biological studies.

Acknowledgements

We are very grateful to the families who participated in this study and thank the UK PCD Family Support Group for their continued support, as well as Dr James Geraets (University of Helsinki) for his image analysis advice. The views expressed are those of the author(s) and not necessarily those of the NHS, the NIHR or the Department of Health. The authors participate in the COST Action BEAT-PCD: Better Evidence to Advance Therapeutic options for PCD network (BM1407). H.M.M. is supported by Great Ormond Street Children's Charity (V1299, V2217) and the NIHR Great Ormond Street Hospital Biomedical Research Centre (GOSH BRC).

Author Contributions: T.B.: wrote the programs; A.S. and T.B.: designed and performed experiments as well as analysed and interpreted data; A.L.P. and F.D.: analysed and interpreted data; A.S., H.M.M.: provided genetic results; A.S., T.B., H.M.M and C.H.: wrote the manuscript.

5

CHAPTER 5

New insights on the motile cilia of zebrafish

In preparation to be submited

Andreia L Pinto[1,2,5], Margarida Rasteiro[2], Catarina Bota[2], Claire Hogg[1,3], Thomas Burgoyne[1,4], Susana S. Lopes[2]

[1] Paediatric Respiratory Medicine, Primary Ciliary Dyskinesia Centre, Royal Brompton & Harefield NHS Trust, London, SW3 6NP, UK
[2] CEDOC, NOVA Medical School, Rua Câmara Pestana nº 6, 6-A, Edifício CEDOC II, 1150-082 Lisboa
[3] Department of Paediatrics, Imperial College London, London, SW3 6LY, UK
[4] UCL institute of Ophthalmology, London, EC1V 9EL, UK
[5] Department of Life Sciences, NOVA School of Science and Technology, Caparica, Portugal

Personal contributions:

I did all the technicological conceptualization, experimental design, bench work and electron microscopy analysis, and manuscript writing for this work. All images were obtained by me, except Figure 1, which was obtained and analysed by my colleague Margarida Rasteiro, who is also responsible for the *Ccdc40*$^{-/-}$ (homozygous) mutant generation, Immunofluorescence and confocal microscopy.

Abstract

Zebrafish (ZF) is a vertebrate teleost widely used in many areas of research. As embryos, they develop quickly and allow unique advantages for research studies owing to their transparency until later stages. Zebrafish has many ciliated organs and presents primary cilia as well as motile cilia. This model organism has two types of motile ciliated cells, mono and multiciliated, and at least two types of motile cilia ultrastructure have been reported (9+2 and 9+0 microtubule arrangement). Using zebrafish as an animal model helps better understanding human diseases such as, Primary Ciliary Dyskinesia (PCD), a genetic disorder that affects cilia motility in an autosomal recessive manner, currently associated with more than 40 genes. To validate zebrafish cilia as organelles to study PCD through the analysis of their axonemal ciliary structure We used conventional Transmission Electron Microscopy (TEM) and Transmission Electron Tomography (ET) for the analysis of zebrafish motile cilia to obtain high-resolution data in both the olfactory pit (OP) and the Left right organiser (LRO). We characterised the wild-type (WT) cilia in the OP and showed the presence of motile cilia (9+2) organised in the periphery of the pit and the presence of immotile cilia (9+2) with absent outer dynein arms (ODA) in the centre of the pit. We reported a variable pattern for the central pair (CP) in the LRO motile cilia. We confirmed the presence of immotile cilia in the central region of the WT OP based on the presence of 9+2 cilia lacking dynein arms. We proposed a new hypothesis for the distribution of cilia in the LRO. We showed that the ODA of the microtubular doublet (MTD) of both OP and LRO cilia are structurally similar to the human respiratory cilia at the resolution of EM and ET.

Keywords: Zebrafish, Primary Ciliary Dyskinesia (PCD), Cilia Ultrastructure, CCDC40, Transmission Electron Microscopy (TEM)

Introduction

Motile Cilia are centriole derived organelles, surrounded by a membrane and containing microtubules formed by protofilaments that can be longer or shorter, depending on the number of tubulin molecules they contain[2,3,15]. This structure is called the ciliary axoneme or ciliary shaft [94], a transversal term throughout species, considering how well the ciliary structure is conversed between them[2]. Axonemal ultrastructure in eukaryotic cells segregates into two significant patterns: 9+2, in which nine microtubule doublets organise around two microtubules in the centre known as the central pair (CP) complex; and the 9+0 organisation, in which the CP is absent [12,395]. Thus, there are two major types of motile ciliated cells, cells that produce from dozens to several hundred 9+2 motile cilia and cells that only generate one solitary cilium.

Monocilia lacking CP were described in the node of mice, hypothesising the presence of motile 9+0 cilia in the node of embryonic mouse[11,34,196]. However, non-motile primary cilia (9+0 configuration and no dynein motor arms) can be found in several organs and tissues having solo sensory functions and lacking movement and can be found in almost every cell type [396,40]. On the other hand, Yu et al. in 2011 identified cilia that showed a 9+2 organisation but are immotile, called kinocilia found in the hair

cells of the inner ear that express *Foxj1b* [79] and in the ciliated receptor cells (primary sensory cells) in the OP of zebrafish[24].

Regarding motile cilia dynamics, multiciliated cell cilia with 9+2 configuration beat metachronically with a planar stroke to clear fluid or promote locomotion [65,66]. Motile cilia lacking CP (9+0) have a specific movement pattern, described as planar rotation, circling or twisting. These monocilia are known to exist in the LRO in vertebrates (called the Kupffer's vesicle in the zebrafish [21,42,194]). In case of disease, cilia wholly or partially lacking the CP are frequently accounted as one of the phenotypes of Primary Ciliary Dyskinesia (PCD), an autosomal recessive disease of the motile cilia [144,229].

Cilia malfunction is linked to many diseases. Mutations in cilia genes may result in several phenotypes (genetic heterogenicity), and mutations in a single gene lead to a wide range of phenotypic manifestations (genetic pleiotropy) [8]. An example is mutations in the *CEP290* gene related to many ciliopathies ranging from severe early-onset developmental disorders like Meckel-Gruber syndrome to mild late-onset disorders like nephronophthisis. Bardet-Biedl and Joubert Syndromes are also well-known disorders linked to *CEP290* [8,397].

Zebrafish started being popular as an animal model in the 1980s (Streisinger work) as a genetically tractable organism, allowing a phenotypic characterisation of a large number of mutations that cause defects in a variety of organ systems [174]. As zebrafish are vertebrates, this gives them leverage as a research tool, compared, for instance, to *Chlamydomonas reinhardtii*, which only major defect from cilia impairment is lack of locomotion [398]. Zebrafish helped shed light on the role of specific genes in human diseases, as their genome has been widely studied, providing insight into their human orthologues [181]. Amongst the many advantages of zebrafish, we will stress the fact that zebrafish embryos contain cilia in nearly every cell type, and their organogenesis defects can be easily characterised using brightfield microscopy as the zebrafish embryo and larvae stays transparent until all major organ systems are formed. Many of the organs and tissues of zebrafish are similar to those of humans and 70% of genes are shared [181]. Motile cilia have been well described in the Kupffer's vesicle or Left-Right Organiser between 3 and 14 somite (ss) stages and in the OP at 48-72 hpf, amongst other locations [178]. Moreover, genetic engineering methodologies like using the CRISPR/Cas9 system are successful in editing the zebrafish genome and have greatly facilitated the generation of zebrafish mutant models mimicking human ciliopathies [8,98,399]

Primary ciliary dyskinesia (PCD) is a genetic disorder distinguished by recurrent infection in the lower and upper respiratory tract [251], reduced fertility ad laterality problems (50% of PCD patients show *situs inversus*) [160]. Ultrastructural defects in motile cilia, or the reduced amount of cilia (in multiciliated cells - oligocilia), are known to cause PCD [160] [158].

Almost all identified PCD genes show homologue genes in zebrafish, as shown in supplementary information table 1 [400]. For this work, and considering the high impact in PCD patients [401], we selected the zebrafish *Ccdc40* (Coiled-Coiled Domain-Containing Protein 40) gene to mimic a human hotspot mutation. The mutant line was generated using CRISPR-Cas9 technology, according to Rasteiro Master Thesis work [250] and consisted in generating a truncated protein Ccdc40, at the amino acid 116, excluding entirely the coiled-coil domain. The loss of function phenotype of the zebrafish *Ccdc40*$^{-/-}$ mutant resembled that of the MO-injected embryos described by Rasteiro: *situs inversus* in 70% of all cases, curved tails, lethargy and cardiac oedema [250]. A previous study by Becker-Heck in 2011 had also compared the effects of zebrafish *Ccdc40* MO knockdown with the zebrafish homozygous mutant *locke,* and showed these to be phenotypically indistinguishable[324]. In addition, the ultrastructure of the defected cilia investigated by Becker et al. in the Kupffer's vesicle (LRO) showed some of the traits found in *CCDC40* patients, namely decentralisation of the central pair [324,311]. The mutation in *locke* homozygous zebrafish[35] is not the same as the one Rasteiro generated, while *locke*$^{-/-}$ has a nonsense mutation at 778 aa. Rasteiro crispr/cas9 mutant has an early stop codon at 116 aa excluding completely the coiled coil domain.

CCDC40 is a well-studied PCD gene [311,324]. When mutated in humans, *CCDC40* does not completely render static cilia, but they were found to beat in a faster flickering way, with very reduced beat amplitude [402].

Coiled-coil domains are frequent in proteins and consist of two to five amphipathic α-helices that twist around each other to form a supercoil [403]. Coiled-coil domains are essential in proteins involved in intracellular transport, molecular recognition, signal transduction and movement regulation [403]. In cilia, *CCDC40* is required for motility, as it is needed for the correct assembly of the Nexin-Dynein Regulatory Complex (N-DRC) and IDA. *CCDC40*, together with *CCDC39*, form a complex identified as a molecular ruler in cilia implicating the specific insertion of the radial spoke (RS) in a 96 nm periodicity [404].

Patients with N-DRC/molecular ruler abnormalities, phenotypically show as microtubular disorganisation, central pair decentralisation and IDA absence, typical traits of *CCDC39* and *CCDC40* biallelic mutations, have a worst prognosis than other PCD cases with dynein defects [330,405]. As observed by Davis et al., these patients are more severely affected, showing a higher rate of neonatal respiratory distress and lower FEV, *situs inversus* (in around 50% of the patients) [310,406], and poorest overall condition.[330,401]. In PCD patients, *CCDC40* is mutated in several called "hotspots". The most frequent mutations are c.248delC and c.3129delC that modify the reading frame [324] and c.2440 C>T, c.961 C>T and c.1345C>T that produce truncated proteins [311].

Despite previous research has been done on zebrafish cilia [24,215,21,227], no study fully characterised the cilia ultrastructure of the OP and LRO. With this work, we aim to determine the similarities and the significant differences in zebrafish cilia compared to human cilia, both for motile cilia present in multiciliated cells and for embryonic LRO cilia (monociliated cells). Moreover, here we inspect

the results obtained from *Ccdc40*$^{-/-}$ mutant zebrafish and compare those with human patients (*CCDC40* patients from the Royal Brompton Hospital, with genetic testing showing orthologous variants). For this, we used wildtype zebrafish (WT) (AB fish lines) and mutant *Ccdc40*$^{+/-}$ zebrafish lines that were in crossed to access the homozygous phenotype of both the LRO cilia in 9-10 ss stage embryos or the OP in 5 day old larvae. Full TEM assessment was performed and sometimes for better understanding of the phenotype presented, transmission Electron Tomography (ET) was performed.

Using Transmission Electron Microscopy (TEM), we confirmed the heterogenic configuration of the zebrafish OP. We also showed by ET the variable presence of a CP in the monocilia of the LRO, a feature already hypothesised in our previous publication by Tavares et al. [21].

Methods

Ethical Approval

The ethics review board approved the Institute of Child Health/Great Ormond Street Hospital study, London (UK) (08/ H0713/82). All subjects gave informed signed consent for genetic testing and surplus diagnostic samples to develop new diagnostic tools.

Animals

The zebrafish used in these experiments (AB WT line and *Ccdc40*$^{+/-}$ (heterozygous) mutant line) were bred and kept in the CEDOC Nova Medical school fish facility under a controlled environment approved by the Direção Geral de Alimentação e Veterinária (DGAV). Embryos and larvae stage 8 to 10 ss and 2 to 5 days post fertilization (dpf) respectively were removed from their chorion if needed and euthanised by being placed in a bleach solution or fixative for TEM and ET analysis.

Ccdc40$^{-/-}$ *mutants genetic engineering*

Zebrafish mutants were obtained using the CRISPR-Cas9 method performed by the Lopes lab in CEDOC Nova medical school according to what was described in the published work of Rasteiro [250]. The *Ccdc40* zebrafish mutant line (in preparation for publication) expresses a truncated protein – mutation at 116 aa – the truncated protein lacks the coiled-coil domain, making the homozygous animal not viable after 7-dpf.

Immunofluorescence and image analysis

Embryos were fixed in 4% PFA (paraformaldehyde) in PBS (phosphate buffer solution) overnight. The embryos were then removed from the PFA and washed five times with PBS, dechorionated, permeabilized with Proteinase K and fixed again in 4% PFA-PBS for 20 minutes. The samples were submitted to antigen retrieval using acetone for 7 minutes at -20^{o}C, and blocking was done using blocking solution (BS) (1% bovine foetal serum (BFS) in PBS) for 1h. The primary antibody

(mouse anti-acetylated alpha-tubulin) was diluted at 1:400 in BS and incubated with the embryos overnight at 4ºC with agitation. The embryos were incubated with secondary antibody overnight (anti-mouse Alexa 546, 1:500) in a solution with equal amounts of PBS and DAPI (4′,6-diamidino-2-phenylindole). Samples were fixed in 4% PFA in PBS and were mounted onto glass slides. Images were taken using a two-photon microscope (40x water objective, NA 0.80, 2.5 optical zoom GaAsP detector).

Transmission Electron Microscopy

Embedding for TEM was performed in zebrafish embryos (9-10 ss) and larvae (5-dpf) from both WT AB and *Ccdc40*$^{-/-}$ mutants. The animals were whole-mount fixed with 2.5% glutaraldehyde (Sigma) 0.1M sodium cacodylate (Sigma) for at least 48 hours, and washed in the same buffer. After, were post-fixed with 1% aqueous osmium tetroxide (EMS), and stained *en bloc* with 1% aqueous uranyl acetate (Agar Scientific). Samples were dehydrated in increasing ethanol concentrations, infiltrated with propylene oxide, and embedded in Epon 812 (EMS). Polymerisation of the Epon was performed at 60°C for 24 hours in bottleneck capsule beems (Agar Scientific). Under a stereoscope, the blocks containing the embryos and larvae were analysed, and the best ones (based on their viability and orientation) were selected for re-embedding in the desired orientation. The tip of the blocks containing the samples was chopped, and the blocks containing the fragments were re-embed in coffin type silicon moulds. For the larvae, only the head was dissected and re-embedded in coffin type silicon moulds in an anterior-posterior position, with the OP facing the plane of sectioning. The 9-10 ss embryos were re-embedded lateral to obtain longitudinal sections along the wider axis to fully access the LRO, the somites, and the yolk sac. (Supplementary Figure 1). The resin was polymerised in an oven at 60°C for at least 24 hours. Ultrathin sections (≥100nm to be able to get at least one complete repeat of the IDA) were obtained in a Reichert Ultracut E ultramicrotome (Leica®) collected to 1% formvar coated copper slot grids (Agar scientific), stained with 2% aqueous uranyl acetate (UA) and lead citrate (LC) (Reynold recipe) and examined in a Jeol 1400 plus transmission electron microscope at an accelerating voltage of 120 kV. Digital images were obtained using an AMT XR16 bottom mid-mount digital camera (AMT). The sections were systematically analysed using AMT600 software, and several high and low magnification images of cilia throughout the whole LRO and the OP of both mutant and WT were acquired. Considering the high abundance of cilia found in the OP, these were counted using a custom-made software developed to quantify cilia for PCD diagnosis [276]. Patient samples were embedded for TEM and analysed as previously described in Andreia L. Pinto et al. [276], following a standard clinical diagnostic sample preparation and assessment procedure.

Electron Tomography

Sections from the same batch of animals were acquired for ET analysis, thick section of 100-120 nm were collected into 1% formvar coated copper slot grids (Agar scientific), stained with 2% aqueous UA, LC (Reynold recipe) and 10 nm colloidal gold (EMS), and examined in a Jeol 1400 plus

transmission electron microscope at an accelerating voltage of 120 kV. For dual-axis ET, selected areas at a magnification of 25.000x were tilted from -60 to 60 degrees in the two axis (the grid was rotated 90 degrees between the collecting tilt series) using a high tilt specimen holder. SerialEM was used for the automatic acquisition of the images. Cilia cross-sections of the LRO and the OP in both WT and *Ccdc40*$^{-/-}$ mutants were assembled in a tomogram using IMOD 3Dmod [407], and both axis were combined for the generation of an electron tomogram of the region of interest. Sub-tomographic averagings were performed using IMOD PEET in both organs of WT and mutant fish. For the 3D analysis of the structures, UCSF Chimera was used. Chimera is a program for the interactive visualisation and analysis of molecular structures and related data. We open the data in Chimera with the averaged ciliary features and produced a model showing the molecular anatomy of the structure, and we used Chimera to measure the volumes of the ODA and MTD [408].

Data analysis

In order to better study the discrepancies between the experimental groups, Student's t-test was performed, and the significance was considered for values below 0.05.

Results

The cilia of zebrafish by light microscopy

Zebrafish shows motile cilia in some of its organs since the early stages of development [8]. Olstad et al. has shown the flow generated by the OP motile cilia before. Moreover, the motile monocilia of the LRO, mainly 9+2 configured axonemes that beat with a rotation and wavy fashion were extensively described and published by Sampaio et al. 2014 and Tavares et al. 2017. These motile monocilia are essential to generate the flow for the determination of left-right asymmetry [21,42,189]. The presence and distribution of cilia in the WT LRO and *Ccdc40*$^{-/-}$ mutant zebrafish was again confirmed by IF upon confocal microscopy image acquisition as shown in the A and B panels of Figure 1, respectively. The monocilia found in the LRO of the mutant *Ccdc40*$^{-/-}$ fish seem to be shorter (arrowheads pointing at cilia in both experimental conditions). The OP cilia of both WT and *Ccdc40*$^{-/-}$ mutant zebrafish were also previously assessed by IF (panels C and D in Figure 1), and three regions of the pit from each condition were selected to show the presence of cilia (labelled in red, marked with an asterisk) throughout the OP. The results shown by IF confirmed the presence of cilia in the OP and the LRO and revealed their 3D tomography which proved useful for future TEM embedding and sectioning procedures. However, confocal microscopy is limited to 180 nm lateral and 500 nm axial resolution and is not appropriate for ultrastuctural studies. We next used TEM and ET to access the ultrastructure of the respective organ cilia.

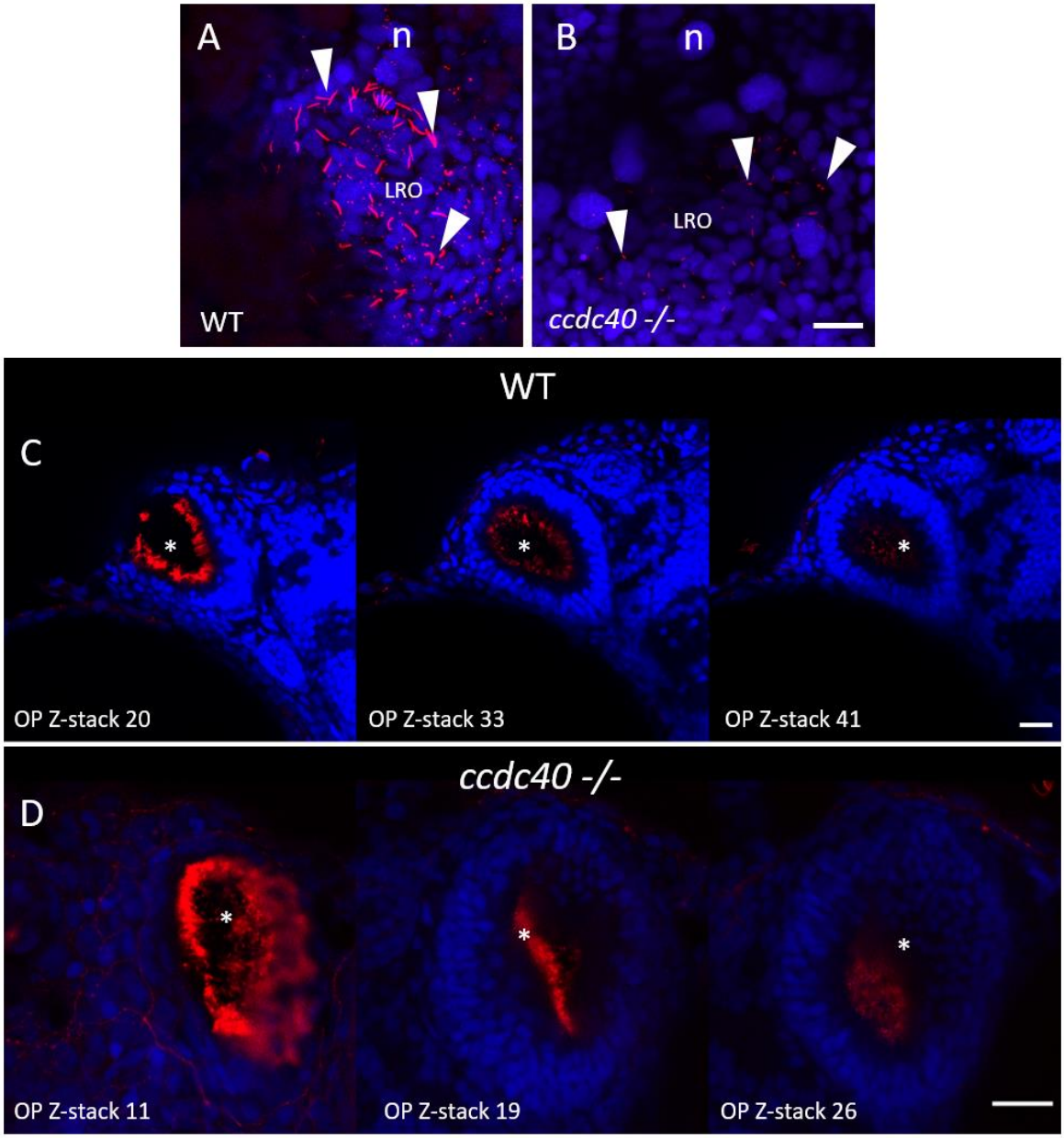

Figure 1. Presence of cilia in the LRO and the OP of wildtype (WT) and *Ccdc40*$^{-/-}$ mutant zebrafish shown by confocal fluorescent microscopy. Distribution of motile monocilia in the LRO of 8-9 ss WT (A) and mutant fish (B), shown in a z-projection of 145 images for the WT and 113 images for the mutant. Arrowheads pointing at cilia. Regarding the OP, three image planes were selected through the pit of WT (C) and mutant *Ccdc40*$^{-/-}$ zebrafish (D) revealing the consistent presence of cilia throughout the organ. Z-projection of confocal stacks (for the assessment of the LRO) and z-stack analysis (of the OP) were done using FIJI. Acetylated α-tubulin labelling was done by Immunofluorescence and appears in red and DAPI in blue in both panels; n – nucleus; * cilia; scale bar 20μm

Different cilia in the WT zebrafish OP

To maximise the ultrastructural characterisation of cilia analysed in the OP, a detailed investigation was done by means of counting more than 50 cilia cross-sections when possible. This was to provide a representative profile of features found in the OP. TEM assessment revealed that the

pit has a bowl shape morphology, and more towards the periphery of this concave structure, all cilia appeared to have 9+2 and outer and inner dynein arms, (ODA and IDA) characteristic of motile cilia. However, more into the centre of the pit, the cilia had absent outer dynein arms (IDA were hard to access in some areas). Quantitative analysis of three different WT animals showed consistently that close to 100 cilia had 60% of 9+2 cilia, and on average, 23% (±1) of cilia presented absent or incomplete dynein arms (most notably in the ODA) (Figure 2 and Table 2). Thus, TEM analysis allowed the first-time quantification of the heterogenicity of the cilia in a specific region of the OP. Cilia observed in the OP thus have a 9+2 motile morphology in a more peripheral area and a 9+2 with ODA and IDA absence towards the centre of the pit.

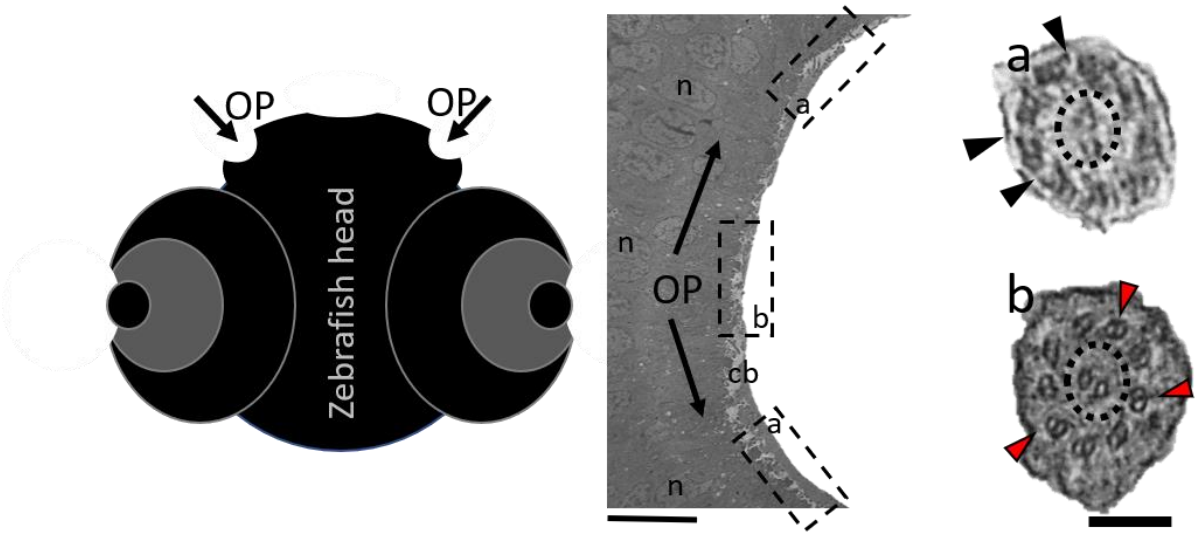

Figure 2. Schematic representation of 5-dpf Zebrafish head, structures of interest are marked with arrows - olfactory placodes/pits (OP). TEM low magnification image shows a cross-section across an OP of a WT zebrafish showing a bowl-shaped structure containing multiciliated cells and cilia in several orientations. In the periphery of this pit (dotted boxes a and inset), cilia containing classical motile structure 9+2 with dynein arms present (black arrowheads). However, in the most internal region of the OP (dotted box b and inset), cilia profile are more frequently 9+2 with absent dynein arms (red arrowheads); this pattern was visible in all WT embryos (n=3). n - nucleus, cb - cilia border, OP – olfactory /pit, thin bar 6µm, thick bar 100nm.

When compared, zebrafish *Ccdc40*$^{-/-}$ and WT samples revealed no significant differences in the number of missing ODAs. However, when it comes to IDAs, the absence of IDA in the mutant is significantly higher (**** $P \leq 0.0001$).

Regarding *CCDC40* PCD patients (table 1), these show an IDA absence combined with MT disarrangement in cilia, with no abnormalities identified in the ODA. On the other hand, the zebrafish OP has a characteristic pattern of absent ODA in about 25% of its cilia (Table 2), which explains the ~15% absent ODA seen in the *Ccdc40*$^{-/-}$ zebrafish mutants OP. We have accessed the number of defects and normal cilia present in the *Ccdc40*$^{-/-}$ mutant zebrafish using the same method used for the human patient samples, and the ODA defect was seen in addition to the *CCDC40* human phenotype that includes disarranged microtubules and complete absence of the (IDA) (table 2).

The percentages of missing ODA and IDA assessed by quantitative method [276] (as shown in Table 2) were compared using Student's t-test in both zebrafish and human samples (WT and *Ccdc40*$^{-/-}$ mutants and with *CCDC40* PCD and control patients) for significance analysis. The differences between the WT zebrafish and the non-PCD patient concerning the presence of ODAs and IDAs is significantly different (ODA *** $P \leq 0.001$; IDA * $P \leq 0.05$);

Between human samples (control non-PCD versus *CCDC40* PCD patient data), there were no significant differences regarding the consistency of the ODA (ODA were always present; ns $P > 0.05$). On the other hand, there was a considerably higher number of IDA absent in the *CCDC40* patient samples (**** $P \leq 0.0001$). Finally, when putting side-by-side, zebrafish *Ccdc40*$^{-/-}$ mutants and Human *CCDC40* PCD patients, differences in the presence of ODA were reported (absent ODA in the zebrafish but not in the human sample; * $P \leq 0.05$). Nevertheless, and in line with what was expected, IDA defects were consistent between the two samples (human and zebrafish mutants show similar profile; ns $P > 0.05$).

The disarrangements found in WT zebrafish were considered similar to secondary defects and fall more in the category of microtubular abnormalities that can be linked to mechanical stress inside the pit (biofilm was identified in WT 2 and 3, and it might be suggestive of accumulation of medium during development, data not shown). Human control samples showed no MT disarrangements in the configuration of the ciliary axoneme.

Table 1 Genetic results of the three PCD patients presenting ultrastructural defects observed in TEM.

***CCDC40* patient 1**	***CCDC40* patient 2**	***CCDC40* patient 3**
CCDC40 homozygous for c.248del, p.Ala83Valfs84*	*CCDC40* homozygous for c.248delC; p.Ala83Valfs84*[311]	*CCDC40* compound heterozygous for c.248del and c.2712-1G>T

Table 2 Full TEM assessment and defects quantification of cilia from the OP in wildtype and *Ccdc40*$^{-/-}$ zebrafish mutant, compared to the finding found in non-PCD human control samples and *CCDC40* PCD human sample.

	Disarranged cilia (%)	**Dynein arms assessment (%)**			
Counted >50 cilia		*Both arms present*	*ODA missing*	*IDA missing*	*Both arms missing*
WT AB zebrafish (n=3)	14 (±8)	62 (±1)	23 (±2)	14 (±2)	14 (±2)
***Ccdc40*$^{-/-}$ zebrafish (n=3)**	94 (±2)	0	14 (±7)	59 (±7)	16 (±7)
Human control (non-PCD) (b=3)	3 (±1)	93 (±12)	1 (±1)	3 (±6)	2 (±4)
***CCDC40* human PCD (n=3)**	51 (±17)	5 (±2)	2 (±2)	91 (±3)	2 (±2)

Next, cilia of the LRO were also analysed in detail, with the expected fewer cilia observed due to the monociliated nature of the LRO. In these cilia, and as shown previously [21], dynein arms were seen in all WT embryos, and some cilia showed an absent or partial configuration of the CP. There was an impression that the cilia might be shorter, but that fact can only be validated using other methods (result confirmed by confocal microscopy, data not shown). When compared, the defects found in the zebrafish *Ccdc40*$^{-/-}$ mutants matched the phenotype of *CCDC40* PCD patients (microtubular disarrangements and IDA defect as shown in panel C of Figure 3).

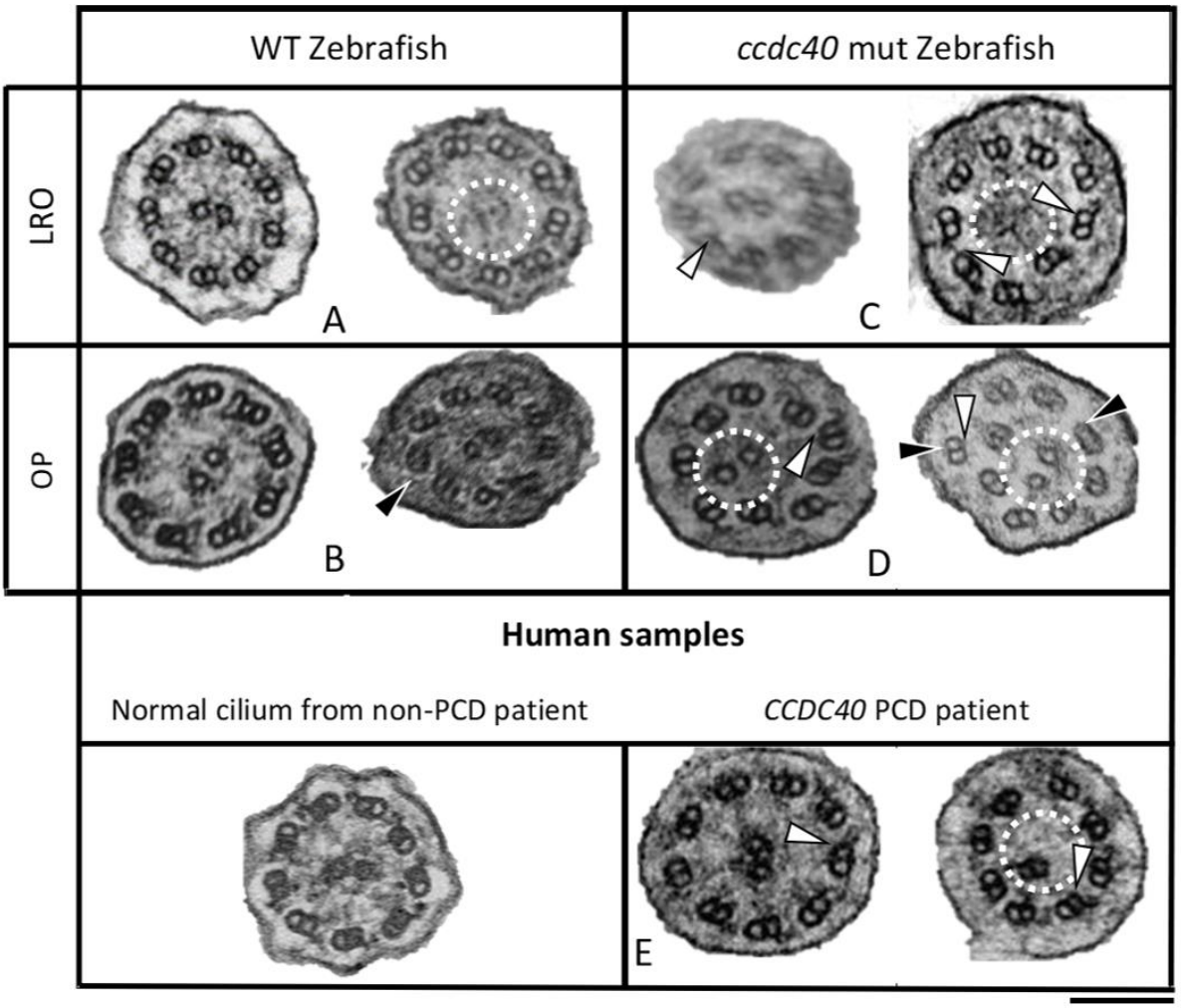

Figure 3. TEM features of cilia showing ultrastructural variations in the LRO of 9/10 somite stage WT zebrafish embryos (A) and the OP of 5-dpf WT zebrafish larvae (B). In the *Ccdc40*$^{-/-}$, zebrafish mutants the LRO presented absence of CP in some cilia (C) and there was an IDA+ODA absence in the cilia of the OP (D). In human samples from PCD patients with *CCDC40* mutations IDAs were absent and MTs disarrangements were present (E). White arrowheads – missing IDA; black arrowheads – missing ODA, dotted circle – abnormal position of/missing CP; scale bar 100nm.

Zebrafish and human have overall similar cilia ultrastructure in multiciliated cells

These results concluded that apart from the particular features of the zebrafish OP, namely the absence of outer dynein arms in cilia from the central region of the pit, the ultrastructure of ciliary components is similar to the cilia found in the human airway. Nevertheless, after assessing the cilia from the LRO by ET, some concern regarding the size of the ODA was raised, as some variation in the size of the outer dynein arms was visible, suggesting it might be smaller (Supplementary data figure 2). To clarify, we used USFC Chimera software to measure the volume of the ODA compared to the total volume of the microtubule doublet (MTD) to make sure the measurements were accurate since there were variations in the size and thickness of the 5 MTD assembled by ET. Furthermore, we analysed the volumetric ratio from averaged MTD from the LRO of 4 different WT zebrafish, and these measurements were compared to the averaged MTD of 3 human control cilia (figure 4). No significant

differences was found between the two samples, indicating that LRO cilia and human airway cilia have similar MTD (ns P>0.05). We also looked at the rendered data of MTD from two different WT zebrafish OP. The ODA ratio showed no significant differences, but the numbers of animals analysed were not enough for the statistical analysis.

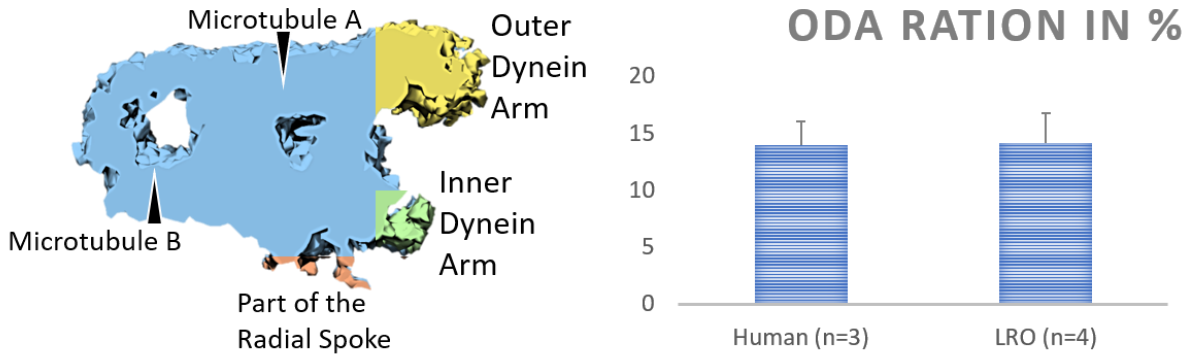

Figure 4. The ratio of the outer dynein arm (ODA) volume compared to whole microtubule doublet (MTD) volume. Sub-tomographic averaging of the MTD of WT zebrafish cilia, showing ODA and IDA, tubules A and B and a portion of the radial spoke. The two sample groups showed no significant difference between them (ns P>0.05) performing a Student's T-test.

The application of Transmission Electron Tomography for the study of the central pair

Despite the visible heterogenicity of the CP of the LRO, there was a need to provide more evidence to validate these findings. The LRO is an organ well embedded in the embryo and hard to access. It is spherical-like in shape, and depending on the plane of sectioning, the cilia will be in different orientations. Additionally, LRO cells are monociliated [409]. To acquire well-oriented cross-sections of many cilia in the LRO is hard and produces sparse results, even in the event of finding an axoneme, the probability of it being well orientated is low. ET offers the advantage of expanding the ability to view structures that fall outside conventional image ranges and bridge the resolution gap [410]. We were able to successfully collect and assemble tilt series from six cilia from two different WT zebrafish LROs (Figure 5, animal 1: cilium 1/4 to 4/4, and animal 2: cilium 1/2 and 2/2). We investigated the prevalence of the CP using IMOD z-projection overlap, which consists in the combination of the slices of the tomogram generating a single image. From this assessment, we could identify a heterogenic pattern regarding the CP. Two cilia showed evidence of a CP; two cilia showed only one of the CP tubules (incomplete phenotype), and two cilia presented no visible CP (Figure 5)

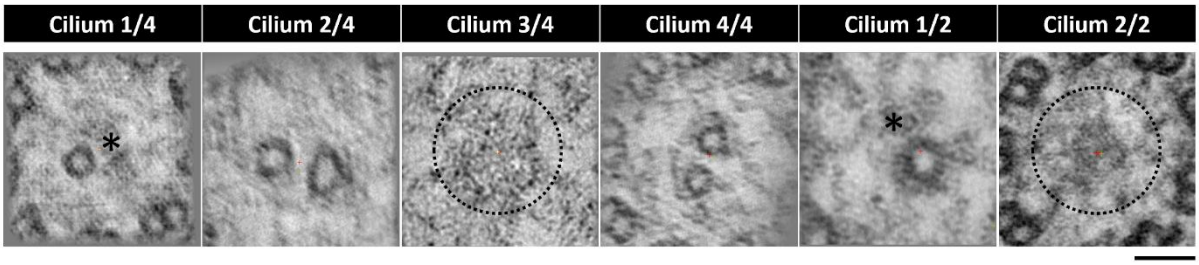

Figure 5. Tomogram z-projection (≥150 stacks) of 6 cilia CP observed in two different WT zebrafish LRO, showing variation in the frequency of the CP. Cilium 1/4 and 1/2 showing only one tubule present, cilium 2/4 and 4/4 showing both tubules present and cilium 3/4 and 2/2 showing no tubules in the central pair region. * missing tubule, incomplete CP; dotted circle missing CP. Bar 50 nm.

Discussion

Cilia are well-studied organelles; over 21.000 studies have been successfully published around this topic, and a thousand only in the last year. Cilia are complex organelles, and the fact that they are involved in many syndromes and diseases makes them essential targets in biology and translational research [94,411]. The difficulty of accessing human embryonic tissues provides the need to find model organisms that resemble human organogenesis and have conserved evolutionary patterns. *Chlamydomonas reinhardtii*, *C. elegans*, and *Leishmania donovani*, promastigote are good models, easy to maintain and proliferate in captivity. However, they lack internal organs and organ to organ communication, crucial for the study of ciliopathies in humans. *Chlamydomonas,* for instance, are simple organisms equipped with a conserved flagellum that has already been widely used for biochemical cilia characterization [8,17,404].

On the other hand, it was already shown using contemporary technologies like computer-assisted image analysis and Cryo-EM that *Chlamydomonas* flagella have structural differences from human cilia [17,392]. Vertebrates like mouse and zebrafish are good models to study ciliopathies since their genomes are well known and contain protein-coding genes with human orthologues [25], meaning, when mutated, these genes may recapitulate the human phenotype. This feature has been shown for PCD in many studies [4,164,412–416]. PCD has already been associated with more than 40 genes known to be causing disease [94], and all of those genes are present in the genome of zebrafish [400] (Supplementary Table 1).

Technology in ultrastructural studies has improved in the last ten years and, higher resolution, better image quality and improved sample preparation have allowed us to go further in studying structures that were once less reachable [16]. The zebrafish Kupffer's vesicle is the fish LRO, equivalent to the mouse node, therefore, an important structure to study in the zebrafish motile cilia research. However, this vesicle is embedded at the end of the notochord and it is challenging to access [42,196]. Even though the zebrafish is transparent, and the LRO is accessible by light microscopy, a more detailed analysis using conventional TEM can be problematic. The organ itself is not bigger than 70 µm in diameter (measured by TEM) and is transient during the zebrafish development [42,194,190]. In addition

to this, the fact that the LRO has a spherical shape, means that cilia will be in many different orientations, making it harder to get a well-orientated cilia cross-section in the organ. Also, the LRO is composed of monociliated cells, and the number of cells in the LRO is around 50 (assessed by light microscopy) [42,194]. Altogether, these features make the LRO a challenging organ to study by conventional TEM. On the other end, the OP is a surface organ that can be more easily reached [227], for this, the orientation of the blocks for TEM is essential, and the sectioning must be done exceptionally carefully since the structure is small (approximately 60 µm in length [227]). The disadvantage is that being more superficial also makes it more vulnerable to external mechanical aggressions like the salts on the embryonic medium and even manipulating and handling the sample during the embedding protocol.

The findings that the OP has a heterogenic pattern of ciliary ultrastructure coincide with what was already described by Reiten et al. 2016 [227] functional tests. At the time, the authors described a difference in the beat frequencies found on the OP, hypothesising that motile cilia in the nose of aquatic vertebrates are specially organised and beat their cilia at distinct frequencies to attract particles, showing no beating in the center of the pit [227]. However, the authors showed no TEM analysis for the cilia in the OP [227]. The work presented here sheds light on the lack of flow detected in the center of the pit, given the immotile profile of the cilia nested in that specific area (lacking dynein arm motor proteins). Our findings and the work done by Reiten seem to agree with observations previously published by Hansen (1998, 2005), in which a subgroup of ciliated sensory neurons are believed to cluster in the centre of the OP and to have a 9+2 configuration with no dynein motors. However, these previous studies were conducted in adult zebrafish, and they do not provide extensive TEM analysis to characterize the ultrastructure of these cilia [24,215].

For this work, we chose to work with a zebrafish mutant *Ccdc40*$^{-/-}$ created in the Lopes lab [250]. The phenotype caused by this mutation in humans is well characterised and affects around 20% of PCD patients [248,267]. It also has a worst clinical prognosis compared to dynein structural gene mutations[326]. In the case of a *CCDC40* mutation, the findings are microtubular disarrangements, acentric location of the CP and absence of the IDA due to disruption on the “nexin-dynein regulatory complex” (N-DRC). In parallel, *Ccdc40*$^{-/-}$ zebrafish mutants show ultrastructural defects comparable to those found in human PCD patients with mutations in the same region of the *CCDC40* gene. These homozygous zebrafish mutants have a very severe phenotype (curly down tail phenotype, *situs inversus* in 50% of the cases [324], lethargy and cardiac oedema [417] and are only viable until approximately 7-dpf. Detailed IDA assessment is vital to make a correct analysis of the *Ccdc40* $^{-/-}$ zebrafish mutants and *CCDC40* patient samples. Cross-sections need to be analysed and, the thickness of these cross-sections is very much essential to assess the IDA morphology.

IDA morphology is heterogeneous in composition, including several dynein heavy chains (DHC) and light and intermediate chains, in an elaborate organisation that repeats every 96 nm. Differently, ODA has a more homogeneous and frequent distribution along the axoneme [129,418]. Therefore, thick sections (≥100 nm), adequate microscope voltage (by applying a high-voltage driving force, electrons

will penetrate through tissue sections), and high signal to noise ratio (meaning more signal than noise, leading to a more accurate assessment) needs to be secure to correctly assess IDAs, due to its heterogeneous morphology. Failure in this can potentially lead the observer to conclude IDAs are absent, leading to a false assessment [129,419,420].

Fortunately, to extract more detail and information from the samples, more sophisticated techniques in EM are available, including dual-axis ET of plastic section to better assess components in the cilium of both LRO and OP in zebrafish. The procedure involves tilting a thick target section and acquiring images at angles of 1-degree increments (tilt range ± 60 degrees) and using these to reconstruct a 3D image [421]. Using ET, we were able to show that the MTD ODA from the LRO resembles the structure of the MTD ODA of the cilia found in the human respiratory epithelium. Through ET was possible to verify a previously hypothesised variation in the LRO cilia, 1) the unequivocal presence of dynein motors proteins (IDA and ODA) in all cilia analysed, suggesting their ability to generate movement, and 2) the apparent heterogenic distribution of the CP throughout the LRO cilia that suggests cilia inside the LRO might be organised in a specialised fashion, which would explain some observed beating patterns [42 194]. This feature might be perhaps linked to their location in the vesicle, but more evidence is needed to advocate for regional differences containing or not a viable central pair. Another hypothesis is that the position of the CP in the axoneme might be partial in a specific area of the axoneme. Due to technological limitations, this was not possible to confirm; however, serial analysis of the LRO and its cilia is recommended. Large volume EM would allow a better understanding of the distribution of the cilia within the LRO and map the heterogenic ciliary ultrastructure inside the vesicle. We attempted SBFSEM [422] (serial-block face SEM) in a selection of well orientated LROs. SBFSEM is a technology that combines ultramicrotomy and scanning electron microscopy, allowing images to be taken in between thousands of thin sections (~30nm) of a specific region automatically. This sequential image acquisition permits a 3D reconstruction of all the images acquired in the depth of the sample [422]. In our sample, the acquisition was unstable due to charging caused by bare resin and a hollow vesicle (*in vivo* would be containing fluid). We stress the need to perform Volume EM in the LRO to better describe the morphologic profile of the cilia inside. For future experiments, Array Tomography would be a more appropriate technique [423] (another Volume EM technique) to resolve the caveats encountered in SBFSEM.

Zebrafish motile cilia resemble the cilia found in the human airway and are accessible for manipulation and analysis. Furthermore, the zebrafish is a suitable model to test the effect of many PCD mutations since it has its whole genome sequenced and human PCD homologue genes identified. Genetic engineering unlocks the potential to understand disease phenotypes and gene interactions, and in that field, zebrafish already revealed to be a valuable tool [243,247,250]. Lastly, Electron Microscopy still represents the primary gold standard technique to analyse the ultrastructure of cilia, and more new and sophisticated techniques will shed light on the ultrastructural details still to unravel. In summary, this work provides strong evidence that zebrafish is a good animal model to study PCD.

6

CHAPTER 6

Discussion and Conclusion

DISCUSSION

The primary purpose of this research study was to improve the diagnosis of PCD. This involves either using the data collected from PCD patients or model organisms like zebrafish (*Danio rerio*) to better understand cilia and ciliopathies [8]. it is possible to manipulate the genome of these organisms and observe and study the effects of a single mutation and assess the phenotype caused in later stages of development.

TEM is a complex analysis tool [424]. However, it is still a critical diagnostic test for PCD [425]. Throughout the assessment of >50 ciliary cross-sections, it is possible to verify the presence, absence, or consequences of the absence of many of the proteins involved in cilia biogenesis and function. TEM sample preparation and data analysis can be done using different workflows, often leading to the same results. However, despite some PCD reference centres recommending TEM as one of a combination of tests to confirm the diagnosis of PCD, there were still concerns on how to designate a defect or a standardised way to report the results, or even which terminology to use.

A crucial work published in 2020 that involved a group of experts from 18 different PCD centres determined a TEM analysis guideline, which includes diagnostic findings being separated into two classes of defects. Patients with a clinical history of symptoms should have at least 50 cross-sections of the ciliary axoneme assessed between several different cells, and the analysis should be done in both proximal and more distal regions of the axoneme. Class 1 defects diagnose PCD, as these have 'hallmark' defects, namely isolated outer dynein arm (ODA) defect, combined ODA and inner dynein arm (IDA) defect, and microtubular disorganisation with IDA defect. Class 2 defects follow the same assessment but need further confirmation with further diagnostic testing. Defects classified as class 2 involve the central pair (CP) abnormalities; mislocalisation of the basal bodies with few or no cilia; microtubular disorganisation with IDA present; ODA absent from 25-50% of cross-sections, and ODA and IDA absent from 25-50% of cross-sections [286].

Additionally, to segregating defects into two classes, the work by Shoemark et al. [286] describes features that should be included in a TEM report to assist multidisciplinary diagnosis of PCD and ways to determine the adequacy of the sample. This study provided the first-ever guideline for the diagnosis of PCD by TEM, which can be used to standardise diagnosis internationally [286].

I was involved in the study mentioned above [286] and the development of the consensus since the meeting at the BEAT-PCD training school and conference in 2017, as well as being involved in TEM sample assessment, classification and reviewing of the manuscript. I was involved in implementing these guidelines in Lisbon/Oporto PCD service and at the PCD reference centre in the Royal Brompton Hospital. I was responsible for sharing the consensus guidelines information and displaying it on the BEAT-PCD website.

As a consequence of the TEM consensus for diagnosis of PCD, as part of the Royal Brompton Hospital PCD research group, I was involved in the development of software to assist in cilia counting and classification, described in detail in Chapter 4. This tool makes it easier to bracket defects found in isolated cilia, which can be distinguished in class 1 or 2 defects based on the percentage of a defect. The Advance Counter for PCD diagnosis is a tool that replaces previous manual counters and handwritten report dictated into a patient electronic record system. Paper notes containing patients scores and diagnostic notes are considered time-consuming and a patient information confidential risk. This counter not only speeds up the collection of results but automatically generates a spreadsheet that can be uploaded to the patient record page. We hope, in the future, the advanced counter tool can be integrated with a machine learning system for the complete automation of the assessment of PCD defects. To validate this advanced counter compared to previous methods, we tested the advanced counter by retrieving paper records of the diagnostic cilia feature counts and sample quality assessment from 48 patients, gathered from three independent evaluations. The paper notes were compared to the values and information generated in the excel spreadsheets by the advanced counter and, all the information was found to match. The creation and implementation of this software counts as an improvement in result delivery and standardisation and further automation reducing diagnosis/reporting turnaround time [276].

The assessment of cilia ultrastructure requires good quality cross and longitudinal sections of cilia. This can be only achieved if samples are treated and handled the best way possible, always considering the final goal. For the analysis of PCD, the observation and detailed analysis of all the identifiable components of the axoneme is essential for a successful diagnosis (IDA and ODA, radial-spoke (RS) and CP). Preservation of the sample is an essential step in sample preparation but, at the endpoint, sample contrast is a significant feature while analysing cilia under the electron microscope. A good contrast (high signal to noise ratio) is essential for imaging. This contrast is achieved through heavy metal stains that can be added en block during the embedding protocol or onto a grid to stain ultra-thin sections. The most common staining used in TEM is uranyl acetate (UA) [372], which is sometimes used in combination with Reynolds's lead citrate. UA has given excellent results throughout the years and is widely used [372]. However, it is radioactive that has led to concerns around safety and its potential use in terrorism [426]. These concerns have forced institutions to regulate the use, handling and storage of UA, and its commercialisation is subject to many restrictions, including when it is shipped overseas. Motivated by this, many alternatives to UA surged in the last years, namely Oolong tea extract, hafnium chloride, platinum blue, UranyLess from EMS, and more recently, Neodymium, UAR from EMS and UA-zero from Agar Scientific [373–376,427,428]. We decided to test only UAR and UZ-zero against UA to determine their suitability for the diagnosis of PCD by TEM. It Is described in detail in chapter 3 how the stains were applied either after fixation (en bloc) during sample preparation or on ultrathin sections on the embedded sample (en grid). Our goal was to find a stain equivalent to UA that provided good sample contrast. UA-zero proved to be a suitable non-radioactive replacement when assessing subtle structures like dynein arms and showed excellent results when used en bloc and

combined with en grid post staining. This has allowed us to identify a safer alternative for assessing ciliary components that will lead to a reliable diagnosis of PCD by TEM.

It is widely discussed and generally agreed that TEM is a demanding, not standardised technique. There are still some variations in protocols and image analysis, which is why there is so much combined effort to write guidelines and find standardisation methods. Comparison of material and constant interinstitutional auditing is commonly used to validate results, the quality of the sample and sample preparation. During a PCD sample assessment, TEM can be challenging when a partial or subtle defect is present. Subtle defects identification is important mainly because PCD is a disease in which more than 40 genes have been identified [94]. It is known that around 25% of the defects caused by mutations in PCD genes [5,424] do not show detectable abnormalities in TEM. Specific genetic mutations causing PCD are known to cause partial or sporadic loss of a ciliary structure, such as the case of *DNAH9* and *DNAH11* gene mutations, that leads to defects in a restrictive region of the axoneme [285,364]. These abnormalities are difficult to detect using conventional TEM, and the patients end up having multiple nasal brushings [364]. This stresses the need for better tools to analyse cilia in detail. To improve the diagnosis of PCD using TEM, we created software to enhance ciliary features assessed by averaging and classifying TEM image data. We develop a package of programs, the PCD detect, that permits selecting and averaging ciliary features from TEM images. Through PCD detect, it is possible to enhance the signal allowing a better assessment of ciliary structures critical for motility. We tested our toolkit using several known cases with known genetic results. We chose mutations in genes that result in subtle phenotypes hard to report in a conventional TEM assessment to test our system. Testing several known cases with genetic mutation classified as subtle and difficult to assess by conventional TEM, we believe we have developed an easy-to-use tool that can help associate a specific genetic mutation with an ultrastructural phenotype. The creation of this PCD detect software contributes to the diagnosis of PCD by TEM by hopefully reducing the number of false-negative undiagnosed cases with apparently normal TEM.

To better understand how genetic mutations affect the ultrastructure of cilia and flagella, animal models such as *Chlamydomonas reinhardtii* and *C. elegans* have been widely used to study the complex genetic basis of ciliopathies. However, vertebrate models like zebrafish can be seen as more advantageous because, similarly to a human, their development involves the organogenesis of complex systems, in which motile and immotile cilia play an essential role [8]. We have been able to do a complete characterisation of zebrafish cilia in the OP, the anterior structure in the zebrafish head confided between the eyes, and in the LRO, embryonic structure homologous to the embryonic node in the mouse. The 9+2 cilia observed in the OP multiciliated cells shows similarities to the respiratory cilia in humans, saving some unique characteristics of normal cilia in both locations. Both cilia from the OP and the LRO show a heterogeneous ultrastructural pattern. Cilia in more internal regions of the WT OP lack dynein arms compared to what is found in the pit periphery, where cilia have dynein arms. In the LRO, two main types of cilia were identified, containing a central complex (two central MT) or showing absence of one or both MT in the CP complex.

It is also known that homologous PCD genes in zebrafish, when mutated, show a disease phenotype, and in some cases, similar to human patients of PCD, heterotaxy disorders. Furthermore, the similarity between human cilia and zebrafish cilia makes zebrafish a suitable animal model to study ciliopathies like PCD. Zebrafish are also easy to maintain and has fast external development.

This work aimed to improve the diagnosis of PCD by TEM and support zebrafish as a good vertebrate model of PCD. It was hypothesised that zebrafish motile cilia share ultrastructural features with human airway motile cilia, and we were able to confirm this. The variations specific to the zebrafish, namely the absence of dynein motor proteins in a specific conserved region of the OP, and the presence and absence of MT in the CP of the monocilia in the LRO, were described in detail. This research agrees in part with what was described previously by Reiten et al. [227]. Regarding a heterogenic beating pattern in the OP that would correlate with our ultrastructure analysis of zebrafish motile cilia. Furthermore, the ultrastructural characterisation of the OP fits with results previously described by Hansen in 1998 and 2005 regarding a type of ciliated sensory neurons (olfactory sensory neurons) that protrude tufts of sensory cilia, 9+2 configuration, but immotile kinetic profile. These ciliated sensory cells were described to locate in the centre of the pit. However, these studies were conducted in adult zebrafish and had no TEM characterisation of the cilia ultrastructure within the different cilia distributions [215].

Previous work referred to zebrafish as a good model of PCD in their studies of the effects of PCD genes mutations in zebrafish cilia and early development [4,229,246]. Adding to this, published and unpublished data from Rasteiro (2017) from Lopes lab shows that CRISPR-cas9 mutation in the *Ccdc40* gene in zebrafish produces ciliary defects comparable to those found in humans. Furthermore, homozygous animals show physical signs of disease and have a poor prognosis [250].

It would be ideal for future work to access more specialised equipment to further assess cilia in zebrafish and human airway. For this work, we attempted to use SBFSEM, but due to the characteristics of the LRO in a WT zebrafish, this generated no results, and unfortunately, we had no other available option to do volume EM of the zebrafish LRO. Complex techniques can be used to analyse the axoneme of the zebrafish motile cilium in more considerable detail. Through serial sectioning and high throughput methods of image acquisition (either with array tomography or manual serial sectioning) could be possible to assess the contents of the LRO, the ultrastructure of the embryonic cilia and the way they are organised inside the organ, and subsequentially how this organisation relates to the generation of flow. Furthermore, with Cryo-ET, for instance, it is possible to confirm at a molecular structural level the similarity between human airway cilia and zebrafish motile cilia.,

PCD is a multisystemic genetic disease that affects the motility of cilia [160]. Depending on the mutated gene and the mutation, PCD translates into a spectrum of ciliary structure and function phenotypes and patient symptoms. This makes PCD hard to diagnose using only a single technique. The workflow to make a diagnosis of PCD involves several techniques and several specialists in many areas: GPs, specialist doctors, geneticists, clinical scientists, laboratory technicians, physiotherapists, and physiologists. TEM is still at the forefront of PCD diagnosis, despite being a time-consuming

technique that requires a highly specialised scientist [5,340]. The latest ERS Taskforce guideline (2017) determines that TEM is a highly specific test to confirm the diagnosis of PCD and play an important key role in the diagnostic workflow and should always be performed when PCD is suspected. Nevertheless, it states that further investigation should be made in patients with normal ultrastructure (HSVM, IF) since around 25% of patients with normal ultrastructure have a genetic mutation in a PCD gene. Patients with 'hallmark' ciliary ultrastructural defects (since 2020 classified as class 1 defects according to the TEM PCD assessment guideline) do not need any other confirmation method [425].

CONCLUSION

TEM is not expected to become obsolete in the diagnostic of PCD, so better practices are essential to maintain high-quality sample assessment and reporting. Throughout this work, new tools and protocol optimisation were undertaken to improve the quality of the diagnosis of PCD using TEM. In addition to this, it was reinforced the importance and relevance of zebrafish as an animal model to study PCD. EM analysis, made more user-friendly, reproducible and efficient, in diagnosis and research are priorities that I will continue to work to improve

BIBLIOGRAPHY

1. Praveen, K., Davis, E. E. & Katsanis, N. Unique among ciliopathies: Primary ciliary dyskinesia, a motile cilia disorder. *F1000Prime Rep.* **7**, (2015).

2. Vincensini, L., Blisnick, T. & Bastin, P. 1001 Model Organisms To Study Cilia and Flagella. *Biol. Cell* **103**, 109–130 (2011).

3. Ishikawa, T. Axoneme structure from motile cilia. *Cold Spring Harb. Perspect. Biol.* **9**, (2017).

4. Austin-Tse, C. *et al.* Zebrafish ciliopathy screen plus human mutational analysis identifies C21orf59 and CCDC65 defects as causing primary ciliary dyskinesia. *Am. J. Hum. Genet.* **93**, 672–686 (2013).

5. Bhatt, R. & Hogg, C. Primary ciliary Dyskinesia: A major player in a bigger game. *Breathe* **16**, 1–12 (2020).

6. Goetz, S. C. & Anderson, K. V. The primary cilium: A signalling centre during vertebrate development. *Nature Reviews Genetics* vol. 11 331–344 (2010).

7. Ishikawa, T., Ueno, H., Omori, T. & Kikuchi, K. Cilia and centrosomes: Ultrastructural and mechanical perspectives. *Seminars in Cell and Developmental Biology* vol. 110 61–69 (2021).

8. Song, Z., Zhang, X., Jia, S., Yelick, P. C. & Zhao, C. Zebrafish as a Model for Human Ciliopathies. *J. Genet. Genomics* **43**, 107–120 (2016).

9. Quarmby, L. M. & Parker, J. D. K. Cilia and the cell cycle? *Journal of Cell Biology* vol. 169 707–710 (2005).

10. Lodish, H. *et al.* Cilia and Flagella: Structure and Movement. (2000).

11. Caspary, T., Larkins, C. E. & Anderson, K. V. The Graded Response to Sonic Hedgehog Depends on Cilia Architecture. *Dev. Cell* **12**, 767–778 (2007).

12. Porter, K. R. The submicroscopic morphology of protoplasm. 1956. *Anat. Rec. A. Discov. Mol. Cell. Evol. Biol.* **287**, 1186–1204 (2005).

13. Choksi, S. P., Lauter, G., Swoboda, P. & Roy, S. Switching on cilia: Transcriptional networks regulating ciliogenesis. *Development (Cambridge)* vol. 141 1427–1441 (2014).

14. Kozminski, K. G., Johnson, K. A., Forscher, P. & Rosenbaum, J. L. A motility in the eukaryotic flagellum unrelated to flagellar beating. *Proc. Natl. Acad. Sci. U. S. A.* **90**, 5519–5523 (1993).

15. Nicastro, D. *et al.* The molecular architecture of axonemes revealed by cryoelectron tomography. *Science (80-.).* **313**, 944–948 (2006).

16. Nicastro, D. Cryo-electron microscope tomography to study axonemal organization. *Methods Cell Biol.* **91**, 1–39 (2009).

17. Nicastro, D. *et al.* Cryo-electron tomography reveals conserved features of doublet microtubules in flagella. *Proc. Natl. Acad. Sci. U. S. A.* **108**, (2011).

18. Bui, K. H., Pigino, G. & Ishikawa, T. Three-dimensional structural analysis of eukaryotic flagella/cilia by electron cryo-tomography. in *Journal of Synchrotron Radiation* vol. 18 2–5 (International Union of Crystallography, 2011).

19. Stepanek, L. & Pigino, G. Microtubule doublets are double-track railways for intraflagellar transport trains. *Science (80-.).* **352**, 721–724 (2016).

20. Jordan, M. A., Diener, D. R., Stepanek, L. & Pigino, G. The cryo-EM structure of intraflagellar transport trains reveals how dynein is inactivated to ensure unidirectional anterograde movement in cilia. *Nature Cell Biology* vol. 20 1250–1255 (2018).

21. Tavares, B. *et al.* Notch/Her12 signalling modulates, motile/immotile cilia ratio downstream of Foxj1a in zebrafish left-right organizer. *Elife* **6**, (2017).

22. Sobkowicz, H. M., Slapnick, S. M. & August, B. K. The kinocilium of auditory hair cells and evidence for its morphogenetic role during the regeneration of stereocilia and cuticular plates. *J. Neurocytol.* **24**, 633–653 (1995).

23. Lidow, M. S. & Menco, B. P. M. Observations on axonemes and membranes of olfactory and respiratory cilia in frogs and rats using tannic acid-supplemented fixation and photographic rotation. *J. Ultrasructure Res.* **86**, 18–30 (1984).

24. Hansen, A. & Zeiske, E. *The Peripheral Olfactory Organ of the Zebrafish, Danio rerio: an Ultrastructural Study*. *Chem. Senses* vol. 23 https://academic.oup.com/chemse/article/23/1/39/360603 (1998).

25. Spassky, N. & Meunier, A. The development and functions of multiciliated epithelia. *Nature Reviews Molecular Cell Biology* vol. 18 423–436 (2017).

26. Steinman, R. M. An electron microscopic study of ciliogenesis in developing epidermis and trachea in the embryo of Xenopus laevis. *Am. J. Anat.* **122**, 19–55 (1968).

27. Kramer-Zucker, A. G. *et al.* Cilia-driven fluid flow in the zebrafish pronephros, brain and Kupffer's vesicle is required for normal organogenesis. *Development* **132**, 1907–1921 (2005).

28. Hagenlocher, C., Walentek, P., Müller, C., Thumberger, T. & Feistel, K. Ciliogenesis and cerebrospinal fluid flow in the developing Xenopus brain are regulated by foxj1. *Cilia* **2**, (2013).

29. Carvalho-Santos, Z. *et al.* BLD10/CEP135 Is a Microtubule-Associated Protein that Controls the Formation of the Flagellum Central Microtubule Pair. *Dev. Cell* **23**, 412–424 (2012).

30. Mitchell, D. R. Evolution of cilia. *Cold Spring Harb. Perspect. Biol.* **9**, (2017).

31. Avidor-Reiss, T. *et al.* Decoding cilia function: Defining specialized genes required for compartmentalized cilia biogenesis. *Cell* **117**, 527–539 (2004).

32. Mitchell, D. R. The evolution of eukaryotic cilia and flagella as motile and sensory organelles. *Advances in Experimental Medicine and Biology* vol. 607 130–140 (2007).

33. Prensier, G., Vivier, E., Goldstein, S. & Schrével, J. Motile flagellum with a '3+0' ultrastructure. *Science (80-.).* **207**, 1493–1494 (1980).

34. Nonaka, S. *et al.* Randomization of left-right asymmetry due to loss of nodal cilia generating leftward flow of extraembryonic fluid in mice lacking KIF3B motor protein. *Cell* **95**, 829–837 (1998).

35. Gibbons, I. R. *Cilia and Flagella of Eukaryotes*. http://rupress.org/jcb/article-pdf/91/3/107s/1075481/107s.pdf.

36. Baccetti, B. Evolutionary trends in sperm structure. *Comparative Biochemistry and Physiology -- Part A: Physiology* vol. 85 29–36 (1986).

37. Silverman, M. A. & Leroux, M. R. Intraflagellar transport and the generation of dynamic, structurally and functionally diverse cilia. *Trends in Cell Biology* vol. 19 306–316 (2009).

38. Takeda, S. & Narita, K. Structure and function of vertebrate cilia, towards a new taxonomy. *Differentiation* **83**, S4–S11 (2012).

39. Nigg, E. A. & Stearns, T. The centrosome cycle: Centriole biogenesis, duplication and inherent asymmetries. *Nature Cell Biology* vol. 13 1154–1160 (2011).

40. Sánchez, I. & Dynlacht, B. D. Cilium assembly and disassembly. *Nature Cell Biology* vol. 18 711–717 (2016).

41. Praetorius, H. A. & Leipziger, J. Primary cilium-dependent sensing of urinary flow and paracrine

purinergic signaling. *Seminars in Cell and Developmental Biology* vol. 24 3–10 (2013).

42. Sampaio, P. *et al.* Article Left-Right Organizer Flow Dynamics: How Much Cilia Activity Reliably Yields Laterality? *Dev. Cell* **29**, 716–728 (2014).

43. Jenkins, P. M., Mcewen, D. P. & Martens, J. R. Olfactory cilia: Linking sensory cilia function and human disease. *Chem. Senses* **34**, 451–464 (2009).

44. Schwander, M., Kachar, B. & Müller, U. The cell biology of hearing. *Journal of Cell Biology* vol. 190 9–20 (2010).

45. Katoh, Y. *et al.* Overall architecture of the intraflagellar transport (IFT)-B complex containing cluap1/IFT38 as an essential component of the IFT-B peripheral subcomplex. *J. Biol. Chem.* **291**, 10962–10975 (2016).

46. Cole, D. G. *et al.* Chlamydomonas kinesin-II-dependent intraflagellar transport (IFT): IFT particles contain proteins required for ciliary assembly in Caenorhabditis elegans sensory neurons. *J. Cell Biol.* **141**, 993–1008 (1998).

47. Pazour, G. J., Dickert, B. L. & Witman, G. B. The DHC1b (DHC2) isoform of cytoplasmic dynein is required for flagellar assembly. *J. Cell Biol.* **144**, 473–481 (1999).

48. Katoh, Y. *et al.* Practical method for targeted disruption of cilia-related genes by using CRISPR/Cas9-mediated, homology-independent knock-in system. *Mol. Biol. Cell* **28**, 898–906 (2017).

49. Eguether, T. *et al.* IFT27 links the bbsome to ift for maintenance of the ciliary signaling compartment. *Dev. Cell* **31**, 279–290 (2014).

50. Funabashi, T. *et al.* Ciliary entry of KIF17 is dependent on its binding to the IFT-B complex via IFT46-IFT56 as well as on its nuclear localization signal. *Mol. Biol. Cell* **28**, 624–633 (2017).

51. Keady, B. T. *et al.* IFT25 Links the Signal-Dependent Movement of Hedgehog Components to Intraflagellar Transport. *Dev. Cell* **22**, 940–951 (2012).

52. Takei, R., Katoh, Y. & Nakayama, K. Robust interaction of IFT70 with IFT52-IFT88 in the IFT-B complex is required for ciliogenesis. (2018) doi:10.1242/bio.033241.

53. Tayeh, M. K. *et al.* Genetic interaction between Bardet-Biedl syndrome genes and implications for limb patterning. *Hum. Mol. Genet.* **17**, 1956–1967 (2008).

54. Lechtreck, K. F. *et al.* The Chlamydomonas reinhardtii BBSome is an IFT cargo required for export of specific signaling proteins from flagella. *J. Cell Biol.* **187**, 1117–1132 (2009).

55. Forsythe, E. & Beales, P. L. Bardet-Biedl syndrome. *Eur. J. Hum. Genet.* **21**, 8–13 (2013).

56. Weihbrecht, K. *et al.* Keeping an Eye on Bardet-Biedl Syndrome: A Comprehensive Review of the Role of Bardet-Biedl Syndrome Genes in the Eye. *Med. Res. Arch.* **5**, (2017).

57. Nachury, M. V. The molecular machines that traffic signaling receptors into and out of cilia. *Current Opinion in Cell Biology* vol. 51 124–131 (2018).

58. Bergmann, C. *et al.* Polycystic kidney disease. *Nature Reviews Disease Primers* vol. 4 50 (2018).

59. Lee, H., Song, J., Jung, J. H. & Ko, H. W. Primary cilia in energy balance signaling and metabolic disorder. *BMB Reports* vol. 48 647–654 (2015).

60. Reiter, J. F. & Leroux, M. R. Genes and molecular pathways underpinning ciliopathies. *Nature Reviews Molecular Cell Biology* vol. 18 533–547 (2017).

61. Marques, S. *et al.* The activity of the Nodal antagonist Cerl-2 in the mouse node is required for correct L/R body axis. *Genes Dev.* **18**, 2342–2347 (2004).

62. Stubbs, J. L., Oishi, I., Izpisúa Belmonte, J. C. & Kintner, C. The forkhead protein Foxj1 specifies node-like cilia in Xenopus and zebrafish embryos. *Nat. Genet.* **40**, 1454–1460 (2008).

63. Tavares, B. & Santos Lopes, S. The importance of Zebrafish in biomedical research. *Acta Med. Port.* **26**, 583–92 (2013).

64. Babu, D. & Roy, S. Left-right asymmetry: cilia stir up new surprises in the node. *Open biology* vol. 3 130052 (2013).

65. Del Bigio, M. R. Ependymal cells: Biology and pathology. *Acta Neuropathologica* vol. 119 55–73 (2010).

66. Satir, P. & Sleigh, M. A. The physiology of cilia and mucociliary interactions. *Annu. Rev. Physiol.* **52**, 137–155 (1990).

67. Bloodgood, R. A. Sensory reception is an attribute of both primary cilia and motile cilia. *Journal of Cell Science* vol. 123 505–509 (2010).

68. Chung, M. I. *et al.* RFX2 is broadly required for ciliogenesis during vertebrate development. *Dev. Biol.* **363**, 155–165 (2012).

69. Yu, X., Ng, C. P., Habacher, H. & Roy, S. Foxj1 transcription factors are master regulators of the motile ciliogenic program. *Nat. Genet.* **40**, 1445–1453 (2008).

70. Bonnafe, E. *et al.* The Transcription Factor RFX3 Directs Nodal Cilium Development and Left-Right Asymmetry Specification. *Mol. Cell. Biol.* **24**, 4417–4427 (2004).

71. Brody, S. L., Yan, X. H., Wuerffel, M. K., Song, S. K. & Shapiro, S. D. Ciliogenesis and left-right axis defects in forkhead factor HFH-4-null mice. *Am. J. Respir. Cell Mol. Biol.* **23**, 45–51 (2000).

72. Chen, J., Knowles, H. J., Hebert, J. L. & Hackett, B. P. Mutation of the mouse hepatocyte nuclear factor/forkhead homologue 4 gene results in an absence of cilia and random left-right asymmetry. *J. Clin. Invest.* **102**, 1077–1082 (1998).

73. Stubbs, J. L., Vladar, E. K., Axelrod, J. D. & Kintner, C. Multicilin promotes centriole assembly and ciliogenesis during multiciliate cell differentiation. *Nat. Cell Biol.* **14**, 140–147 (2012).

74. Alten, L. *et al.* Differential regulation of node formation, nodal ciliogenesis and cilia positioning by Noto and Foxj1. *Development* **139**, 1276–1284 (2012).

75. Bisgrove, B. W., Makova, S., Yost, H. J. & Brueckner, M. RFX2 is essential in the ciliated organ of asymmetry and an RFX2 transgene identifies a population of ciliated cells sufficient for fluid flow. *Dev. Biol.* **363**, 166–178 (2012).

76. Liu, Y., Pathak, N., Kramer-Zucker, A. & Drummond, I. A. Notch signaling controls the differentiation of transporting epithelia and multiciliated cells in the zebrafish pronephros. *Development* **134**, 1111–1122 (2007).

77. Hellman, N. E. *et al.* The zebrafish foxj1a transcription factor regulates cilia function in response to injury and epithelial stretch. *Proc. Natl. Acad. Sci. U. S. A.* **107**, 18499–18504 (2010).

78. Ashique, A. M. *et al.* The Rfx4 transcription factor modulates Shh signaling by regional control of ciliogenesis. *Sci. Signal.* **2**, (2009).

79. Yu, X., Lau, D., Ng, C. P. & Roy, S. Cilia-driven fluid flow as an epigenetic cue for otolith biomineralization on sensory hair cells of the inner ear. *Development* **138**, 487–494 (2011).

80. El Zein, L. *et al.* RFX3 governs growth and beating efficiency of motile cilia in mouse and controls the expression of genes involved in human ciliopathies. *J. Cell Sci.* **122**, 3180–3189 (2009).

81. Cachero, S. *et al.* The gene regulatory cascade linking proneural specification with differentiation in Drosophila sensory neurons. *PLoS Biol.* **9**, (2011).

82. Newton, F. G. *et al.* Forkhead Transcription Factor Fd3F Cooperates with Rfx to Regulate a

Gene Expression Program for Mechanosensory Cilia Specialization. *Dev. Cell* **22**, 1221–1233 (2012).

83. Swoboda, P., Adler, H. T. & Thomas, J. H. The RFX-type transcription factor DAF-19 regulates sensory neuron cilium formation in C. Elegans. *Mol. Cell* **5**, 411–421 (2000).

84. Dubruille, R. *et al.* Drosophila regulatory factor X is necessary for ciliated sensory neuron differentiation. *Development* **129**, 5487–5498 (2002).

85. Didon, L. *et al.* RFX3 Modulation of FOXJ1 regulation of cilia genes in the human airway epithelium. *Respir. Res.* **14**, (2013).

86. Cruz, C. *et al.* Foxj1 regulates floor plate cilia architecture and modifies the response of cells to sonic hedgehog signalling. *Development* **137**, 4271–4282 (2010).

87. Neugebauer, J. M., Amack, J. D., Peterson, A. G., Bisgrove, B. W. & Yost, H. J. FGF signalling during embryo development regulates cilia length in diverse epithelia. *Nature* **458**, 651–654 (2009).

88. Caron, A., Xu, X. & Lin, X. Wnt/β-catenin signaling directly regulates Foxj1 expression and ciliogenesis in zebrafish Kupffer's vesicle. *Development* **139**, 514–524 (2012).

89. Lopes, S. S. *et al.* Notch signalling regulates left-right asymmetry through ciliary length control. *Development* **137**, 3625–3632 (2010).

90. Ma, M. & Jiang, Y. J. Jagged2a-notch signaling mediates cell fate choice in the zebrafish pronephric duct. *PLoS Genet.* **3**, 0133–0145 (2007).

91. Tan, F. E. *et al.* Myb promotes centriole amplification and later steps of the multiciliogenesis program. *Dev.* **140**, 4277–4286 (2013).

92. Boskovski, M. T. *et al.* The heterotaxy gene GALNT11 glycosylates Notch to orchestrate cilia type and laterality. *Nature* **504**, 456–459 (2013).

93. Hashimoto, M. *et al.* Planar polarization of node cells determines the rotational axis of node cilia. *Nat. Cell Biol.* **12**, 170–176 (2010).

94. Legendre, M., Zaragosi, L. E. & Mitchison, H. M. Motile cilia and airway disease. *Semin. Cell Dev. Biol.* (2020) doi:10.1016/j.semcdb.2020.11.007.

95. Yuan, S. *et al.* Motile cilia of the male reproductive system require miR-34/miR-449 for development and function to generate luminal turbulence. *Proc. Natl. Acad. Sci. U. S. A.* **116**, 3584–3593 (2019).

96. SOROKIN, S. P. Reconstructions of Centriole Formation and Ciliogenesis in Mammalian Lungs. *J. Cell Sci.* **3**, (1968).

97. Anderson, R. G. W. & Brenner, R. M. The formation of basal bodies (centrioles) in the rhesus monkey oviduct. *J. Cell Biol.* **50**, 10–34 (1971).

98. Liu, D. *et al.* Efficient Gene Targeting in Zebrafish Mediated by a Zebrafish-Codon-Optimized Cas9 and Evaluation of Off-Targeting Effect. *Journal of Genetics and Genomics* vol. 41 43–46 (2014).

99. Terré, B. *et al.* GEMC 1 is a critical regulator of multiciliated cell differentiation . *EMBO J.* **35**, 942–960 (2016).

100. Kyrousi, C. *et al.* Mcidas and gemc1 are key regulators for the generation of multiciliated ependymal cells in the adult neurogenic niche. *Dev.* **142**, 3661–3674 (2015).

101. Arbi, M. *et al.* GemC1 controls multiciliogenesis in the airway epithelium. *EMBO Rep.* **17**, 400–413 (2016).

102. Zhou, F. *et al.* Gmnc Is a Master Regulator of the Multiciliated Cell Differentiation Program. *Curr.*

Biol. **25**, 3267–3273 (2015).

103. Lu, H. *et al.* Mcidas mutant mice reveal a two-step process for the specification and differentiation of multiciliated cells in mammals. *Dev.* **146**, (2019).

104. Lewis, M. & Stracker, T. H. Transcriptional regulation of multiciliated cell differentiation. *Seminars in Cell and Developmental Biology* vol. 110 51–60 (2021).

105. Cilia, flagella, and centrioles | Celebrate Cytochemistry | Gwen V. Childs, Ph.D. http://cytochemistry.net/cell-biology/cilia.htm.

106. Rao, V. G. & Kulkarni, S. S. Xenopus to the rescue: A model to validate and characterize candidate ciliopathy genes . *genesis* **59**, e23414 (2021).

107. Kobayashi, T. & Dynlacht, B. D. Regulating the transition from centriole to basal body. *Journal of Cell Biology* vol. 193 435–444 (2011).

108. Shakya, S. & Westlake, C. J. Recent advances in understanding assembly of the primary cilium membrane. *Fac. Rev.* **10**, (2021).

109. Jana, S. C., Mendonça, S., Werner, S. & Bettencourt-Dias, M. Methods to study centrosomes and cilia in drosophila. in *Methods in Molecular Biology* vol. 1454 215–236 (Humana Press Inc., 2016).

110. Izawa, I., Goto, H., Kasahara, K. & Inagaki, M. Current topics of functional links between primary cilia and cell cycle. *Cilia* vol. 4 12 (2015).

111. Jana, S. C. *et al.* Differential regulation of transition zone and centriole proteins contributes to ciliary base diversity. *Nat. Cell Biol.* **20**, 928–941 (2018).

112. Reiter, J. F., Blacque, O. E. & Leroux, M. R. The base of the cilium: Roles for transition fibres and the transition zone in ciliary formation, maintenance and compartmentalization. *EMBO Reports* vol. 13 608–618 (2012).

113. Bayless, B. A., Giddings, T. H., Winey, M. & Pearson, C. G. Bld10/Cep135 stabilizes basal bodies to resist cilia-generated forces. *Mol. Biol. Cell* **23**, 4820–4832 (2012).

114. Garcia-Gonzalo, F. R. *et al.* A transition zone complex regulates mammalian ciliogenesis and ciliary membrane composition. *Nat. Genet.* **43**, 776–784 (2011).

115. Cavalier-Smith, T. Basal body and flagellar development during the vegetative cell cycle and the sexual cycle of Chlamydomonas reinhardii. *J. Cell Sci.* **16**, 529–556 (1974).

116. Li, S., Fernandez, J. J., Marshall, W. F. & Agard, D. A. Three-dimensional structure of basal body triplet revealed by electron cryo-tomography. *EMBO J.* **31**, 552–562 (2012).

117. O'Toole, E. T., Giddings, T. H., McIntosh, J. R. & Dutcher, S. K. Three-dimensional organization of basal bodies from wild-type and δ-tubulin deletion strains of Chlamydomonas reinhardtii. *Mol. Biol. Cell* **14**, 2999–3012 (2003).

118. Geimer, S. & Melkonian, M. The ultrastructure of the Chlamydomonas reinhardtii basal apparatus: Identification of an early marker of radial asymmetry inherent in the basal body. *J. Cell Sci.* **117**, 2663–2674 (2004).

119. Rasi, M. Q., Parker, J. D. K., Feldman, J. L., Marshall, W. F. & Quarmby, L. M. Katanin knockdown supports a role for microtubule severing in release of basal bodies before mitosis in Chlamydomonas. *Mol. Biol. Cell* **20**, 379–388 (2009).

120. Nakazawa, Y., Hiraki, M., Kamiya, R. & Hirono, M. SAS-6 is a Cartwheel Protein that Establishes the 9-Fold Symmetry of the Centriole. *Curr. Biol.* **17**, 2169–2174 (2007).

121. Linck, R. W. & Stephens, R. E. Functional protofilament numbering of ciliary, flagellar, and centriolar microtubules. *Cell Motility and the Cytoskeleton* vol. 64 489–495 (2007).

122. Keller, L. C., Romijn, E. P., Zamora, I., Yates, J. R. & Marshall, W. F. Proteomic analysis of isolated Chlamydomonas centrioles reveals orthologs of ciliary-disease genes. *Curr. Biol.* **15**, 1090–1098 (2005).

123. Sui, H. & Downing, K. H. Molecular architecture of axonemal microtubule doublets revealed by cryo-electron tomography. *Nature* **442**, 475–478 (2006).

124. Movassagh, T., Bui, K. H., Sakakibara, H., Oiwa, K. & Ishikawa, T. Nucleotide-induced global conformational changes of flagellar dynein arms revealed by in situ analysis. *Nat. Struct. Mol. Biol.* **17**, 761–767 (2010).

125. Chrétien, D. & Wade, R. H. New data on the microtubule surface lattice. *Biol. Cell* **71**, 161–174 (1991).

126. Sakato, M. & King, S. M. Design and regulation of the AAA+ microtubule motor dynein. in *Journal of Structural Biology* vol. 146 58–71 (J Struct Biol, 2004).

127. Goodenough, U. W. Cilia, flagella and the basal apparatus. *Curr. Opin. Cell Biol.* **1**, 58–62 (1989).

128. Neuwald, A. F. The hexamerization domain of N-ethylmaleimide-sensitive factor: Structural clues to chaperone function. *Structure* vol. 7 (1999).

129. Porter, M. E. Axonemal dyneins: Assembly, organization, and regulation. *Curr. Opin. Cell Biol.* **8**, 10–17 (1996).

130. Smith, E. F. & Yang, P. The Radial Spokes and Central Apparatus: Mechano-Chemical Transducers That Regulate Flagellar Motility. *Cell Motility and the Cytoskeleton* vol. 57 8–17 (2004).

131. Koutoulis, A. *et al.* The Chlamydomonas reinhardtii ODA3 gene encodes a protein of the outer dynein arm docking complex. *J. Cell Biol.* **137**, 1069–1080 (1997).

132. Kamiya, R. Functional diversity of axonemal dyneins as studied in Chlamydomonas mutants. *Int. Rev. Cytol.* **219**, 115–155 (2002).

133. Osinka, A. *et al.* Ciliary Proteins: Filling the Gaps. Recent Advances in Deciphering the Protein Composition of Motile Ciliary Complexes. *Cells* **8**, 730 (2019).

134. Mastronarde, D. N., O'Toole, E. T., McDonald, K. L., McIntosh, J. R. & Porter, M. E. Arrangement of inner dynein arms in wild-type and mutant flagella of Chlamydomonas. *J. Cell Biol.* **118**, 1145–1162 (1992).

135. Gardner, L. C., O'Toole, E., Perrone, C. A., Giddings, T. & Porter, M. E. Components of a 'dynein regulatory complex' are located at the junction between the radial spokes and the dynein arms in Chlamydomonas flagella. *J. Cell Biol.* **127**, 1311–1325 (1994).

136. Ueno, H. *et al.* Mouse respiratory cilia with the asymmetric axonemal structure on sparsely distributed ciliary cells can generate overall directional flow. *Nanomedicine Nanotechnology, Biol. Med.* **8**, 1081–1087 (2012).

137. Witman, G. B., Plummer, J. & Sander, G. Chlamydomonas flagellar mutants lacking radial spokes and central tubules. Structure, composition, and function of specific axonemal components. *J. Cell Biol.* **76**, 729–747 (1978).

138. Woolley, D. M. Studies on the eel sperm flagellum. I. The structure of the inner dynein arm complex. *J. Cell Sci.* **110**, 85–94 (1997).

139. Lindemann, C. B., Macauley, L. J. & Lesich, K. A. The counterbend phenomenon in dynein-disabled rat sperm flagella and what it reveals about the interdoublet elasticity. *Biophys. J.* **89**, 1165–1174 (2005).

140. Song, K. *et al.* In situ localization of N and C termini of subunits of the flagellar nexin-dynein regulatory complex (N-DRC) using SNAP tag and cryo-electron tomography. *J. Biol. Chem.* **290**,

5341–5353 (2015).

141. Smith, E. F. & Lefebvre, P. A. The role of central apparatus components in flagellar motility and microtubule assembly. *Cell Motility and the Cytoskeleton* vol. 38 1–8 (1997).

142. Oda, T., Yanagisawa, H., Yagi, T. & Kikkawa, M. Mechanosignaling between central apparatus and radial spokes controls axonemal dynein activity. *J. Cell Biol.* **204**, 807–819 (2014).

143. Pigino, G. & Ishikawa, T. Axonemal radial spokes. *Bioarchitecture* **2**, 50–58 (2012).

144. Yoke, H. *et al.* Rsph4a is essential for the triplet radial spoke head assembly of the mouse motile cilia. *PLoS Genet.* **16**, (2020).

145. Ringo, D. L. Flagellar motion and fine structure of the flagellar apparatus in Chlamydomonas. *J. Cell Biol.* **33**, 543–571 (1967).

146. Dentler, W. L. & Rosenbaum, J. L. Flagellar elongation and shortening in chlamydomonas. III. Structures attached to the tips of flagellar microtubules and their relationship to the directionality of flagellar microtubule assembly. *J. Cell Biol.* **74**, 747–759 (1977).

147. Dentler, W. L. Attachment of the cap to the central microtubules of Tetrahymena cilia. *J. Cell Sci.* **66**, 167–173 (1984).

148. Rosenbaum, J. L. & Carlson, K. Cilia regeneration in Tetrahymena and its inhibition by colchicine. *J. Cell Biol.* **40**, 415–425 (1969).

149. Sale, W. S. The axonemal axis and Ca2+-induced asymmetry of active microtubule sliding in sea urchin sperm tails. *J. Cell Biol.* **102**, 2042–2052 (1986).

150. Omoto, C. K. & Kung, C. Rotation and twist of the central-pair microtubules in the cilia of paramecium. *J. Cell Biol.* **87**, 33–46 (1980).

151. Mitchell, D. R. Orientation of the central pair complex during flagellar bend formation in Chlamydomonas. *Cell Motil. Cytoskeleton* **56**, 120–129 (2003).

152. Carbajal-González, B. I. *et al.* Conserved structural motifs in the central pair complex of eukaryotic flagella. *Cytoskeleton* **70**, 101–120 (2013).

153. Mitchell, D. R. Reconstruction of the projection periodicity and surface architecture of the flagellar central pair complex. *Cell Motil. Cytoskeleton* **55**, 188–199 (2003).

154. Loreng, T. D. & Smith, E. F. The central apparatus of cilia and eukaryotic flagella. *Cold Spring Harb. Perspect. Biol.* **9**, (2017).

155. Warner, F. D. *CILIARY INTER-MICROTUBULE BRIDGES*. *J. Cell Sci. ao* (1976).

156. Kiesel, P. *et al.* The molecular structure of mammalian primary cilia revealed by cryo-electron tomography. *Nat. Struct. Mol. Biol.* **27**, 1115–1124 (2020).

157. Mitchell, D. R. & Sale, W. S. Characterization of a Chlamydomonas insertional mutant that disrupts flagellar central pair microtubule-associated structures. *J. Cell Biol.* **144**, 293–304 (1999).

158. Mitchison, H. M. & Valente, E. M. Motile and non-motile cilia in human pathology: from function to phenotypes. *J. Pathol.* **241**, 294–309 (2017).

159. Corkins, M. E., Krneta-Stankic, V., Kloc, M. & Miller, R. K. Aquatic models of human ciliary diseases. *Genesis* (2021) doi:10.1002/dvg.23410.

160. Lucas, J. S. *et al.* Diagnosis and management of primary ciliary dyskinesia. *Archives of Disease in Childhood* vol. 99 850–856 (2014).

161. Mall, M. A. Role of cilia, mucus, and airway surface liquid in mucociliary dysfunction: lessons from mouse models. *Journal of aerosol medicine and pulmonary drug delivery* vol. 21 13–24

(2008).

162. Wanner, A., Salathe, M. & O'Riordan, T. G. Mucociliary clearance in the airways. *American Journal of Respiratory and Critical Care Medicine* vol. 154 1868–1902 (1996).

163. Hirst, R. A. *et al.* Culture of Primary Ciliary Dyskinesia Epithelial Cells at Air-Liquid Interface Can Alter Ciliary Phenotype but Remains a Robust and Informative Diagnostic Aid. doi:10.1371/journal.pone.0089675.

164. Oura, S. *et al.* Cfap97d1 is important for flagellar axoneme maintenance and male mouse fertility. *PLoS Genet.* **16**, 1–22 (2020).

165. Shingyoji, C., Murakami, A. & Takahashi, K. Local reactivation of Triton-extracted flagella by iontophoretic application of ATP [30]. *Nature* vol. 265 269–270 (1977).

166. Jana, S. C., Girotra, M. & Ray, K. Heterotrimeric kinesin-II is necessary and sufficient to promote different stepwise assembly of morphologically distinct bipartite cilia in Drosophila antenna. *Mol. Biol. Cell* **22**, 769–781 (2011).

167. Bujakowska, K. M., Liu, Q. & Pierce, E. A. Photoreceptor cilia and retinal ciliopathies. *Cold Spring Harbor Perspectives in Biology* vol. 9 (2017).

168. Yano, J., Valentine, M. & Van Houten, J. Novel Insights into the Development and Function of Cilia Using the Advantages of the Paramecium Cell and Its Many Cilia. *Cells* **4**, 297–314 (2015).

169. Langousis, G. & Hill, K. L. Motility and more: The flagellum of Trypanosoma brucei. *Nature Reviews Microbiology* vol. 12 505–518 (2014).

170. Mukhopadhyay, A. G. & Dey, C. S. Reactivation of flagellar motility in demembranated Leishmania reveals role of cAMP in flagellar wave reversal to ciliary waveform. *Sci. Rep.* **6**, 1–14 (2016).

171. Jana, S. C., Bettencourt-Dias, M., Durand, B. & Megraw, T. L. Drosophila melanogaster as a model for basal body research. *Cilia* vol. 5 22 (2016).

172. Li, H. H., Huang, P., Dong, W., Zhu, Z. Y. & Liu, D. [A brief history of zebrafish research--toward biomedicine]. *Yi chuan = Hereditas / Zhongguo yi chuan xue hui bian ji* vol. 35 410–420 (2013).

173. Rosenthal, N. & Ashburner, M. Taking stock of our models: The function and future of stock centres. *Nat. Rev. Genet.* **3**, 711–717 (2002).

174. Driever, W. *et al.* A genetic screen for mutations affecting embryogenesis in zebrafish. *Development* **123**, 37–46 (1996).

175. Driever, W., Stemple, D., Schier, A. & Solnica-Krezel, L. Zebrafish: genetic tools for studying vertebrate development. *Trends in Genetics* vol. 10 152–159 (1994).

176. TMF - Mouse Husbandry, Breeding and Development. https://web.archive.org/web/20070704035747/http://www.research.uci.edu/tmf/husbandry.htm#guidelines.

177. Ackerman, S. D. & Monk, K. R. The scales and tales of myelination: using zebrafish and mouse to study myelinating glia. *Brain Research* vol. 1641 79–91 (2016).

178. Drummond, I. & Austin-Tse, C. Zebrafish cilia. in *Methods in Enzymology* vol. 525 219–244 (Academic Press Inc., 2013).

179. Rihel, J. & Ghosh, M. Zebrafish. in *Drug Discovery and Evaluation: Pharmacological Assay, Fourth Edition* 4071–4155 (Springer International Publishing, 2015). doi:10.1007/978-3-319-05392-9_135.

180. Jung, H. *et al.* The Ancient Origins of Neural Substrates for Land Walking. *Cell* **172**, 667-682.e15 (2018).

181. Howe, K. *et al.* The zebrafish reference genome sequence and its relationship to the human genome. *Nature* **496**, 498–503 (2013).

182. Lieschke, G. J. & Currie, P. D. Animal models of human disease: Zebrafish swim into view. *Nat. Rev. Genet.* **8**, 353–367 (2007).

183. Nasevicius, A. & Ekker, S. C. Effective targeted gene 'knockdown' in zebrafish. *Nat. Genet.* **26**, 216–220 (2000).

184. Hammerschmidt, M., Blader, P. & Strähle, U. Chapter 7: Strategies to Perturb Zebrafish Development. *Methods Cell Biol.* **59**, 87–115 (1998).

185. Ando, H., Furuta, T., Tsien, R. Y. & Okamoto, H. Photo-mediated gene activation using caged RNA/DNA in zebrafish embryos. *Nat. Genet.* **28**, 317–325 (2001).

186. Jurisch-Yaksi, N. *et al.* Rer1p maintains ciliary length and signaling by regulating γ-secretase activity and Foxj1a levels. *J. Cell Biol.* **200**, 709–720 (2013).

187. Collignon, J., Varlet, I. & Robertson, E. J. Relationship between asymmetric nodal expression and the direction of embryonic turning. *Nature* **381**, 155–158 (1996).

188. Levin, M. & Palmer, A. R. Left-right patterning from the inside out: Widespread evidence for intracellular control. *BioEssays* vol. 29 271–287 (2007).

189. Dasgupta, A. & Amack, J. D. Cilia in vertebrate left - Right patterning. *Philosophical Transactions of the Royal Society B: Biological Sciences* vol. 371 (2016).

190. Essner, J. J., Amack, J. D., Nyholm, M. K., Harris, E. B. & Yost, H. J. Kupffer's vesicle is a ciliated organ of asymmetry in the zebrafish embryo that initiates left-right development of the brain, heart and gut. *Development* **132**, 1247–1260 (2005).

191. Lohr, J. L., Danos, M. C. & Yost, H. J. Left-right asymmetry of a nodal-related gene is regulated by dorsoanterior midline structures during Xenopus development. *Development* **124**, 1465–1472 (1997).

192. Field, S. *et al.* Pkd1l1 establishes left-right asymmetry and physically interacts with Pkd2. *Development* **138**, 1131–1142 (2011).

193. Kamura, K. *et al.* Pkd1l1 complexes with Pkd2 on motile cilia and functions to establish the left-right axis. *Development* **138**, 1121–1129 (2011).

194. Roxo-Rosa, M. & Santos Lopes, S. The Zebrafish Kupffer's Vesicle: A Special Organ in a Model Organism to Study Human Diseases. in *Zebrafish in Biomedical Research* (IntechOpen, 2020). doi:10.5772/intechopen.88266.

195. Nakamura, T. *et al.* Fluid flow and interlinked feedback loops establish left-right asymmetric decay of Cerl2 mRNA. *Nat. Commun.* **3**, (2012).

196. Nonaka, S., Shiratori, H., Saijoh, Y. & Hamada, H. Determination of left-right patterning of the mouse embryo by artificial nodal flow. *Nature* **418**, 96–99 (2002).

197. Tsukui, T. *et al.* Multiple left-right asymmetry defects in Shh-/- mutant mice unveil a convergence of the Shh and retinoic acid pathways in the control of Lefty-1. *Proc. Natl. Acad. Sci. U. S. A.* **96**, 11376–11381 (1999).

198. Hamada, H. Molecular Mechanisms of Left-Right Development. in *Heart Development and Regeneration* 297–306 (Elsevier Inc., 2010). doi:10.1016/B978-0-12-381332-9.00014-1.

199. Lowe, L. A. *et al.* Conserved left-right asymmetry of nodal expression and alterations in murine situs inversus. *Nature* **381**, 158–161 (1996).

200. McGrath, J., Somlo, S., Makova, S., Tian, X. & Brueckner, M. Two populations of node monocilia initiate left-right asymmetry in the mouse. *Cell* **114**, 61–73 (2003).

201. Okada, Y. *et al.* Abnormal nodal flow precedes situs inversus in iv and inv mice. *Mol. Cell* **4**, 459–468 (1999).

202. Tabin, C. J. & Vogan, K. J. A two-cilia model for vertebrate left-right axis specification. *Genes and Development* vol. 17 1–6 (2003).

203. Pazour, G. J., San Agustin, J. T., Follit, J. A., Rosenbaum, J. L. & Witman, G. B. Polycystin-2 localizes to kidney cilia and the ciliary level is elevated in orpk mice with polycystic kidney disease. *Current Biology* vol. 12 R378–R380 (2002).

204. Yuan, S., Zhao, L., Brueckner, M. & Sun, Z. Intraciliary calcium oscillations initiate vertebrate left-right asymmetry. *Curr. Biol.* **25**, 556–567 (2015).

205. Pennekamp, P., Menchen, T., Dworniczak, B. & Hamada, H. Situs inversus and ciliary abnormalities: 20 years later, what is the connection? *Cilia* vol. 4 (2015).

206. Schottenfeld, J., Sullivan-Brown, J. & Burdine, R. D. Zebrafish curly up encodes a Pkd2 ortholog that restricts left-side-specific expression of southpaw. *Development* **134**, 1605–1615 (2007).

207. Jacinto, R., Sampaio, P., Roxo-Rosa, M., Pestana, S. & Lopes, S. S. Pkd2 Affects Cilia Length and Impacts LR Flow Dynamics and Dand5. *Front. Cell Dev. Biol.* **9**, 756 (2021).

208. Roxo-Rosa, M., Jacinto, R., Sampaio, P. & Lopes, S. S. The zebrafish Kupffer's vesicle as a model system for the molecular mechanisms by which the lack of Polycystin-2 leads to stimulation of CFTR. *Biol. Open* **4**, 1356–1366 (2015).

209. Ahrens, K. & Schlosser, G. Tissues and signals involved in the induction of placodal Six1 expression in Xenopus laevis. *Dev. Biol.* **288**, 40–59 (2005).

210. Schlosser, G. Making Senses. Development of Vertebrate Cranial Placodes. in *International Review of Cell and Molecular Biology* vol. 283 129–234 (Elsevier Inc., 2010).

211. Sjödal, M., Edlund, T. & Gunhaga, L. Time of Exposure to BMP Signals Plays a Key Role in the Specification of the Olfactory and Lens Placodes Ex Vivo. *Dev. Cell* **13**, 141–149 (2007).

212. Maier, E. C., Saxena, A., Alsina, B., Bronner, M. E. & Whitfield, T. T. Sensational placodes: Neurogenesis in the otic and olfactory systems. *Dev. Biol.* **389**, 50–67 (2014).

213. Cheung, K. Y. *et al.* Olfactory Rod Cells: A Rare Cell Type in the Larval Zebrafish Olfactory Epithelium With a Large Actin-Rich Apical Projection. *Front. Physiol.* **12**, (2021).

214. Axel, R. The molecular logic of smell. *Scientific American* vol. 273 154–159 (1995).

215. Hansen, A. & Zielinski, B. S. Diversity in the olfactory epithelium of bony fishes: Development, lamellar arrangement, sensory neuron cell types and transduction components. *J. Neurocytol.* **34**, 183–208 (2005).

216. Sato, Y., Miyasaka, N. & Yoshihara, Y. Mutually exclusive glomerular innervation by two distinct types of olfactory sensory neurons revealed in transgenic zebrafish. *J. Neurosci.* **25**, 4889–4897 (2005).

217. Parisi, V. *et al.* Immunohistochemical characterization of the crypt neurons in the olfactory epithelium of adult zebrafish. *Ann. Anat.* **196**, 178–182 (2014).

218. Biechl, D., Tietje, K., Gerlach, G. & Wullimann, M. F. Crypt cells are involved in kin recognition in larval zebrafish. *Sci. Rep.* **6**, (2016).

219. Bettini, S., Milani, L., Lazzari, M., Maurizii, M. G. & Franceschini, V. Crypt cell markers in the olfactory organ of Poecilia reticulata: analysis and comparison with the fish model Danio rerio. *Brain Struct. Funct.* **222**, 3063–3074 (2017).

220. Sepahi, A. *et al.* Olfactory sensory neurons mediate ultrarapid antiviral immune responses in a TrkA-dependent manner. *Proc. Natl. Acad. Sci. U. S. A.* **116**, 12428–12436 (2019).

221. Ahuja, G. *et al.* Kappe neurons, a novel population of olfactory sensory neurons. *Sci. Rep.* **4**, (2015).

222. Genovese, F. & Tizzano, M. Microvillous cells in the olfactory epithelium express elements of the solitary chemosensory cell transduction signaling cascade. *PLoS One* **13**, (2018).

223. Hansen, A. & Zeiske, E. Development of the olfactory organ in the zebrafish, Brachydanio rerio. *J. Comp. Neurol.* **333**, 289–300 (1993).

224. Byrd, C. A. & Brunjes, P. C. Organization of the olfactory system in the adult zebrafish: Histological, immunohistochemical, and quantitative analysis. *J. Comp. Neurol.* **358**, 247–259 (1995).

225. Demirler, M. C. *et al.* Purinergic signalling selectively modulates maintenance but not repair neurogenesis in the zebrafish olfactory epithelium. *FEBS J.* **287**, 2699–2722 (2020).

226. Kraus, A. & Salinas, I. Olfactory sensory neurons regulate mucosal antiviral immune responses. *J. Immunol.* **204**, (2020).

227. Reiten, I. *et al.* Motile-Cilia-Mediated Flow Improves Sensitivity and Temporal Resolution of Olfactory Computations. *Curr. Biol.* **27**, 166–174 (2017).

228. Vasilyev, A. & Drummond, I. A. Live imaging kidney development in Zebrafish. *Methods Mol. Biol.* **886**, 55–70 (2012).

229. Castleman, V. H. *et al.* Mutations in radial spoke head protein genes RSPH9 and RSPH4A cause primary ciliary dyskinesia with central-microtubular-pair abnormalities. *Am. J. Hum. Genet.* **84**, 197–209 (2008).

230. Grewal, S. An interview with didier stainier. *Development (Cambridge)* vol. 142 2861–2863 (2015).

231. Stainier, D. Y. R., Kontarakis, Z. & Rossi, A. Making sense of anti-sense data. *Developmental Cell* vol. 32 7–8 (2015).

232. Lai, J. K. H., Gagalova, K. K., Kuenne, C., El-Brolosy, M. A. & Stainier, D. Y. R. Induction of interferon-stimulated genes and cellular stress pathways by morpholinos in zebrafish. *Dev. Biol.* **454**, 21–28 (2019).

233. Laale, H. W. The biology and use of zebrafish, Brachydanio rerio in fisheries research.. A literature review. *J. Fish Biol.* **10**, 121–173 (1977).

234. Ishino, Y., Shinagawa, H., Makino, K., Amemura, M. & Nakatura, A. Nucleotide sequence of the iap gene, responsible for alkaline phosphatase isoenzyme conversion in Escherichia coli, and identification of the gene product. *J. Bacteriol.* **169**, 5429–5433 (1987).

235. Bolotin, A., Quinquis, B., Sorokin, A. & Dusko Ehrlich, S. Clustered regularly interspaced short palindrome repeats (CRISPRs) have spacers of extrachromosomal origin. *Microbiology* **151**, 2551–2561 (2005).

236. Mojica, F. J. M., Díez-Villaseñor, C., García-Martínez, J. & Soria, E. Intervening sequences of regularly spaced prokaryotic repeats derive from foreign genetic elements. *J. Mol. Evol.* **60**, 174–182 (2005).

237. Makarova, K. S. *et al.* Evolution and classification of the CRISPR-Cas systems. *Nature Reviews Microbiology* vol. 9 467–477 (2011).

238. Wiedenheft, B., Sternberg, S. H. & Doudna, J. A. RNA-guided genetic silencing systems in bacteria and archaea. *Nature* vol. 482 331–338 (2012).

239. Jinek, M. *et al.* A programmable dual-RNA-guided DNA endonuclease in adaptive bacterial immunity. *Science (80-.).* **337**, 816–821 (2012).

240. Wallmeier, J. *et al.* TTC25 Deficiency Results in Defects of the Outer Dynein Arm Docking

Machinery and Primary Ciliary Dyskinesia with Left-Right Body Asymmetry Randomization. *Am. J. Hum. Genet.* **99**, 460–469 (2016).

241. Lewis, W. R. *et al.* Mutation of Growth Arrest Specific 8 Reveals a Role in Motile Cilia Function and Human Disease. *PLoS Genet.* **12**, (2016).

242. Abbasi, F. *et al.* RSPH6A is required for sperm flagellum formation and male fertility in mice. *J. Cell Sci.* **131**, (2018).

243. Lebedeva, S., de Jesus Domingues, A. M., Butter, F. & Ketting, R. F. Characterization of genetic loss-of-function of Fus in zebrafish. *RNA Biol.* **14**, 29–35 (2017).

244. Yang, J. *et al.* Deletion of Pr130 interrupts cardiac development in zebrafish. *Int. J. Mol. Sci.* **17**, (2016).

245. Zhu, X. *et al.* An efficient genotyping method for genome-modified animals and human cells generated with CRISPR/Cas9 system. *Sci Rep* **4**, 6420 (2014).

246. Jaffe, K. M. *et al.* C21orf59/kurly Controls Both Cilia Motility and Polarization. *Cell Rep.* **14**, 1841–1849 (2016).

247. Xie, S. *et al.* Centrosomal protein FOR20 is essential for cilia-dependent development in zebrafish embryos. *FASEB J.* **33**, 3613–3622 (2019).

248. Blanchon, S. *et al.* Delineation of CCDC39/CCDC40 mutation spectrum and associated phenotypes in primary: Ciliary dyskinesia. *J. Med. Genet.* **49**, 410–416 (2012).

249. Davis, S. D. *et al.* Clinical features of childhood primary ciliary dyskinesia by genotype and ultrastructural phenotype. *Am. J. Respir. Crit. Care Med.* **191**, 316–324 (2015).

250. Rasteiro, M. O. A. Creation of a Danio rerio mutant using CRISPR-Cas9 as a model system to study Primary Ciliary Dyskinesia (PCD). **9**, (2017).

251. Kouis, P. *et al.* Prevalence of primary ciliary dyskinesia in consecutive referrals of suspect cases and the transmission electron microscopy detection rate: a systematic review and meta-analysis. *Pediatr. Res.* N.PAG-N.PAG (2016) doi:10.1038/pr.2016.263.

252. Behan, L., Rubbo, B., Lucas, J. S. & Dunn Galvin, A. The patient's experience of primary ciliary dyskinesia: a systematic review. *Qual. Life Res.* **26**, 2265–2285 (2017).

253. Shapiro, A. J. *et al.* Diagnosis, monitoring, and treatment of primary ciliary dyskinesia: PCD foundation consensus recommendations based on state of the art review. *Pediatr. Pulmonol.* **51**, 115–132 (2016).

254. Kesson, A. M. & Kakakios, A. Immunocompromised children: conditions and infectious agents. *Paediatric Respiratory Reviews* vol. 8 231–239 (2007).

255. Mishra, M., Kumar, N., Jaiswal, A., Verma, A. K. & Kant, S. Kartagener's syndrome: A case series. *Lung India* **29**, 366–369 (2012).

256. Dixit, R., Dixit, K., Jindal, S. & Shah, K. An unusual presentation of immotile-cilia syndrome with azoospermia: Case report and literature review. *Lung India* **26**, 142–145 (2009).

257. Leigh, M. W. *et al.* Clinical and genetic aspect of Primary Ciliary Dyskinesia / Kartagener syndrome. **11**, 473–487 (2013).

258. Afzelius, B. A. A human syndrome caused by immotile cilia. *Science (80-.).* **193**, 317–319 (1976).

259. Knowles, M. R., Daniels, L. A., Davis, S. D., Zariwala, M. A. & Leigh, M. W. Primary ciliary dyskinesia: Recent advances in diagnostics, genetics, and characterization of clinical disease. *Am. J. Respir. Crit. Care Med.* **188**, 913–922 (2013).

260. Lucas, J. S., Paff, T., Goggin, P. & Haarman, E. Diagnostic Methods in Primary Ciliary

Dyskinesia. *Paediatr. Respir. Rev.* **18**, 8–17 (2016).

261. Young, K. *Anatomy and Phisiology*. (2016).

262. Vestibule | of the nose | Britannica. https://www.britannica.com/science/vestibule-of-the-nose.

263. Lateral Wall of Nasal Cavity. https://www.netterimages.com/lateral-wall-of-nasal-cavity-labeled-multiple-publications-general-anatomy-frank-h-netter-4877.html.

264. L., R. *Pathologic Basic Disease*. (W.B. Saunders Company, 1989).

265. Hirst, R. A., Rutman, A., Williams, G. & O'Callaghan, C. Ciliated air-liquid cultures as an aid to diagnostic testing of primary ciliary dyskinesia. *Chest* **138**, 1441–1447 (2010).

266. Schwabe, G. C. *et al.* Primary ciliary dyskinesia associated with normal axoneme ultrastructure is caused by DNAH11 mutations. *Hum. Mutat.* **29**, 289–298 (2008).

267. Papon, J. F. *et al.* A 20-year experience of electron microscopy in the diagnosis of primary ciliary dyskinesia. *Eur. Respir. J.* **35**, 1057–1063 (2010).

268. Amack, J. D. Salient features of the ciliated organ of asymmetry. *Bioarchitecture* **4**, 6–15 (2014).

269. Afzelius, B. A. The Immotile-Cilia syndrome and other ciliary diseases. *Int. Rev. Exp. Pathol.* **VOL. 19**, 1–43 (1979).

270. Edwards, D. F., Patton, C. S. & Kennedy, J. R. Primary ciliary dyskinesia in the dog. *Problems in veterinary medicine* vol. 4 291–319 (1992).

271. Stannard, W. A., Chilvers, M. A., Rutman, A. R. & Williams, C. D. Diagnostic Testing of Patients Suspected of Primary Ciliary Dyskinesia. doi:10.1164/rccm.200903-0459OC.

272. Kuek, L. E. & Lee, R. J. First contact: The role of respiratory cilia in host-pathogen interactions in the airways. *American Journal of Physiology - Lung Cellular and Molecular Physiology* vol. 319 L603–L619 (2020).

273. Amirav, I. *et al.* A reach-out system for video microscopy analysis of ciliary motions aiding PCD diagnosis. *BMC Res. Notes* **8**, 71 (2015).

274. Sturgess, J. M., Chao, J. & Turner, J. A. P. Cilia with defective radial spokes: A cause of human respiratory disease. *Bull. Int. Union Tuberc.* **54**, 397–398 (1979).

275. Mygind, N., Pedersen, M. & Nielsen, M. H. Acta Oto-Laryngologica Primary and Secundary Ciliary Dyskinesia. (2009) doi:10.3109/00016488309139463.

276. Pinto, A. L., Rai, R. K., Hogg, C. & Burgoyne, T. Ciliary feature counter: A program for the quantitative assessment of cilia to diagnose primary ciliary dyskinesia. *Diagnostics* **10**, 1–8 (2020).

277. Chilvers, M. A., Rutman, A. & O'Callaghan, C. Ciliary beat pattern is associated with specific ultrastructural defects in primary ciliary dyskinesia. *J. Allergy Clin. Immunol.* **112**, 518–24 (2003).

278. Ben Khelifa, M. *et al.* Mutations in DNAH1, which encodes an inner arm heavy chain dynein, lead to male infertility from multiple morphological abnormalities of the sperm flagella. *Am. J. Hum. Genet.* **94**, 95–104 (2014).

279. O'Callaghan, C., Rutman, A., Williams, G. M. & Hirst, R. A. Inner dynein arm defects causing primary ciliary dyskinesia: Repeat testing required. *Eur. Respir. J.* **38**, 603–607 (2011).

280. Stannard, W., Rutman, A., Wallis, C. & O'Callaghan, C. Central microtubular agenesis causing primary ciliary dyskinesia. *Am. J. Respir. Crit. Care Med.* **169**, 634–637 (2004).

281. Knowles, M., Leigh, M., Carson, J. & Davis, S. Mutations of DNAH11 in Primary Ciliary Dyskinesia Patients with Normal Ciliary Ultrastructure. *Thorax* **67**, 433–441 (2012).

282. Olbrich, H. *et al.* Recessive HYDIN mutations cause primary ciliary dyskinesia without

randomization of left-right body asymmetry. *Am. J. Hum. Genet.* **91**, 672–684 (2012).

283. Boon, M. *et al.* MCIDAS mutations result in a mucociliary clearance disorder with reduced generation of multiple motile cilia. *Nat. Commun.* **5**, 4418 (2014).

284. Wirschell, M. The nexin-dynein regulatory complex subunit DRC1 is essential for motile cilia function in algae and humans. *Nat. Publ. Gr.* (2013).

285. Loges, N. T. *et al.* Recessive DNAH9 Loss-of-Function Mutations Cause Laterality Defects and Subtle Respiratory Ciliary-Beating Defects. *Am. J. Hum. Genet.* **103**, 995–1008 (2018).

286. Shoemark, A. *et al.* International consensus guideline for reporting transmission electron microscopy results in the diagnosis of Primary Ciliary Dyskinesia (BEAT PCD TEM Criteria). *Eur. Respir. J.* **55**, (2020).

287. Autosomal Recessive Disorder - an overview | ScienceDirect Topics. https://www.sciencedirect.com/topics/medicine-and-dentistry/autosomal-recessive-disorder.

288. Riordan, J. R. *et al.* Identification of the cystic fibrosis gene: Cloning and characterization of complementary DNA. *Science (80-.).* **245**, 1066–1073 (1989).

289. Hornef, N. *et al.* DNAH5 mutations are a common cause of primary ciliary dyskinesia with outer dynein arm defects. *Am. J. Respir. Crit. Care Med.* **174**, 120–126 (2006).

290. Lucas, J. S. *et al.* Static respiratory cilia associated with mutations in Dnahc11/DNAH11: A mouse model of PCD. *Hum. Mutat.* **33**, 495–503 (2012).

291. Kennedy, M. P. *et al.* Congenital heart disease and other heterotaxic defects in a large cohort of patients with primary ciliary dyskinesia. *Circulation* **115**, 2814–2821 (2007).

292. Onoufriadis, A. *et al.* Combined exome and whole-genome sequencing identifies mutations in ARMC4 as a cause of primary ciliary dyskinesia with defects in the outer dynein arm. *J. Med. Genet.* **51**, 61–7 (2014).

293. Knowles, M. R. *et al.* Exome sequencing identifies mutations in CCDC114 as a cause of primary ciliary dyskinesia. *Am. J. Hum. Genet.* **92**, 99–106 (2013).

294. Hjeij, R. *et al.* CCDC151 mutations cause primary ciliary dyskinesia by disruption of the outer dynein arm docking complex formation. *Am. J. Hum. Genet.* **95**, 257–274 (2014).

295. Fassad, M. R. *et al.* Mutations in Outer Dynein Arm Heavy Chain DNAH9 Cause Motile Cilia Defects and Situs Inversus. *Am. J. Hum. Genet.* **103**, 984–994 (2018).

296. Pazour, G. J., Agrin, N., Walker, B. L. & Witman, G. B. Identification of predicted human outer dynein arm genes: Candidates for primary ciliary dyskinesia genes. *J. Med. Genet.* **43**, 62–73 (2006).

297. Horváth, J. *et al.* Identification and analysis of axonemal dynein light chain 1 in primary ciliary dyskinesia patients. *Am. J. Respir. Cell Mol. Biol.* **33**, 41–47 (2005).

298. Panizzi, J. R. *et al.* CCDC103 mutations cause primary ciliary dyskinesia by disrupting assembly of ciliary dynein arms. *Nat. Genet.* **44**, 714–719 (2012).

299. Zariwala, M. A. *et al.* ZMYND10 is mutated in primary ciliary dyskinesia and interacts with LRRC6. *Am. J. Hum. Genet.* **93**, 336–345 (2013).

300. Diggle, C. P. *et al.* HEATR2 Plays a Conserved Role in Assembly of the Ciliary Motile Apparatus. *PLoS Genet.* **10**, (2014).

301. Z. Bukowy-Bieryłło. RPGR mutations might cause reduced orientation of respiratory cilia. *Pediatr. Pulmonol.* (2012).

302. Gakovic, M. *et al.* The role of RPGR in cilia formation and actin stability. *Hum. Mol. Genet.* **20**, 4840–4850 (2011).

303. Chagot, M. E. *et al.* Binding properties of the quaternary assembly protein SPAG1. *Biochem. J.* **476**, 1679–1694 (2019).

304. Olcese, C. *et al.* X-linked primary ciliary dyskinesia due to mutations in the cytoplasmic axonemal dynein assembly factor PIH1D3. *Nat. Commun.* **8**, 1–15 (2017).

305. Hartill, V. L. *et al.* DNAAF1 links heart laterality with the AAA+ ATPase RUVBL1 and ciliary intraflagellar transport. *Hum. Mol. Genet.* **27**, 529–545 (2018).

306. Tarkar, A. *et al.* DYX1C1 is required for axonemal dynein assembly and ciliary motility. *Nat. Genet.* **45**, 995–1003 (2013).

307. Manuscript, A. Ktu/PF13 is required for cytoplasmic pre-assembly of axonemal dyneins. **456**, 611–616 (2012).

308. Mitchison, H. M. *et al.* Mutations in axonemal dynein assembly factor DNAAF3 cause primary ciliary dyskinesia. *Nat. Genet.* **44**, 381–389 (2012).

309. Fassad, M. R. *et al.* C11orf70 Mutations Disrupting the Intraflagellar Transport-Dependent Assembly of Multiple Axonemal Dyneins Cause Primary Ciliary Dyskinesia. *Am. J. Hum. Genet.* **102**, 956–972 (2018).

310. Merveille, A. C. *et al.* CCDC39 is required for assembly of inner dynein arms and the dynein regulatory complex and for normal ciliary motility in humans and dogs. *Nat. Genet.* **43**, 72–78 (2011).

311. Antony, D. *et al.* Mutations in CCDC39 and CCDC40 are the Major Cause of Primary Ciliary Dyskinesia with Axonemal Disorganization and Absent Inner Dynein Arms. *Hum. Mutat.* **34**, 462–472 (2013).

312. Thomas, L. *et al.* TTC12 Loss-of-Function Mutations Cause Primary Ciliary Dyskinesia and Unveil Distinct Dynein Assembly Mechanisms in Motile Cilia Versus Flagella. *Am. J. Hum. Genet.* **106**, 153–169 (2020).

313. Jeanson, L. *et al.* Mutations in GAS8, a Gene Encoding a Nexin-Dynein Regulatory Complex Subunit, Cause Primary Ciliary Dyskinesia with Axonemal Disorganization. *Hum. Mutat.* **37**, 776–785 (2016).

314. Bower, R. *et al.* DRC2/CCDC65 is a central hub for assembly of the nexin–dynein regulatory complex and other regulators of ciliary and flagellar motility. *Mol. Biol. Cell* **29**, 137–153 (2018).

315. Bustamante-Marin, X. M. *et al.* Identification of genetic variants in CFAP221 as a cause of primary ciliary dyskinesia. *J. Hum. Genet.* **65**, 175–180 (2020).

316. Wallmeier J, Al-Mutairi DA, Chen CT, Loges NT, Pennekamp P, Menchen T, Ma L, Shamseldin HE, Olbrich H, Dougherty GW, Werner C, Alsabah BH, Köhler G, Jaspers M, Boon M, Griese M, Schmitt-Grohé S, Zimmermann T, Koerner-Rettberg C, Horak E, Kintner C, Alkura, O. H. Mutations in CCNO result in congenital mucociliary clearance disorder with reduced generation of multiple motile cilia. *Nat. Genet.* (2014).

317. Bukowy-Bieryllo, Z. *et al.* Truncating mutations in exons 20 and 21 of OFD1 can cause primary ciliary dyskinesia without associated syndromic symptoms. *J. Med. Genet.* **56**, 769–777 (2019).

318. Chivukula, R. R. *et al.* A human ciliopathy reveals essential functions for NEK10 in airway mucociliary clearance. *Nature Medicine* vol. 26 244–251 (2020).

319. Bustamante-Marin, X. M. *et al.* Mutation of CFAP57, a protein required for the asymmetric targeting of a subset of inner dynein arms in Chlamydomonas, causes primary ciliary dyskinesia. *PLoS Genet.* **16**, (2020).

320. Bonnefoy, S. *et al.* Biallelic Mutations in LRRC56, Encoding a Protein Associated with Intraflagellar Transport, Cause Mucociliary Clearance and Laterality Defects. *Am. J. Hum. Genet.* **103**, 727–739 (2018).

321. Bustamante-Marin, X. M. *et al.* Lack of GAS2L2 Causes PCD by Impairing Cilia Orientation and Mucociliary Clearance. *Am. J. Hum. Genet.* **104**, 229–245 (2019).

322. Horani, A. & Ferkol, T. W. Advances in the Genetics of Primary Ciliary Dyskinesia: Clinical Implications. *Chest* vol. 154 645–652 (2018).

323. Li, Y. *et al.* DNAH6 and Its Interactions with PCD Genes in Heterotaxy and Primary Ciliary Dyskinesia. *PLoS Genet.* **12**, (2016).

324. Becker-heck, A. *et al.* The coiled-coil domain containing protein CCDC40 is essential for motile cilia function and left-right axis formation. **43**, 79–84 (2011).

325. Dougherty, G. W. *et al.* DNAH11 localization in the proximal region of respiratory cilia defines distinct outer dynein arm complexes. *Am. J. Respir. Cell Mol. Biol.* **55**, 213–224 (2016).

326. Shoemark, A. *et al.* Topological data analysis reveals genotype-phenotype relationships in primary ciliary dyskinesia. *Eur. Respir. J.* 2002359 (2021) doi:10.1183/13993003.02359-2020.

327. Knowles, M. R. *et al.* Mutations in RSPH1 cause primary ciliary dyskinesia with a unique clinical and ciliary phenotype. *Am. J. Respir. Crit. Care Med.* **189**, 707–717 (2014).

328. Best, S. *et al.* Risk factors for situs defects and congenital heart disease in primary ciliary dyskinesia. *Thorax* **74**, 203–205 (2019).

329. Irving, S. *et al.* Primary Ciliary Dyskinesia Due to Microtubular Defects is Associated with Worse Lung Clearance Index. *Lung* **196**, 231–238 (2018).

330. Davis, S. D. *et al.* Clinical features of childhood primary ciliary dyskinesia by genotype and ultrastructural phenotype. *Am. J. Respir. Crit. Care Med.* **191**, 316–324 (2015).

331. Ghandourah, H. & Dell, S. D. Severe disease due to CCDC40 gene variants and the perils of late diagnosis in primary ciliary dyskinesia. *BMJ Case Rep.* **2018**, (2018).

332. Behan, L. *et al.* PICADAR: A diagnostic predictive tool for primary ciliary dyskinesia. *Eur. Respir. J.* **47**, 1103–1112 (2016).

333. Hogg, C. Primary ciliary dyskinesia: when to suspect the diagnosis and how to confirm it. *Paediatr. Respir. Rev.* **10**, 44–50 (2009).

334. Olm, M. A. K., Caldini, E. G. & Mauad, T. Diagnóstico de discinesia ciliar primária. *J. Bras. Pneumol.* **41**, 251–263 (2015).

335. Kouis, P., Evriviadou, A. & Yiallouros, P. K. Nasal nitric oxide measurement for primary ciliary dyskinesia diagnosis: The impact of underlying genetic defects on diagnostic accuracy. *Pediatr. Investig.* **3**, 214–216 (2019).

336. Shapiro, A. J. *et al.* Accuracy of nasal nitric oxide measurement as a diagnostic test for primary ciliary dyskinesia a systematic review and meta-analysis. *Annals of the American Thoracic Society* vol. 14 1184–1196 (2017).

337. Collins, S. A., Gove, K., Walker, W. & Lucas, J. S. A. Nasal nitric oxide screening for primary ciliary dyskinesia: Systematic review and meta-analysis. *Eur. Respir. J.* **44**, 1589–1599 (2014).

338. Selimoglu, E. Nitric Oxide in Health and Disease from the Point of View of the Otorhinolaryngologist. *Curr. Pharm. Des.* **11**, 3051–3060 (2005).

339. Li, D., Shirakami, G., Zhan, X. & Johns, R. A. Regulation of ciliary beat frequency by the nitric oxide-cyclic guanosine monophosphate signaling pathway in rat airway epithelial cells. *Am. J. Respir. Cell Mol. Biol.* **23**, 175–181 (2000).

340. Lucas, J. S. *et al.* European Respiratory Society guidelines for the diagnosis of primary ciliary dyskinesia. *Eur. Respir. J.* ERJ-01090-2016 (2016) doi:10.1183/13993003.01090-2016.

341. Walker, W. T., Jackson, C. L., Lackie, P. M., Hogg, C. & Lucas, J. S. Nitric oxide in primary

ciliary dyskinesia. *European Respiratory Journal* vol. 40 1024–1032 (2012).

342. Sampaio, P. *et al.* CiliarMove: new software for evaluating ciliary beat frequency helps find novel mutations by a Portuguese multidisciplinary team on primary ciliary dyskinesia. *ERJ Open Res.* **7**, 00792–02020 (2021).

343. Chilvers, M. A. & O'callaghan, C. *Analysis of ciliary beat pattern and beat frequency using digital high speed imaging: comparison with the photomultiplier and photodiode methods*. *Thorax* vol. 55 (2000).

344. Bush, A. *et al.* Primary ciliary dyskinesia: Diagnosis and standards of care. *European Respiratory Journal* vol. 12 982–988 (1998).

345. Raidt, J. *et al.* Ciliary beat pattern and frequency in genetic variants of primary ciliary dyskinesia. doi:10.1183/09031936.00052014.

346. Stannard, W. & O'Callaghan, C. Ciliary function and the role of cilia in clearance. *Journal of Aerosol Medicine: Deposition, Clearance, and Effects in the Lung* vol. 19 110–115 (2006).

347. Shapiro, A. J. *et al.* Diagnosis, monitoring, and treatment of primary ciliary dyskinesia: PCD foundation consensus recommendations based on state of the art review. *Pediatr. Pulmonol.* **51**, 115–132 (2016).

348. Saint-Criq, V. *et al.* Choice of Differentiation Media Significantly Impacts Cell Lineage and Response to CFTR Modulators in Fully Differentiated Primary Cultures of Cystic Fibrosis Human Airway Epithelial Cells. *Cells* **9**, (2020).

349. Lechner, J. F. *et al. Clonal Growth of Epithelial Cells from Normal Adult Human Bronchus*. (1981).

350. Hiemstra, P. S., Tetley, T. D. & Janes, S. M. Airway and alveolar epithelial cells in culture. *Eur. Respir. J.* **54**, (2019).

351. Gruenert, D. C., Finkbeiner, W. E. & Widdicombe, J. H. Culture and transformation of human airway epithelial cells. *American Journal of Physiology - Lung Cellular and Molecular Physiology* vol. 268 (1995).

352. Dvorak, A., Tilley, A. E., Shaykhiev, R., Wang, R. & Crystal, R. G. Do airway epithelium air-liquid cultures represent the in vivo airway epithelium transcriptome? *Am. J. Respir. Cell Mol. Biol.* **44**, 465–473 (2011).

353. BéruBé, K., Prytherch, Z., Job, C. & Hughes, T. Human primary bronchial lung cell constructs: The new respiratory models. *Toxicology* vol. 278 311–318 (2010).

354. de Jong, P. M. *et al.* Ciliogenesis in human bronchial epithelial cells cultured at the air-liquid interface. *Am. J. Respir. Cell Mol. Biol.* **10**, 271–277 (1994).

355. Fan, Q. *et al.* Page 1 of 39 1. 1–39 (2017).

356. Liu, Z. *et al.* A quantitative super-resolution imaging toolbox for diagnosis of motile ciliopathies. *Sci. Transl. Med.* **12**, 71 (2020).

357. Gardner, L. E. *et al.* Proceedings of the 4th BEAT-PCD Conference and 5th PCD Training School. *BMC Proc.* **14**, 7 (2020).

358. Shoemark, A. *et al.* Accuracy of Immunofluorescence in the Diagnosis of Primary Ciliary Dyskinesia. *Am. J. Respir. Crit. Care Med.* **196**, 94–101 (2017).

359. Zariwala, M. A. *et al.* Mutations of DNAI1 in primary ciliary dyskinesia: Evidence of founder effect in a common mutation. *Am. J. Respir. Crit. Care Med.* **174**, 858–866 (2006).

360. Amirav, I. *et al.* Systematic Analysis of CCNO Variants in a Defined Population: Implications for Clinical Phenotype and Differential Diagnosis. *Hum. Mutat.* **37**, 396–405 (2016).

361. Richards, S. *et al.* Standards and guidelines for the interpretation of sequence variants: A joint consensus recommendation of the American College of Medical Genetics and Genomics and the Association for Molecular Pathology. *Genet. Med.* **17**, 405–424 (2015).

362. Marshall, C. R. *et al.* Whole-exome sequencing and targeted copy number analysis in primary ciliary dyskinesia. *G3 Genes, Genomes, Genet.* **5**, 1775–1781 (2015).

363. Boon, M. *et al.* Primary ciliary dyskinesia: critical evaluation of clinical symptoms and diagnosis in patients with normal and abnormal ultrastructure. *Orphanet J. Rare Dis.* **9**, 11 (2014).

364. Shoemark, A. *et al.* Primary ciliary dyskinesia with normal ultrastructure: Three-dimensional tomography detects absence of DNAH11. *Eur. Respir. J.* **51**, (2018).

365. De Rosier, D. J. & Klug, A. Reconstruction of three dimensional structures from electron micrographs. *Nature* **217**, 130–134 (1968).

366. Ercius, P., Alaidi, O., Rames, M. J. & Ren, G. Electron Tomography: A Three-Dimensional Analytic Tool for Hard and Soft Materials Research. *Advanced Materials* vol. 27 5638–5663 (2015).

367. Shoemark, A. *et al.* PCD Detect: enhancing ciliary features through image averaging and classification. *Am. J. Physiol. Cell. Mol. Physiol.* **319**, L1048–L1060 (2020).

368. Dehlink, E., Hogg, C., Carr, S. B. & Bush, A. Clinical phenotype and current diagnostic criteria for primary ciliary dyskinesia. *Expert Review of Respiratory Medicine* vol. 10 1163–1175 (2016).

369. Shapiro, A. J. *et al.* Diagnosis of primary ciliary dyskinesia: An official American thoracic society clinical practice guideline. *Am. J. Respir. Crit. Care Med.* **197**, e24–e39 (2018).

370. Olbrich, H. *et al.* Mutations in DNAH5 cause primary ciliary dyskinesia and randomization of left-right asymmetry. *Nat. Genet.* **30**, 143–144 (2002).

371. Burgoyne, T., Dixon, M., Luther, P., Hogg, C. & Shoemark, A. Generation of a three-dimensional ultrastructural model of human respiratory cilia. *Am. J. Respir. Cell Mol. Biol.* **47**, 800–806 (2012).

372. Watson, M. L. Staining of tissue sections for electron microscopy with heavy metals. *J. Cell Biol.* **4**, 475–478 (1958).

373. Inaga, S. *et al.* Platinum blue as an alternative to uranyl acetate for staining in transmission electron microscopy. *Arch. Histol. Cytol.* **70**, 43–49 (2007).

374. Sato, S., Adachi, A., Sasaki, Y. & Ghazizadeh, M. Oolong tea extract as a substitute for uranyl acetate in staining of ultrathin sections. *J. Microsc.* **229**, 17–20 (2008).

375. Ikeda, K. I., Inoue, K., Kanematsu, S., Horiuchi, Y. & Park, P. Enhanced effects of nonisotopic hafnium chloride in methanol as a substitute for uranyl acetate in TEM contrast of ultrastructure of fungal and plant cells. *Microsc. Res. Tech.* **74**, 825–830 (2011).

376. Nakakoshi, M., Nishioka, H. & Katayama, E. New versatile staining reagents for biological transmission electron microscopy that substitute for uranyl acetate. *J. Electron Microsc. (Tokyo).* **60**, 401–407 (2011).

377. Inaba, Y. *et al.* Transport of the outer dynein arm complex to cilia requires a cytoplasmic protein Lrrc6. *Genes to Cells* **21**, 728–739 (2016).

378. Shoemark, A., Dixon, M., Corrin, B. & Dewar, A. Twenty-year review of quantitative transmission electron microscopy for the diagnosis of primary ciliary dyskinesia. *Journal of Clinical Pathology* vol. 65 267–271 (2012).

379. Goutaki, M. *et al.* The international primary ciliary dyskinesia cohort (iPCD cohort): Methods and first results. *Eur. Respir. J.* **49**, (2017).

380. Burgoyne, T. *et al.* Characterizing the ultrastructure of primary ciliary dyskinesia transposition

defect using electron tomography. *Cytoskeleton* **71**, 294–301 (2014).

381. Rutland, J., Griffin, W. M. & Cole, P. J. Human ciliary beat frequency in epithelium from intrathoracic and extrathoracic airways. *Am. Rev. Respir. Dis.* **125**, 100–105 (1982).

382. Fliegauf, M. *et al.* Mislocalization of DNAH5 and DNAH9 in respiratory cells from patients with primary ciliary dyskinesia. *Am. J. Respir. Crit. Care Med.* **171**, 1343–1349 (2005).

383. Shoemark, A. *et al.* High prevalence of CCDC103 p.His154Pro mutation causing primary ciliary dyskinesia disrupts protein oligomerisation and is associated with normal diagnostic investigations. *Thorax* **73**, 157–166 (2018).

384. Davidson, A. E. *et al.* Mutations in ARL2BP, encoding ADP-ribosylation-factor-like 2 binding protein, cause autosomal-recessive retinitis pigmentosa. *Am. J. Hum. Genet.* **93**, 321–329 (2013).

385. Mitchison, H. M. & Shoemark, A. Motile cilia defects in diseases other than primary ciliary dyskinesia: The contemporary diagnostic and research role for transmission electron microscopy. *Ultrastructural Pathology* vol. 41 415–427 (2017).

386. Zariwala, M. A., Omran, H. & Ferkol, T. W. The emerging genetics of primary ciliary dyskinesia. in *Proceedings of the American Thoracic Society* vol. 8 430–433 (Proc Am Thorac Soc, 2011).

387. Takada, S., Wilkerson, C. G., Wakabayashi, K. I., Kamiya, R. & Witman, G. B. The outer dynein arm-docking complex: Composition and characterization of a subunit (Oda1) necessary for outer arm assembly. *Mol. Biol. Cell* **13**, 1015–1029 (2002).

388. Kispert, A. Genotype-phenotype correlations in PCD patients carrying DNAH5 mutations. *Thorax* **58**, 552-b-554 (2003).

389. Afzelius, B. A., Dallai, R., Lanzavecchia, S. & Bellon, P. L. Flagellar structure in normal human spermatozoa and in spermatozoa that lack dynein arms. *Tissue Cell* **27**, 241–247 (1995).

390. Carson, J. L., Hu, S. C. S. & Collier, A. M. Computer-assisted analysis of radial symmetry in human airway epithelial cilia: Assessment of congenital ciliary defects in primary ciliary dyskinesia. *Ultrastruct. Pathol.* **24**, 169–174 (2000).

391. Escudier, E. *et al.* Computer-assisted analysis helps detect inner dynein arm abnormalities. *Am. J. Respir. Crit. Care Med.* **166**, 1257–1262 (2002).

392. O'Toole, E. T., Giddings, T. H., Porter, M. E. & Ostrowski, L. E. Computer-assisted image analysis of human cilia and chlamydomonas flagella reveals both similarities and differences in axoneme structure. *Cytoskeleton* **69**, 577–590 (2012).

393. Schroeder, J. A. Application of laboratory and digital techniques for visual enhancement during the ultrastructural assessment of cilia. *Ultrastruct. Pathol.* **41**, 399–407 (2017).

394. Wheway, G. *et al.* Opportunities and challenges for molecular understanding of ciliopathies–the 100,000 genomes project. *Frontiers in Genetics* vol. 10 (2019).

395. Satir, P. & Christensen, S. T. Overview of Structure and Function of Mammalian Cilia. *Annu. Rev. Physiol.* **69**, 377–400 (2007).

396. Gluenz, E. *et al.* Beyond 9+0: noncanonical axoneme structures characterize sensory cilia from protists to humans. *FASEB J.* **24**, 3117–3121 (2010).

397. Coppieters, F., Lefever, S., Leroy, B. P. & De Baere, E. CEP290, a gene with many faces: Mutation overview and presentation of CEP290base. *Hum. Mutat.* **31**, 1097–1108 (2010).

398. Liu, G., Wang, L., Pan, J. & Yao, X. Chlamydomonas WDR92 in association with R2TP-like complex and multiple DNAAFs to regulate ciliary dynein preassembly. *J. Mol. Cell Biol.* **11**, 770–780 (2019).

399. Chang, N. *et al.* Genome editing with RNA-guided Cas9 nuclease in Zebrafish embryos. *Cell*

Res. **23**, 465–472 (2013).

400. Yates, A. D. *et al.* Ensembl 2020. *Nucleic Acids Res.* **48**, D682–D688 (2020).

401. Sui, W. *et al.* CCDC40 mutation as a cause of primary ciliary dyskinesia: a case report and review of literature. *Clin. Respir. J.* **10**, 614–621 (2016).

402. Casey, J. P. *et al.* Unexpected genetic heterogeneity for primary ciliary dyskinesia in the Irish Traveller population. *Eur. J. Hum. Genet.* **23**, 210–217 (2015).

403. Burkhard, P., Stetefeld, J. & Strelkov, S. V. Coiled coils: A highly versatile protein folding motif. *Trends in Cell Biology* vol. 11 82–88 (2001).

404. Oda, T., Yanagisawa, H., Kamiya, R. & Kikkawa, M. A molecular ruler determines the repeat length in eukaryotic cilia and flagella. *Science (80-.).* **346**, 857–860 (2014).

405. Davis, S. D. *et al.* Primary ciliary dyskinesia: Longitudinal study of lung disease by ultrastructure defect and genotype. *Am. J. Respir. Crit. Care Med.* **199**, 190–198 (2019).

406. Cannarella, R. *et al.* Ultrastructural Sperm Flagellum Defects in a Patient With CCDC39 Compound Heterozygous Mutations and Primary Ciliary Dyskinesia/Situs Viscerum Inversus. *Front. Genet.* **11**, (2020).

407. Computer Visualization of Three-Dimensional Image Data Using IMOD. https://bio3d.colorado.edu/imod/paper/.

408. UCSF Chimera Home Page. https://www.rbvi.ucsf.edu/chimera/.

409. Montenegro-Johnson, T. D., Baker, D. I., Smith, D. J. & Lopes, S. S. Three-dimensional flow in Kupffer's Vesicle. *J. Math. Biol.* **73**, 705–725 (2016).

410. Zheng, S. Q., Sedat, J. W. & Agard, D. A. Automated data collection for electron microscopic tomography. in *Methods in Enzymology* vol. 481 283–315 (Academic Press Inc., 2010).

411. Waters, A. M. & Beales, P. L. Ciliopathies: An expanding disease spectrum. *Pediatric Nephrology* vol. 26 1039–1056 (2011).

412. Mangos, S. *et al.* The ADPKD genes pkd1a/b and pkd2 regulate extracellular matrix formation. *DMM Dis. Model. Mech.* **3**, 354–365 (2010).

413. Obara, T. *et al.* Polycystin-2 immunolocalization and function in zebrafish. *J. Am. Soc. Nephrol.* **17**, 2706–2718 (2006).

414. Bataille, S. *et al.* Association of PKD2 (Polycystin 2) mutations with left-right laterality defects. *Am. J. Kidney Dis.* **58**, 456–460 (2011).

415. Vick, P. *et al.* An Early Function of Polycystin-2 for Left-Right Organizer Induction in Xenopus. *iScience* **2**, 76–85 (2018).

416. Rachev, E. *et al.* CFAP43 modulates ciliary beating in mouse and Xenopus. *Dev. Biol.* **459**, 109–125 (2020).

417. Zhao, C. & Malicki, J. Genetic defects of pronephric cilia in zebrafish. *Mech. Dev.* **124**, 605–616 (2007).

418. Bui, K. H., Sakakibara, H., Movassagh, T., Oiwa, K. & Ishikawa, T. Molecular architecture of inner dynein arms in situ in Chlamydomonas reinhardtii flagella. *J. Cell Biol.* **183**, 923–932 (2008).

419. Burgess, S. A., Carter, D. A., Dover, S. D. & Woolley, D. M. The inner dynein arm complex: compatible images from freeze-etch and thin section methods of microscopy. *J. Cell Sci.* **100**, (1991).

420. King, S. J. & Dutcher, S. K. Phosphoregulation of an inner dynein arm complex in

Chlamydomonas reinhardtii is altered in phototactic mutant strains. *J. Cell Biol.* **136**, 177–191 (1997).

421. Neumüller, J. main topic Electron tomography-a tool for ultrastructural 3D visualization in cell biology and histology Elektronentomografie-Ein Verfahren zur 3D-Visualisierung von ultrastrukturellen Details in Zellbiologie und Histologie. *Wiener Medizinische Wochenschrift* **168**, 322–329 (2018).

422. Paredes, A. M. Microscopy: Scanning Electron Microscopy. in *Encyclopedia of Food Microbiology: Second Edition* 693–701 (Elsevier Inc., 2014). doi:10.1016/B978-0-12-384730-0.00215-9.

423. Smith, S. J. Q&A: Array tomography. *BMC Biology* vol. 16 98 (2018).

424. Jackson, C. L. *et al.* Accuracy of diagnostic testing in primary ciliary dyskinesia. *Eur. Respir. J.* **47**, 837–848 (2016).

425. Lucas, J. *et al.* ERS Task Force guideline for the diagnosis of primary ciliary dyskinesia. *Eur. Respir. J.* **49**, 1–54 (2016).

426. Tindall, R. Use and Disposal of Uranyl Acetate in the Electron Microscope Laboratory: Glow in the Dark or Walk in the Park? *Micros. Today* **12**, 40–41 (2004).

427. Kuipers, J. & Giepmans, B. N. G. Neodymium as an alternative contrast for uranium in electron microscopy. *Histochem. Cell Biol.* **153**, 271–277 (2020).

428. Benmeradi, N., Payre, B. & Goodman, S. L. Easier and Safer Biological Staining: High Contrast UranyLess Staining of TEM Grids using mPrep/g Capsules. *Microsc. Microanal.* **21**, 721–722 (2015).

APPENDICES

Supplementary information of Chapter 3

UA-Zero as a uranyl acetate replacement when diagnosing primary ciliary dyskinesia by transmission electron microscopy

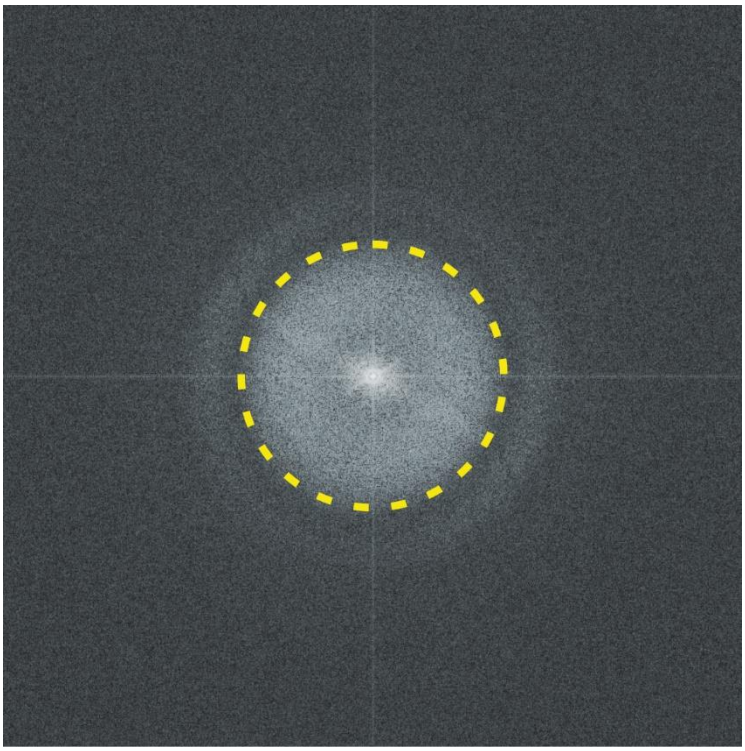

Supplementary Figure 1. Representative fast Fourier transform (FFT) used to set the defocus when images were acquired for the survey. All images were acquired with a defocus of 0.7µm avoiding beam astigmatism and sample drift.

Supplementary information of Chapter 4

PCD Detect: Enhancing ciliary features though image averaging and classification

The PCD Detect programs have been built for both 32- and 64-bit windows machines and are include in the supplementary zip files. The toolkit includes a guide (PCD Detect Guide.pdf) within the zip files and there are also compressed test images. These files are as following; PCD Detect 32-bit part 1.zip, PCD Detect 32-bit part 2.zip, PCD Detect 64-bit.zip, Test images for PCD Detect.zip. Supplementary figures, table and programs are available to download from Figshare; https://figshare.com/s/bc7920e94ad14fba2ee8.

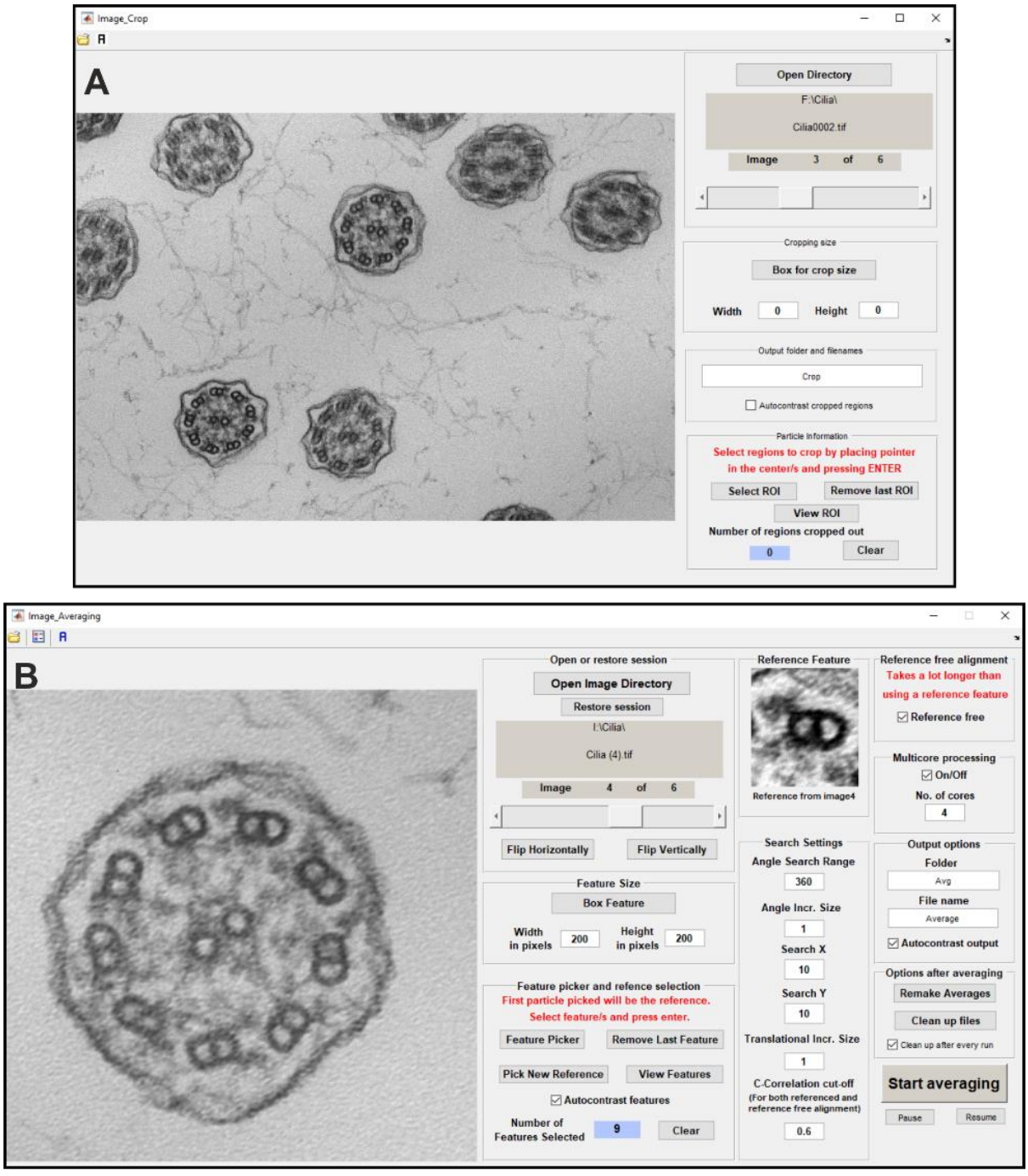

Supplementary Figure 1. PCD Detect Crop and Average screenshots. (A) Cilia Crop that has been designed to extract ciliary cross-sections from transmission electron microscopy images. (B) Cilia Average program used to pick cilia features (in this case MTDs) by performing a rotational and translational search before averaging them together.

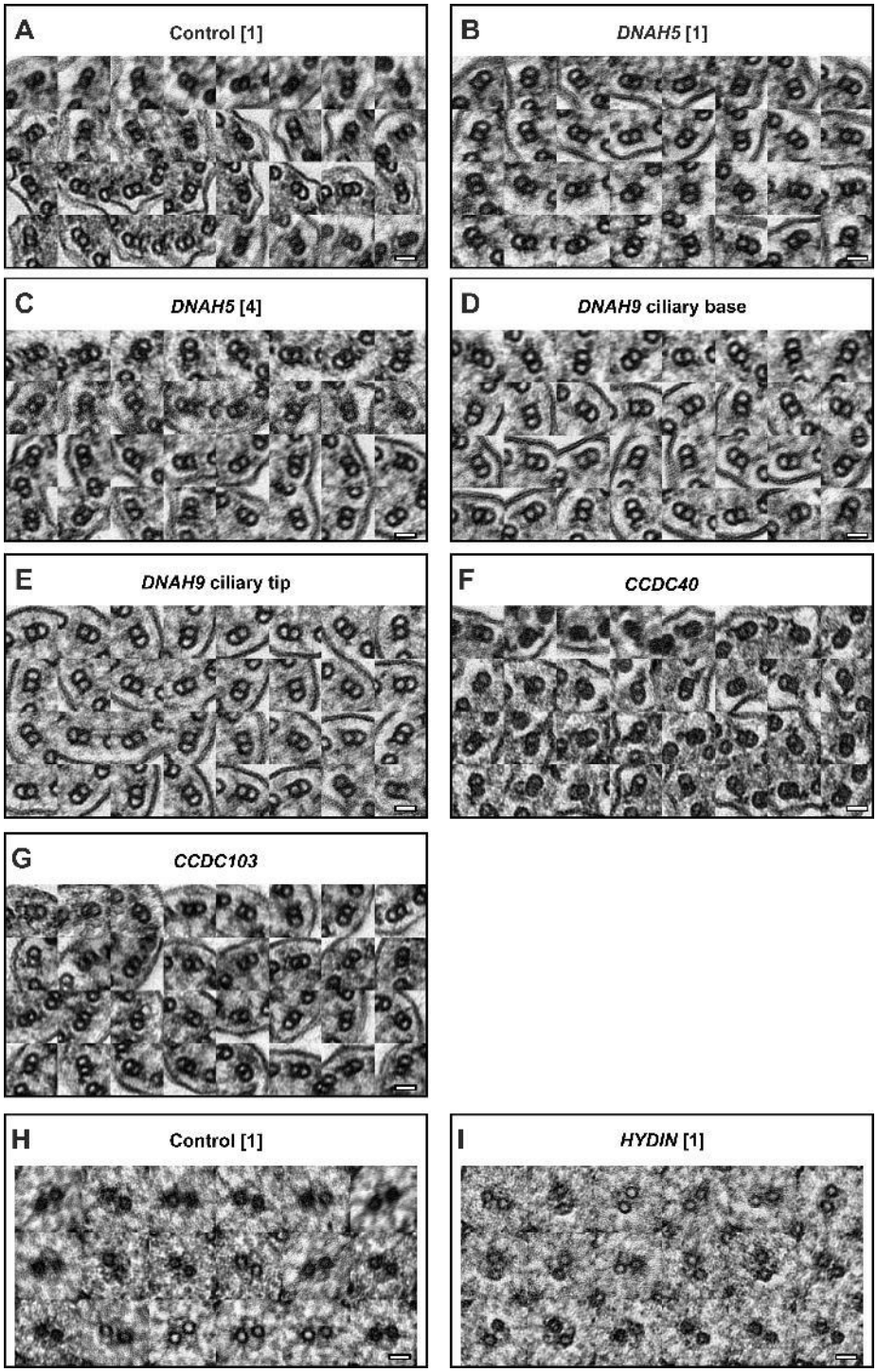

Supplementary Figure 2. Montages of some of the features (MTDs and CPs) of subjects carrying different gene mutations (Table 1) extracted by PCD Average before performing a rotation and translation search. Scale bars (A-I) 25nm.

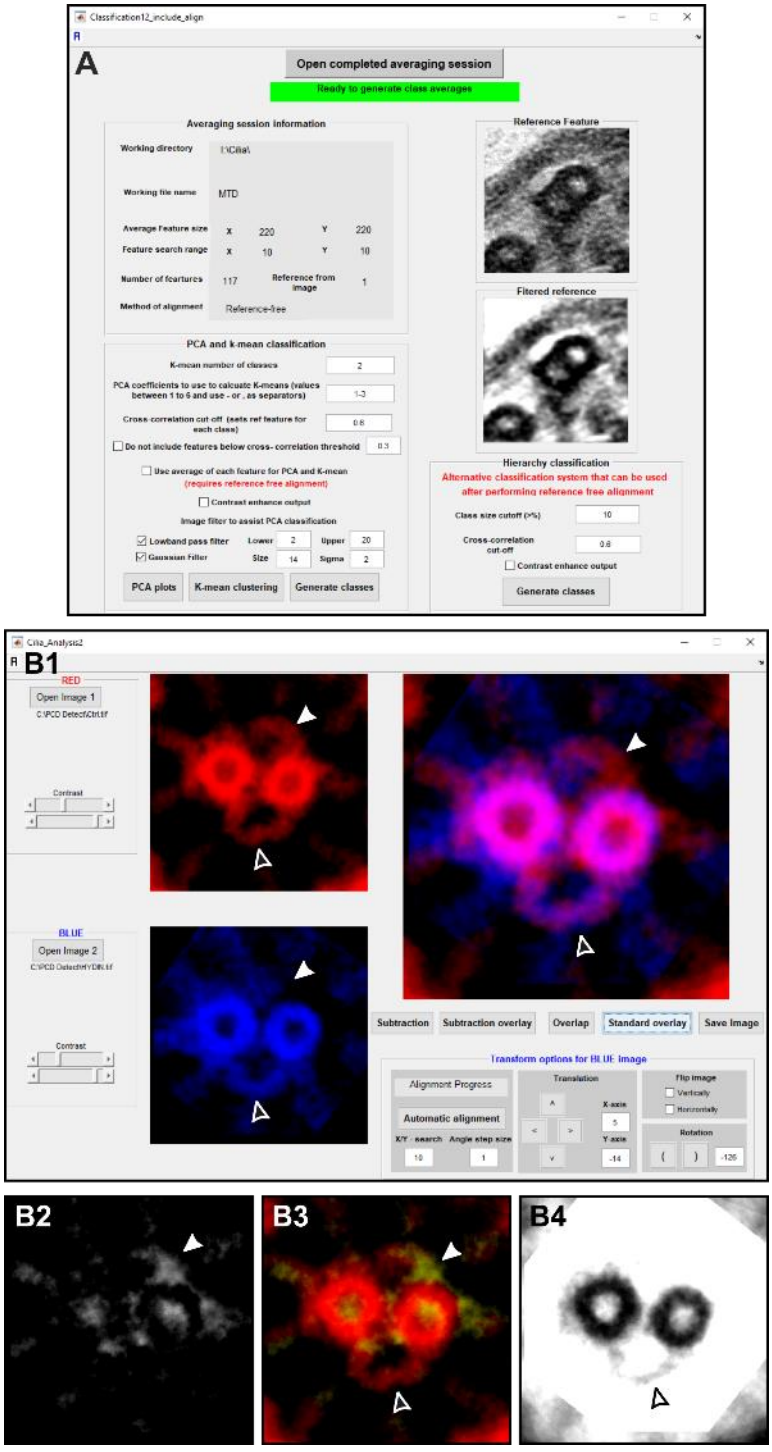

Supplementary Figure 3. Screenshots of PCD Detect Classification and Analysis programs. (A) Cilia Classification has been designed for subject samples that have a non-homogeneous defect in order to group images based on structural similarity, before generating a number of averaged outputs. (B) Analysis program designed to overlay images and highlight ciliary structural differences. The hollow arrowheads indicate the presence of the C1a and C2a CP complexes (see Figure 1). Whereas, the white arrow shows the position of the C2b CP component that is absent in the *HYDIN* case (in blue) compared to the control (in red). (B1) The program interface showing an overlay of two average images of the CP, control in red and a *HYDIN* defect in blue. (B1-B4) Shows the different images that can be generated by the program when comparing two averaged images. (B2) A subtraction image showing the difference between the red and blue images. (B3) The subtraction image overlaid (in yellow) onto the red image (image 1). (B4) Image showing overlapping detail from the two images.

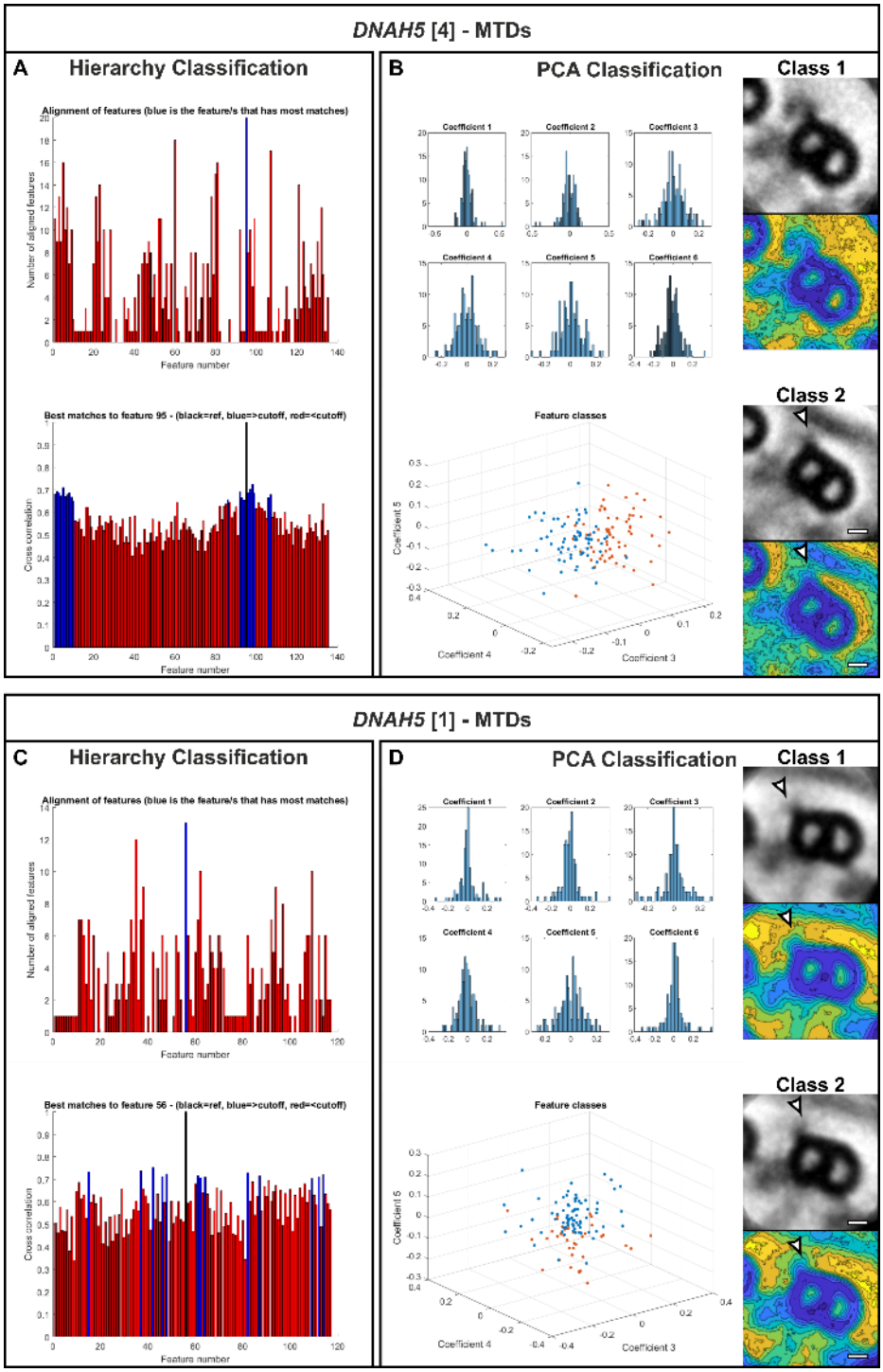

Supplementary Figure 4. The outputs from hierarchy and PCA classification of MTDs. (A-B) Classification outputs for a subject that has an atypical pathogenic variant in *DNAH5* and (C-D) pathogenic variants in *DNAH5*. (A, C) Graphs generated for hierarchy classification show the feature that has been picked as the reference and the corresponding features used to generate the first class average. (B, D) Graphs of the first six PCA coefficients calculated from MTD features, as well as cluster analysis using k-means to group the features into two classes. The white filled arrowheads indicate absence of the ODA. Scale bar (B, D) 10nm.

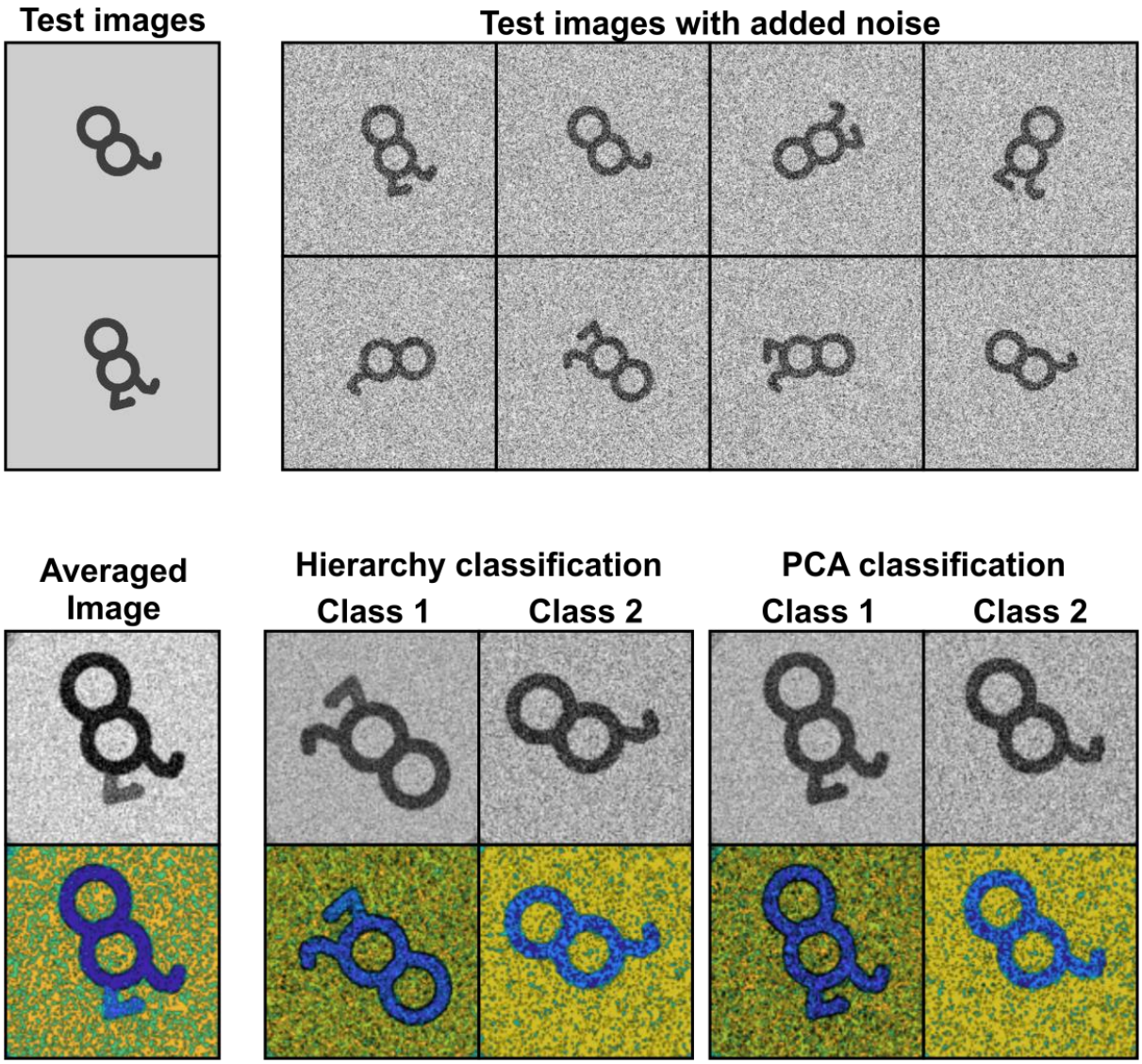

Supplementary Figure 5. Test of selected images with added noise that have been put through PCD Detect.

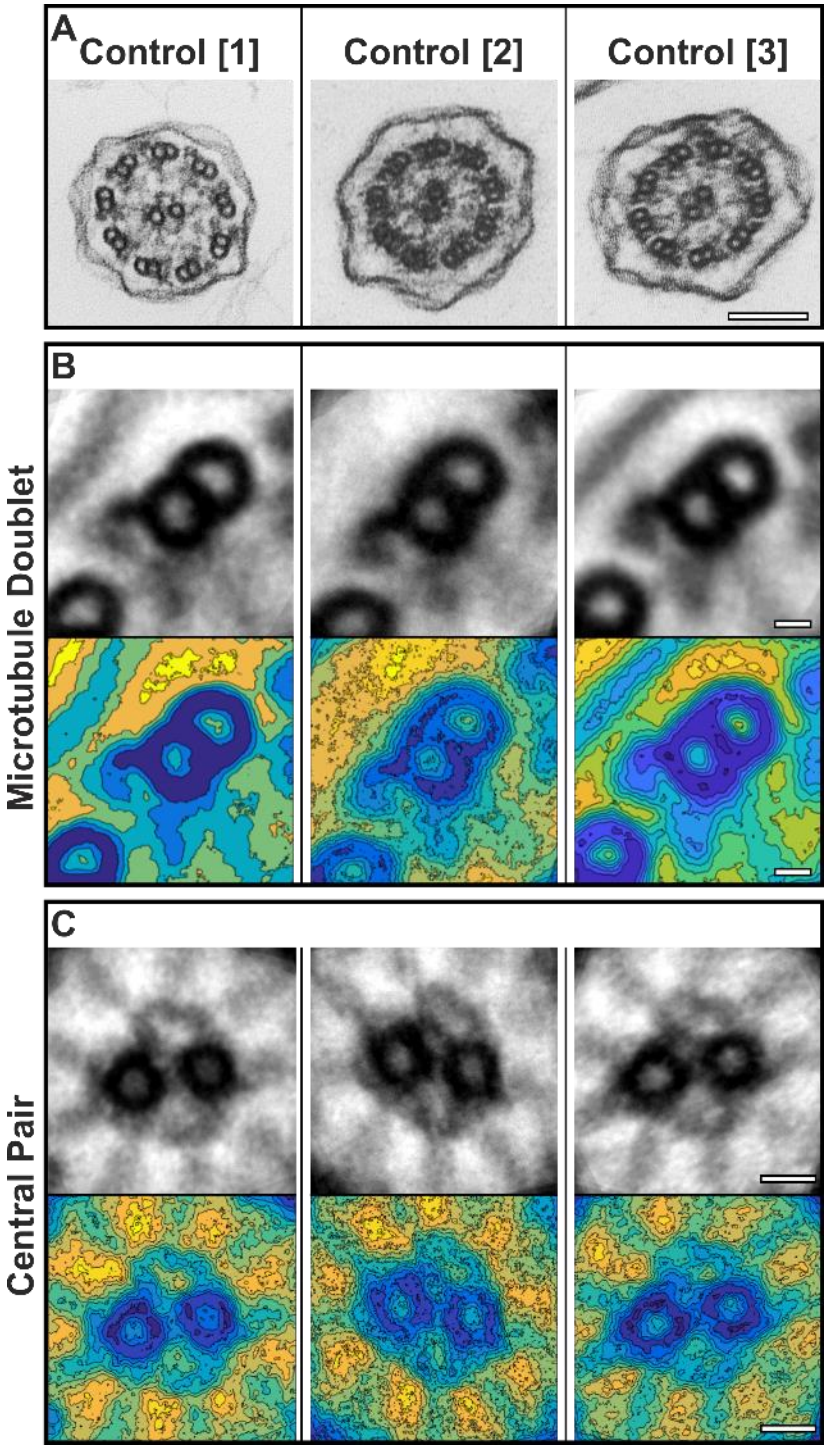

Supplementary Figure 6. Examples of averaged structures generated from healthy controls. Scale bars (A) 100nm (B-C) 10nm.

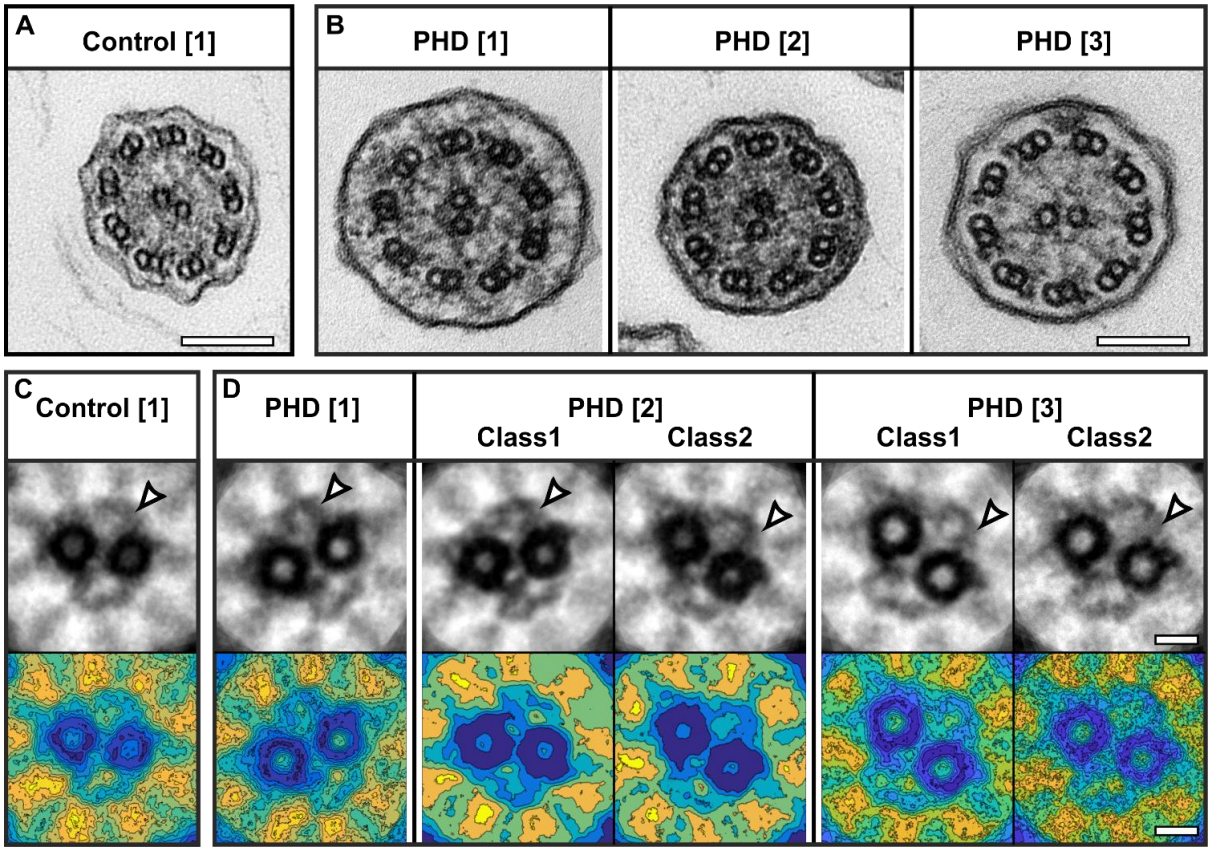

Supplementary Figure 7. Subjects predicted to have a potential *HYDIN* defect (PHD) were found to have present C2b CP component. (A) Cilia from a control healthy subject and (B) three subjects predicted to have a PHD. (C-D) Average CP structures from the subjects examined. When generating class averages using the same settings only one class is given for Control [1] and PHD [1], whereas multiple classes are given for PHD [2] and PHD [3]. This is likely to be due to a larger number of features input into PCD detect for PHD [2-3] leading to the detection of minor variations of the features including image tilt. Even so, there is no visible defect of the CP when comparing to the control. The white filled arrowheads indicate the position of the C2b CP component. Scale bars (A – B) 100nm and (C – E) 20nm.

Supplementary Table 1. Three cases that were studied using PCD Detect due to previous testing indicating a potential *HYDIN* defect (PHD). PHD [2] and PHD [3] are siblings.

Subject	Patients symptoms and clinical diagnostic criteria	Average nNO nL min^{-1} (Normal nasal nitric oxide (nNO) >77 nL min-1)	Average light microscopy CBF (Hz)	No of nasal brushing to make PCD diagnosis	Genotype	Number of ciliary images input into PCD detect to generate MTD and/or CP averages	Number of Features selected in PCD detect	Features used by PCD detect to generate final average
PHD [1]	Persistent, minimal ear problems and retinitis pigmentosa	53 (± 29 SEM)	11.50 (± 0.86 SEM)	4	No genetic information	CP – 28	CP - 28	CP - 14
PHD [2]	Rhinitis and wet cough, otitis media and hearing impairment.	424 (±170 SEM)	9.55 (± 1.40 SEM)	4	Seven variants of unknown significance (VUS) in *HYDIN*	CP – 63	CP - 63	Class 1 - 39 Class 2 – 19
PHD [3]	Later onset rhinitis	567	12.37 (± 1.84 SEM)	2	No genetic information	CP – 36	CP - 36	Class 1 - 23 Class 2 - 11

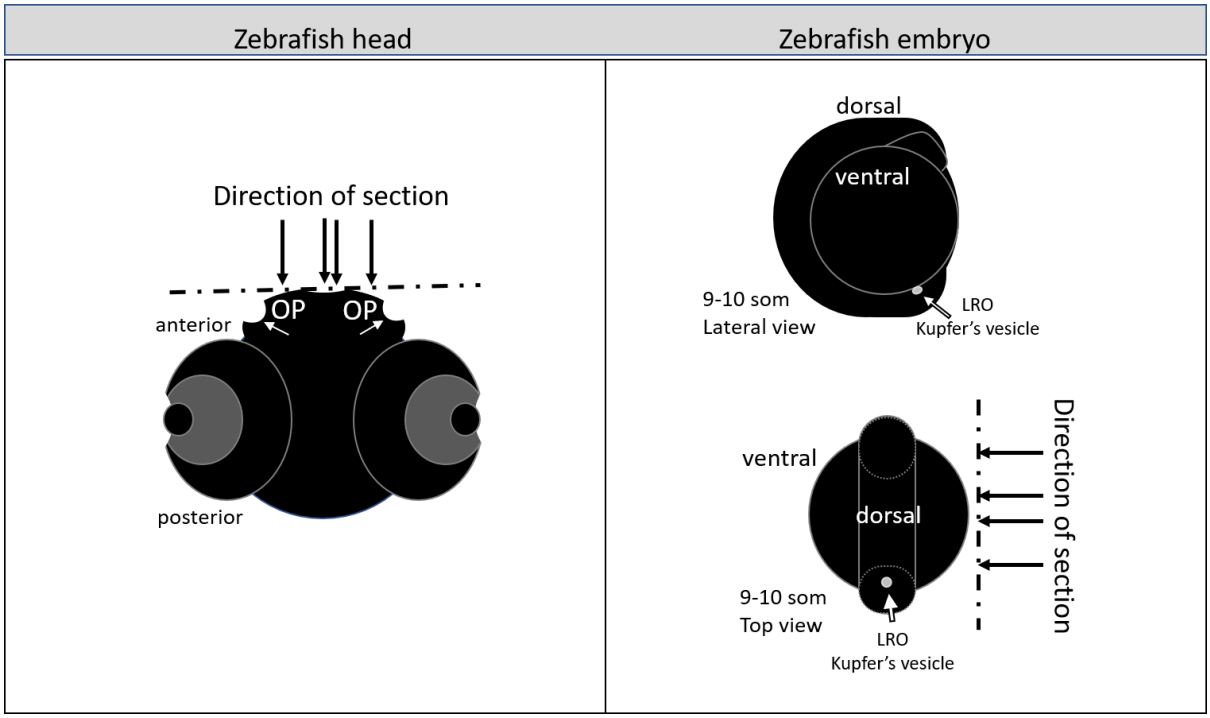

Supplementary Figure 1- 5-dpf Zebrafish head and 9-10 somite stage embryo diagrams showing the direction of section for obtaining thin sections for further Electron Microscopic evaluation.

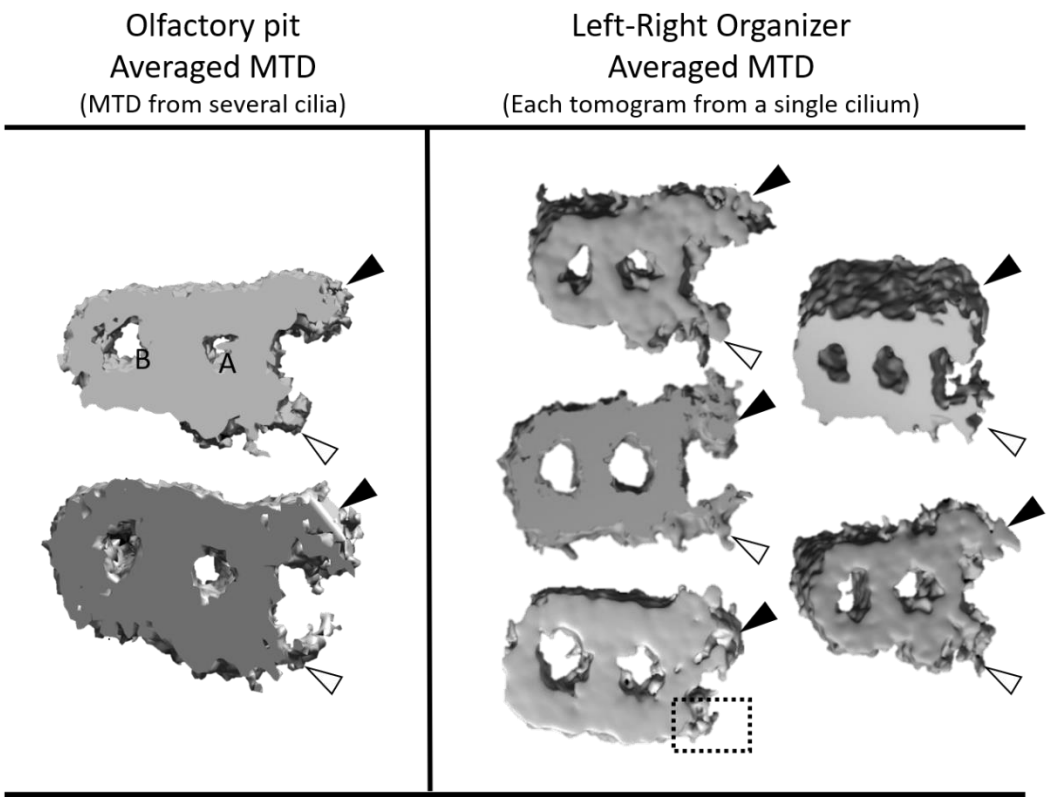

Supplementary Figure 2 - Models of the MTD, product of the tomogram acquisition of both LRO cilia and OP cilia. due to the fact the OP have multiciliated cells, It was possible to aquire tomograms containing several cilia, and so, these were averages together (9+ MTD per field of view), resulting In 2 sub-tomogram averagings assembled using Chimera. On the other hand, in the LRO, there was only one cilia per field of view, and subsequentially, only one cilia to average from (only 9 MTD were averaged per cilium) these too, were assembled in Chimera and models were generated. In Chimera the volume of the ODA was measured in comparisson to the total volume of the MTD using volume measurement tool. Black arrow heads – ODA; white arrow heads – IDA; dotted square – not visible IDA, maybe due to the low resolution of the image, or a location in the axoneme where the IDA was not repeating.

Supplementary data Table 1 - Human-Zebrafish homologue PCD genes as described in Ensemble.org [400]

PCD gene	Zebrafish transcript name	Zebrafish transcript ID
DNAH5	*dnah5-201*	ENSDART00000123150.4
	dnah5-202	ENSDART00000191818.1
CCDC114 (ODAD1)	*ccdc114-201*	ENSDART00000023745.8
ARMC4 (ODAD2)	*cr847789.1-201*	ENSDART00000186851.1
	armc4-201	ENSDART00000077453.5
	armc4-204	ENSDART00000170018.2
	armc4-203	ENSDART00000153115.2
	armc4-202	ENSDART00000152887.2
TTC25 (ODAD4)	*ttc25-201*	ENSDART00000080946.5
DNAH9	*dnah9-201*	ENSDART00000160926.2
DNAH11	*dnah11-201*	ENSDART00000148294.4
	dnah11-202	ENSDART00000020821.10
	dnah11-203	ENSDART00000138744.4
DNAI1	*dnai1.2-201*	ENSDART00000080431.5
	dnai1.2-202	ENSDART00000142468.3
	dnai1.1-205	ENSDART00000170205.2
	dnai1.1-201	ENSDART00000160163.2
	dnai1.1-204	ENSDART00000169676.2
	dnai1.1-202	ENSDART00000163063.2
	dnai1.1-203	ENSDART00000165798.2
DNAI2	*dnai2a-201*	ENSDART00000162579.2
	dnai2a-202	ENSDART00000164199.2
	dnai2b-203	ENSDART00000188726.1
	dnai2b-201	ENSDART00000003339.9
	dnai2b-202	ENSDART00000188648.1
DNAL1	*dnal1-203*	ENSDART00000188500.1
	dnal1-202	ENSDART00000156182.2
	dnal1-201	ENSDART00000043651.7
TXNDC3 (NME8)	*nme8-201*	ENSDART00000163684.2
CCDC103	*ccdc103-201*	ENSDART00000075493.4
	ccdc103-202	ENSDART00000132293.2
CFAP298 (C21orf59)	*cfap298-201*	ENSDART00000051197.6
	cfap298-202	ENSDART00000130093.3
	cfap298-203	ENSDART00000181950.1
CFAP300 (c11orf70)	*cfap300-201*	ENSDART00000151109.2
	cfap300-202	ENSDART00000192737.1
DNAAF1 (LRRC50)	*dnaaf1-201*	ENSDART00000145762.4
	dnaaf1-203	ENSDART00000173909.2
	dnaaf1-202	ENSDART00000173853.2
DNAAF2 (KTU)	*dnaaf2-201*	ENSDART00000167840.2
DNAAF3	*dnaaf3l-201*	ENSDART00000079233.5
DNAAF4 (DYX1C1)	*dnaaf4-201*	ENSDART00000165855.2
DNAAF5 (HEATR2)	*lo018183.1-201*	ENSDART00000194031.1
DNAAF6 (PIH1D3)	*pih1d3-201*	ENSDART00000056375.5
	pih1d3-203	ENSDART00000145388.3
	pih1d3-202	ENSDART00000136858.2
	pih1d3-204	ENSDART00000183524.1
	pih1d3-205	ENSDART00000191761.1
LRRC6	*lrrc6-203*	ENSDART00000188883.1
	lrrc6-202	ENSDART00000132346.3
	lrrc6-201	ENSDART00000075347.5
RPGR	*rpgrb-201*	ENSDART00000088624.5
	rpgrb-202	ENSDART00000124471.3
	rpgrip-201	ENSDART00000138541.3
	rpgrip-203	ENSDART00000190953.1
	rpgrip-202	ENSDART00000179003.2
	rpgrip1l-202	ENSDART00000185324.1

	rpgrip1l-201	ENSDART00000126326.5
SPAG1	*spag1b-201*	ENSDART00000101207.5
	spag1a-202	ENSDART00000185960.1
	spag1a-201	ENSDART00000130537.3
ZMYND10	*zmynd10-201*	ENSDART00000017413.10
	zmynd10-202	ENSDART00000189261.1
	zmynd10-203	ENSDART00000183251.1
CCDC39	*ccdc39-202*	ENSDART00000190769.1
	ccdc39-201	ENSDART00000169709.2
CCDC40	*ccdc40-202*	ENSDART00000169752.2
	Ccdc40-201	ENSDART00000164275.2
	Ccdc40-203	ENSDART00000182267.1
TTC12	*ttc12-201*	ENSDART00000156234.2
	ttc12-202	ENSDART00000157380.2
CCDC65 (DRC2)	*ccdc65-201*	ENSDART00000043946.8
	ccdc65-202	ENSDART00000177219.2
CCDC164 (DRC1)	*drc1-201*	ENSDART00000061829.5
GAS8	*gas8-202*	ENSDART00000170982.2
	gas8-201	ENSDART00000165126.2
CFAP221	not found in ZF	
DNAJB13	*dnajb13-204*	ENSDART00000148093.3
	dnajb13-201	ENSDART00000063365.6
	dnajb13-203	ENSDART00000139097.2
	dnajb13-202	ENSDART00000133505.2
HYDIN	*hydin-201*	ENSDART00000143265.4
	hydin-202	ENSDART00000145701.2
	hydin-203	ENSDART00000169861.2
	bx571975.1-201	ENSDART00000185269.1
NME5	*nme5-201*	ENSDART00000060998.6
RSPH1	*rsph1-201*	ENSDART00000160273.3
	ct573248.3-201	ENSDART00000181186.1
RSPH3	*rsph3-202*	ENSDART00000128823.5
	rsph3-201	ENSDART00000103394.3
RSPH4a	*rsph4a-201*	ENSDART00000097340.5
RSPH9	*rsph9-201*	ENSDART00000010903.8
STK36	*stk36-201*	ENSDART00000086765.5
	stk36-202	ENSDART00000139065.2
SPEF2	*spef2-201*	ENSDART00000159718.2
	spef2-202	ENSDART00000168984.2
CFAP57	*cfap57-201*	ENSDART00000080900.6
	cfap57-202	ENSDART00000149309.3
LRRC56	*lrrc56-202*	ENSDART00000161369.2
	lrrc56-201	ENSDART00000150364.2
GAS2L2	*gas2l2-201*	ENSDART00000112744.4
NEK10	*nek10-201*	ENSDART00000155162.2
OFD1	*ofd1-201*	ENSDART00000000552.12
CCNO	*fq311924.1-201*	ENSDART00000158096.2
FOXJ1	*foxj1b-201*	ENSDART00000126676.2
	foxj1b-203	ENSDART00000181942.1
	foxj1b-202	ENSDART00000153327.2
	foxj1a-201	ENSDART00000157772.2
	foxj1a-202	ENSDART00000168280.2
MCIDAS	*cu633857.1-201*	ENSDART00000192716.1